Investigating and Leveraging Machine Learning Techniques for High Energy Particle Identification and Reconstruction

Inaugural dissertation
of the Faculty of Science,
University of Bern

presented by

Meinrad Schefer

Supervisor of the doctoral thesis:
Prof. Dr. Hans Peter Beck
Albert Einstein Center for Fundamental Physics
Laboratorium für Hochenergiephysik
Physikalisches Institut

Investigating and Leveraging Machine Learning Techniques for High Energy Particle Identification and Reconstruction

Inaugural dissertation
of the Faculty of Science,
University of Bern

presented by

Meinrad Schefer

Supervisor of the doctoral thesis:
Prof. Dr. Hans Peter Beck
Albert Einstein Center for Fundamental Physics
Laboratorium für Hochenergiephysik
Physikalisches Institut

Accepted by the Faculty of Science.

Bern, **1st of October 2025**

The Dean
Prof. Dr. Jean-Louis Reymond

Abstract

Recent advances in artificial intelligence have revolutionised data analysis across scientific disciplines, and high energy physics is no exception. This thesis explores advancements in experimental particle physics through the integration of machine learning techniques in high energy physics experiments and simulations. The Standard Model of particle physics and the general theory of relativity are representing our current understanding of physics, however there are observations left unexplained. Phenomena, such as the matter-antimatter asymmetry, neutrino oscillations and the presence of dark matter, motivate the search for physics beyond the Standard Model. These searches are often heavily relying on advanced simulation tools and novel AI technologies, providing and classifying key signatures. The ATLAS experiment at the Large Hadron Collider plays a crucial role in searching for physics beyond the Standard Model, such as Supersymmetry, by applying sophisticated data acquisition and analysis techniques.
A major contribution of this work is the application of the NeuralRinger algorithm for forward electron identification in ATLAS. By extending this machine learning based approach to regions of high pseudorapidity, electron reconstruction can be significantly improved, enhancing event selection for physics analyses. To further refine its performance, the NeuralRinger was integrated into the Lorenzetti Showers framework, a novel and highly flexible calorimetry simulation tool. Facilitating the NeuralRinger for forward regions in that framework allowed for further developments of the simulation tool and for direct comparison with the corresponding ATLAS studies. Finally, this thesis presents a search for pair production of the supersymmetric top squark in all-hadronic final states, utilising signatures identified by a novel graph neural network tool, recently developed within ATLAS. The promising results of the studies presented in this thesis, which are collectively relying on machine learning techniques, demonstrate the growing role of AI-driven methodologies in experimental particle physics. They offer improved detection capabilities and enhance the search for new physics beyond the Standard Model.

Acknowledgements

Doing this PhD was a very interesting and exciting experience for me. Participating in ATLAS, one of the world's largest research collaborations, offered me countless fascinating insights. Additionally, I was able to explore a whole new part of earth thanks to the collaborative effort with several Brazilian research groups. Therefore, I want to thank all the people very much who guided me, or helped me, or participated with me in the projects I am now able to present in this thesis.

Firstly, I want to thank Hans Peter for supervising me through the last years, for discussing so many relevant topics in physics and beyond physics, and for discovering remote corners in Brazil together.
Then, I would like to give my thanks to Eduardo for being my external referee, helping me with my Lorenzetti project, and for showing me the beautiful city of Salvador.
I also want to give my thanks to Prof. Dr. Thomas Becher for being the ceremony master of my defence.

Special thanks go to Michele for being a great leader of the Bern ATLAS group, to Bernardo for helping me a lot in the beginning of my PhD and for organising my stay in Nova Friburgo, to Augusto for guiding me and Hans Peter around in Rio and in Juiz de Fora, to Juan for helping me so much with the NeuralRinger and Lorenzetti, to Seixas for coordinating so many efforts on the NeuralRinger, and to Silke for proofreading my thesis.

Furthermore, I want give my thanks to all the people of the Stop team, who helped me with my analysis project, thank you Aaron, Jonas, Marco, Claudia and Daniele.
More thanks go to the people of the egamma and the HLTcalo teams who helped me with my qualification task. Thank you Chris, Fernando, Denis, Joao, Micael, Batool and Edmar.
Then, I also want to thank all the people who I met at CERN and with whom I spent many nice lunchtimes and breaks. Thank you Antonio, Kevin, Lucas, Lucca, Pedro, Camila, Catarina, Melissa, Carolina, Clara, Gabriel, Luis, Andre, Gabriela, Gustavo, Carlos, and many more.

Further thanks go to all the people who were in the Bern ATLAS group or participated in our weekly meetings. Thank you Lea, Roman, Armin, Megh, Laura, John, Saverio, Isidre, Lucas, Marianna, Una and Joseph.
I also want to give my thanks to the LHEP IT people for their invaluable support, thank you Gianfranco, Marco and Filippo.
Then, I want to thank all the LHEP people for sharing this great particle physics division and for always keeping a very nice atmosphere in our common break room B52.
And very special thanks go to Ursula and Marcella for helping everybody in LHEP so much with their administrative work.

Lastly, I want to thank all the people who I forgot to mention but also contributed in one way or the other to the effort presented here. Thank you all so much!

Statement on the Supportive Use of ChatGPT

During the preparation of this thesis, OpenAI's ChatGPT was employed as a supplementary tool to assist with several non-analytical aspects of the writing process. The use of ChatGPT was limited to tasks such as summarising scientific texts and background literature, rephrasing content to enhance clarity and readability, locating preliminary source material, and aiding in certain formatting-related aspects, including reference organisation and general structuring. These applications were intended to streamline the writing and editorial process, allowing for more efficient communication of complex physical concepts and the overall flow of the thesis.

It is important to note that ChatGPT was not used for any critical or interpretive work related to the scientific studies or data presented in this thesis. In particular, it did not contribute to the design, guidance, execution, or analysis of the research, nor was it used to interpret results, evaluate theories, or draw conclusions from experimental or simulated data. All scientific reasoning, theoretical discussions, data interpretations, and final conclusions presented herein are the result of the author's own work and understanding, in accordance with academic standards and scientific integrity.

Contents

Introduction

Particle physics seeks to uncover the fundamental building blocks of nature and their interactions, driving forward our understanding of the universe at its most fundamental level. While the Standard Model (SM) has successfully explained numerous experimental observations, there are still some phenomena left unexplained, such as the matter-antimatter asymmetry. Therefore, new physics models Beyond the Standard Model (BSM) are suggested and investigated. This pursuit has led to extensive theoretical and experimental efforts, with the Large Hadron Collider (LHC) at the European Organization for Nuclear Research (CERN) serving as the world's most advanced tool for exploring the frontiers of high-energy physics [1].

The ATLAS experiment, one of the LHC's flagship detectors, is designed to analyse high-energy proton-proton collisions to probe both, SM predictions and potential signatures of new physics [2]. Operating at the highest energy scales ever achieved in a laboratory setting, ATLAS provides a unique platform for testing theoretical models, including Supersymmetry (SUSY), which offers solutions to several open questions in particle physics [3]. As collision rates and hence data volumes increase, the challenge of extracting meaningful signals from vast amounts of background noise requires sophisticated detection, reconstruction, and analysis techniques.

Recently, ground-breaking advancements in the development and application of AI through Machine Learning (ML) were made. These techniques have been increasingly employed and further evolved for specific purposes in various physics environments. ML strategies are now widely embedded in both, hardware and software of particle detector experiments such as ATLAS, optimising data selection, event reconstruction and physics analyses [4]. All the studies this thesis is based on, were either applying or utilising ML techniques. The first study investigated the extension of an ML based electron identification algorithm, used for event selection, into the more challenging forward regions of the ATLAS detector. For the second project, a novel calorimeter detector simulation tool was used to simulate the conditions, faced in the first study. Then, the same ML strategy was applied to identify electrons in these simulations and thereby further testing both, the algorithm and the simulation tool. In the last study, independent from the other two, recent ATLAS data was examined in order to look for signatures matching the ones coming from specific SUSY models. This new ATLAS data, obtained from simulated and actual collision events, was reconstructed using a cutting edge Graph Neural Network (GNN) identifier, able to recognise key signatures efficiently [5].

This thesis is structured into six chapters, addressing critical aspects of particle physics, experimental techniques, and advanced data analysis methods. Chapter 1 provides an overview of the SM with all its particles. It discusses phenomena which cannot be explained with our current understanding of physics, emphasizing the motivations for extending the SM with theories such as SUSY. The concept of superpartners is introduced and it is discussed how the Minimal Supersymmetric Standard Model (MSSM) can resolve key theoretical issues such as the hierarchy problem and the nature of dark matter.
Chapter 2 describes the LHC and the ATLAS experiment, detailing their purpose and functionalities. Special attention is given to the major components of the ATLAS detector, in particular the Inner Detector (ID), the calorimeters, and the muon spectrometer. Additionally, this chapter discusses past and future upgrades to both, the LHC and ATLAS, ensuring that the experiment remains at the forefront of high-energy physics research.
Chapter 3 focuses on the ATLAS Trigger and Data Acquisition (TDAQ) system, which is responsible for selecting and processing relevant events from the vast number of collisions occurring within the LHC. Given the high collision rate of the LHC, an efficient triggering system is crucial for identifying events that could contain signatures of new physics. The chapter outlines the multi-level trigger architecture, data processing techniques, and the role of advanced algorithms in optimising data collection. Furthermore, the most important signatures for analyses with ATLAS data are discussed, and how they are reconstructed.
The last three chapters of this thesis explore the specific research contributions, aimed at enhancing particle identification and searching for new physics. Chapter 4 examines the extension of the NeuralRinger algorithm for forward electron identification in the ATLAS experiment. Traditionally, electron reconstruction in the forward regions of the ATLAS detector has been challenging due to increased background noise and reduced detector granularity. The NeuralRinger, an ML based approach, significantly improves electron identification by analysing calorimeter ring patterns [6]. This work extends the NeuralRinger's applicability to the forward detector regions, demonstrating its effectiveness in enhancing event selection and data quality.
Chapter 5 builds on this by integrating the NeuralRinger into the Lorenzetti Showers framework, a powerful calorimetry simulation tool [7]. Lorenzetti Showers provides a detailed modelling environment for studying electromagnetic and hadronic showers, enabling refined investigation and optimisation of particle identification techniques. This framework allows to set all the relevant parameters as required to imitate the conditions investigated in the NeuralRinger study for ATLAS. By comparing both studies, their results can be more easily validated and the capabilities of Lorenzetti Showers simulations can be tested and evaluated.

Finally, Chapter 6 focuses on the search for top squark pair production in all-hadronic final states. The top squark is very interesting for SUSY searches, as it is predicted to be the lightest quark superpartner in many models and therefore it is one of the supersymmetric particles with the highest probability to be produced in LHC collisions. In the considered models, the top squark is decaying into a top quark and a neutralino, which makes an excellent dark matter candidate. These neutralinos can only be seen indirectly with the ATLAS detector through the absence of energy depositions. Since top quark signatures can now be identified more efficiently with the application of a novel GNN architecture, searches like this one are potentially gaining a lot of sensitivity. It is anticipated that this still ongoing analysis can significantly contribute to the efforts to constrain SUSY parameter space and guide future searches at the LHC.

Taken together, these contributions highlight the more and more essential role of ML in experimental particle physics. Through the integration of sophisticated algorithms into traditional analysis frameworks, this thesis demonstrates how modern methods can enhance object reconstruction, improve search sensitivity, and prepare the ATLAS experiment for the challenges of future high-energy collisions. By handling experimental challenges with advanced computational techniques, this research contributes to the broader goal of understanding the fundamental structure of the universe and potentially unveiling physics beyond the SM.

Chapter 1

The Standard Model and Supersymmetry

Over the past century, the SM of particle physics has been developed to explain the nature of elementary particles and their interactions. This extensive framework successfully describes electromagnetic, weak, and strong interactions, but notably does not include gravity. Additionally, the SM systematically classifies all known elementary particles. As a quantum field theory, it depicts elementary particles as discrete excitations of underlying fields. Experimental results have consistently confirmed the SM's predictions, including the discovery of all predicted particles, such as the Higgs boson in 2012 [8]. This chapter explores elementary particles and their interactions, then it examines unexplained physics phenomena. It also discusses extensions of the SM, with a particular emphasis on supersymmetric models, and concludes by explaining the motivations for introducing SUSY.

1.1 The Elementary Particles

Elementary particles are the smallest indivisible components of matter. These fundamental particles are classified into two categories, fermions and bosons. Fermions obey Fermi-Dirac statistics and are governed by the Pauli exclusion principle, with a half-integer spin quantum number. There are 12 fermionic elementary particles, consisting of six types of quarks and six types of leptons.

Quarks are further divided based on their fractional electric charges. Three quarks have a charge of $+2/3$, known as "up-type" quarks, while the other three have a charge of -1/3, known as "down-type" quarks [9]. These fractional charges are expressed in terms of the elementary charge, defined as the negative charge of an electron of -1.602 $\cdot$ 10^{-19} C. To simplify expressions of masses and spins of elementary particles, universal constants like the speed of light (c) and the reduced Planck constant ($\hbar$) are normalized to 1, what is known as their "natural units". The quarks are grouped into three generations. The lightest quarks, known as

the first-generation quarks, are the positively charged up quark and the negatively charged down quark. The second-generation quarks include the positively charged charm quark and the negatively charged strange quark. The third generation consists of the heaviest quarks, the positively charged top quark and the negatively charged bottom quark. The top quark, with a mass of 173.1 GeV, is the heaviest particle in the SM. Each quark has a corresponding antiquark with opposite charge.
Leptons are classified into three charged and three neutral types. The charged leptons, electrons, muons, and taus, each have an intrinsic electric charge of -1 in units of the elementary charge. Each of these charged leptons has a corresponding neutrino, which is a neutral lepton. These neutrinos are named based on their associated charged lepton, referred to as their flavour. For instance, the neutrino associated with the muon is called the muon neutrino. Neutrinos are significantly lighter than the charged leptons and all other SM particles. There are three distinct neutrino mass states which are in superposition. Depending on this superposition a neutrino has a certain probability to interact with each of the three flavour states. The composition of the mass states can be described with phases. These phases advance while neutrinos propagate through space. That changes the probability of a neutrino to interact with a certain flavour, which is known as neutrino oscillation. Like quarks, each lepton has a corresponding antilepton, carrying a charge opposite to that of their leptonic counterparts. Table 1.1 provides a summary of all SM fermions categorized by their generation.

Classification		Generation		
		I	II	III
Up-type quarks charge $\frac{2}{3}$, spin $\frac{1}{2}$	Name Symbol Mass	up u 2.16 MeV	charm c 1.27 GeV	top t 172.57 GeV
Down-type quarks charge $\frac{-1}{3}$, spin $\frac{1}{2}$		down d 4.7 MeV	strange s 93.5 MeV	bottom b 4.18 GeV
Charged leptons charge -1, spin $\frac{1}{2}$		electron e 0.511 MeV	muon μ 105.66 MeV	tau τ 1.78 GeV
Neutral leptons charge 0, spin $\frac{1}{2}$		electron neutrino ν_e $<$ 0.8 eV	muon neutrino ν_μ $<$ 0.8 eV	tau neutrino ν_τ $<$ 0.8 eV

Table 1.1: All SM fermions listed with their corresponding notation and mass from [9]. They are sorted by their generation and the quarks in their up or down type and the leptons in charged or neutral.

Gauge bosons are fundamental particles with a spin quantum number of 1. These include the photon and gluons, which are massless and electrically neutral. The massive Z boson is also electrically neutral, while the massive W^+ boson carries a charge of $+1$, and the W^- boson carries a charge of -1. The Higgs boson is unique among fundamental bosons as it is not a mediator of one of the SM forces. It is a scalar particle with a spin quantum number of 0 and, with a mass of around 125 GeV, it is the second heaviest elementary particle in the SM after the top quark. The Higgs boson results from an excitation of the Higgs field, which is essential for explaining the masses of particles in the SM. The Higgs field was introduced to account for the masses of the bosons mediating the weak force (W^+, W^-, Z^0), which would otherwise need to be massless to maintain gauge invariance. The process by which the weak gauge bosons gain mass through interaction with the Higgs field is known as the Brout-Englert-Higgs mechanism [10]. Thereby, the SM particles' masses are obtained through couplings with the Higgs field. The more massive particles have stronger couplings. Table 1.2 lists all the SM bosons, detailing their notation, mass, intrinsic charge and spin.

	Gauge bosons					Scalar boson
Name	photon	W^+ boson	W^- boson	Z boson	gluon	Higgs boson
Symbol	γ	W^+	W^-	Z^0	g	h
Mass	0	80.37 GeV	80.37 GeV	91.19 GeV	0	125.2 GeV
Charge	0	1	-1	0	0	0
Spin	1	1	1	1	1	0

Table 1.2: List of all the SM bosons. They are divided in gauge and scalar bosons and their properties in notation, mass, charge and spin are indicated [9].

1.2 Standard Model Interactions

The SM is a gauge theory, meaning that its interactions are mathematically described by gauge fields with corresponding symmetries [11, 12]. For the electromagnetic, weak and strong interactions they are U(1) × SU(2) × SU(3). The different gauge symmetries define the behaviour and properties of the fundamental forces. For each type of interaction, there is an associated conserved charge, the electric charge (Q) for electromagnetic interactions, the third component of the weak isospin (T_3) for weak interactions, and the colour charge (C) for strong interactions. In this framework, the forces of the SM are mediated by specific particles known as gauge bosons, which act as force carriers.

For electromagnetic interactions described by Quantum Electrodynamics (QED), the force is carried exclusively by the photon, a massless particle. On the other hand, the weak force is transmitted by the three massive gauge bosons, the Z boson, the W^+ boson and the W^- boson. Each of these plays a distinct role in mediating weak interactions. The W^+ and W^- bosons are responsible for interactions that involve the transfer of electric charge, facilitating processes where particles change their charge state. In contrast, the Z boson, which is electrically neutral, mediates neutral weak interactions, where no charge exchange occurs. Interestingly, the electromagnetic and weak forces are not entirely separate. In the SM they are unified into a single framework called the electroweak interaction, which describes both forces as different aspects of the same underlying phenomenon. This unification is possible because the electroweak force is carried by four gauge bosons, W_1, W_2, W_3 and B^0. Specifically, the W^+ and W^- bosons of the SM are superpositions of the W_1 and W_2 states, which are given by

$$W^{\pm} = \frac{1}{\sqrt{2}}(W_1 \mp iW_2). \tag{1.1}$$

The mass eigenstates of the Z boson and the photon are derived by mixing the gauge eigenstates W_3 and B^0. This mixing is achieved through the Weinberg angle θ_W by

$$\begin{pmatrix}\gamma\\ Z\end{pmatrix} = \begin{pmatrix}\cos(\theta_W) & \sin(\theta_W)\\ -\sin(\theta_W) & \cos(\theta_W)\end{pmatrix}\begin{pmatrix}B^0\\ W_3\end{pmatrix}. \tag{1.2}$$

This can be viewed as a rotation into a different basis. The Weinberg angle, also known as the weak mixing angle, is experimentally determined to be $\sin^2(\theta_W) = 0.231$ [9].

Quantum Chromodynamics (QCD), based on the SU(3) gauge symmetry, describes the strong interactions which are mediated by eight distinct types of gluons. These interactions take place between elementary particles that carry colour charge, namely quarks and gluons. The colour charge, which is a fundamental property of the strong force, is represented by one of three colours red, blue, or green. Quarks always possess one of those three colour charges, whereas antiquarks have an anticolour charge as in antired, antiblue or antigreen. Gluons, in turn, possess a combination of colour and anticolour charges, such as red and antigreen. Due to the non-abelian nature of the strong force, particles with colour charge cannot exist in isolation. The coupling of the strong force increases the further quarks and gluons are separated. For instance, quarks that are produced in an interaction immediately undergo a process known as hadronisation (see subsection 3.3.2), where they combine to form colour-neutral hadrons. In this regard, the strong interaction differs from all other known forces which become weaker the more two interacting particles are separated.

For now, the SM has been very effective in describing the known fundamental particles and three of the four forces in the universe. It is the most extensively tested theory of particle physics, and experiments over decades have confirmed its predictions with remarkable precision. Figure 1.1 shows the proton-proton collision cross section summary of various processes measured by the ATLAS experiment at CERN. This describes the effective area a particle is presenting for a specific type of process, which tells us with what probability the corresponding processes takes part in a collision event. It can be seen that the vast majority of cross sections correspond very well with the given theoretical predictions of the SM.

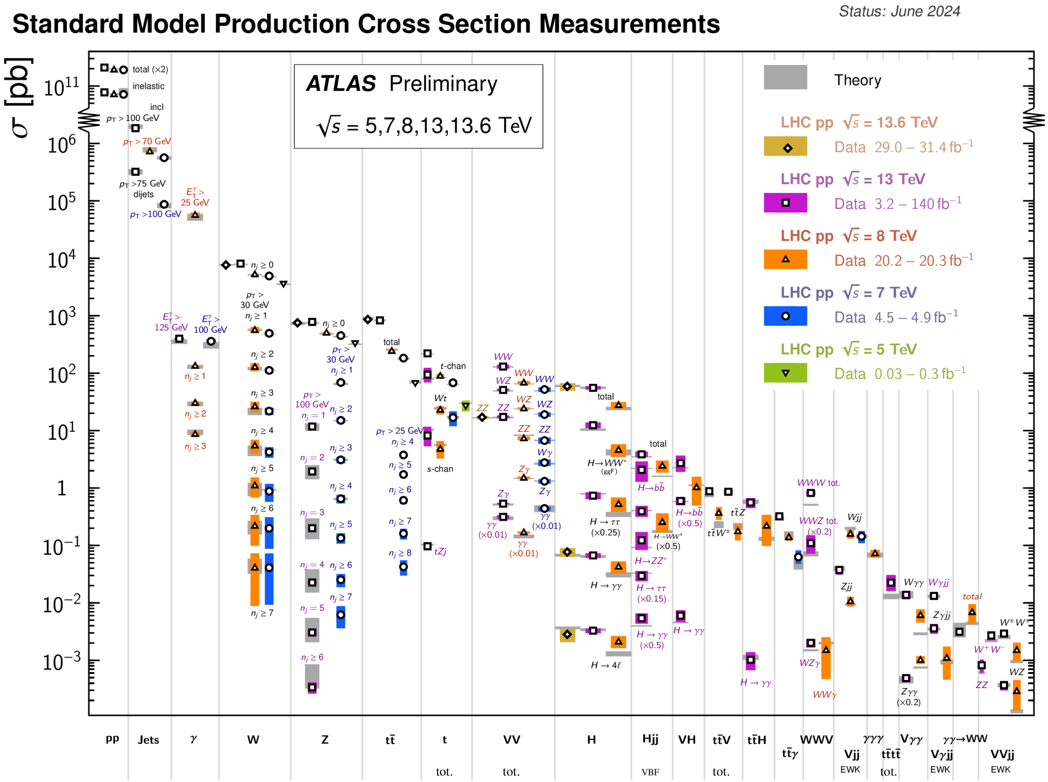

Figure 1.1: Standard Model production cross section measurement summary of the ATLAS experiment from [13]. This overview lists a selection of highly relevant measured production cross sections together with their theoretical values from Standard Model predictions.

1.3 Unexplained Physics Phenomena

Despite the successful experimental validation of the SM and general relativity [14], both theories combined fall short of explaining all observed phenomena [15]. For instance, numerous cosmological observations suggest the existence of an unknown component termed dark matter. One prominent example comes from observing the rotation velocities of galaxies. In most galaxies, visible matter appears to be concentrated in the central region, typically around a black hole. Based on this distribution, it would be expected that the velocities of stars orbiting a galactic centre would diminish with distance, similar to the velocity pattern of planets orbiting in our solar system, which follow Kepler's laws. These laws predict that velocities should decrease with the square root of the radius to the centre. Yet, observations reveal that the rotational velocities of stars in a galaxy remain nearly constant, regardless of their distance from the galaxy's centre. This phenomenon suggests a mass distribution within the galaxy that is more or less uniform, rather than concentrated at the centre. Such a pattern implies the presence of invisible, evenly distributed matter.

According to data from the Planck space observatory, approximately 31.5% of the universe's energy content exists in the form of matter, with dark matter constituting about 85% of the total matter [16]. Among the leading candidates for dark matter particles are Weakly Interacting Massive Particles (WIMPs), which would need to be extremely stable to account for such a substantial fraction of the universe's mass.
Additionally, other cosmological observations indicate that the universe is expanding at an accelerating rate, a phenomenon potentially explained by introducing the concept of dark energy, a force not accounted for within the SM and the general theory of relativity.

Another phenomenon left unexplained by the SM is the perceived imbalance between matter and antimatter in the observable universe. It is known as the matter-antimatter asymmetry, with antimatter being significantly scarce. This suggests that the Big Bang did not generate equal amounts of matter and antimatter, though no definitive explanation has been established for this imbalance. Additionally, the SM does not clarify why the Higgs boson has a mass of 125 GeV, as noted in Section 1.1, nor does it account for the specific masses observed in SM particles or explain why neutrinos have such small masses compared to other particles. Finally, the SM does not encompass gravitational theory as formulated by Einstein's general relativity. To address these gaps and provide theoretical insights into these phenomena, theorists have proposed various models that extend beyond the SM.

1.4 Supersymmetry as a Standard Model Extension

Among the most popular extensions to the SM are theories based on supersymmetry (SUSY) [3]. SUSY introduces a symmetry between fermions and bosons, which means that each SM boson is paired with a new fermionic partner, and each SM fermion with a new bosonic partner. These partner particles are referred to as superpartners. Since fermions have half-integer spins and bosons have integer spins, the superpartners differ in spin from their SM counterparts by 1/2. To switch a fermionic state into a bosonic state, or vice versa, SUSY employs an anti-commuting spinor operator Q with the following operations

$$Q\,|\text{Boson}\rangle = |\text{Fermion}\rangle\,, \quad Q\,|\text{Fermion}\rangle = |\text{Boson}\rangle\,. \tag{1.3}$$

Since Q is a complex spinor, it is possible to define its Hermitian conjugate operator $Q^\dagger$. Together, these operators follow specific commutation and anti-commutation relations given by

$$\{Q, Q^\dagger\} = P^\mu \tag{1.4}$$
$$\{Q, Q\} = \{Q^\dagger, Q^\dagger\} = 0 \tag{1.5}$$
$$\{P^\mu, Q\} = \{P^\mu, Q^\dagger\} = 0, \tag{1.6}$$

where P^μ is the conserved four-momentum generator of spacetime translations. In a supersymmetric theory, every particle state is part of a supermultiplet along with its superpartner. These supermultiplets are irreducible representations of the SUSY algebra. Since the squared mass operator, $-P^2$, commutes with both, Q and $Q^\dagger$, all particles within a single supermultiplet must share the same mass. If SM particles and their supersymmetric partners had identical masses, SUSY would be considered an "unbroken symmetry". However, since no supersymmetric particles have been observed thus far, their masses must differ from those of their SM counterparts, assuming they do exist. Thus, SUSY must be a broken symmetry.

1.5 The Minimal Supersymmetric Standard Model

One of the most prominent supersymmetric models is the MSSM, which introduces the smallest possible set of new parameters to transform the SM into a supersymmetric framework [3]. In this model, the supersymmetric partners of SM particles are denoted by the same symbol but marked with a tilde.

To account for the distinct behaviour of the SM fermions' left- and right-handed components under gauge transformations, each component is paired with two scalar fields within supermultiplets. These supermultiplets, containing a two-component fermion and a complex scalar, are referred to as chiral multiplets. The scalar superpartners of SM particles are given names similar to their SM counterparts, prefixed with an "s". For example, the superpartner of the top quark t is the stop ($\tilde{t}$), and the superpartner of the electron e is the selectron ($\tilde{e}$), categorized as a squark or a slepton, respectively. The MSSM's chiral supermultiplets are detailed in Table 1.3. Additionally, their degrees of freedom with respect to SU(3) for strong interactions, SU(2) for weak interactions, and the electroweak hypercharge Y are given. The hypercharge Y is defined by the relation $Y = Q - T_3$, where Q denotes the electric charge and T_3 represents the third component of the isospin. This definition provides insight into each multiplet's properties within the MSSM's gauge structure.

Additionally, the MSSM requires inclusion of the Higgs boson and its superpartner. Because the Higgs boson has a spin of 0, it fits within a chiral supermultiplet and is thus also included in Table 1.3. However, to avoid gauge anomalies and to enable mass generation for both up-type quarks and down-type quarks (as well as charged leptons), two distinct Higgs supermultiplets are necessary. Each of these contains a spin-0 and a spin-1/2 doublet. The Higgs supermultiplet responsible for providing mass to the up-type quarks has a weak hypercharge of $Y = 1/2$, while the one responsible for down-type quarks and charged leptons has $Y = -1/2$. Accordingly, the Higgs bosons with $Y = 1/2$ are labeled H_u^0 and H_u^+, and those with $Y = -1/2$ are labeled H_d^0 and H_d^-. The SM Higgs boson can then be expressed as a linear combination of H_u^0 and the H_d^0. The supersymmetric partners of these scalar Higgs bosons, known as Higgsinos, are denoted by $\tilde{H}_u^0$, $\tilde{H}_u^+$, $\tilde{H}_d^0$ and $\tilde{H}_d^-$.

Names		spin 0	spin 1/2	$SU(3)_C, SU(2)_L, U(1)_Y$
squarks, quarks	Q	$(\tilde{u}_L \;\; \tilde{d}_L)$	$(u_L \;\; d_L)$	$(\mathbf{3}, \mathbf{2}, \frac{1}{6})$
(×3 families)	$\bar{u}$	$\tilde{u}_R^*$	$\tilde{u}_R^\dagger$	$(\bar{\mathbf{3}}, \mathbf{1}, -\frac{2}{3})$
	$\bar{d}$	$\tilde{d}_R^*$	$d_R^\dagger$	$(\bar{\mathbf{3}}, \mathbf{1}, \frac{1}{3})$
sleptons, leptons	L	$(\tilde{\nu} \;\; \tilde{e}_L)$	$(\nu \;\; e_L)$	$(\mathbf{1}, \mathbf{2}, -\frac{1}{2})$
(×3 families)	$\bar{e}$	$\tilde{e}_R^*$	$e_R^\dagger$	$(\mathbf{1}, \mathbf{1}, 1)$
Higgs, higgsinos	H_u	$(H_u^+ \;\; H_u^0)$	$(\tilde{H}_u^+ \;\; \tilde{H}_u^0)$	$(\mathbf{1}, \mathbf{2}, +\frac{1}{2})$
	H_d	$(H_d^0 \;\; H_d^-)$	$(\tilde{H}_d^0 \;\; \tilde{H}_d^-)$	$(\mathbf{1}, \mathbf{2}, -\frac{1}{2})$

Table 1.3: Overview of the chiral supermultiplets in the MSSM, as referenced in [3]. It includes multiplets associated with quarks and their superpartners, the squarks, leptons and their supersymmetric counterparts, the sleptons and finally, the Higgs bosons along with the Higgsinos. Only the first-generation families of quarks, squarks, leptons, and sleptons are specified in this table for simplicity. The third column provides the degrees of freedom for each multiplet under the relevant gauge groups, SU(3) for strong interactions, SU(2) for weak interactions, and the weak hypercharge Y.

The SM gauge bosons are organised within supermultiplets, where they are paired with fermionic superpartners known as gauginos. These gauginos are spin 1/2 particles, what distinguishes them from their spin 1 bosonic counterparts. The combination of spin 1 gauge bosons with their corresponding gaugino partners forms what is called a gauge supermultiplet. In this context, the supersymmetric partners of the gluons are named gluinos. Likewise, the electroweak gauge bosons, specifically W_1, W_2, W_3 and B^0, each have associated superpartners, referred to as winos and the bino. A detailed list of these gauge multiplets is provided in Table 1.4, again with their degrees of freedom with respect to SU(3) for strong interactions, SU(2) for weak interactions, and their electroweak hypercharge Y.

All interactions in supersymmetric theories such as the MSSM are governed by a superpotential, as described in [3]. However, without further constraints, this potential would allow interactions in which baryon number and lepton number are not necessarily conserved, potentially leading to processes that violate these conservation laws. Since experimental evidence does not support the existence of such processes, an additional symmetry is introduced to ensure baryon and

Names	spin 1/2	spin 1	$SU(3)_C, SU(2)_L, U(1)_Y$
gluino, gluon	$\tilde{g}$	g	$(\mathbf{8}, \mathbf{1}, 0)$
winos, W bosons	$\tilde{W}^{\pm}\ \tilde{W}^0$	$W^{\pm}\ W^0$	$(\mathbf{1}, \mathbf{3}, 0)$
bino, B boson	$\tilde{B}^0$	B^0	$(\mathbf{1}, \mathbf{1}, 0)$

Table 1.4: Summary of MSSM gauge multiplets from [3]. The table includes multiplets containing the gluons and their supersymmetric partners the gluinos, the W bosons and their superpartners the winos, and the B boson with its superpartner the bino. The third column provides the particles' degrees of freedom with respect to SU(3) for strong interactions, SU(2) for weak interactions, and the electroweak hypercharge Y.

lepton number conservation. This symmetry is known as R-parity and serves as a key feature in stabilizing supersymmetric theories. R-parity is defined for each particle by the relation

$$P_R = (-1)^{3(B-L)+2s} \tag{1.7}$$

where B represents the baryon number, L the lepton number, and s the particle's spin. Based on this definition, all SM particles have $P_R = +1$, while their supersymmetric counterparts have $P_R = -1$. To conserve R-parity at any interaction vertex, the number of supersymmetric particles involved must be even. This conservation rule implies that the lightest supersymmetric particle (LSP) must be entirely stable, as it cannot decay further without violating R-parity.

In the MSSM, the neutralinos represent a key category of particles and are composed of superpositions of the neutral wino $\tilde{W}^0$, the bino $\tilde{B}^0$, and two neutral higgsinos, $\tilde{H}_u^0$ and $\tilde{H}_d^0$. These combinations result in four distinct neutralino states, labeled $\tilde{\chi}_1^0, \tilde{\chi}_2^0, \tilde{\chi}_3^0$, and $\tilde{\chi}_4^0$, with $\tilde{\chi}_1^0$ being the lightest among them. In many models, $\tilde{\chi}_1^0$ is assumed to be the LSP and consequently completely stable.

1.6 Incentives for Introducing Supersymmetry

To generate predictions using a physical theory, a specific cut-off scale is typically introduced, a point beyond which the theory is no longer valid or applicable. If we were to choose the Planck energy E_P of roughly 10^{19} eV as this cut-off scale for the SM, it would lead to a theoretical problem by the predicted mass of the Higgs boson becoming divergent. The Planck energy is defined as $E_P = m_P c^2$, where the Planck mass m_P, is derived from the fundamental constants, the speed of light c, Planck's reduced constant $\hbar$, and the gravitational constant G, with the relationship

$$m_P = \sqrt{\frac{\hbar c}{G}}. \tag{1.8}$$

The Higgs mass receives quantum correction contributions generated by each particle that couples with the Higgs boson. These quantum corrections can be significantly larger than the bare or intrinsic mass of the Higgs boson itself. To manage these large corrections, a technique known as fine-tuning can be applied. Fine-tuning requires the parameters influencing the Higgs mass to be adjusted with extreme precision. However, this approach is problematic because it forces physical parameters to take on what seem to be arbitrary values, which conflicts with the principle of naturalness. The naturalness principle holds that dimensionless parameters within a theory should generally be of the same order of magnitude to reflect the inherent symmetries and simplicity of nature [17].
Supersymmetric extensions of the SM, such as the MSSM, offer a potential solution to this fine-tuning problem. In SUSY, the quantum corrections to the Higgs mass due to fermions and bosons have opposite signs, effectively balancing each other out and reducing the need for fine-tuning. As shown in Figure 1.2, the one-loop corrections to the Higgs squared mass differ between a fermion f and a scalar particle S. It is crucial to note that the fermionic one-loop correction involves two interaction vertices, while the scalar correction has only one. Consequently, the fermion correction term is proportional to the square of its coupling constant $|\lambda_f|^2$, while the scalar correction term is proportional to $|\lambda_S|$. This balance between bosonic and fermionic contributions provides a natural mechanism for stabilizing the Higgs mass.

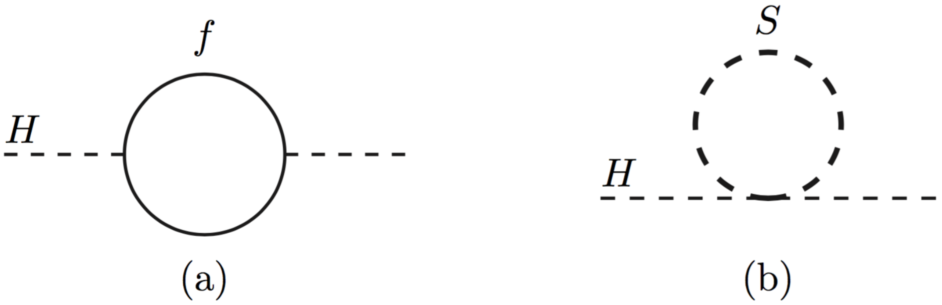

Figure 1.2: First-order loop corrections to the Higgs squared mass of a fermionic (a) and a scalar (b) particle, as presented in [3].

A fermionic particle's quantum correction to the squared Higgs mass (m_H^2) are

$$\Delta m_H^2 = -\frac{|\lambda_f|^2}{8\pi^2}[\Lambda_{UV}^2 + ...] \tag{1.9}$$

and the ones from a scalar particle of mass m_S are

$$\Delta m_H^2 = \frac{\lambda_S}{16\pi^2}[\Lambda_{UV}^2 - 2m_S^2 \ln(\Lambda_{UV}/m_S) + ...]. \tag{1.10}$$

The ultraviolet momentum cut-off Λ_{UV} defines the limit up to which the theory remains valid. Since supersymmetric models introduce two scalar partner states for each fermion, with couplings to the Higgs field of $\lambda_S = \lambda_f^2$, all the Λ_{UV}^2 corrections to the Higgs mass cancel each other out perfectly. This would prevent the Higgs mass corrections from diverging rapidly.

At a certain energy scale, the electromagnetic and weak forces merge into a single fundamental interaction. This energy scale, known as the electroweak unification scale, corresponds to the vacuum expectation value of the Higgs field, at approximately 246 GeV [12]. As a result, electromagnetic and weak forces are understood to be two manifestations of the same underlying force, which only appear distinct at low energies. This leads to the question of whether an even higher energy exists at which the strong force might also unify with the electroweak force.
Theories that propose such a unification are referred to as Grand Unified Theories (GUTs). If grand unification were achievable, it would imply that, at a particular high energy, the coupling constants of all three fundamental interactions of the SM would converge to a single value. However, when these three coupling constants are extrapolated to very high energies using only the SM parameters, they do not meet at a single energy scale. In contrast, when additional parameters from supersymmetric particles with masses around the TeV scale are included, a grand unification appears feasible.
This potential GUT could be seen as an important step towards an ultimate “theory of everything” (TOE), which would unify all three SM forces with gravity. Figure 1.3 illustrates how the coupling constants of the fundamental forces evolve with increasing energy for both the SM and the MSSM. The figure suggests that, within the MSSM, there could indeed be an energy scale around 10^{16} TeV where grand unification occurs.

A final, essential motivation for considering SUSY is that the $\tilde{\chi}_1^0$ would make an ideal dark matter candidate in a large fraction of supersymmetric theories. In these theories, this neutralino is predicted to be the LSP, which, if R-parity is conserved, would render it absolutely stable. This stability would allow the neutralino to exist in vast quantities throughout the universe. Because it lacks both electric and colour charge, the neutralino interacts only through the weak force and gravity, explaining why it remains so challenging to detect despite its potential abundance. These characteristics make the $\tilde{\chi}_1^0$ an excellent WIMP, a promising candidate for dark matter.

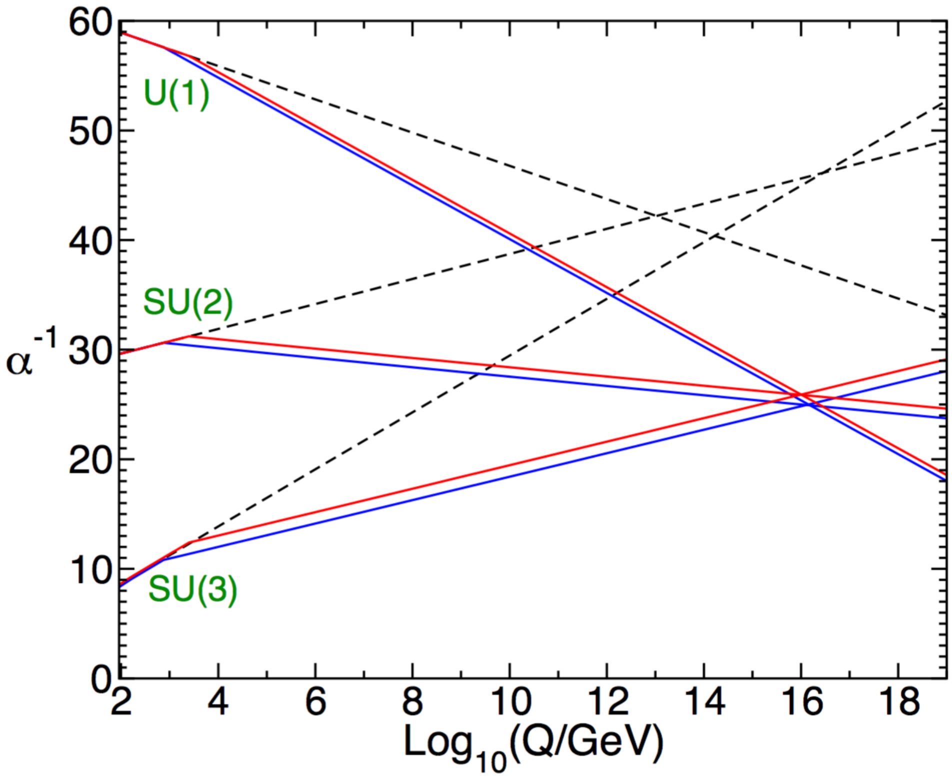

Figure 1.3: The progression of the electromagnetic U(1), weak SU(2) and strong SU(3) coupling constants up to an energy scale of 10^{18} GeV, as shown in [3]. The dashed lines represent the SM parameters, while the coloured solid lines correspond to the MSSM parameters, with the sparticle mass threshold set between 750 GeV and 2.5 TeV.

Chapter 2

The LHC and the ATLAS Experiment

Many studies conducted in this thesis rely on proton-proton collision data gathered by the ATLAS experiment situated at the CERN LHC facility. Consequently, this chapter provides an overview of the LHC, explains the coordinates used by the experiments at the LHC, discusses proton-proton collisions and details the ATLAS detector. Additionally, the upgrade plans for both, the LHC and ATLAS, are described.

2.1 The Large Hadron Collider

Encompassing a circumference of 26.7 kilometres, the LHC stands as the largest particle accelerator worldwide [1]. Constructed by CERN from 1998 to 2008 in the vicinity of Geneva, the LHC operates as a synchrotron accelerator. Synchrotrons accelerate particles along a circular path with a constant radius using electric fields generated by radio frequency (RF) cavities. The particles' paths are bent through the Lorentz force by the application of strong magnetic fields. The acting Lorentz force on the particles is

$$\vec{F}_L = q(\vec{v} \times \vec{B}), \tag{2.1}$$

where q is the particle's charge, $\vec{v}$ the particle's velocity and $\vec{B}$ the magnetic field. To confine particles within their designated paths, the magnetic field is generated perpendicularly to the momenta of the particles. No magnetic fields are employed in the region where particles undergo linear acceleration by electrical fields generated by RF cavities. For particles kept on a circular path of radius r, the following relation must be satisfied.

$$\frac{p}{r} = qB \tag{2.2}$$

Here p and B are the absolute values of the particle's momentum and magnetic field. Equation (2.2) shows that for particles with a high momentum an accordingly strong magnetic field is needed to keep them on the track. Therefore, the magnetic field must continuously synchronise when the particle's are accelerated to higher and higher momenta.

Another challenge encountered in synchrotron accelerators stems from a phenomenon known as synchrotron radiation. Grounded in the principle of bremsstrahlung, this effect prompts particles interacting with electric and magnetic fields to emit photons. The energy dissipated by particles through this mechanism is proportional to

$$\Delta E \propto \frac{E^4}{m^4 r}, \tag{2.3}$$

where E is the particle's energy, m its mass and r the bending of the track [18]. Because the mass of a proton is approximately 2000 times greater compared to the electron mass, protons experience significantly reduced energy loss from synchrotron radiation, on the order of 10^{13}. This characteristic makes protons a more favourable choice for acceleration to TeV-scale energies. With the current technologies, the acceleration of electrons is limited to one magnitude below the TeV-scale for circular accelerators with a radius like the LHC of around 4.3 km.

The LHC has the capability to accelerate protons or heavy ions, such as lead ions [1]. The research presented in this thesis exclusively involves proton-proton collision data. Prior to entering the LHC, these particles undergo a sequence of four preaccelerators. Initially, the acceleration of protons starts in the linear particle accelerator called Linac 4, where negatively charged hydrogen ions are injected [19]. The acceleration of heavy ions starts with a different one called Linac 3. The hydrogen ions in Linac 4 are accelerated up to 160 MeV. Subsequently, they are proceeded to the Proton Synchrotron Booster (PSB), whereby the ions are stripped of both electrons. In the PSB, a synchrotron accelerator with a 25 m radius, the energy of the now proton beam is increased up to 1.4 GeV. The next stage is the Proton Synchrotron (PS), featuring a circumference of 628 m, where protons attain energies of approximately 25 GeV. Before reaching the LHC, the particles undergo further acceleration in the Super Proton Synchrotron (SPS), which has a circumference of 6.9 km. Protons reach an energy level of 450 GeV and are subsequently injected into the LHC, where they undergo acceleration to energies up to 6.8 TeV [20].

The LHC operates with two beam tubes and accelerates particles in both directions along the circular track, featuring four crossing points. Employing RF-cavities for proton acceleration, the proton beam is divided into 2808 bunches per ring. At the four crossing points, bunches accelerated in opposite directions collide with $\sqrt{s} = 13.6$ TeV centre-of-mass energies. The LHC was designed with a bunch crossing rate of 40 MHz and with each bunch containing around 10^{11} particles, resulting in an instantaneous luminosity of 10^{34} cm^{-2}s^{-1}. Luminosity, a measure of particle flux through a given space per second, is calculated as

$$L = \frac{nN_1N_2f}{4\pi\sigma_x\sigma_y}, \tag{2.4}$$

with n being the number of bunches, N_1 and N_2 being the numbers of particles in the colliding bunches, f being the bunch crossing frequency and σ_x and σ_y being the root-mean-square transverse beam sizes in the horizontal and vertical direction [21].

Each of the four collision points within the LHC features a different main experiment which is recording the collisions. These experiments are named ATLAS (A Toroidal LHC ApparatuS) [2], CMS (Compact Muon Solenoid) [22], LHCb (Large Hadron Collider beauty) [23], and ALICE (A Large Ion Collider Experiment) [24]. Figure 2.1 illustrates a schematic of the LHC acceleration chain, starting from the Linacs and ending with the LHC where the four main experiments at the crossing points are highlighted in blue.

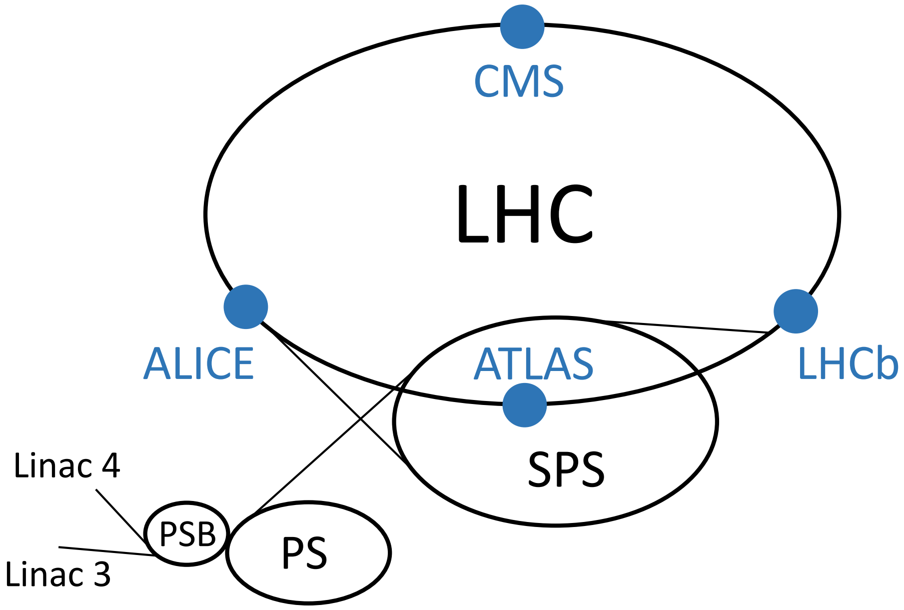

Figure 2.1: This graphic of the LHC illustrates both the preaccelerators and the four main experiments situated at the interaction points. The linear accelerators, Linac 4 and Linac 3, supply protons and ions, respectively, to the Proton Synchrotron Booster (PSB). Subsequently, particles progress from the PSB to the Proton Synchrotron (PS) before being directed to the Super Proton Synchrotron (SPS). Accelerated particles from the SPS then enter the LHC, where they collide in bunches at four designated crossing points. Each of these points is equipped with one of the four experiments ATLAS, CMS, ALICE, and LHCb.

2.2 Coordinate System for the LHC Experiments

To accurately reconstruct and analyse the events generated by particle collisions, a well-defined coordinate system is essential. The coordinate system, generally used by the experiments situated at the LHC, provides a standardised framework for describing the positions and movements of particles and detector components, enabling precise measurements and consistent communication of results among physicists.These coordinates which are also used for the ATLAS detector are presented in Figure 2.2. Thereby, the standard Cartesian framework using x, y, z is transformed into a spherical one, using the radius from the interaction point r as radial distance, the pseudorapidity η as a measure of the polar angle and ϕ as the azimuthal angle.

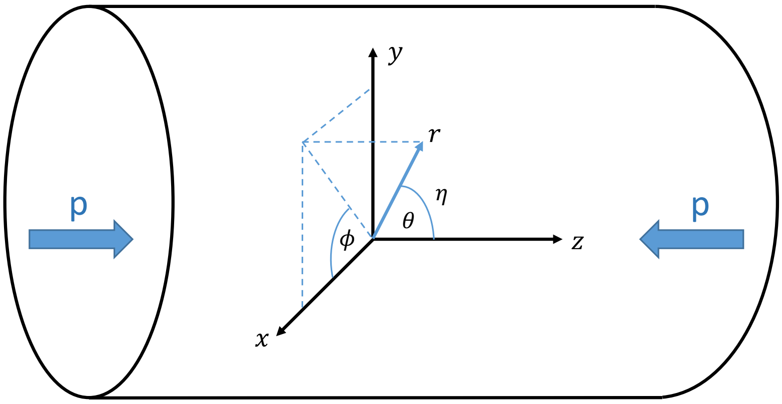

Figure 2.2: Schematics of the ATLAS coordinates. Radial coordinates are used with the angle ϕ and the pseudorapidity η. The direction x is pointing towards the centre of the LHC, y is pointing upwards and z points along the beam pipe. The interaction point serves as origin.

The pseudorapidity is used instead of the more common polar angle θ as the coordinate describing the angle relative to the direction of the beam pipe. It is derived from the rapidity y (not to be confused with the Cartesian coordinate y) defined for a particle in a beam as

$$y \equiv \frac{1}{2} \ln(\frac{E + p_L}{E - p_L}), \tag{2.5}$$

where E is the particle's energy and p_L is its longitudinal momentum in the direction of the beam. Differences in rapidity are Lorentz invariant for boosts in the longitudinal direction. In the case of the LHC where the particles' energies exceed their rest mass by far ($E >> m_0c^2$) Equation (2.5) can be transformed to the definition of the pseudorapidity η

$$\eta = -\ln(\tan(\theta/2)). \tag{2.6}$$

Here θ is the deflection angle from the longitudinal direction of the beam pipe into the transverse direction given in radians, the standard unit of angle. The azimuthal angle of the transverse plane ϕ is simply given in radians.

2.3 Proton-Proton Collisions at the LHC

In the high-energy proton-proton collisions at the LHC, the partons (quarks and gluons) inside the protons participate in the primary interactions [25]. Hard scattering events with high momentum transfer are the central processes of interest. The other constituents of the protons contribute to the underlying collision event. Gluons are radiated from the partons before and after the main interaction as initial and final state radiation, respectively. Additionally, more than one pair of partons from the two protons can interact in softer interactions with lower momentum transfer. Also, partons from different pairs of protons are typically interacting within one bunch crossing at the LHC. The overlapping of multiple interactions, originating from different protons within one bunch crossing, is called pile-up, denoted as μ for indicating the number of those interactions. The rest of the protons, not participating in scattering events, follows along the beam axis as beam remnants.

The interacting partons carry only a fraction of the total momentum of the proton. This fraction is denoted with the Bjorken x. The various types of partons have different probabilities for taking part in an interaction depending on their Bjorken x. These probabilities have been precisely measured for many different energy scales and summarised as parton distribution functions (PDFs). PDFs are typically shown at a fixed resolution scale Q^2 which is the negative squared of the four momentum transfer q. With the high centre-of-mass energies of $\sqrt{s} = 13.6\,\text{TeV}$ at the LHC, PDFs are explored in new kinematic domains of Q^2 and x values. The kinematic regions probed by the LHC in comparison with previous collider and fixed target experiments are shown in Figure 2.3. It demonstrates that the LHC expands the domains in Q^2 and x values by several orders of magnitude.
As the two partons participating in a hard scattering event at the LHC typically carry a different fraction of the proton's momentum, interactions are often highly boosted along the longitudinal beam axis. Since differences in the pseudorapidity η between particles of $E >> m_0c^2$ are independent of the longitudinal boost, it is very helpful to use it as deflection angle from the interaction point for analysing collision events. Similarly, it is very interesting to study the transverse energies E_T and transverse momenta p_T of particles produced in hard scattering events, as those properties are also Lorentz invariant under longitudinal boosts. Since the protons in the LHC do not have any transverse momentum before a collision, the

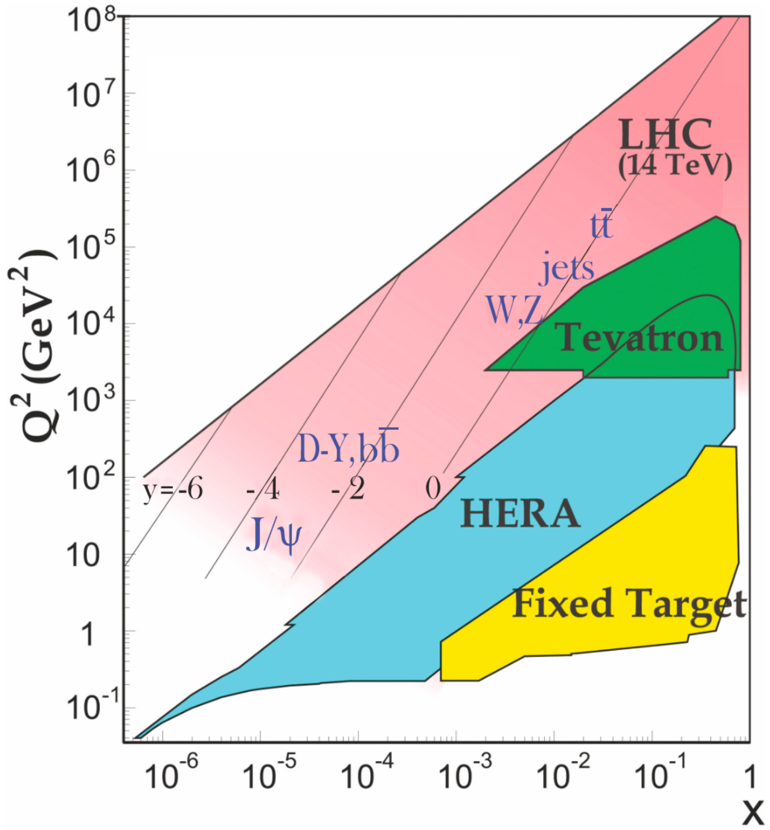

Figure 2.3: Kinematic regions in Q^2 and x explored by the LHC, HERA and Tevatron collider experiments and by fixed target experiments [9]. For the LHC, centre-of-mass energies up to $\sqrt{s} = 14\,\text{TeV}$ are assumed. Corresponding rapidity y values are given for the domains covered by the LHC.

net transverse momentum after the collision also must be zero. This makes the transverse plane very useful for reconstructing and interpreting event kinematics. Any imbalance in transverse momentum in the final state can signal the presence of undetected particles, detector inefficiencies, noise or new physics processes.

2.4 The ATLAS Experiment

With dimensions of 44 m in length and 25 m in width, ATLAS is the largest of the experiments conducted at the LHC [2]. Designed as a general-purpose detector, ATLAS is capable of measuring a wide range of signals generated by collisions. Consequently, ATLAS incorporates a multitude of different detector types, collectively weighing approximately 7000 tonnes. Figure 2.4 presents a schematic representation of the ATLAS detector.

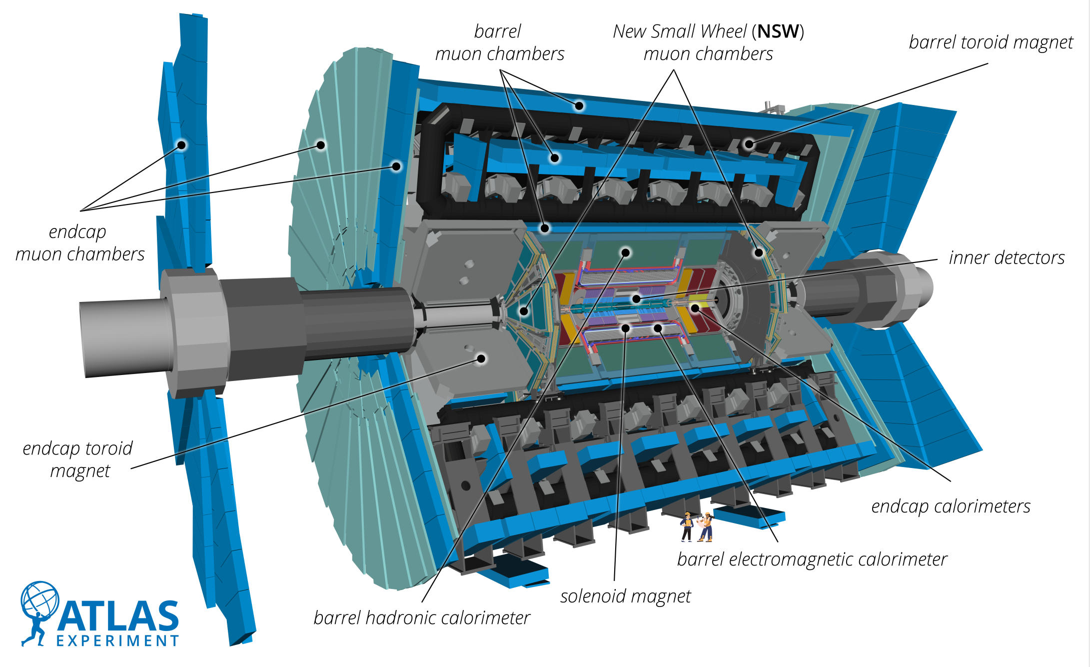

Figure 2.4: Schematics of the ATLAS detector with people in front to indicate the size, ATLAS Experiment © 2025 CERN. It shows the central beam pipe encircled by the Inner Detector. The Inner Detector comprises the Pixel Detector, the Semiconductor Tracker, and the Transition Radiation Tracker. It is followed by the calorimeter detector system, which features electromagnetic and hadronic liquid argon calorimeters and hadronic tile calorimeters. The muon detector system comprising multiple layers of muon chambers, is situated around the entire detector.

2.4.1 The Inner Detector

The ID is situated in close proximity to the collisions in the beam pipe [2]. It is embedded in a 2 T magnetic field, generated by a solenoid magnet. The ID is designed to facilitate high-precision measurements of the momenta and vertices of the particles emerging from collisions. It comprises three sub-detectors. The innermost is the Pixel Detector, which features high-granularity silicon pixel layers including the Insertable B-Layer (IBL). Subsequently, the Semi-Conductor Tracker (SCT) consists of silicon strip detectors, while the Transition Radiation Tracker (TRT) is constructed from numerous 4 mm diameter straw tubes. Figure 2.5 illustrates the ID from the side, whereas Figure 2.6 shows a cross-sectional view of the central part around the interaction point with the distances from the beam pipe.

The operational principles of the Pixel Detector and the SCT are based on the fundamental principles of semiconductor detectors. The atoms in these semiconductors are arranged in lattice structures, wherein they share valence electrons through covalent bonds [27]. The energy levels of these valence electrons con-

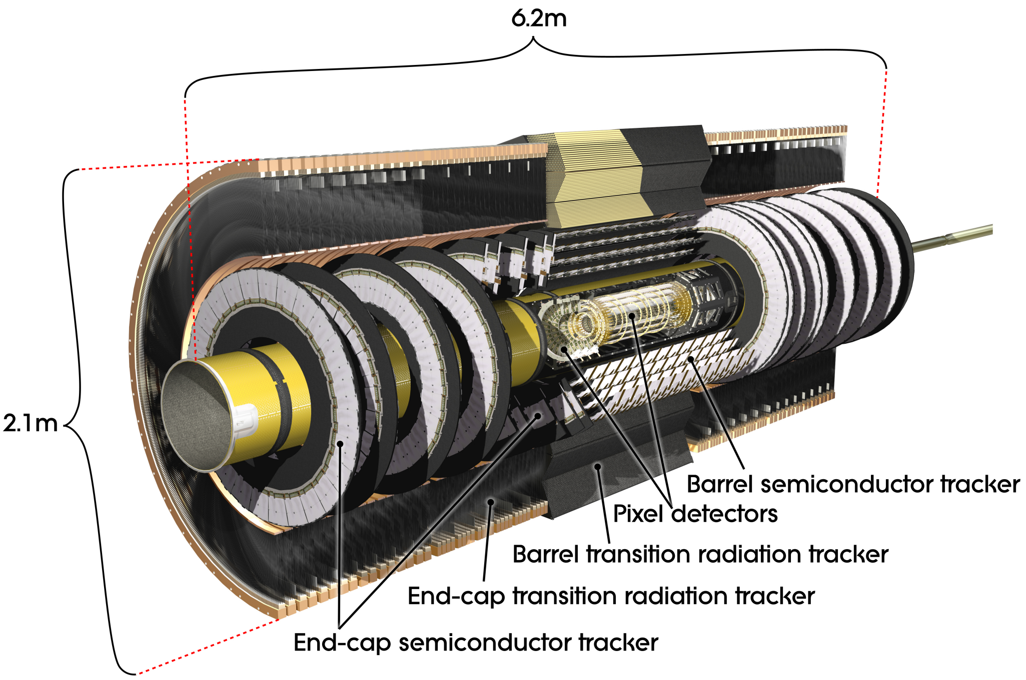

Figure 2.5: Schematics of the ATLAS Inner Detector, ATLAS Experiment © 2025 CERN. It comprises the Pixel Detector, the Semiconductor Tracker and the Transition Radiation Tracker.

stitute the valence band. If the atoms in the lattice are excited, electrons are transferred from the valence to the conduction band. In this state, the electrons are no longer bound through covalent bonds and can move freely throughout the lattice. However, this results in a disruption to the covalent bonds of the excited atom. These gaps are referred to as holes. The aforementioned holes can be filled with another valence electron from an adjacent atom which results in the holes moving freely in a manner analogous to the electrons in the conduction band. Semiconductors may be doped with atoms of a different kind. Dopants with fewer valence electrons than those of the semiconductor are referred to as acceptors. Fewer valence electrons lead to the formation of additional holes in the conduction band. Dopants with more valence electrons than those of the semiconductor are called donors. These extra electrons are not required for the formation of covalent bonds which leads to the generation of additional electrons in the conduction band. Semiconductors doped with acceptors are designated as p-type, while those doped with donors are classified as n-type. A p-n junction is a semiconductor where one side is doped with acceptors and the other side with donors. The application of an electrical potential difference between the two sides of a p-n junction, results in the drift of electrons in the conduction band towards the anode and the drift of the holes towards the cathode. This process creates a depletion region where there are no free charge carriers. The passage of an

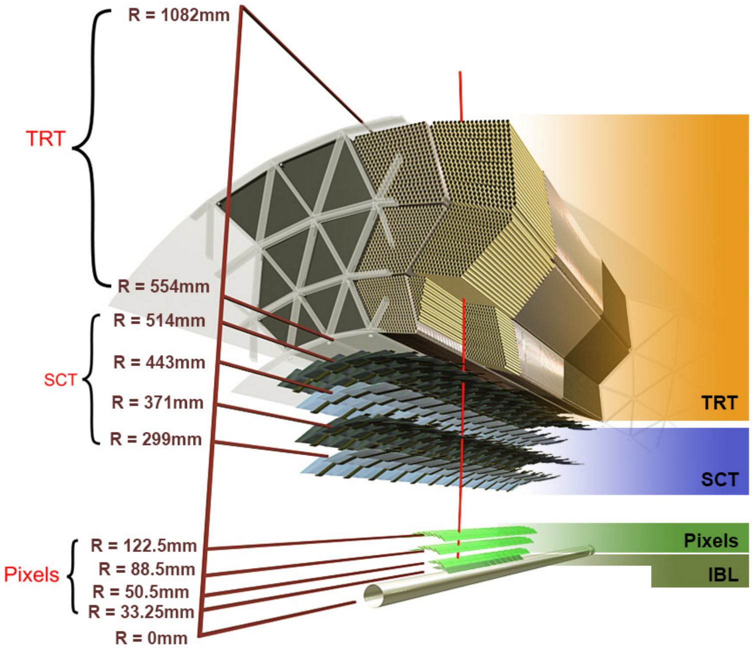

Figure 2.6: Cross-sectional view of the ATLAS inner detector (ID) around the interaction point, featuring the beam line distances of the sub-detectors from [26]. Next to the interaction point we have the pixel detectors with the insertable B-layer (IBL) being closest. The pixels are surrounded by the semiconductor tracker (SCT) and then follows the transition radiation tracker (TRT).

ionising particle through such a depleted p-n junction results in the promotion of valence electrons to the conduction band. The promoted electrons leave behind holes. The electrons and holes subsequently drift to the anode and cathode, respectively, creating a pulse that is measured in fluctuations of the potential difference. This principle is employed to detect and track ionising particles in semiconductor detectors.
The straw tubes of the TRT are filled with a gas mixture that was initially predominantly composed of Xenon. In the centre of the tubes there is a tungsten wire which serves as an anode at ground level. The tube walls are the cathodes which are typically kept at $-1.53\,\mathrm{kV}$. They are constructed from several polyimide films, in which charged particles, that pass by, emit transition radiation. The information from the detected radiation is used to reconstruct the particles that produced it.

2.4.2 The Calorimeter System

The calorimeter detector system is situated around the ID [2]. Its main purpose is to quantify the energies of electrons, photons, and hadrons. It is crucial for the calorimeter that the particles are contained within the detector system in order to measure their total energy depositions. Those sampling calorimeters comprise alternating layers of dense absorber materials and active materials, the latter of which are responsible for detecting the particle showers created in the absorbers. Given the different behaviours exhibited by electromagnetic and hadronic showers, two distinct types of calorimeters are employed. Both calorimeters are segmented in various layers, comprising numerous cells which are individually read out. The electromagnetic calorimeters (ECALs), containing liquid argon (LAr) and lead absorber plates, are employed for the detection of electrons and photons. Radiation resistant kapton electrodes along the absorber plates are used for collecting the ionisation charge produced by particles passing through the liquid argon. For arranging the absorbers and electrodes in the ECAL an accordion shaped geometry has been designed, allowing for improved charge collection and detector coverage. Figure 2.7 depicts the accordion geometry of the ECAL in the low pseudorapidity regions. The granularity of the cells is given by their $\Delta\eta \times \Delta\phi$. Additionally, the corresponding radiation lengths (X_0) are indicated which add up to 24 X_0. One radiation length corresponds to the distance in a material in which the energy of a high energetic electron is reduced by a factor of Euler's number e through bremsstrahlung.

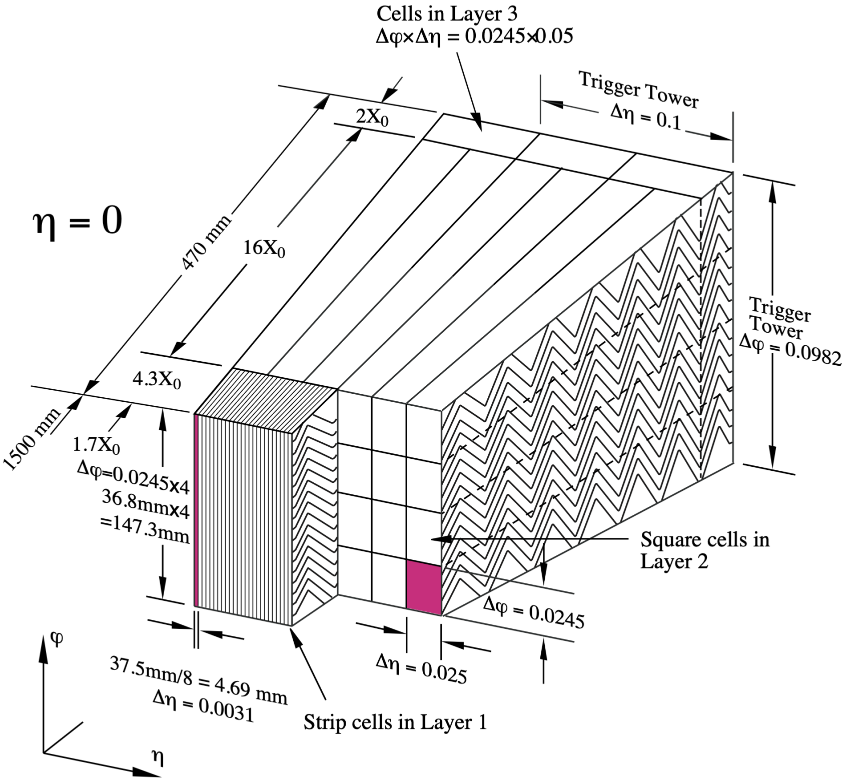

Figure 2.7: Schematics of the ATLAS electromagnetic calorimeter's accrodion shaped geometry around the $\eta = 0$ region [2]. Distances from the beam line are given in mm and in radiation lengths X_0. The cell granularity is indicated in terms of $\Delta\eta$ and $\Delta\phi$.

The electromagnetic calorimeters are situated directly after the ID and the solenoid magnets, and are divided into three sections, a barrel-shaped segment encircling the interaction point and two end-cap sections extending in both directions along the beam pipe. To guarantee that the Argon remains in a liquid state, each component is equipped with a dedicated cryostat.

The hadronic calorimeters (HCAL) are employed for the measurement of energies resulting from strong interactions of hadronic particles with the detector material. The calorimeters are composed of tile structures, with a primary barrel situated again around the interaction point and an extended barrel extending in each direction along the beam pipe. Light from the tile scintillators is collected by embedded wavelength-shifting fibers, which guide the light to photomultiplier tubes (PMTs). The PMTs then convert the scintillation light into electrical signals. In both end-cap regions, two wheel-shaped hadronic calorimeter detectors, containing liquid Argon, are present. The liquid Argon forward calorimeters are located in close proximity to the beam pipe in the end-cap regions. The tile calorimeters have steel absorbers, whereas the end-cap and forward calorimeters utilise copper plates. Additionally, the forward calorimeters feature tungsten as an absorber. A schematic of the ATLAS calorimeter system is presented in Figure 2.8.

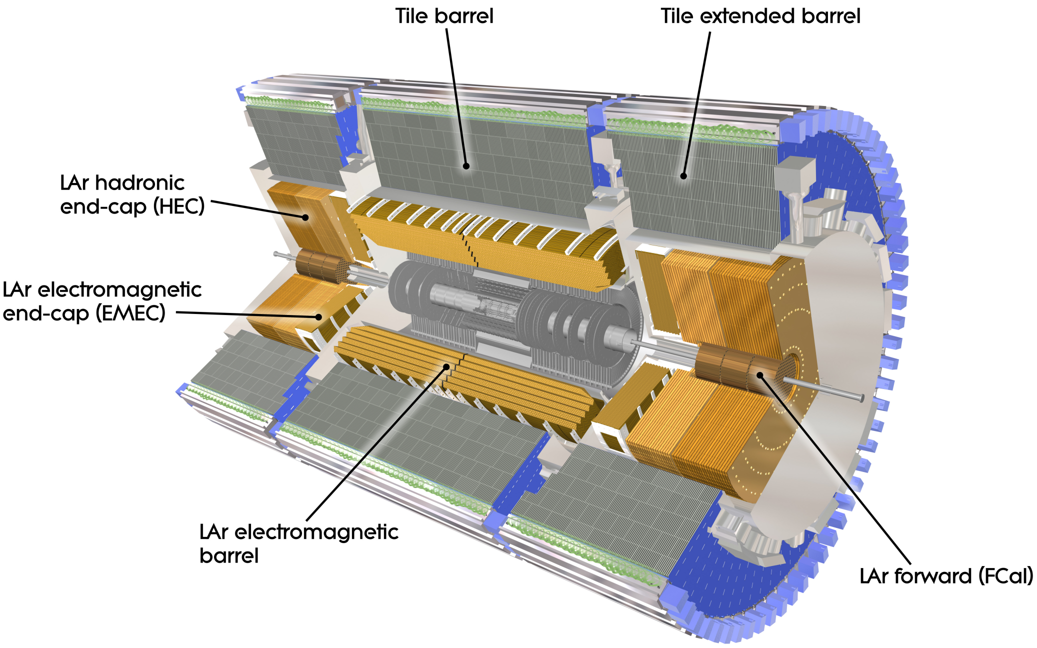

Figure 2.8: Schematics of the ATLAS calorimeter system, ATLAS Experiment © 2025 CERN. The electromagnetic calorimeters, which feature LAr, are situated around the ID. The hadronic calorimeters are composed of tiles in the barrel region and liquid Argon in the end-cap regions.

Additionally, a summary of all the calorimeter layers with their $|\eta|$ coverages and their $\Delta\eta \times \Delta\phi$ granularities is presented in Table 2.1.

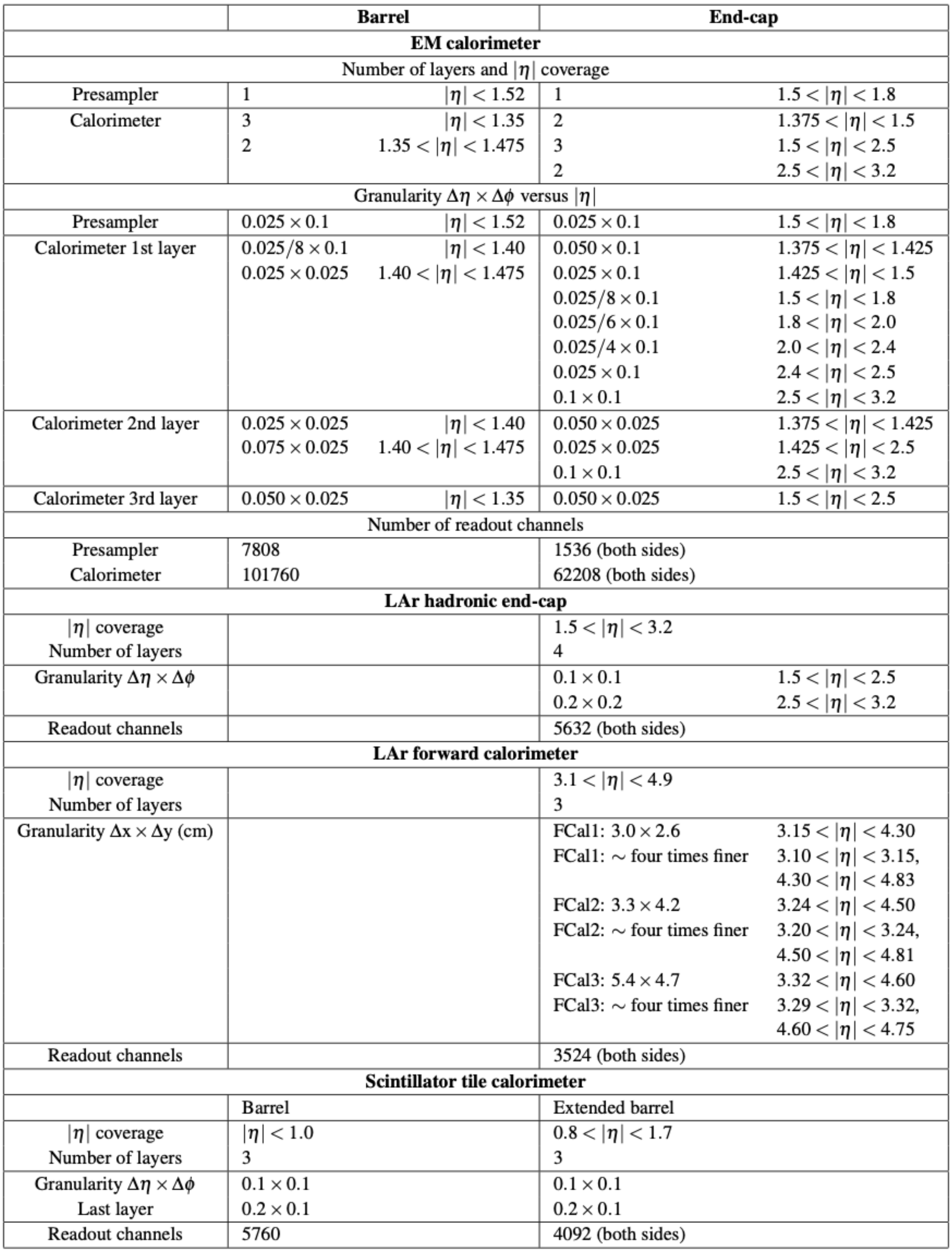

	Barrel		**End-cap**	
EM calorimeter				
Number of layers and $\lvert\eta\rvert$ coverage				
Presampler	1	$\lvert\eta\rvert < 1.52$	1	$1.5 < \lvert\eta\rvert < 1.8$
Calorimeter	3	$\lvert\eta\rvert < 1.35$	2	$1.375 < \lvert\eta\rvert < 1.5$
	2	$1.35 < \lvert\eta\rvert < 1.475$	3	$1.5 < \lvert\eta\rvert < 2.5$
			2	$2.5 < \lvert\eta\rvert < 3.2$
Granularity $\Delta\eta \times \Delta\phi$ versus $\lvert\eta\rvert$				
Presampler	0.025×0.1	$\lvert\eta\rvert < 1.52$	0.025×0.1	$1.5 < \lvert\eta\rvert < 1.8$
Calorimeter 1st layer	$0.025/8 \times 0.1$	$\lvert\eta\rvert < 1.40$	0.050×0.1	$1.375 < \lvert\eta\rvert < 1.425$
	0.025×0.025	$1.40 < \lvert\eta\rvert < 1.475$	0.025×0.1	$1.425 < \lvert\eta\rvert < 1.5$
			$0.025/8 \times 0.1$	$1.5 < \lvert\eta\rvert < 1.8$
			$0.025/6 \times 0.1$	$1.8 < \lvert\eta\rvert < 2.0$
			$0.025/4 \times 0.1$	$2.0 < \lvert\eta\rvert < 2.4$
			0.025×0.1	$2.4 < \lvert\eta\rvert < 2.5$
			0.1×0.1	$2.5 < \lvert\eta\rvert < 3.2$
Calorimeter 2nd layer	0.025×0.025	$\lvert\eta\rvert < 1.40$	0.050×0.025	$1.375 < \lvert\eta\rvert < 1.425$
	0.075×0.025	$1.40 < \lvert\eta\rvert < 1.475$	0.025×0.025	$1.425 < \lvert\eta\rvert < 2.5$
			0.1×0.1	$2.5 < \lvert\eta\rvert < 3.2$
Calorimeter 3rd layer	0.050×0.025	$\lvert\eta\rvert < 1.35$	0.050×0.025	$1.5 < \lvert\eta\rvert < 2.5$
Number of readout channels				
Presampler	7808		1536 (both sides)	
Calorimeter	101760		62208 (both sides)	
LAr hadronic end-cap				
$\lvert\eta\rvert$ coverage			$1.5 < \lvert\eta\rvert < 3.2$	
Number of layers			4	
Granularity $\Delta\eta \times \Delta\phi$			0.1×0.1	$1.5 < \lvert\eta\rvert < 2.5$
			0.2×0.2	$2.5 < \lvert\eta\rvert < 3.2$
Readout channels			5632 (both sides)	
LAr forward calorimeter				
$\lvert\eta\rvert$ coverage			$3.1 < \lvert\eta\rvert < 4.9$	
Number of layers			3	
Granularity $\Delta x \times \Delta y$ (cm)			FCal1: 3.0×2.6	$3.15 < \lvert\eta\rvert < 4.30$
			FCal1: $\sim$ four times finer	$3.10 < \lvert\eta\rvert < 3.15$, $4.30 < \lvert\eta\rvert < 4.83$
			FCal2: 3.3×4.2	$3.24 < \lvert\eta\rvert < 4.50$
			FCal2: $\sim$ four times finer	$3.20 < \lvert\eta\rvert < 3.24$, $4.50 < \lvert\eta\rvert < 4.81$
			FCal3: 5.4×4.7	$3.32 < \lvert\eta\rvert < 4.60$
			FCal3: $\sim$ four times finer	$3.29 < \lvert\eta\rvert < 3.32$, $4.60 < \lvert\eta\rvert < 4.75$
Readout channels			3524 (both sides)	
Scintillator tile calorimeter				
	Barrel		Extended barrel	
$\lvert\eta\rvert$ coverage	$\lvert\eta\rvert < 1.0$		$0.8 < \lvert\eta\rvert < 1.7$	
Number of layers	3		3	
Granularity $\Delta\eta \times \Delta\phi$	0.1×0.1		0.1×0.1	
Last layer	0.2×0.1		0.2×0.1	
Readout channels	5760		4092 (both sides)	

Table 2.1: Summary table of all the ATLAS calorimeter layers [2]. The number of layers, the $|\eta|$ coverages and the $\Delta\eta \times \Delta\phi$ granularities are given for all the different sub-detectors of the ATLAS calorimeter system.

2.4.3 The Muon Spectrometer

The muon spectrometer is situated around the hadronic calorimeter [2]. The ID and the calorimeters have only a slight effect on muons, which leave bent tracks when passing through them. The muon system initially comprised four distinct detector types, each based on tubes or chambers filled with gas. All of them measure the interactions of the muons with the gas. The muon spectrometer system is designed for both, the high-precision tracking and the triggering of muons (further discussed in Chapter 3). Large superconducting toroidal magnets are used to bend the tracks of the muons which allows for a better resolution of their momenta. The muon tracks are then measured by three cylindrical layers of Monitored Drift Tubes (MDTs) in the barrel region. The endcap regions feature MDTs as well but they are arranged in plane layers. In the barrel region, Resistive-Plate Chambers (RPCs) are used for the muon trigger, while Thin Gap Chambers (TGCs) are utilised at the end-caps. Initially, Cathode Strip Chambers (CSCs) were employed in the Small Wheels located in the endcaps. However, the muon spectrometer system went through a larger upgrade when those Small Wheels were replaced by the New Small Wheels (NSWs) [28]. The NSW upgrade focused on replacing the old MDTs and CSCs in the small wheels, which are closer to the beam pipe and experience higher particle fluxes. These chambers were more susceptible to issues under higher radiation and collision rates expected with LHC upgrades (further discussed in Section 2.5). The NSWs feature MicroMegas (MM) and small-strip Thin Gap Chamber (sTGC) detectors, with the former providing high spatial resolution for tracking and the latter offering precise timing resolution. Figure 2.9 illustrates the configuration of the ATLAS muon spectrometer before the NSW upgrade.

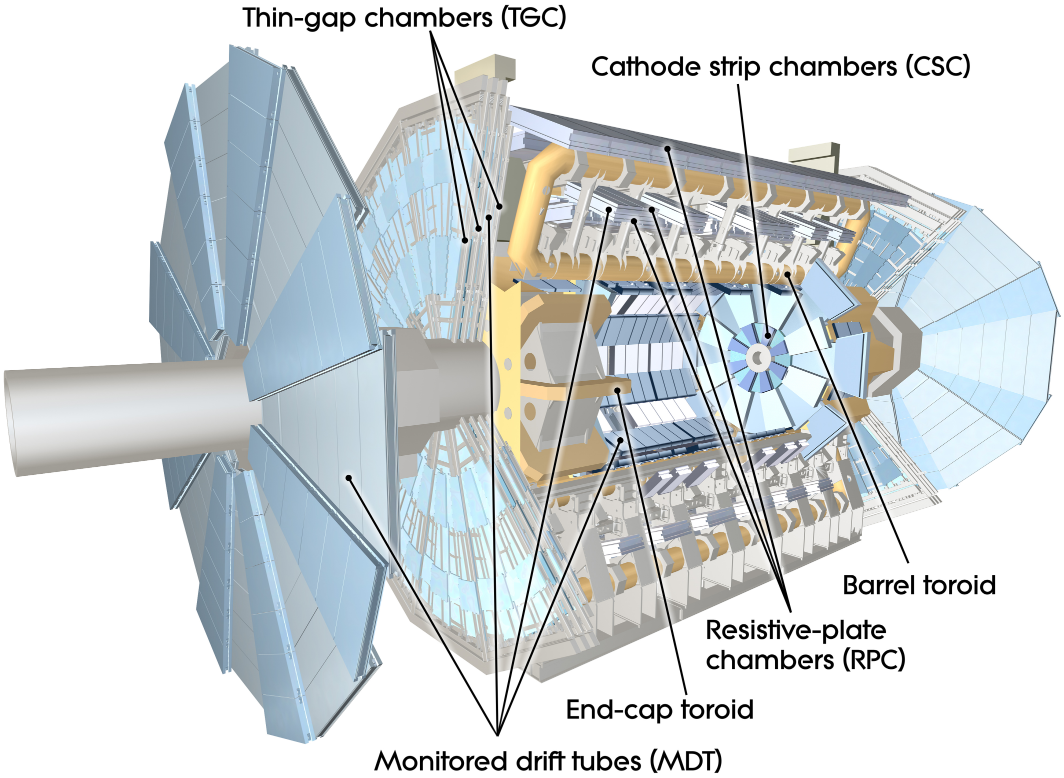

Figure 2.9: Schematics of the initial ATLAS muon spectrometer system, ATLAS Experiment © 2025 CERN. The four sub-detector types, Monitored Drift Tubes, Cathode Strip Chambers, Resistive-Plate Chambers and Thin Gap Chambers are marked, as well as the toroid magnets in the barrel and end-cap regions. The New Small Wheels, featuring the new Micromegas and small-strip Thin Gap Chamber detectors, have replaced the small wheels located at the indicated Cathode Strip Chambers.

2.5 LHC and ATLAS Upgrades

To further enhance the LHC's capabilities and continue probing the fundamental nature of matter, CERN has defined an ambitious upgrade plan, transforming it into the High-Luminosity Large Hadron Collider (HL-LHC) [29]. The primary objective of the HL-LHC upgrade is to significantly increase the collider's luminosity. With this increase in luminosity the detectors will be able to take much more data, allowing for deeper investigations of possible BSM physics processes and to strengthen our understanding of the SM. One of the core aspects of the upgrade involves replacing and enhancing the superconducting magnets that guide and focus the particle beams. New quadrupole magnets, made from Niobium-Tin (Nb3Sn) alloys, will produce stronger magnetic fields than the current Niobium-Titanium (NbTi) magnets, allowing for tighter beam focusing and thus higher collision rates. Another important feature of the HL-LHC is the im-

plementation of crab cavities. These are special RF cavities designed to tilt the particle bunches just before they collide, effectively increasing the overlap of the particle bunches at the interaction. This increases the probability of collisions, contributing to higher luminosity. The crab cavities are also used to keep the instantaneous luminosity stable over most of the duration of a beam fill by adjusting the tilt of the bunches. This elaborate technique is called luminosity levelling. Furthermore, the upgrade will introduce inner triplets, which are a set of focusing magnets near the collision points. Upgrading these magnets with higher field gradients will enable better beam focusing, which is critical for achieving the desired luminosity improvements. Additionally, the systems responsible for safely dumping the beam and managing stray particles will be enhanced to handle the increased beam intensity and energy, ensuring the safety and efficiency of operations. Alongside the accelerator upgrades, also the detectors and their data acquisition systems will be upgraded to handle the higher collision rates. Enhanced computing infrastructure will be necessary to process the vast amount of data generated, with improvements in both, storage and processing capabilities. The HL-LHC is expected to mainly operate with these upgrades in the 2030s, extending the LHC's operational life and scientific output. This allows for many fundamental physics studies as previously indicated, thereby improving our understanding of the universe. However, there are many more fields profiting from the HL-LHC. The development and implementation of new technologies, such as the advanced superconducting materials for magnets, have broad applications beyond particle physics, potentially benefiting sectors like medical imaging, energy, and computing.
Executing the HL-LHC upgrade presents several technical and logistical challenges, requiring international collaboration among scientists, engineers, and institutions. The complexity of designing and integrating new components, maintaining strict safety standards, and ensuring seamless transitions during upgrades necessitates careful planning and coordination. Overall, the HL-LHC upgrade represents a significant leap forward in particle physics research, promising to deepen our understanding of the fundamental constituents of the universe while driving technological innovation. Figure 2.10 features a schematic of the LHC upgrade plan from 2011 to 2041, including the HL-LHC.

As mentioned before, with the HL-LHC upgrade also the experiments are set to undergo significant upgrades in preparation for Run 4. For ATLAS they are scheduled to commence in 2026. These upgrades are crucial to maintaining ATLAS's cutting-edge capabilities as the LHC transitions into its high-luminosity phase, where the intensity of proton-proton collisions will be significantly increased. The primary objective of these upgrades is to enhance the detector's performance to handle the unprecedented conditions, thereby ensuring continued success in exploring the fundamental constituents of the universe.
While the HL-LHC's significant increase in instantaneous luminosity offers a lot of potential for physics studies, it also presents serious challenges. The ATLAS

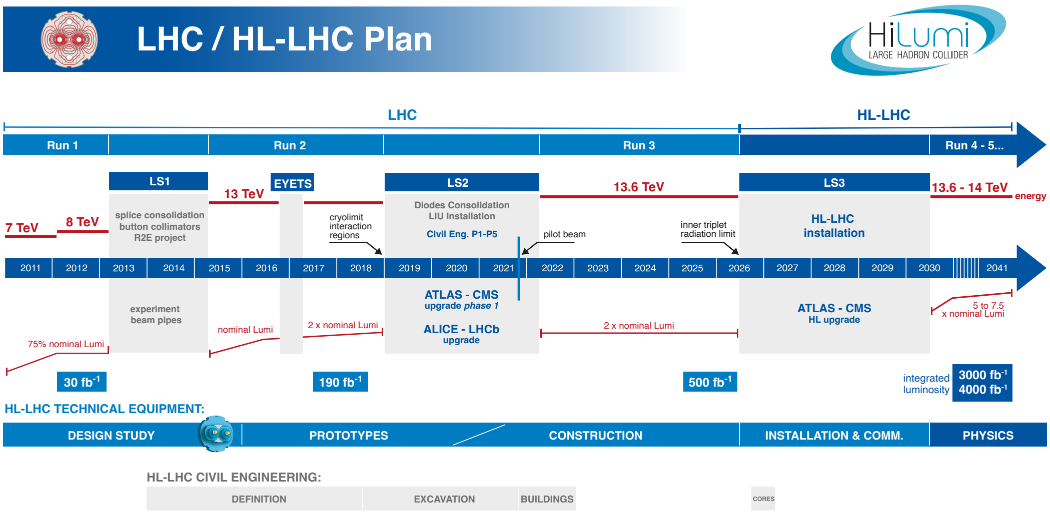

Figure 2.10: Schematics of the LHC upgrade schedule from 2011 to 2041, updated from [29]. The planned energies and luminosities are shown with the red bands. The abbreviations LS and EYETS are standing for Long Shutdown and Extended Year End Technical Stop, respectively.

detector, originally designed for lower instantaneous luminosity conditions, must be upgraded to cope with the increased radiation levels, higher data rates, and greater pile-up values.

One of the most critical upgrades is the complete replacement of the ATLAS ID with a new all-silicon Inner Tracker (ITk) [30] [31]. The ITk will feature both pixel and strip detectors, designed to offer improved resolution and withstand the higher radiation doses expected at the HL-LHC. Additionally, the pseudorapidity spectrum will be widely increased to cover regions up to $|\eta| < 4$, from currently $|\eta| < 2.5$. This upgrade will significantly enhance the ATLAS detector's ability to track charged particles with high precision, even in the dense environment of the HL-LHC.

The ATLAS TDAQ system (discussed in more detail in Chapter 3), responsible for selecting and recording interesting events from the billions of collisions occurring each second, will be overhauled to handle the increased data flow [32]. The upgraded system will employ more sophisticated algorithms and advanced hardware to ensure that ATLAS can continue to capture and process the most relevant events in real-time, minimising data loss and maximising discovery potential.

The calorimeter system, will also undergo significant upgrades [33] [34]. The electronics of the LAr calorimeters will be replaced to improve its capabilities to measure energy deposits with greater precision. This upgrade is essential for maintaining the high performance of the ATLAS experiment in identifying and reconstructing particles such as electrons, photons, and jets under HL-LHC

conditions.
The Muon Spectrometer will be enhanced with additional detector layers and upgraded electronics [35]. These improvements will ensure the continued accurate detection and measurement of muons, which continue to be very interesting for many physics analyses, for example to better determine the parameters of the Higgs boson with the increased statistics.

In summary, the ATLAS Run 4 upgrades will significantly enhance the experiment's ability to explore the SM of particle physics and search for new phenomena beyond it. With higher precision and greater data collection capacity, ATLAS will be very well equipped for the challenges that come with the upgrade. Overall, the ATLAS Run 4 upgrades represent a critical step forward in preparing for the challenges and opportunities presented by the HL-LHC, ensuring that ATLAS remains at the forefront of particle physics research.

Chapter 3

The ATLAS TDAQ System and Data Reconstruction

The studies presented in Chapter 4 of this thesis are based within the framework of the ATLAS Trigger and Data AcQuisition (TDAQ) system which is responsible for selecting and recording interesting events amongst the countless collisions during the running of the LHC [2]. Additionally, all the studies discussed in the following chapters are heavily relying on collision data that has been well reconstructed to provide the most important signatures for analyses. Therefore, this chapter is first detailing the ATLAS trigger, followed by explaining the data acquisition system and ending with going through the reconstruction of various important signatures for the studies presented in the subsequent chapters.

3.1 The Trigger System

The ATLAS trigger system, an integral component of the ATLAS detector, is designed to efficiently and accurately select the most relevant proton-proton collision events from bunch crossings occuring at a rate of 40 MHz. Each collision can generate multiple particles and complex interactions that are detected by the various components of the ATLAS detector. Currently, the data collected for one collision event corresponds to about 3 MB which would lead to a rate of 120 TB/s to store all the information recorded by ATLAS [36]. Given that it is impossible to store or process all of this raw data due to computational and storage limitations, the ATLAS trigger system plays a vital role in sifting through these collisions in real time, deciding which events hold the most promise for advancing particle physics research.

The ATLAS trigger system operates under highly configurable algorithms that are periodically optimized and updated, particularly after each LHC upgrade or maintenance period, to align with the evolving physics goals of the ATLAS experiment. The selection criteria, also known as trigger menus, are tailored to prioritize events that have specific physics signatures associated with phenomena like Higgs boson production, SUSY, or other potential signs of new physics beyond the SM. Trigger thresholds can be adjusted depending on the luminosity of the LHC beams or particular experimental goals. This adaptability is crucial, as the LHC's performance varies across runs and with upgrades, making it essential to adjust the trigger parameters to handle the different collision rates and energy scales.

The trigger system is structured in a multi-tiered, hierarchical design comprising two main stages, the Level-1 (L1) Trigger and the High-Level Trigger (HLT). Each of these stages applies specific criteria to the event data, reducing it progressively while preserving events with the highest potential scientific value.

3.1.1 The Level-1 Trigger

The L1 trigger in ATLAS is built on custom hardware using Field Programmable Gate Arrays (FPGAs) and Application-Specific Integrated Circuits (ASICs) [2]. The system consists of three main subsystems which are the Calorimeter Trigger (L1Calo), the Muon Trigger (L1Muon) and the Central Trigger Processor (CTP) [32]. Particle signatures being processed by the trigger are called candidates.

L1Calo processes data from the electromagnetic and hadronic calorimeters to identify high-energy electrons, photons, and jets. The signatures originating from quarks and gluons in calorimeters are called jets. They are going to be described in more detail in subsection 3.3.2. L1Calo also identifies missing transverse energy (explained in more detail in subsection 3.3.7) and total transverse energy, crucial for identifying events that may involve neutrinos or new particles that do not directly interact with the detector. The L1Calo subsystem features five different main processors, the Cluster Processor (CP), the Jet/Energy Processor (JEP), the electron Feature EXtractor (eFEX), the jet Feature EXtractor (jFEX) and the global Feature EXtractor (gFEX). Data from the tile calorimeter is specifically transferred by the new Tile REciever eXchange (TREX) to these processors. The data from the CP, JEP and the Feature EXtractors (FEXes) is then processed by the Level-1 Topological Processor (L1Topo) which reconstructs the geometrics and kinematics of the particle candidates and also their relations to each other within a given event.

The L1Muon trigger uses data from the muon spectrometer to identify high-energy muons. It looks for signatures which are matching high transverse momentum muons coming from the interaction region. Since muons are one of the cleanest signatures in high-energy physics experiments, due to their relatively low interaction with detector material, the muon trigger is essential for many SM studies focusing on the Higgs boson or for searching for new physics phenomena beyond the SM. L1Muon uses a Barrel Sector Logic, and Endcap Sector Logic and a NSW Trigger Processor. The Muon Central Trigger Processor Interface (MUCTPI) is used to collect and combine muon trigger information. The combined information is then passed on to the L1Topo and the CTP.

The CTP is the decision-making hub that combines data from the calorimeter and muon triggers and applies predefined conditions or thresholds to decide whether an event meets the criteria for further processing. It then sends its decision to the readout system to either store the data for further processing or to discard it.
The most important characteristic for selecting events with the L1 trigger is the transverse energy (E_T). Events must meet specific energy levels in E_T to be considered for higher-level processing. These energy thresholds help filter out low-energy events which are less likely to reveal significant physics discoveries.

Once an event is selected by the L1 trigger, Regions of Interest (RoIs) are defined, which pinpoint specific parts of the detector with activity. This approach allows the subsequent HLT to focus only on relevant portions of the detector data, optimizing processing speed. The processing within the L1 trigger starts with fast but coarse resolution data. For example, the calorimeter data used at the L1 stage has a lower spatial granularity than what is eventually available, allowing for fast decisions. If the L1 trigger identifies a region with significant energy, that event is flagged for further evaluation by the HLT.
It is crucial for the L1 trigger to make decisions extremely quickly. From the time a collision occurs, the system has only about $2.5\,\mu$s to decide whether to keep the data or not. This rapid decision-making is achieved through parallelised data processing within FPGAs and ASICs, which provide the necessary speed and computational power. If an event passes the L1 trigger, it is sent to a buffer system where it awaits further analysis by the HLT.
The L1 trigger is able to reduce the event processing rate from 40 MHz to 100 kHz. This corresponds to about 300 GB of data being accepted by the L1 trigger per second. It ensures that only events with interesting signatures, such as high-energy jets, isolated photons, or missing transverse energy, make it to the next trigger stage.

The L1 trigger plays a fundamental role in the success of the ATLAS experiment, ensuring that no significant events are missed while reducing the amount of data by several orders of magnitude. Like that it is a sophisticated, high-speed data selection system that allows the study of the most interesting events generated by the LHC. By reducing the data rate by a factor of 400, the L1 trigger makes the ATLAS experiment feasible and efficient. Its hardware-based design, relying on calorimeter and muon data, and rapid decision-making ability make it one of the most critical components of ATLAS.
With the LHC upgrades and increased luminosity in the coming years, the ATLAS L1 trigger will also be upgraded to handle even higher data rates and complexity. The upgrades will include more advanced FPGAs and ASICs to improve gran-

ularity and precision, further enhancing ATLAS's ability to explore new physics in the coming decade.

3.1.2 The High Level Trigger

The HLT selection process is based on identifying specific physics signatures associated with particles and processes of interest [32]. Some of the highly important signatures are stemming from electrons and photons. Their candidates are reconstructed in the HLT with high precision, considering both, the calorimeter data and tracking information, to eliminate fake signatures and isolate genuine signals. Furthermore, the HLT performs more detailed muon reconstruction than the L1 trigger, using data from the muon spectrometer and the ID to verify the identity and energy of muon candidates. Additionally, the HLT analyses jets and calculates missing transverse energy with greater accuracy by combining data from the calorimeter and tracker, allowing it to identify signatures that might suggest new physics, such as invisible particles. Lastly, the HLT is also specialised in identifying particles containing heavy quarks, such as bottom quarks, by analysing secondary vertices or displacement from the primary collision point. At peak luminosity in Run 2 the HLT had a mean processing time of about 400 ms [36]. For Run 3 it is even higher, around 600 ms, due to the more extensive use of hadronic track reconstruction.

One of the critical advantages of the HLT is its flexibility. Since it is software-based, algorithms can be updated, refined, and even reconfigured during ATLAS operations. This flexibility allows the HLT to adapt to changes in the detector environment, collision energy, and luminosity, as well as shifts in the physics focus. For instance, the HLT can adjust to prioritize certain signatures if there is a particular interest in detecting new particles or studying specific decay channels. Calibration is another important aspect of the HLT. Because of the high granularity of data used by the HLT, it can account for detailed detector conditions in real-time. Calibrations that account for temperature changes, electronic noise, and other factors are applied continuously, ensuring the accuracy of the event selection and reconstruction processes.
After processing, the HLT makes a final decision on each event, reducing the data rate from 100 kHz to around 3 kHz now in Run 3. With a data compression from 3 MB to 2 MB per event, there are approximately 6 GB of ATLAS data being permanently stored per second [37]. This drastic reduction ensures that the volume of data put out by the ATLAS experiment remains within manageable storage limits. The data reduction achieved by the HLT is essential for the ATLAS experiment, as it allows the experiment to focus on a much smaller, yet more relevant, subset of the initial collision data. This subset contains the events that are most likely to hold valuable information about fundamental particles and interactions, including potential discoveries.

The ATLAS HLT is a highly innovative, software-based system that refines event selection beyond the L1 trigger, allowing ATLAS to focus on events with high scientific value. Through its detailed reconstruction and flexible algorithms, the HLT reduces the data rate to a manageable level, enabling efficient data storage and analysis. Its combination of RoI-based processing and full-event reconstruction has proven essential for isolating rare physics events, making it a cornerstone of ATLAS's success in exploring fundamental particles and interactions. In the future, with the LHC's planned luminosity upgrades, the HLT will need to process an even higher number of collisions per second, demanding further upgrades to its algorithms, processing power, and data management capabilities.

3.2 Data Acquisition and Monitoring

The ATLAS Data AcQuisition (DAQ) system is a highly sophisticated infrastructure designed to manage the enormous data rates and complexity generated by the ATLAS detector [32]. Its primary objective is to collect, filter, process, and store data from the detector's multiple subsystems to enable the study of high-energy particle collisions. Given that the LHC operates at a collision rate of 40 million events per second, the DAQ must handle a data flow of several petabytes annually, making it one of the most advanced data handling systems in the world.

The data acquisition process in ATLAS begins at the detector, where signals from collisions are captured by thousands of sensors distributed across the subsystems. These signals are analogue pulses representing energy deposits and hits, which are then digitized by specialized front-end electronics located close to the detectors. The digitized data is transmitted to the ReadOut System (ROS), which forms the backbone of the data collection by managing the flow of data passing the L1 trigger. ReadOut Drivers (RODs) are used to transmit the data from the L1 trigger to the ROS where it is buffered and then passed on to the HLT via the Data Collection Network (DCN). The ROS is using the Front-End Link eXchange (FELIX) system as an interface between the DAQ system and all detector specific front-end electronics. The RoI information coming from the L1 trigger is passed on from the ROS to the DCN. Thereafter, the DCN efficiently routes the RoI information to the appropriate HLT processing nodes. The DCN facilitates a partial event building phase. Instead of transferring the entire raw event data, the DCN passes only the RoI data to the HLT. This selective data transfer is crucial because it minimizes data traffic and focuses the HLT's resources, allowing a quicker decision-making process. If the HLT determines that an RoI is of particular interest, it can request additional data from the detector regions surrounding the RoI via the DCN. In cases where the HLT requires a full event, the DCN coordinates the collection of data fragments from all parts of the detector for the selected event. This full event building is managed by the event builder system, which is part of the DCN infrastructure. It consolidates

the different data fragments into a single, coherent dataset that represents the entire event. The HLT and DCN work together in real-time, meaning that while the HLT is analysing and filtering events, the DCN is continuously handling and routing the selected data.
After the HLT processing, the DCN takes the output data and puts it in the SubFarm Output (SFO), where it is buffered until it can be transferred to the permanent data storage systems. Figure 3.1 summarizes the data acquisition procedure including the two trigger steps. It represents the current ATLAS DAQ used in Run 3.

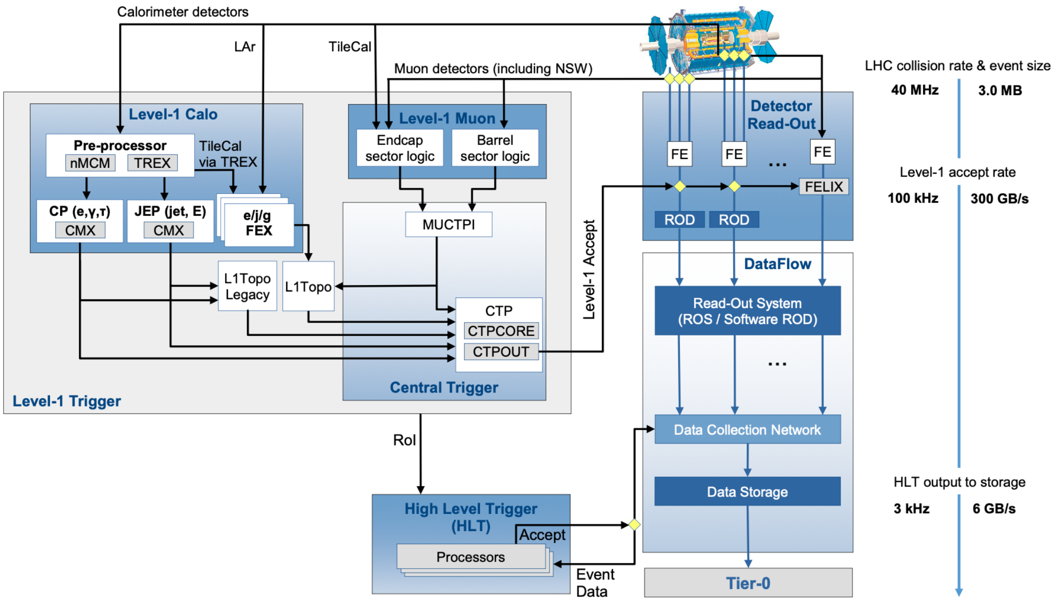

Figure 3.1: Schematics of the ATLAS trigger and data acquisition system from the detectors to the data storage [36]. On the right the output rates of the detector systems, the L1 trigger and the HLT are shown in terms of event rate and size. It's important to not that the size of the detectors' output of 3.0 MB is given per event, which corresponds to a total of 120 TB/s.

After the buffering in the SFO, the selected data is transferred to the event storage located at CERN's Tier-0 data centre. This data centre handles the raw data processing. The refined datasets are then distributed worldwide to Tier-1 and Tier-2 centres via the Worldwide LHC Computing Grid (WLCG), a distributed computing network that provides global access for analysis.

To ensure the reliability and accuracy of the data, the ATLAS DAQ includes an integrated Data Quality Monitoring (DQM) system. The DQM operates in real-time, analysing data as it is collected to detect anomalies or errors. It examines the data integrity, signal quality, and alignment between detector subsystems. If any issues are detected, alerts are sent to operators, who can intervene to correct potential problems. This real-time feedback loop is crucial for maintaining high data quality, as any errors in the data can significantly affect the physics results. The system is designed with redundancy to ensure that data acquisition remains robust even in the case of hardware failures or network interruptions. Multiple copies of critical components and parallel data paths allow the DAQ to recover from faults without data loss.

3.3 Data Reconstruction

The data collected by the DAQ system undergoes processing to reconstruct the events of interest. This involves analysing the detector information and matching it to characteristic signatures associated with different types of particles. Figure 3.2 illustrates various signatures produced by several particles as they interact with different components of the detector. These signatures typically manifest as either curved tracks or particle showers, though some particles may leave no detectable signatures in certain parts of the detector. By examining these signatures, it can be understood how specific particles interact with the inner tracking system, calorimeters, and muon chambers, which are designed to detect and measure their properties.

In the ID's tracking system, tracks created by charged particles are recorded, whereas uncharged particles usually do not produce a signature since they interact minimally with the detector material. The electromagnetic calorimeters capture the particle showers generated by electrons and photons, which are usually entirely absorbed in this section, as it is specifically designed for that purpose. Hadronic particles also generate showers in the electromagnetic calorimeters but generally continue their interactions in the hadronic calorimeters, where they are eventually stopped. Muons, due to their ability to penetrate through the entire detector system, leave behind bent tracks and exit the detector after passing the muon spectrometer.

The following sections provide an overview of the key methods and tools used for identifying and reconstructing the particle signatures measured by the ATLAS detector, highlighting their critical role in understanding particle interactions and event reconstruction.

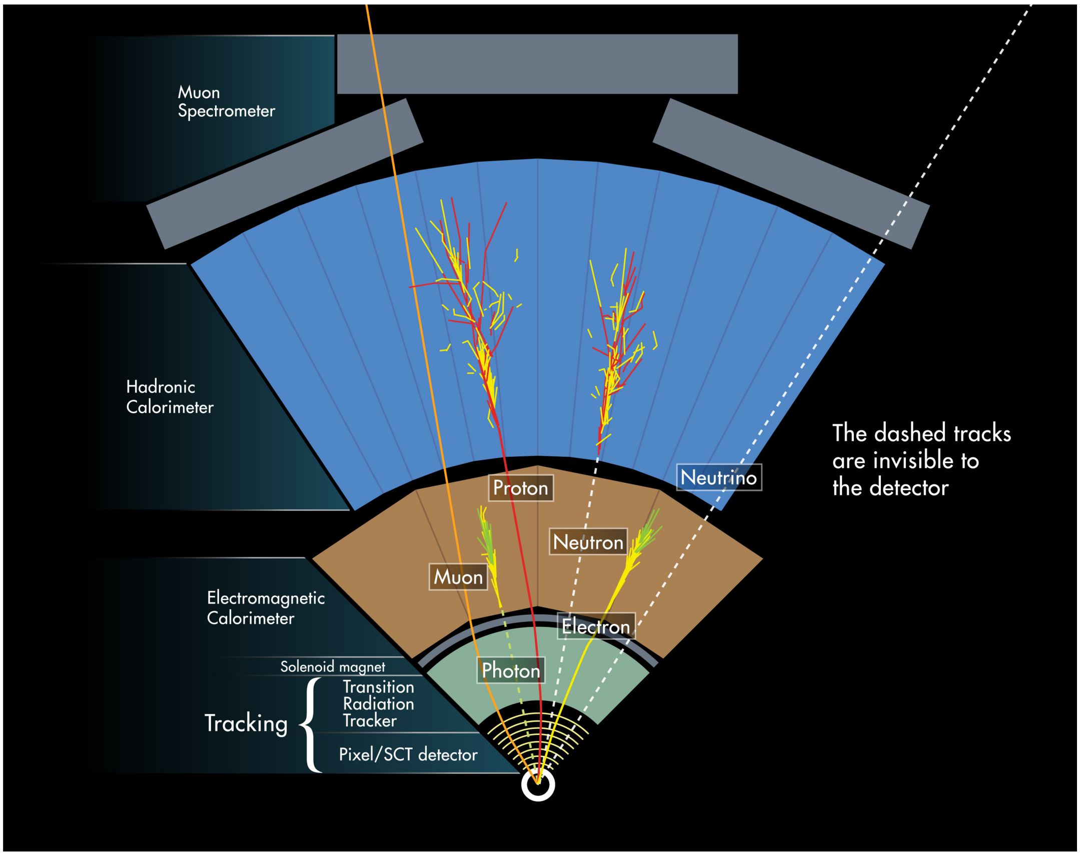

Figure 3.2: Schematic of a cross cut through the various ATLAS detector systems with the signatures of some of the most common particles produced in proton-proton collisions from [38]. This illustration highlights the unique characteristics and behaviours of particles as they traverse the detector, leaving distinct features that enable their identification and analysis.

3.3.1 Tracking

Tracking refers to the process of reconstructing the paths of charged particles as they move through the detector components [2]. This process uses data collected by the ID, specifically from particles with a transverse momentum (p_{T}) below 0.5 GeV and an absolute pseudorapidity ($|\eta|$) below 2.5. The reconstruction procedure is divided into three main steps, each crucial for accurately identifying and analysing the particle tracks.

The first step involves preprocessing the raw data. Information from the Pixel detector and the SCT is organized into clusters, while data from the TRT is processed to identify drift circles. These circles are at a radius around the TRT wires corresponding to the drift distance of electrons ionised by transition radiation. All the prepared data elements serve as the foundation for track reconstruction.

In the second step, the focus shifts to identifying tracks. Using the highly detailed information from the Pixel detector and SCT, tracks originating from the interaction region, referred to as prompt tracks, are located. The process begins with forming track seeds by combining hits from the Pixel layers and the first SCT layer. These seeds are then extended across the entire SCT to generate candidate tracks. Subsequently, data from the TRT, including information about the drift circles, is incorporated into these tracks. The tracks are then refitted using data from all three subsystems of the ID to ensure precision.

The third and final step applies advanced algorithms to reconstruct the primary and secondary vertices, as well as photon conversion points. This step enhances the understanding of particle interactions and decay processes within the detector. Figure 3.3 shows a visualisation of an early ATLAS event where the reconstructed tracks in the ID are clearly visible, showcasing the result of the tracking process.

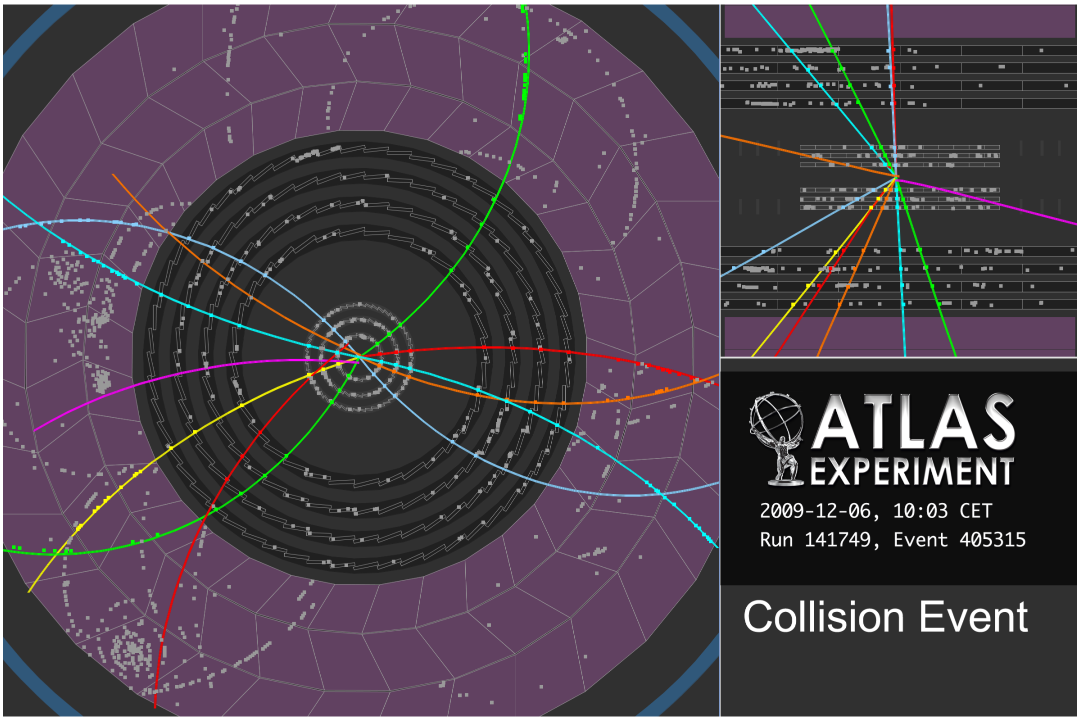

Figure 3.3: Particle tracks reconstructed from an early proton proton collision event in the Inner Detector of ATLAS [39].

3.3.2 Jet Reconstruction

In particle detectors, quarks and gluons are observed indirectly through distinctive patterns called jets. Jets are the result of a complex process known as hadronisation and they are what we measure in the detectors. Because quarks and gluons carry a colour charge, they cannot exist freely in isolation. Instead, they hadronise, combining with quark-antiquark pairs or gluon pairs that are spontaneously generated. When highly energetic quarks move away from each other, the strong coupling between them increases drastically, leading to the cre-

ation of additional particle pairs from the vacuum. These newly formed particles combine with the original quarks and gluons. This chain reaction continues until the quarks and gluons lose sufficient kinetic energy to prevent further separation. The resulting particles from a single quark or gluon combined form a jet.
Figure 3.4 illustrates the process of jet formation during a proton-proton collision, highlighting how jets emerge from the hadronisation of partons (quarks q and gluons g) forming hadrons like pions (π) or kaons (K) and how they are subsequently detected and reconstructed using the calorimeter cells.

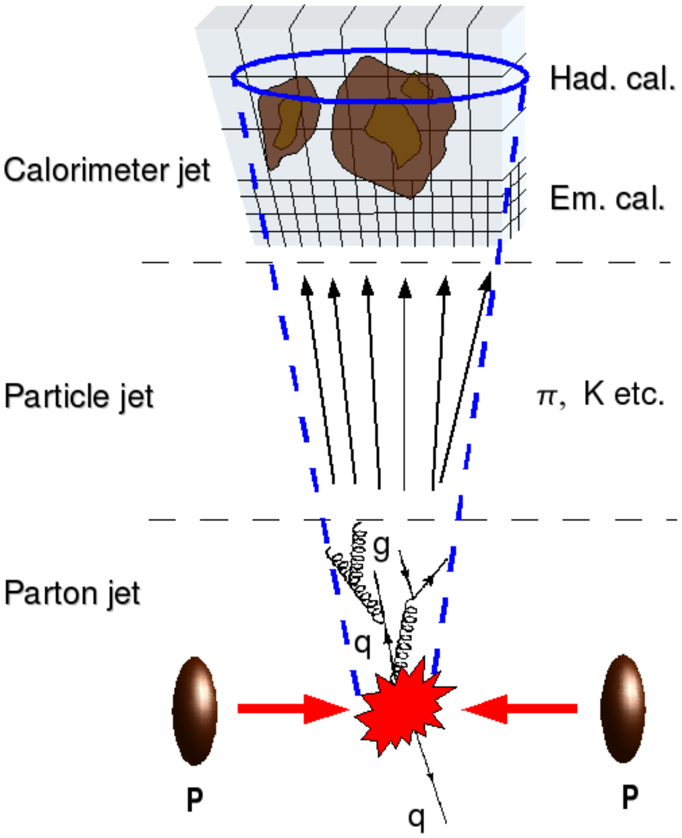

Figure 3.4: Illustration of jet formation in a proton proton collision from the initial parton to the detection in electromagnetic (em.) and hadronic (had.) calorimeters [40].

Jets are reconstructed using data collected by the detector's calorimeters, where the energy deposits are organized into clusters [2]. The ATLAS detector measures jets with barrel calorimeters in the region of $|\eta| < 3.2$ and with forward calorimeters in the region $3.2 < |\eta| < 4.9$. However, the total energy of a jet cannot be directly registered, as there is always some energy lost because neutral particles and muons are generated in the showering processes which are not well or not at all recorded. Some more minor losses of registered energy occur in parts of inactive material, such as the cryostats surrounding the calorimeters. For jets with high momentum, these energy losses can become more significant as more detector layers are involved in the measurement.Therefore, corrections are required that can account for up to 5% of the jet's total energy.

The jet clustering algorithms employed by the ATLAS experiment can be broadly classified into two main categories, the seeded cone algorithms and successive recombination algorithms. For the data analysed in this thesis, the anti-k_T algorithm, a type of recombination algorithm, has been utilised [41]. Recombination algorithms operate by iteratively merging clusters that are closer together than a specified distance parameter, $R = \sqrt{\Delta y^2 + \Delta \phi^2}$, into jets. In the studies presented here, distance parameters of $R = 0.4$ for regular jets and $R = 1.0$ for large radius jets have been used.

The anti-k_t algorithm follows a specific procedure by prioritizing the merging of clusters based on their transverse momentum, starting with those that have the highest p_T. This approach prevents low-p_T clusters from combining with each other to form jets. As a result, jets reconstructed with the anti-k_t algorithm exhibit shapes that are much less influenced by low-p_T particles, leading to more regular and consistent jet geometries.

In the anti-k_t algorithm, two distance parameters are defined, d_{ij} which measures the distance between two particles i and j, and d_{iB} which represents the distance between a particle i and the beam. These definitions form the basis of the clustering procedure, ensuring that jets are reconstructed systematically and with well-defined properties

$$d_{ij} = \min(k_{ti}^{2p}, k_{tj}^{2p})\frac{\Delta_{ij}^2}{R^2}, \tag{3.1}$$

$$d_{iB} = k_{ti}^{2p}, \tag{3.2}$$

where Δ_{ij}^2 is defined by $(y_i - y_j)^2 + (\phi_i - \phi_j)^2$ and k_{ti} is the transverse momentum, y_i the rapidity and ϕ_i the azimuthal angle of a particle i. In the anti-k_t algorithm, the parameter p, which determines the power relationship between the energy and the geometric separation (Δ_{ij}), is set to -1. The algorithm proceeds iteratively, merging pairs of particles (i and j), starting with those having the smallest distance, d_{ij}. Once two particles are combined, resulting in a new list of particles, the distances between all remaining particles are recalculated.

If the smallest distance in the recalculated list is d_{iB}, the particle i is identified as a jet. At this stage, i is removed from the list of particles and combined particles. This iterative process continues until all remaining distances exceed the specified distance parameter R, at which point the clustering is complete.

3.3.3 Identification of b-jets

The process of identifying the flavour of the quark that initiated a jet is known as tagging [2]. This technique is an essential tool in many physics analyses, particularly for identifying jets originating from bottom quarks, commonly referred to as b-jets. The tagging of b-jets takes advantage of the relatively long lifetime of hadrons containing b quarks. These B hadrons are produced shortly after the initial b quark is generated and travel a measurable distance within the detector, typically on the order of a few millimetres, before decaying. The identification process starts by finding tracks in the vicinity of a b-jet candidate's origin, determining their alignment and then calculating their impact parameters. The transverse impact parameter (d_0) and the longitudinal impact parameter (z_0) are key metrics, both defined relative to the primary vertex of the collision. In addition to the primary impact parameters, b-jets can be further distinguished by analysing secondary vertices, points where the B hadron decays into other particles. This may involve studying the entire decay chain of the b quark, including the subsequent decay of a charm quark, which itself has well-defined impact parameters. To perform a comprehensive evaluation, likelihood-ratio tagging algorithms are employed. These algorithms assess the probability that a jet originates from a b quark based on its properties. Figure 3.5 provides a schematic representation of a b-jet, showing the primary and the secondary vertex, as well as the transverse impact parameter d_0. It also shows two light jets originating from the primary vertex, which are a typical signature of a top quark decay in association with a b-jet. The term “light jet” refers to a jet which originates from one of the lighter quarks (u, d, s) or from a gluon.

The jets tagged in the analysis presented in Chapter 6 of this thesis have been identified using the second generation Graph Neural Network (GNN) tagger GN2. As the particles forming jets can be naturally represented as a graph, GNNs are very well suited for analysing them and to be used as flavour taggers [5]. Especially, tracks and vertices can be well modelled as nodes in a graph. For b-tagging GN2 largely uses track information, vertex parameters and general jet features to provide a score which can be translated into a likelihood for the jet originating from a b quark. Those inputs mainly contain geometry and kinematic information, including the aforementioned impact parameters. GN2 outperforms its predecessor GN1 by an enhanced separation of jets with a different flavour, as well as a better performance over an increased range of event topologies [43]. This is mainly achieved by a more sophisticated network architecture, including a transformer, and a massively increased training sample size.

3.3.4 Top-tagging

In the ATLAS experiment, top-tagging refers to the identification of jets originating from highly energetic top quarks in proton-proton collision events [44]. This process is crucial for analyses involving BSM physics, SM precision measurements, and searches for new particles that decay to top quarks. Top quarks are the heaviest known fundamental particles and decay almost exclusively to a bottom quark and a W boson. For boosted top quark which was generated with a high momentum, its decay products can be considered collectively in a

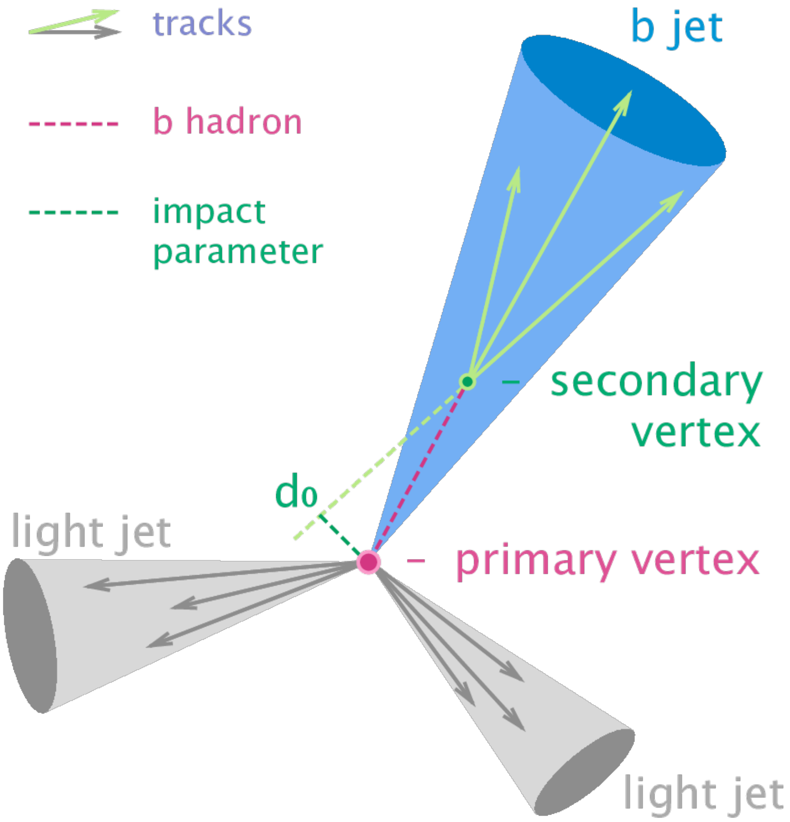

Figure 3.5: Depiction of a b-jet showing the secondary vertex and the impact parameter [42].

large-radius (large-R) jet.
The ATLAS experiment uses specific jet-clustering algorithms to reconstruct such large-R jets, typically employing the anti-k_t algorithm with a large radius parameter (e.g. $R = 1.0$) to capture the entire top quark decay products. The top-tagged large radius jets used in the study presented in Chapter 6 have been identified by sophisticated ML based taggers. They especially excel in using low-level detector information, like individual particle tracks, to identify top jets with high accuracy. As ML based taggers can identify b-jets with high precision, which are a direct decay product of top quarks, also the capability of correctly reconstructing top quark events has strongly improved. Especially in top quark pair production events ($t\bar{t}$), this helps to reconstruct the full $t\bar{t}$ system. Single top quark production usually only involves one b-jet,where ML helps isolating it to discriminate background. When produced with high transverse momentum, top quark decay products, a b-jet and two jets or leptons from the W boson decay, become highly collimated. Leptonically decaying W bosons are leaving one charged lepton and one neutrino which remains undetected by ATLAS, leaving missing energy. The top quark products often appear as a single jet with a large radius in the detector rather than separate jets. Thereby it can first be checked if the mass of the large

radius jet compares to the top quark mass of 173.1 GeV, which should add up if the W boson decays hadronically. Additionally, ML techniques help in identifying b-subjets within the large jet, as well as distinguishing top jets from jets originating from gluons or lighter quarks.

3.3.5 Electron and Photon Reconstruction

Electron candidates are identified based on seed clusters in the electromagnetic calorimeters that are matched to reconstructed tracks from the ID data [2]. In contrast, photon candidates originate from similar seed clusters in the electromagnetic calorimeters but lack a matching reconstructed track. However, photon candidates can have an associated photon conversion reconstruction, which distinguishes them from electrons.

The identification of high transverse momentum electrons relies on selection criteria applied to the shapes of their tracks and electromagnetic showers. These criteria are usually divided into three levels of stringency, “loose”, “medium”, and “tight”. “Loose” selections require minimal matching between the reconstructed track and shower cluster, with only basic constraints on the shower shape. These selections aim for broad acceptance, ensuring a higher reconstruction efficiency at the expense of some background contamination. “Medium” selections impose stricter requirements. They demand tighter constraints on the shower shape and introduce additional restrictions on the properties of the reconstructed track. This strikes a balance between efficiency and background rejection. “Tight” selections are the most restrictive. They involve extensive matching between the calorimeter cluster and the track, detailed scrutiny of the ID measurements for the reconstructed track, and stringent requirements on the energy deposition patterns in the calorimeters. This level of selection significantly enhances background rejection but reduces reconstruction efficiency. Each of these selection levels corresponds to varying electron reconstruction efficiencies, allowing for flexibility depending on the specific demands of the analysis. The identification of electrons will be further discussed in more detail in Chapter 4, where a Neural Network (NN) strategy is discussed which identifies electromagnetic showers with specific ring structures in calorimeter cells.

3.3.6 Muon Reconstruction

The reconstruction of muons in the ATLAS experiment leverages data primarily from the muon spectrometers while also incorporating measurements from the ID and calorimeters [2]. This comprehensive approach enables the reconstruction of muons with transverse momenta ranging from 3 GeV up to 3 TeV. The design of the muon spectrometers is optimized for detecting higher-energy muons, particularly those with momenta exceeding 30 GeV. At lower energies, the ID provides more accurate measurements, enhancing the overall reconstruction precision.

To accommodate the diverse energy ranges and experimental conditions, different reconstruction methods are employed for muons. The simplest method, referred to as “stand-alone” reconstruction, relies exclusively on measurements from the muon spectrometers. In this approach, track segments are first reconstructed within the spectrometers, then extrapolated and merged with matching segments to form complete tracks.

The “combined” reconstruction method, by contrast, integrates information from both, the muon spectrometers and the ID. Tracks reconstructed in the muon spectrometers are propagated back into the ID, with the energy depositions in the calorimeters factored into this extrapolation. The resulting combination of data allows for more precise muon measurements, particularly at intermediate energy ranges.

Another reconstruction strategy, known as the “segment tag” method, begins with tracks reconstructed in the ID. These tracks are extrapolated to the inner muon chambers, where they are then associated with corresponding track segments from the muon spectrometers. This method is particularly effective for linking ID tracks to muon spectrometer data in scenarios where a full combined reconstruction may not be feasible.

3.3.7 Missing Transverse Energy

To conserve momentum, the transverse momenta of all particles produced in a single collision at the LHC should theoretically sum to zero. This expectation arises because the colliding protons have no transverse momentum in the laboratory frame. Consequently, the energy deposited in the detector should ideally balance between opposite sides. However, in practice, this balance is not observed. This discrepancy arises because not all particles produced in the collision can be detected.

For instance, the ATLAS detector is not designed to measure neutrino interactions, as neutrinos interact only weakly with matter [2]. As a result, neutrinos traverse the detector without depositing energy. These unmeasured contributions to the transverse energy lead to what is termed missing transverse energy, denoted as $E_{\mathrm{T}}^{\mathrm{miss}}$. Missing transverse energy is a critical parameter in many physics analyses conducted at the ATLAS experiment, particularly those investigating phenomena beyond the SM, such as supersymmetric theories. In these theories, potential dark matter candidates, like the neutralino ($\tilde{\chi}_1^0$), only interact weakly and leave no detectable energy in the detector, further contributing to $E_{\mathrm{T}}^{\mathrm{miss}}$.

To maximize the detection of the energy carried by particles produced in collisions, the ATLAS detector is designed to cover a broad range of pseudorapidity η values. Special attention is given to minimizing gaps in the coverage, particularly in the transition regions between different sub-detectors. These regions can result in undetected energy if particles pass through them without interacting. Among the sub-detectors, the calorimeters and the muon spectrometers play a central role in reconstructing $E_{\mathrm{T}}^{\mathrm{miss}}$. To avoid double-counting muon energies, only the momenta reconstructed by the muon spectrometers are used in these calculations. The missing transverse energy of an event is determined as the negative vector sum of the transverse momenta of all identified leptons, photons, and jets ($\vec{p}_{\mathrm{T}}(e)$, $\vec{p}_{\mathrm{T}}(\mu)$, $\vec{p}_{\mathrm{T}}(\tau)$, $\vec{p}_{\mathrm{T}}(\gamma)$, $\vec{p}_{\mathrm{T}}(jets)$). Additionally, a soft term ($\vec{p}_{\mathrm{T}}(soft)$) is included to account for tracks that cannot be associated with any reconstructed electron, muon, photon, or jet. This ensures that contributions from low-energy particles not associated with hard scatterings are incorporated. The missing transverse energy $E_{\mathrm{T}}^{\mathrm{miss}}$, is ultimately calculated as the magnitude of this summed vector, providing a key observable for detecting physics processes involving weakly interacting or undetected particles. It is given by

$$E_{\mathrm{T}}^{\mathrm{miss}} = |\vec{p}_{\mathrm{T}}^{\,\mathrm{miss}}|, \tag{3.3}$$

where the $\vec{p}_{\mathrm{T}}^{\,\mathrm{miss}}$ is calculated as

$$\vec{p}_{\mathrm{T}}^{\,\mathrm{miss}} = -(\vec{p}_{\mathrm{T}}(e) + \vec{p}_{\mathrm{T}}(\gamma) + \vec{p}_{\mathrm{T}}(\tau) + \vec{p}_{\mathrm{T}}(jets) + \vec{p}_{\mathrm{T}}(\mu) + \vec{p}_{\mathrm{T}}(soft)). \tag{3.4}$$

Chapter 4

Studying Forward Electrons in ATLAS with the NeuralRinger Algorithm

In 2017, the ATLAS experiment has implemented the NeuralRinger algorithm within its HLT framework enabling rapid and accurate electron identification for event selection in real time [45]. Only electron candidates with a p_{T} greater than 15 GeV and a pseudorapidity smaller than 2.5 are being selected by the NeuralRinger. The others are still passed through the conventional method of cutbased criteria. To make fast electron identification with the NeuralRinger also possible in different phase space regions, the studies presented here have tested the application of the algorithm in extended pseudorapidity regions of $2.5 < |\eta| < 3.2$. As the key decision taking component of the NeuralRinger is ML based, a short outline over ML techniques used for high energy physics is presented first. Then, the NeuralRinger algorithm is described together with its performance within the ATLAS HLT system. Thereafter, it is discussed how the NeuralRinger has been extended to perform studies in the more forward pseudorapidity regions. And finally the results are presented on how this NeuralRinger implementation compares to the currently used cutbased selection within $2.5 < |\eta| < 3.2$.

4.1 Machine Learning in High Energy Physics

In high energy physics, ML has become an indispensable tool for extracting meaningful insights from the vast and complex datasets generated by modern particle physics experiments, such as those conducted at the LHC [46]. Among the most important ML strategies employed in high energy physics are Deep Neural Networks (DNNs), Multi Layer Perceptrons (MLPs), Boosted Decision Trees (BDTs), and increasingly GNNs. These methods are used across a wide range of tasks, including event classification, particle identification, tracking, jet tagging, and anomaly detection.

A foundational architecture in deep learning is the MLP [47]. An MLP consists of an input layer, multiple hidden layers, and an output layer. Each layer comprises nodes, or artificial neurons, which compute a weighted sum of their inputs and then apply a nonlinear activation function. This introduction of nonlinearity is essential, as it enables the NNs to model complex functions and relationships that go beyond simple linear mappings [48]. MLPs are a type of a feedforward NN, which pass information between layers only in one direction. The connections between nodes in adjacent layers are associated with weights that are adjusted during training via backpropagation and optimisation algorithms like stochastic gradient descent. The goal of this process is to minimise the mismatch between the NN prediction and the true values of the training data. The stochastic gradient descent algorithm iteratively optimises the gradient of a function by only considering a small subset of the entire dataset which makes it very important if large amounts of data are considered.

Among the most widely used activation functions in high energy physics applications is the Rectified Linear Unit (ReLU), defined as $f(x) = \max(0, x)$. ReLU is computationally efficient and helps mitigate the vanishing gradient problem, which frequently occurs during the training of DNNs. This issue describes that the gradients used for updating the weights strongly decrease during the backpropagation which hinders the first layers from learning.

Another commonly used activation function is the sigmoid function, defined as $f(x) = \frac{1}{1+e^{-x}}$, which maps input values to the range [0, 1]. The sigmoid function, with its steep slope for input values around zero, is particularly suited for scenarios where outputs need to be interpreted as probabilities, such as binary classification tasks. The outputs of the sigmoid function are always positive. This can lead to inefficient gradient updates, especially in deep networks, as it introduces a bias in the activations. Furthermore, the sigmoid function saturates at extreme values, so that for large positive or negative input values, the function flattens and its derivative approaches zero. This makes it prone to the vanishing gradient problem. Despite these drawbacks, the sigmoid function remains useful for binary classifiers and in NN architectures where probabilistic interpretation of the output is required.

Another frequently applied activation function is the hyperbolic tangent (tanh), defined as $f(x) = \tanh(x) = \frac{e^x - e^{-x}}{e^x + e^{-x}}$, with output values between -1 and 1. Unlike the sigmoid function, the tanh function is zero-centred, making it preferable over the sigmoid function, when dealing with input distributions centred around zero. It can capture both, positive and negative, activations and is useful in problems where signed information is significant, such as charge or momentum direction in particle tracks. However, like the sigmoid function, tanh suffers from saturation at the extremes, where gradients become very small and learning slows down.

Figure 4.1 shows the three common activation functions ReLU, sigmoid and tanh in the interval from -5 to 5.

While MLPs and other feedforward networks are effective at learning from fixed-size, structured input features, such as kinematic variables or detector-level quan-

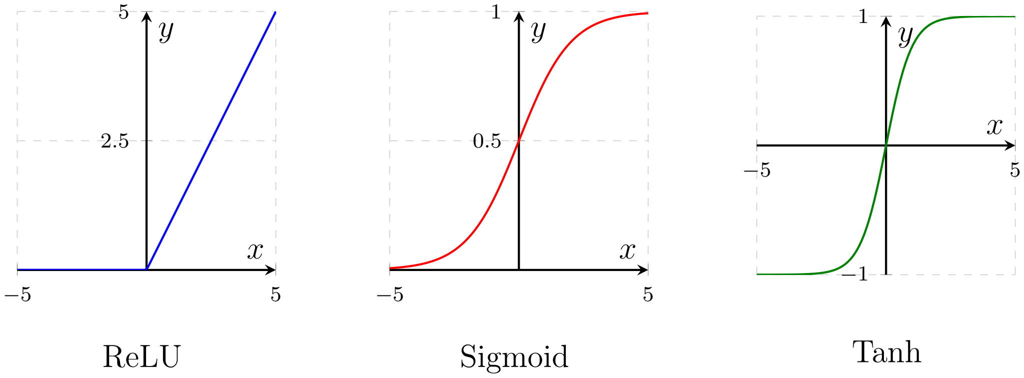

Figure 4.1: ReLU, sigmoid, and tanh activation function diagrams for input values between -5 and 5.

tities, GNNs represent a significant advancement for dealing with data that naturally has a graph-like structure. In high energy physics, this is especially relevant for modelling relationships between particles in an event or hits in a detector, where the data does not conform to a regular grid [49]. GNNs generalise NNs to operate on graphs, where nodes represent physical objects, such as particles or detector hits, and edges represent relationships, such as spatial proximity, physical connections or kinematic correlations. Through a process called “message passing”, GNNs allow each node to iteratively update its state by aggregating information from its neighbours, capturing both local and global structures in data. This is particularly powerful in applications such as jet classification, track reconstruction, and particle flow algorithms, where the spatial and relational context is crucial.

In parallel, boosted decision trees (BDTs) remain popular due to their excellent performance on structured, tabular data and their interpretability [50]. BDTs operate by iteratively combining multiple weakly learning simple decision trees to form a strong ensemble classifier that reduces the prediction error over successive iterations. They are highly effective in scenarios where the input features are well engineered and where transparency and ease of understanding are valuable.

Together, these ML strategies provide high energy physics research with a powerful set of tools for maximising the scientific output of experiments. By combining the flexibility and depth of DNNs and GNNs with the interpretability and robustness of BDTs, models are designed that learn directly from raw detector inputs or high-level features, improving precision measurements of known processes or potentially uncovering subtle signals of new physics. As both, ML techniques and computing resources, continue to advance, their role in high energy physics is expected to grow even more.

4.2 The NeuralRinger Algorithm

As previously discussed in Chapter 3, ATLAS employs a sophisticated trigger system to efficiently select events of interest from the vast number of particle collisions occurring every second. A critical component of this system is the HLT, which refines initial selections made by the L1 trigger. Within the HLT, the NeuralRinger algorithm has been developed to enhance electron and photon identification, thereby improving the experiment's overall performance [45].

Electron and photon identification in high-energy physics experiments like ATLAS is challenging due to the need of distinguishing genuine electrons and photons from various background processes. Traditional identification methods rely on predefined selection criteria based on detector signatures, which may not fully capture the complexities of particle interactions. To address this, the NeuralRinger algorithm was introduced to leverage ML techniques for more efficient and accurate particle identification.

The Neural Ringer algorithm utilizes an ensemble of NNs to process calorimeter information for electron and photon candidates. The term "Ringer" refers to the concentric ring-based sampling of calorimeter energy deposits, which serves as input to the NNs. This method captures the radial energy distribution pattern characteristics of electrons and photons, enabling the NNs to effectively distinguish them from background noise.

In 2017, the NeuralRinger algorithm was integrated into the ATLAS HLT for electron triggers. This integration aimed to reduce the computational demands of the trigger system while maintaining or improving identification performance. By employing NNs, the algorithm can process complex calorimeter data more efficiently than traditional methods, allowing for faster decision-making within the stringent time constraints of the HLT.

In the HLT step photon and electron reconstruction is initiated for each RoI identified by the L1 trigger in the EM calorimeters, provided it meets the E_{T} and isolation thresholds defined in the trigger menu [6]. For an electron or photon to be isolated, it must have a minimum angular separation from all other considerable energy deposits in the same trigger. This reconstruction goes through a series of stages, as depicted in Figure 4.2. The process begins with fast algorithms, which are computationally efficient, allowing the subsequent execution of precision algorithms at a lower event rate later in the sequence. Calorimeter and ID data within the RoI are analysed by the fast algorithms to preliminarily identify photon and electron candidates while filtering out background signals early. When a candidate passes the fast selection criteria, precision algorithms are activated in the HLT, requesting the DCN to provide additional detector data from outside the RoI for further refinement.

In Figure 4.2 it can be seen that the NeuralRinger has been applied in the beginning of the fast stage of the HLT for electron candidates. However, it still isn't implemented for photons yet.

The NeuralRinger algorithm processes energy deposits in the calorimeters by or-

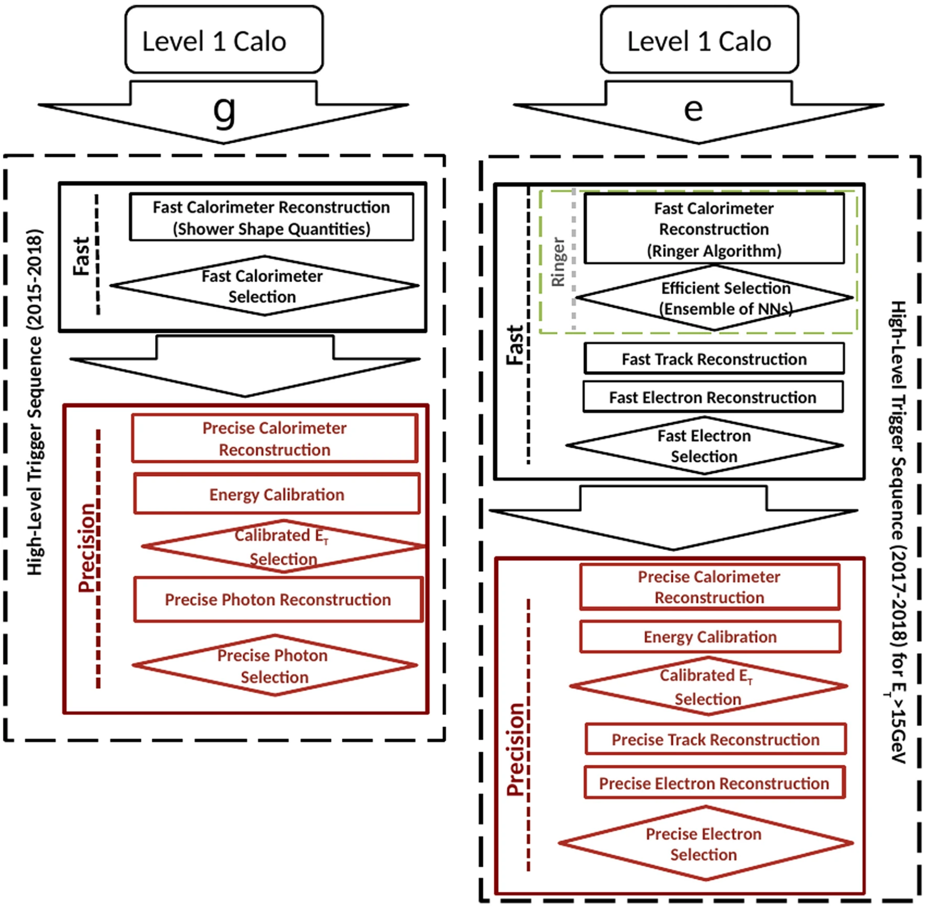

Figure 4.2: Photon (g) and electron (e) ATLAS HLT sequences for non-isoltated candidates in 2017 and 2018 [6].

ganizing them into concentric rings around the particle's trajectory. The process of constructing rings begins by identifying the cell with the highest energy in the first layer of the ECAL within the RoI. This so called "hottest" cell forms the first ring. The eight adjacent cells surrounding this initial cell define the second ring. Subsequent rings are created by including cells surrounding the outermost ring, with the process repeating until a specified number of rings is constructed in the first layer. This method is then applied to the next layer, continuing through all layers of the ECAL. In the HCAL, the first rings of each layer are defined as the cell which matches best the η and ϕ coordinates of the most energetic cell of the second ECAL layer. The following rings in the HCAL layers are then constructed in the same way as the ones in the ECAL, by using the surrounding cells. In the pseudorapidity regions for which the NeuralRinger is active ($|\eta| < 2.5$), there are three regular calorimeter layers in both the ECAL and the HCAL. In addition, there's a thin sampling layer in front of the regular layers in the ECAL called "Presampler" which is also considered in the ring building process. In each, the Presampler, the second and the third layers of the ECAL, 8 rings are built, whereas in the first ECAL layer a total of 64 rings are built. As the HCAL cells are bigger, there are only 4 rings built in each of the three layers. By adding up the number of rings from all those seven layers, ultimately a total number of 100 rings is reached. Figure 4.3 shows an example of how the ring building looks in each of the layers. It can clearly be seen that the Layer 1 of the ECAL is most granular, meaning that the highest number of cells fit in a defined area, allowing for 64 rings to be built.

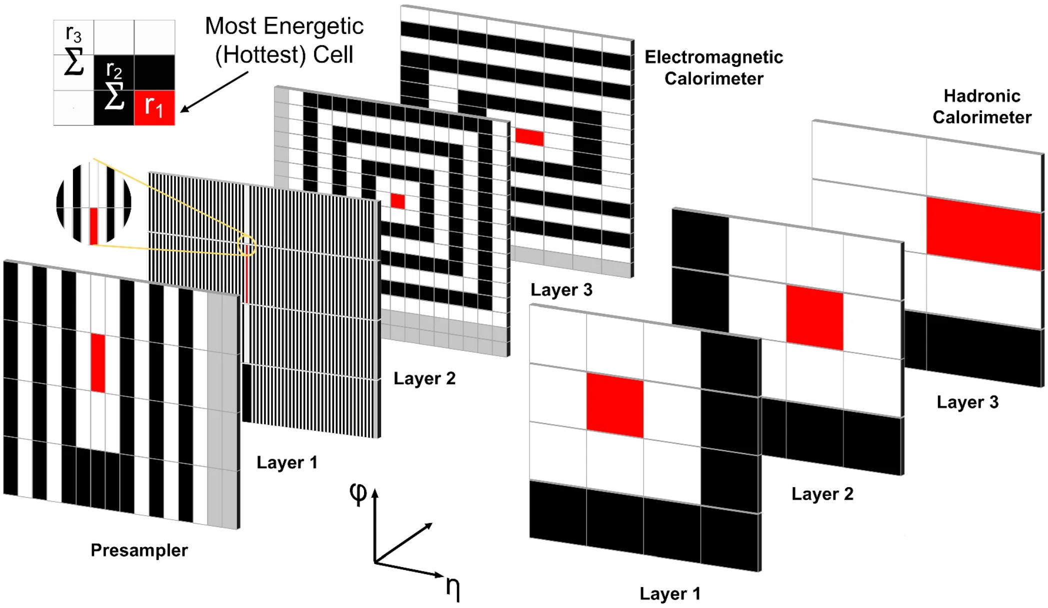

Figure 4.3: Depiction of the ring building process for all the ECAL and HCAL layers [6]. The first ring of every layer, given by the hottest cells in the ECAL, are marked in red. The following layers are coloured in black and white alternating. The grey cells visible in the ECAL layers are outside the given number of rings built in the corresponding layer and therefore not considered by the NeuralRinger.

For each of these 100 rings, the individual total E_T is calculated by summing the transverse energies of all the cells within the ring. These energy sums are then normalised by dividing each by the total transverse energy across all 100 rings. The normalised values are used as input features for an ensemble of NNs, which decides whether the electron candidate should be accepted or rejected. The NNs are trained on extensive Monte Carlo (MC) simulations, which include both real and fake electron candidates. Fake electron candidates, or non-prompt electrons, originate from other particles that mimic the energy deposition patterns of electrons in the detector. Figure 4.4 illustrates some example energy depositions of a true and a fake electron candidate in the second ECAL layer and how the ring sums are calculated. It can be seen that the real electrons' ring sums are focused on the first ring, whereas for the fake ones they are more spread. This feature can generally be observed in the ECAL and can largely be exploited by the NNs to distinguish real from fake candidates.

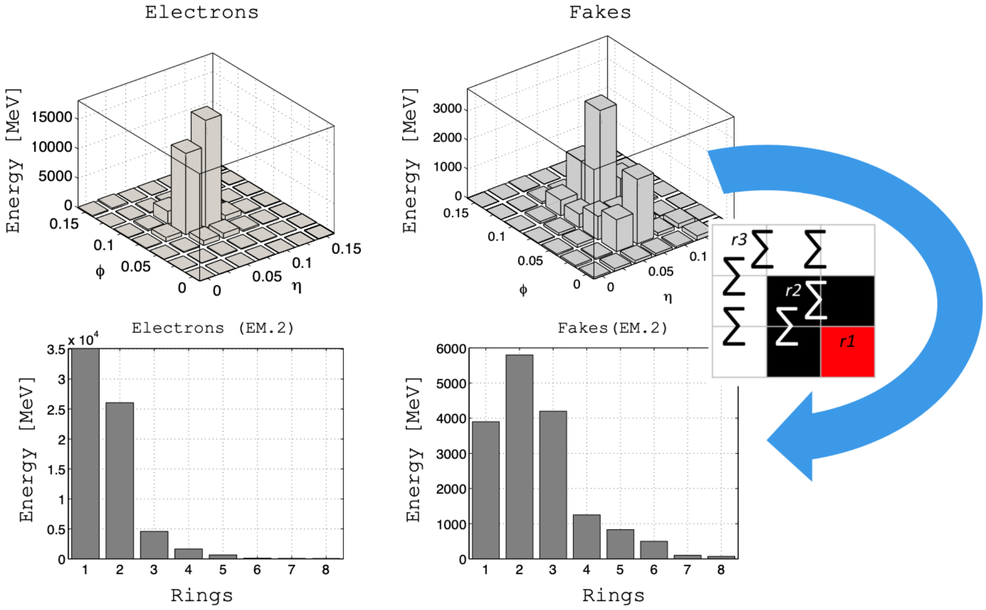

Figure 4.4: Illustration of energies deposited in the second ECAL layer and how the ring sums are calculated using them [51]. The depicted energy depositions and ring sums are showing some typical features for real and fake electrons and the indicated energies don't directly correspond to each other.

Before the data-taking periods the sets of NNs were trained for different regions in η and E_{T}. The optimised models with the best performance in each kinematic region then form the ensemble of NNs that's used in the selection step of the electron trigger. This ensemble approach, combining multiple NN, enhances robustness and generalization, leading to more reliable identification across various event conditions. For 2017, the first year in which the NeuralRinger has been implemented, the NN models were trained with simulated $Z \to ee$ samples as signal, meaning that the real candidates are originating from a Z boson decaying into an electron positron pair. As background samples, providing the fake candidates for the training, various types of simulated events containing multiple jets in the final state were used. Then, for the following years of data-taking, also ATLAS collision data from the previous years was used in the trainings.
The NN of choice for the application of the NeuralRinger in the ATLAS trigger has been and currently still is the MLP. Because of their relatively simple construction compared with other modern NNs, it only takes little computational time to calculate the output of an MLP. This makes their usage attractive for

applications like the ATLAS trigger where processing time is critical. During the multiple NeuralRinger trainings, the same tuning parameters for the MLPs have been used. The MLPs featured only one hidden layer with normally not more than ten neurons. A hyperbolic tangent activation function has been used for the neurons in the hidden layer and for the output neuron. For the cross-validation procedure a tenfold strategy has been used, meaning that the datasets were split in ten subsets, where nine of them were used for training and one for validation in all the ten possible combinations. Figure 4.5 depicts a schematic of an MLP with a single hidden layer and one output neuron, like it is being used by the NeuralRinger. Thereby, the last input node N would be 100, corresponding to the total number of rings.

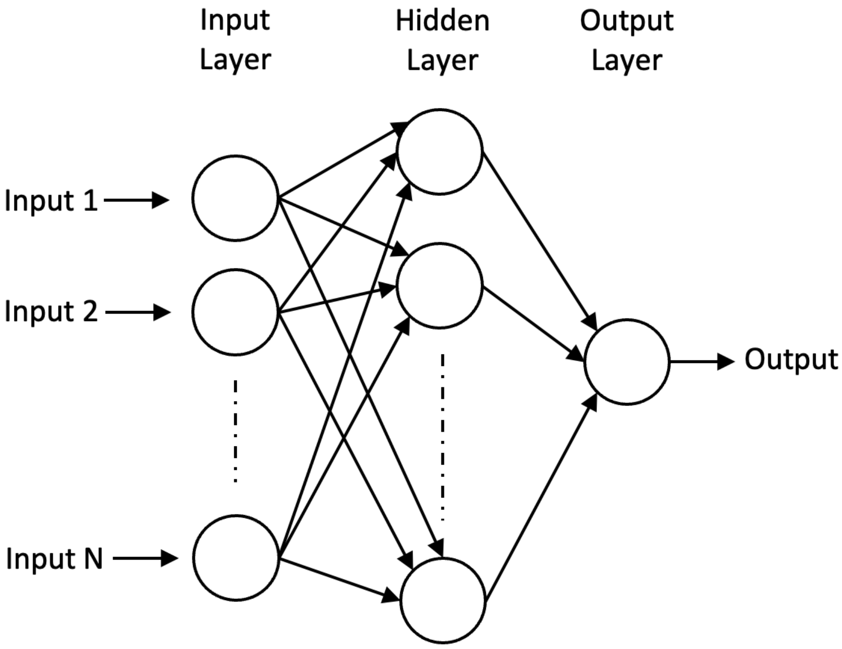

Figure 4.5: Schematics of an MLP with N inputs, one hidden layer and one output like the ones the NeuralRinger uses.

After the tunings, separation cuts on the output are applied such that the same working point efficiencies as in the cut-based selection are obtained. Like that the same rates of real electron candidates are passing the selection while rejecting much more fake candidates. To account for shifts in those working points for different values of average pile-up $\langle \mu \rangle$, a linear pile-up correction has been applied. The therefore used parameters have been derived by evaluating the NeuralRinger performance using data from the previous years with different average pile-up values.

It actually takes the electron trigger around half a millisecond more time to apply the NeuralRinger than just using the cutbased selection. However, because of the reduction of fake candidates, the subsequent fast track reconstruction time can be reduced in the order of tens of milliseconds. This step is not existing for photons as they leave no track. Therefore, a better selection of photon candidates with the NeuralRinger would come at the cost of processing time.

The adoption of the NeuralRinger algorithm has led to several notable improvements in the ATLAS trigger system. The algorithm's ability to model complex patterns in calorimeter data results in higher identification efficiency for electrons, increasing the likelihood of capturing events of interest. By accurately distinguishing between genuine particles and background noise, the NeuralRinger reduces the rate of false positives, ensuring that data storage and analysis resources are focused on relevant events. Additionally, the efficiency of NN processing allows the HLT to operate within its computational limits, even as collision rates increase with LHC upgrades.

The success of the Neural Ringer algorithm in electron identification has prompted considerations for its extension to other particle types and detector regions. Ongoing research focuses on adapting the algorithm for photon identification and exploring its applicability in the endcap regions of the detector which is the focus in the following sections of this chapter. Lastly, advancements in ML techniques, such as deep learning and convolutional NNs, are being investigated to further enhance the algorithm's performance.

4.3 Expanding Ring Building to Forward Regions

As the ATLAS ID currently only covers the pseudorapidity range of $|\eta| < 2.5$, there is no tracking information available for more forward particles. Therefore, it is very hard to determine whether an electromagnetic shower in the high $|\eta|$ region was originated by a prompt electron or a prompt photon. This changes with the planned upgrades to extend the ATLAS pixel detector for Run 4 to cover pseudorapidities up to $|\eta| = 4.0$ previously mentioned in Section 2.5. Hence it is becoming increasingly important to enhance the electron trigger algorithms in these forward regions. Improved trigger performance in those areas could provide significant benefits for many physics studies, along with the increased sensitivity and precision of the ATLAS ITk in the forward regions in Run 4. However, these regions present unique challenges due to reduced tracking information, lower granularity, and the presence of more inactive material within the detector.

Extending the NeuralRinger algorithm to cover more forward regions is a promising approach to addressing these challenges. Initial studies on its implementation in the $2.5 < |\eta| < 3.2$ region are presented here. $|\eta| = 3.2$ was used as the upper limit for these studies because it is the pseudorapidity limit of the endcap calorimeters. By keeping it, rings can be built regularly with fixed $\eta \times \phi$ granularities per layer, as no new topologies from the Forward Calorimeters, with $|\eta| > 3.2$, have to be considered. In this region, the relevant calorimeter subdetectors include the two layers of the ElectroMagnetic Endcap Calorimeter (EMEC 1 and EMEC 2) and the three layers of the Hadronic Endcap Calorimeter (HEC 0, HEC 1&2, and HEC 3. HEC 1 and HEC 2 are individual layers geometrically, but their information is combined in the $2.5 < |\eta| < 3.2$ region in the read-out process. Therefore, they are taken together as HEC 1&2, Figure 4.6 depicts a quarter slice of the ATLAS calorimeter system, indicating the region in this study's focus of $2.5 < |\eta| < 3.2$. Due to the significantly larger cell size in $\eta \times \phi$ within these regions, it is not feasible to construct the same number of 100 rings as used in regions with $|\eta| < 2.5$. Specifically, the EMEC layers have cells measuring 0.1×0.1 in $\eta \times \phi$, allowing for at most four rings to be fully constructed within the $2.5 < |\eta| < 3.2$ range, which spans seven cells in η. In the HEC layers, where cells measure 0.2×0.2 in $\eta \times \phi$, only two rings can be built.

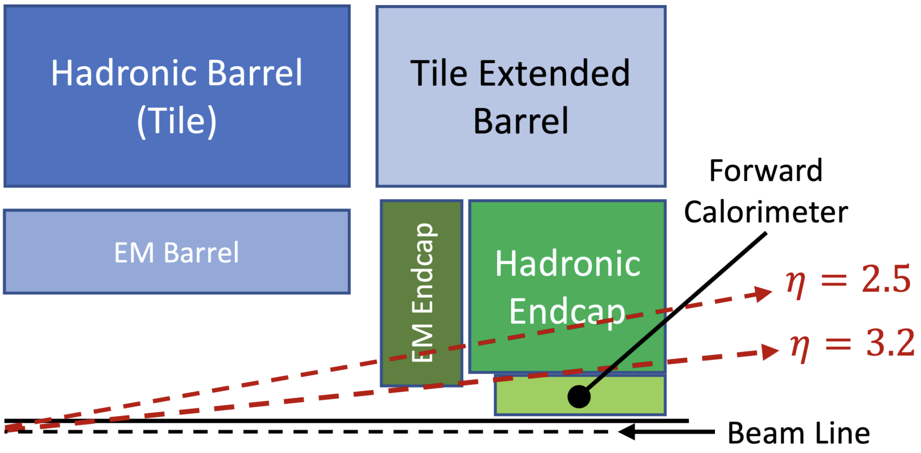

Figure 4.6: Illustration of a quarter cut of the ATLAS calorimeter system where the $2.5 < |\eta| < 3.2$ region is indicated. It is shown that the subdetectors covering this region are the electromagnetic (EM) endcap and the hadronic endcap calorimeters.

For this study, a design comprising four rings in each EMEC layer and two rings in each HEC layer was chosen, resulting in a total of 14 rings. Rings that extend beyond the bounds of the $2.5 < |\eta| < 3.2$ region were truncated at the region's borders for these initial investigations. Figure 4.7 illustrates examples of the constructed forward rings within the EMEC and HEC layers where the hottest cells lies in the centre of the region with a mean η value of 2.85.
Section 4.4 will discuss how this implementation of the NeuralRinger for forward electrons performs by training NNs with simulated samples of real and fake electron candidates. The results of those trainings are being compared with the cutbased selection currently applied for the identification of forward electrons of $2.5 < |\eta| < 4.9$ within ATLAS [52]. As there's no tracking information available, those selections are only relying on variables defined for the shower shape given by the candidate's energy clusters in the calorimeter cells. Six variables are being used for those selections, whereof four are so called cluster moments. The n-th moment of a variable x is calculated by

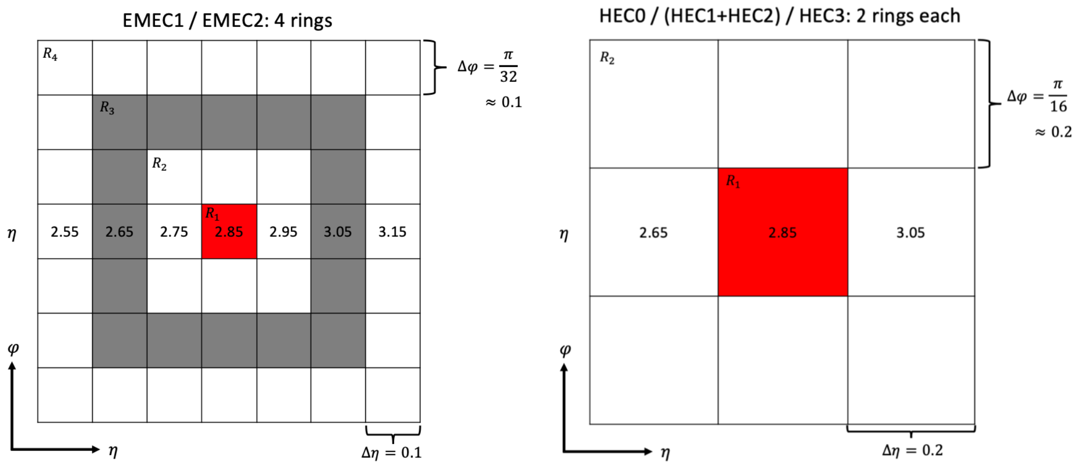

Figure 4.7: Schematic representation of the rings proposed in this studies for expanding the NeuralRinger to the $2.5 < |\eta| < 3.2$ region. On the left the four rings for the EMEC layers are presented, while the right side shows those for the HEC layers. In both cases the most energetic cell in red is positioned at the centre of the region. The mean pseudorapidity values are indicated in the corresponding cells with same ϕ value as central cell. The ring number for the layers is given on the top left of each ring, comprising the connected cells of the same colour.

$$\langle x^n \rangle = \frac{1}{E_{\text{cluster}}} \sum_{i \in \text{cells}} E_i x_i^n, \tag{4.1}$$

where E_{cluster} is the total energy of a cluster, given by the sum of all the energies E_i of the individual cells inside the cluster and the x_i are the x values of the individual cells. All the six variables used for the cutbased identification of forward electrons are listed in Table 4.1.

By applying different sets of selection cuts on the variables in Table 4.1, the three electron identification working points, “loose”, “medium” and “tight” are obtained for forward candidates. As electromagnetic showers are on average more narrow and contained than hadronic showers, electron candidates are passed if their shower shape values are lower than a certain threshold. This applies to all the variables from Table 4.1 except for f_{max} (see Table 4.1), where candidates are required to have a large ratio of their highest energetic cell to the energy of the whole cluster.

4.4 Forward NeuralRinger Performance Studies

So far ATLAS hasn’t been constructing RoIs for electron candidates of $|\eta| > 2.5$ during the data taking because of the lack of tracking information and because

Variable name	**Description**	**Term**
Shower depth	Distance along the shower axis from the first calorimeter layer to the shower centre (r_i)	λ_{centre}
Second longitudinal moment	Second moment of each cell's distance along the shower axis to the shower centre (λ_i)	$\langle\lambda^2\rangle$
Second transverse moment	Second moment of each cell's transverse distance to the shower centre with regards to the shower axis	$\langle r^2\rangle$
Maximal cell energy fraction	Fraction of the highest energy of a cluster's cells to its total energy	$f_{\max}$
Normalised lateral moment	w_2 is calculated like $\langle r^2\rangle$ by leaving out the two most energetic cells. For $w_{\max}$, only the two highest energetic cells are taken into account by setting their distance $r_i = 4$ cm	$\frac{w_2}{w_2+w_{\max}}$
Normalised longitudinal moment	l_2 is calculated like $\langle\lambda^2\rangle$ by leaving out the two most energetic cells. For $l_{\max}$, only the two highest energetic cells are taken into account by setting their distance $\lambda_i = 10$ cm	$\frac{l_2}{l_2+l_{\max}}$

Table 4.1: List of all the six variables used to identify electrons of $2.5 < |\eta| < 4.9$ in ATLAS, adapted from [52]. The first column gives the variable's name, the second one describes how it is derived and what quantities are thereby used, and the third column gives the notation.

the electromagnetic calorimeter measurements are less precise in that region[2]. Therefore, the studies presented here have only been relying on simulated events. For studying the performance of the NeuralRinger in the $2.5 < |\eta| < 3.2$ regions of ATLAS with simulated events, two different sets of samples with electron candidates have been used as the signal. Both studies were using the same simulated dijet samples to provide fake electron candidates as the background events. Dijets are collision events where two higher energetic jets emerge. These jets themselves or some constituents of them are frequently confused and accepted as electron candidates. This is likely to happen when electrons or photons are created within a jet. For example, neutral pions which decay into two photons are very commonly produced within jets. The first study, discussed in the next subsection 4.4.1, investigated, how well forward candidates from so called electron gun samples can be distinguished from dijets, using the NeuralRinger. Subsequently, in subsection 4.4.2 it will be discussed how well the NeuralRinger performed for forward electron candidates from $Z \to ee$ samples.

4.4.1 Studying the NeuralRinger in Forward Regions with Electron Gun Samples

For the first performance study of the NeuralRinger in forward regions an electron gun sample was used to provide real electron candidates. In those electron gun samples, electrons with a certain energy and direction are simulated emerging from the ATLAS interaction point without simulating an interaction itself. Therefore, the detector signatures of these samples are very clean, as there are no other particles present, like they would be numerously produced in proton-proton collisions. For the initial studies presented here, those pure electron signatures were ideal to see whether the rings designed for the forward regions, also show the anticipated behaviour. The used electron gun sample has been produced for ATLAS Run 2 studies in the MC16 campaign [53] with an even distribution of transverse energies between 20 GeV and 100 GeV and with an even pseudo-rapidity distribution in $2.3 < \eta < 4.3$. Those samples only contained simulated electrons with positive η values. The electron candidates outside $2.5 < \eta < 3.2$ were not considered in this study, as well as the ones with $E_\mathrm{T} < 15\,\mathrm{GeV}$. The dijet samples used for fake electron candidates were also produced in the Run 2 MC16 campaign by the Pythia 8 event generator framework [54]. Pythia 8 is widely used in high-energy physics for simulating events at particle colliders. The jets were produced with $E_\mathrm{T} > 50\,\mathrm{GeV}$ over all regions of η, though most electron candidates from constituents of them had lower transverse energies. The average pile-up value of the dijet samples is around $\langle\mu\rangle = 40$. Again only the candidates within $2.5 < |\eta| < 3.2$ and with $E_\mathrm{T} > 15\,\mathrm{GeV}$ were considered here. Figure 4.8 shows the E_T and η distribution of the electron candidates under consideration from the electron gun signal and the dijet background samples.

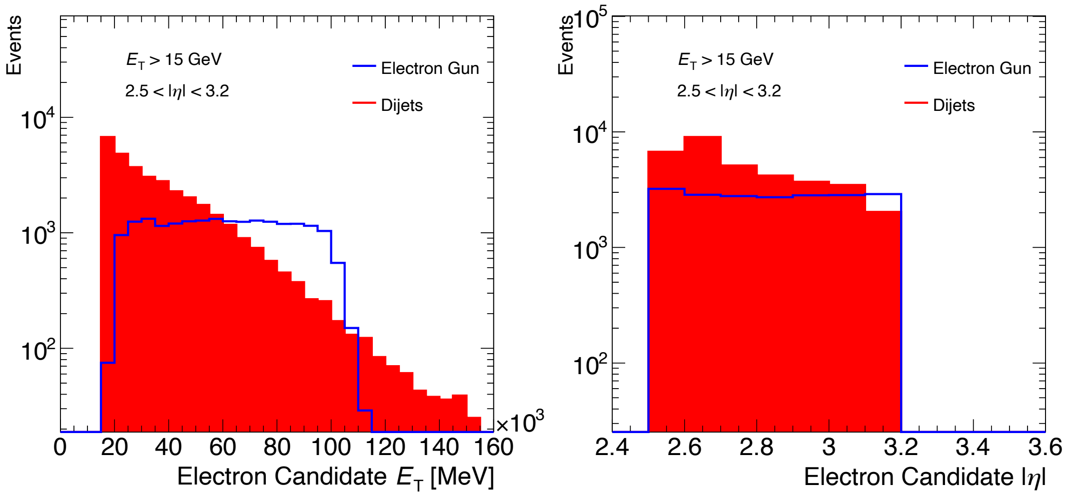

Figure 4.8: E_T and η distributions of the considered electron candidates from electron gun signal and dijet background samples. The E_T of the electron gun sample candidates shows a flat distribution between 20 GeV and 100 GeV, whereas the number of candidates from dijet samples rapidly decrease with higher energies. The number of candidates from the electron gun samples is very evenly distributed over the considered η values and for the candidates from dijet samples it's getting lower towards the higher η values.

It can be seen in Figure 4.8 that both sampels show good statistics of 1000 or more candidates per 5 GeV bin within $20\,\mathrm{GeV} < E_\mathrm{T} < 70\,\mathrm{GeV}$. Also, the η distributions show well suited numbers of more than 1000 candidates per 0.1 η for both samples over the whole spectrum of $2.5 < |\eta| < 3.2$. All the considered candidates from Figure 4.8 were put through a reconstruction process where the 14 forward rings discussed in Section 4.3 were constructed. Then, still in the reconstruction process, the ring sums were calculated and stored in a vector for each candidate. Those vectors for all the real and fake electron candidates were then passed on to the test environment for NN tunings with the NeuralRinger, based on tensorflow [55]. In this framework the ring sums are normalised and then used to train sets of NNs, as described in Section 4.2. Likewise, MLPs with one hidden layer were used as the NNs. The number of neurons in the hidden layer was varied from two to ten, to check whether there is a strong tendency for a better performance with more neurons. Like in the tunings for the barrel region, a hyperbolic tangent activation function was used for the neurons in the hidden layer and the output neuron. The tenfold cross-validation strategy was applied again and each set was tuned with ten distinct initialisations. With the nine variations coming from the different numbers of neurons, a total number of 900 MLP models was trained. Figure 4.9 shows the mean profile of the normalised rings for the electron gun signal and dijet background samples. It represents the mean values of the 14 direct inputs to the NNs that were trained.

It can be seen in Figure 4.9 that the real electron candidates have much higher average values for the first ring, whereas the fake ones have notably higher entries for the rings 9-12, corresponding to the first two HEC layers. These discrepancies can be learned and exploited by the NNs, allowing for a good separation between signal and background.

For the MLPs to evaluate their learning progress during the trainings, a Mean Square Error (MSE) loss function was used. The tunings were concluded if the NN validation failed to improve the Sum Product (SP) index in 25 successive iterations. The SP index is given by

$$\mathrm{SP} = \sqrt{\sqrt{P_\mathrm{D}(1 - F_\mathrm{R})} \cdot \frac{1}{2}(P_\mathrm{D} + 1 - F_\mathrm{R})}, \tag{4.2}$$

with the probability of detection P_D and the fake rate F_R. The P_D represents the likelihood of a signal candidate being correctly identified by the NN, while the F_R denotes the probability of a background candidate being misclassified as a signal. The P_D, also known as true positive rate, gives a measure of sensitivity to the signal, and the term “1 - F_R” is known as true negative rate, giving a measure of specificity to correctly identify background candidates. By combining both the sensitivity and specificity, the SP index is a very balanced indicator of classifier performance. This is especially important when aiming for both, a high P_D and a low F_R value at the same time.

As the output of all the trained MLPs is determined by a hyperbolic tangent function, they all classify each candidate with an output between -1 and +1. The closer one candidate's output to +1, the more likely it is that its ring sums stem

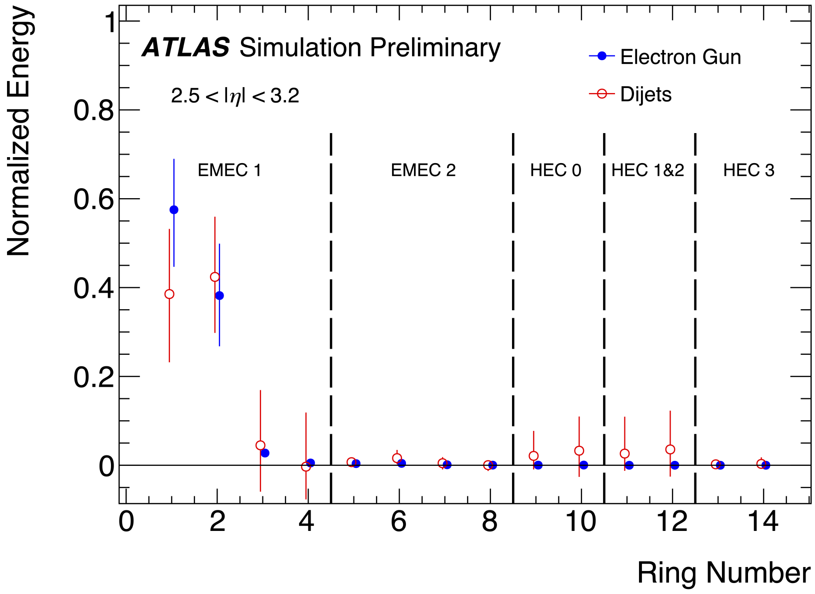

Figure 4.9: The rings' mean profiles for signal and background forward electron candidates from electron gun and dijet samples, respectively. Both profiles are normalised such that the sum of the values across the 14 rings equals 1.0. The error bars represent the RMS width of the individual normalised ring sums. For clarity, the markers for both samples have been slightly offset within the same bin. Electron candidates from electron gun samples have much higher relative energy depositions in the first ring, whereas candidates from dijet samples have higher average depositions in the last rings corresponding to the HEC layers.

from a real electron. Different thresholds can be set on the outputs to let a desired number of candidates pass the selection. In order to evaluate the performance of the individual trained NNs, the SP index can be used again. Figure 4.10 shows the output distribution of signal and background of the MLP which achieved the highest SP index out of the 900 trained models. This MLP model had nine neurons in the single hidden layer. The maximum SP of 0.961 is received for a treshold value of 0.662, which corresponds to a P_{D} and F_{R} of 0.991 and 0.069, respectively.

Figure 4.10 demonstrates a very effective separation of real from fake electron candidates with a NN. Various configurations of MLPs with differing numbers of neurons in the hidden layer were evaluated, all of which generally performed well. However, MLPs with only two neurons in the hidden layer exhibited noticeably poorer performances compared to the others. Beyond three neurons, only a slight improvement in performance was observed as the number of neurons increased. The performance of the NNs was also compared to that of the current cut-based approach used for forward electron detection. In Table 4.2 the average performance of the MLP models with different numbers of neurons in the hidden

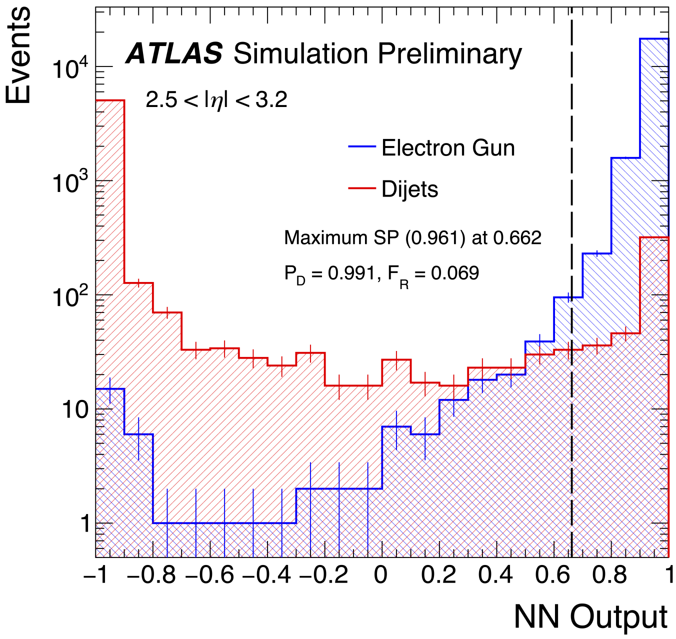

Figure 4.10: NN output values of the MLP achieving the highest SP index of the 900 models trained with electron candidates from electron gun and dijet samples. The maximum SP value together with its corresponding threshold, P_D and F_R are indicated as well. The output values range from -1 to +1, where for each of the bins an error for its statistical error is given. The dashed line at 0.662 marks the threshold for the maximum SP index.

layer is compared to the cutbased selection at a P_D around 94%, matching the "medium" working point.

Firstly, it is clearly visible in Table 4.2 that the F_R of the majority of the trained MLPs could be reduced by more than a factor of 15 compared to the cutbased one at the "medium" working point. This demonstrates a huge potential for improvement in identifying electrons in the regions of $2.5 < |\eta| < 3.2$ with NNs. Additionally, it can be noticed in Table 4.2 that the average F_R of the models with only two neurons in the hidden layer is almost 50% higher than the ones of the models with more neurons. However, for the other configurations the F_R stays quite constant with slight fluctuations. Therefore, it can be concluded that it's not necessary to strongly increase the number of neurons for better results.

The same studies were also conducted for the "loose" and the "tight" working points, located around P_D values of 97.0% and 90.8%, respectively. In both cases the performance of the MLP models with only two neurons in the hidden layer was again worse with close to 50% increased fake rates. The high cutbased "loose" reference F_R of 14.9% was reduced by an average factor around 20 for the models with three or more neurons in the hidden layer. For the cutbased "tight" working point, the reduction factor of the reference F_R at 5.9% was a bit less, but still very significant with a value of a bit more than ten on average.

Configuration	$P_{\mathrm{D}}[\%]$	$F_{\mathrm{R}}[\%]$
Reference	94.17	9.14
2 Neurons	94.22 ± 0.17	0.81 ± 0.61
3 Neurons	94.17 ± 0.09	0.56 ± 0.35
4 Neurons	94.14 ± 0.11	0.56 ± 0.43
5 Neurons	94.21 ± 0.16	0.56 ± 0.43
6 Neurons	94.11 ± 0.21	0.68 ± 0.55
7 Neurons	94.20 ± 0.09	0.55 ± 0.38
8 Neurons	94.17 ± 0.12	0.53 ± 0.36
9 Neurons	94.11 ± 0.07	0.66 ± 0.51
10 Neurons	94.22 ± 0.19	0.55 ± 0.39

Table 4.2: Comparison of the average MLP performance for each number of neurons in the hidden layer with the cutbased selection evaluated at a P_{D} around 94% corresponding to the “medium” working point. The reference belongs to the cutbased selection and the following entries show the average P_{D} and F_{R} values for the 100 models trained with the indicated number of neurons in the hidden layer. For the P_{D} values, the threshold was increased in steps of 0.01 along the NN output and stopped at the value which was closest to the reference. The errors given for P_{D} and F_{R} are the standard deviation of the values obtained by the 100 models with the same number of neurons in the hidden layer.

After the success of this first training of MLPs with forward rings, it was repeated by splitting all the candidates with $E_{\mathrm{T}} < 40\,\mathrm{GeV}$ from the ones with higher E_{T}. The goal of this study was to see whether the performance differs depending on which energy spectrum is considered. The same types of samples as before were used for both, signal and background. However, their statistics were expanded by increasing the total number of events by around 50%. The results for both E_{T} bins showed a much better performance than the cutbased reference, but it can clearly be seen that the MLP models trained in the lower energy bin of $15\,\mathrm{GeV} < E_{\mathrm{T}} < 40\,\mathrm{GeV}$ performed better than the $E_{\mathrm{T}} >\ 40\,\mathrm{GeV}$ ones. Table 4.3 shows the average performance of the MLP models with various numbers of neurons in the hidden layer compared to the cutbased selection at P_{D} values corresponding to the “medium” working points in the $15\,\mathrm{GeV} < E_{\mathrm{T}} < 40\,\mathrm{GeV}$ and the $E_{\mathrm{T}} > 40\,\mathrm{GeV}$ energy bin.

Table 4.3 shows that the MLPs trained on forward rings achieved much better separation of real and fake electron candidates of lower energetic candidates with $15\,\mathrm{GeV} < E_{\mathrm{T}} < 40\,\mathrm{GeV}$. The F_{R} values of those candidates could even be more reduced than the values from the previously discussed studies with a single energy bin, shown in Table 4.2. In contrast, the F_{R} reduction of candidates with $E_{\mathrm{T}} > 40\,\mathrm{GeV}$ is much less. But it’s still much lower than the one of the corresponding cutbased reference by almost a factor of eight. This worse performance of the NeuralRinger for forward electron candidates of higher energies can be

	15 GeV $< E_\mathrm{T} <$ 40 GeV		$E_\mathrm{T} >$ 40 GeV	
Configuration	P_D[%]	F_R[%]	P_D[%]	F_R[%]
Reference	93.13	9.44	95.54	8.74
2 Neurons	93.09 ± 0.08	0.44 ± 0.13	94.58 ± 0.07	1.17 ± 0.03
3 Neurons	93.12 ± 0.12	0.45 ± 0.26	94.57 ± 0.08	1.17 ± 0.05
4 Neurons	93.09 ± 0.16	0.41 ± 0.24	94.53 ± 0.03	1.16 ± 0.05
5 Neurons	93.15 ± 0.15	0.34 ± 0.03	94.58 ± 0.07	1.14 ± 0.05
6 Neurons	93.11 ± 0.10	0.41 ± 0.20	94.53 ± 0.09	1.14 ± 0.03
7 Neurons	93.16 ± 0.20	0.32 ± 0.03	94.52 ± 0.07	1.13 ± 0.01
8 Neurons	93.11 ± 0.15	0.32 ± 0.04	94.52 ± 0.08	1.15 ± 0.04
9 Neurons	93.14 ± 0.16	0.33 ± 0.03	94.54 ± 0.06	1.13 ± 0.03
10 Neurons	93.06 ± 0.06	0.33 ± 0.02	94.54 ± 0.08	1.14 ± 0.05

Table 4.3: Comparison of the average performances of differently configured MLPs in the 15 GeV $< E_\mathrm{T} <$ 40 GeV and the $E_\mathrm{T} >$ 40 GeV energy bins with the cutbased selections corresponding to the "medium" working point. The reference values vary because the cutbased selection accepts different numbers of candidates in both energy bins. The following entries show the average P_D and F_R values for the 100 models trained with the indicated number of neurons in the hidden layer in both energy ranges. For the P_D values, the threshold was increased in steps of 0.01 along the NN output and stopped at the value which was closest to the reference. The errors given for P_D and F_R are the standard deviation of the values obtained by the 100 models with the same number of neurons in the hidden layer.

explained with the much smaller number of background candidates available in the dijet samples for those energies, as seen in Figure 4.8. Therefore, it is harder for the NNs to find common patterns which help identifying and discriminating background. Interestingly, the performances of the various MLP configurations seem to get slowly better with more neurons in the hidden layer for both E_T bins. This is different from the behaviour, observed in Table 4.3, where there was just a big difference between configurations with two and three neurons in the hidden layer and then almost no difference anymore for configurations with more neurons. This could be due to more similarities between the candidates of the same energy range, making it more demanding for the NNs to find distinct features between signal and background. The performances of MLP models with seven or more neurons in the hidden layer seem to be very constant again for both energy bins. Very similar behaviours as previously discussed and shown in Table 4.3 were also seen for the "loose" and "tight" working points in both energy bins.

Generally, it can be said that the application of the NeuralRinger on forward electron candidates from electron gun and dijet samples was very successful. The hundreds of trained MLPs overall showed a much better performance in separating real from fake candidates than the cutbased selections currently implemented by ATLAS. A worse performance of the NNs for higher energetic candidates has been observed. That could have been caused by the more limited amount of background available. But still it was much better than the cutbased reference. However, it has to be noted that the electron gun samples provide very clean electron signatures in a way that is not representative for proton proton collisions at the LHC. Therefore, these studies were repeated using $Z \rightarrow ee$ samples instead of electron gun samples, which are discussed in the following subsection 4.4.2.

4.4.2 Studying the NeuralRinger in Forward Regions with $Z \rightarrow ee$ Samples

In contrast to electron gun samples, $Z \rightarrow ee$ samples are simulated with underlying collision events. A set of $Z \rightarrow ee$ samples simulated by Pythia 8 with electrons going in the more forward regions of $2.5 < |\eta| < 3.2$ was used in the studies presented here to provide real electron candidates. The fake electron candidates were provided again by the same dijet samples as the ones used in the studies presented before in subsection 4.4.1, but with more statistics. Like the dijet events, the $Z \rightarrow ee$ events were simulated with an average pile-up value around $\langle\mu\rangle = 40$. As in the studies before, only candidates with $2.5 < |\eta| < 3.2$ and $E_\mathrm{T} > 15\,\mathrm{GeV}$ were considered. Figure 4.11 shows the E_T and η distributions of the electron candidates under consideration from the $Z \rightarrow ee$ signal and the dijet background samples.

Figure 4.11 shows high numbers of much more than 1000 candidates per 10 GeV bin within $15\,\mathrm{GeV} < E_\mathrm{T} < 55\,\mathrm{GeV}$ for both samples. Due to the increased statistics of both samples compared to the previous study (Figure 4.8), their η distributions show more candidates in every bin over the whole spectrum of $2.5 < |\eta| < 3.2$. All the considered candidates were put again through a reconstruction process where the 14 forward rings discussed in Section 4.3 were constructed. Thereafter, the ring sums were calculated and stored in a vector for each candidate. The vectors for all the electron candidates from the $Z \rightarrow ee$ and dijet samples were then passed on to the NN tuning framework of the NeuralRinger. All the tuning configurations were kept the same as for the previous tunings discussed in subsection 4.4.1, except for the binning, where a lower E_T separation threshold was set. An E_T separation at 30 GeV gives the NNs more dijet background candidates in the higher E_T bin, allowing for better training results. Figure 4.12 depicts the normalised rings mean profile for the $Z \rightarrow ee$ signal and dijet background samples. Thereby, the mean values of the 14 direct inputs of the NNs that were trained are shown.

It can be seen again in Figure 4.12 that the first ring shows much higher average values for real electron candidates whereas rings 9-12 have notably higher entries for fake electron candidates. However by comparing Figure 4.12 with the electron gun rings from Figure 4.9, one can notice that the yields of the $Z \rightarrow ee$ candidates are a bit closer to the dijet ones. Therefore, the performances of the NN trainings

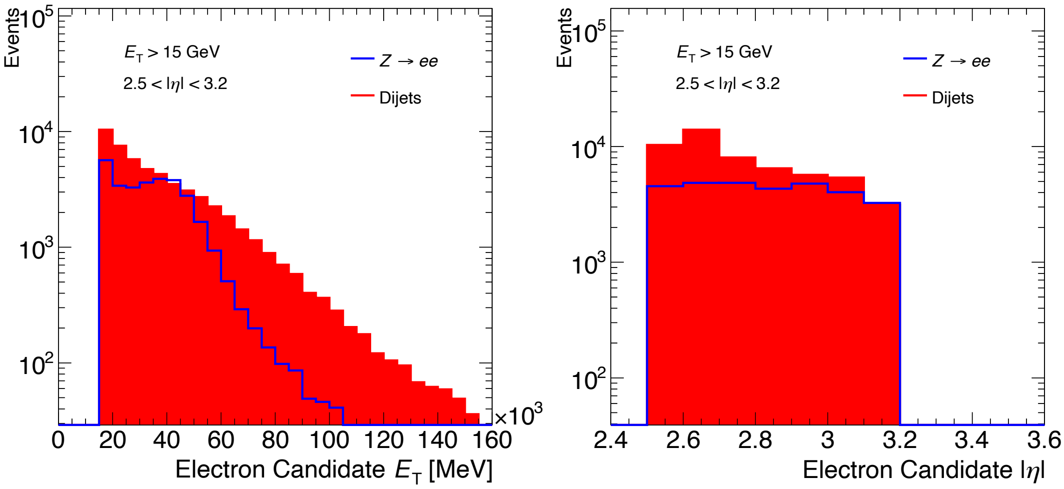

Figure 4.11: E_T and η distributions of the considered electron candidates from $Z \rightarrow ee$ signal and dijet background samples. The E_T distribution on the left shows that the number of candidates from $Z \rightarrow ee$ samples drastically decreases for $E_\mathrm{T} > 50\,\mathrm{GeV}$, while the number of candidates from dijet samples decreases more continuously with higher energies. The number of candidates from the $Z \rightarrow ee$ samples is very evenly distributed over the considered η values and for the candidates from dijet samples it's getting lower towards the higher η values.

with $Z \rightarrow ee$ samples are expected to be a bit worse than the ones with electron candidates from electron gun samples. Despite these similarities, there are still many discrepancies between the rings mean profiles of real electron candidates from $Z \rightarrow ee$ samples to the ones of fake candidates from dijet samples, that can be learned and exploited by the NNs.

After the tuning of the 900 MLP models each for both E_T bins, the results are compared with the cutbased selections of the three working points "loose", "medium" and "tight" again. In Table 4.4 the average performance of the MLP models with different numbers of neurons in the hidden layer is compared to the cutbased selections corresponding to the "medium" working point for both bins of the $Z \rightarrow ee$ signal and dijet background candidates.
Table 4.4 shows a very big difference of more than 30% in the reference P_D value between the lower and the higher energy bin. Also, in the binned tuning using electron gun samples, more higher real electron candidates were accepted in the higher energy bin, as can be seen in Table 4.3. However, there the difference was only a few percent. This means that the cutbased selections are much less efficient in correctly identifying low energetic forward electrons from simulated collisions with pile-up, than higher energetic ones. This tendency cannot be observed for the NeuralRinger selections, as they show much smaller F_R values in the lower energetic bin. But as the NeuralRinger performance was evaluated around the

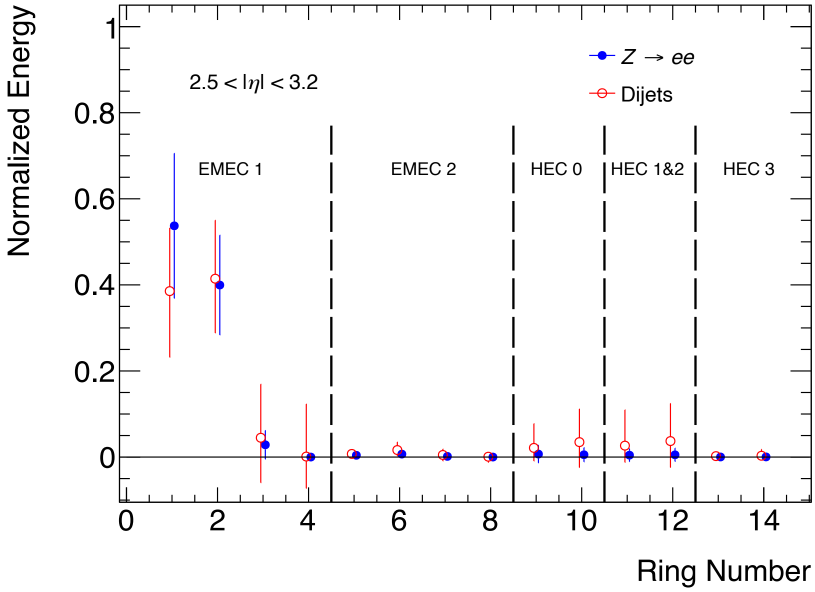

Figure 4.12: The rings' mean profiles for signal and background forward electron candidates from $Z \to ee$ and dijet samples respectively. Both profiles are normalised such that the sum of the values across the 14 rings equals 1.0. The indicated errors represent the RMS width of the individual normalised ring sums. For clarity, the markers for both samples have been slightly offset within the same bin. Electron candidates from $Z \to ee$ samples have much higher relative energy depositions in the first ring, whereas candidates from dijet samples have higher average depositions in the last rings corresponding to the HEC layers.

same P_D as the cutbased reference, it also shows these low values around 50% in Table 4.4. However, this value can be significantly increased by using the NeuralRinger instead of the cutbased selection without letting the F_R escalate.
For many MLP models in the lower energy bin the fake rate can be very substantially reduced, by almost a factor of 50 with respect to the cutbased reference. The models with two neurons in the hidden layer were again clearly less successful, so that their average F_R values were around a factor of 2.5 higher than those of most other models. Also, the performance of the MLP configurations with three neurons in the hidden were a bit worse than the ones with more neurons, but their results were already similar For the other configurations, the fake rates were mostly around 20% with only little variation.
In the $E_\mathrm{T} > 30\,\mathrm{GeV}$ bin, the MLP models were able to reduce the fake rate by an average factor around 9. Again, the models with two neurons in the hidden layer showed the worst average performance, however, a strong tendency cannot be observed. The average F_R values vary a lot, which is also shown by the large standard deviations of the models with the same number of neurons.
The overall very successful NeuralRinger tunings with $Z \to ee$ samples strongly

	15 GeV $< E_\mathrm{T} <$ 30 GeV		$E_\mathrm{T} >$ 30 GeV	
Configuration	P_D[%]	F_R[%]	P_D[%]	F_R[%]
Reference	49.57	9.62	83.33	8.82
2 Neurons	49.60 ± 0.41	0.55 ± 0.08	83.32 ± 0.05	1.28 ± 0.64
3 Neurons	49.59 ± 0.10	0.29 ± 0.04	83.34 ± 0.07	0.80 ± 0.51
4 Neurons	49.60 ± 0.35	0.23 ± 0.04	83.31 ± 0.05	0.87 ± 0.54
5 Neurons	49.63 ± 0.15	0.21 ± 0.01	83.32 ± 0.09	0.94 ± 0.59
6 Neurons	49.61 ± 0.47	0.20 ± 0.01	83.35 ± 0.09	0.94 ± 0.62
7 Neurons	49.54 ± 0.22	0.21 ± 0.02	83.31 ± 0.08	1.14 ± 0.59
8 Neurons	49.32 ± 0.25	0.20 ± 0.01	83.33 ± 0.07	0.71 ± 0.46
9 Neurons	49.49 ± 0.16	0.21 ± 0.02	83.31 ± 0.09	1.16 ± 0.58
10 Neurons	49.59 ± 0.29	0.20 ± 0.01	83.33 ± 0.03	0.94 ± 0.52

Table 4.4: Comparison of the average performances of differently configured MLPs in the 15 GeV $< E_\mathrm{T} <$ 30 GeV and the $E_\mathrm{T} >$ 30 GeV energy bins, with the cutbased selections corresponding to the "medium" working point. The reference values vary because the cutbased selection accepts different numbers of candidates in both energy bins. The following entries show the average P_D and F_R values for the 100 models trained with the indicated number of neurons in the hidden layer in both energy ranges. For the P_D values, the threshold was increased in steps of 0.01 along the NN output and stopped at the value which was closest to the reference. The errors given for P_D and F_R are the standard deviation of the values obtained by the 100 models with the same number of neurons in the hidden layer.

indicate that analyses considering forward electrons with ATLAS could greatly benefit from an extension to $|\eta| = 3.2$.

Chapter 5

Simulating and Studying Forward Electrons with Lorenzetti Showers

Detector simulations play a crucial role in developing experiments, designing sub-detectors, interpreting results, and guiding upgrades in particle physics. For example, they are especially important for ATLAS while preparing for the unprecedented levels of pile-up coming with the HL-LHC as described in Section 2.5. However, most of the simulation and reconstruction software used for ATLAS is specifically tailored to the experiment. High energy physics experiments are usually strongly relying on custom software. In contrast, the newly developed Lorenzetti Showers framework offers a versatile, general-purpose environment for calorimetry that can be adapted to suit various detector specifications [7]. The very general design of the framework, based on the readout and processing of every signal in the active components, also allows for studying systems contributing to, or depending on calorimeters. This can involve signal processing, triggering, data reconstruction or even theoretical physics studies. As the NeuralRinger algorithm presented in Section 4.2 is fully relying on calorimeter information, Lorenzetti Showers can be a very useful tool to support NeuralRinger developments. This chapter discusses, how Lorenzetti Showers helped extending the studies on the NeuralRinger for forward electrons presented in Chapter 4. By recreating very similar scenarios to this previous study, both the simulation capacities of Lorenzetti Showers and the more general usage of the NeuralRinger have been tested and verified.

Firstly, the Lorenzetti Showers framework is presented in more detail. Then, it is discussed how it was used to provide simulated samples for investigating forward electron signatures and how they could be prepared for the NeuralRinger. Subsequently, the NeuralRinger training of Lorenzetti Showers simulated electron and $Z \to ee$ signal and dijet background events is detailed. And lastly in this chapter, it is addressed how pile-up was simulated with Lorenzetti Showers and how it affected the NeuralRinger performance.

5.1 The General-Purpose Calorimetry Framework Lorenzetti Showers

The Lorenzetti Showers framework is a versatile and modular software platform designed to facilitate the development and testing of advanced algorithms for signal processing and event reconstruction in high-energy physics experiments. Its primary focus is on calorimeter data, enabling detailed simulations of particle interactions and detector responses. This framework is also very interesting to design and refine algorithms for triggering, leveraging ML and other advanced techniques.

Lorenzetti Showers' general-purpose calorimeter simulation is a cornerstone of the framework, offering users a highly flexible and realistic representation of detector geometries, particle showers, and associated signals. By integrating state-of-the-art tools like Pythia 8 and Geant4 (GEometry ANd Tracking) [56], Lorenzetti Showers provides a unified environment for studying calorimetry in a wide variety of experimental settings.

At the heart of the Lorenzetti Showers framework lies the simulation of particle collision events. This is currently achieved through the integration of the external particle interaction generator Pythia 8, which has already been used to produce many of the samples studied in Chapter 4.Pythia 8 provides Lorenzetti Showers with simulated event data by the generation of realistic particle interactions based on predefined physics models. For example, proton-proton collisions with subsequent jet formation can be simulated with precise kinematics. Pythia 8 enables the configuration of initial conditions, beam energies, particle types, and specific processes to simulate the desired physical phenomena.Generated events are stored in the HepMC (High Energy Physics Monte Carlo) format, ensuring compatibility with downstream processing tools. This event generation process provides the initial conditions for subsequent stages of simulation and reconstruction. However, Lorenzetti Showers has been conceptualised in a general manner, so that also other event generators can be integrated via HepMC.

Lorenzetti Showers' calorimeter simulation supports a modular and configurable design, making it adaptable to a wide range of experimental setups. The framework's standard calorimeter was inspired by ATLAS and consists as well of ECAL and HCAL layers. As for its inspiration, the standard Lorenzetti Showers calorimeter is arranged in a cylindrical geometry around the interaction point, with layers extending radially outward. Most layers are simulated with the same measures and materials as the corresponding layers of the ATLAS calorimeter. However, there are important differences. For example, the Lorenzetti Showers ECAL does not have an accordion shaped geometry, instead its cuboid cells are arranged in a straight line. Further differences, which are particularly important for the studies presented here, are discussed in Section 5.2. But importantly the Lorenzetti Showers parameters are not fixed, so that many properties can be further specified. For instance, the number of calorimeter layers, as well as the thickness and segmentation of each can be adjusted. Furthermore, the resolution of calorimeter cells can be defined to study fine-scale or large-scale energy deposition patterns. Ultimately, the material can be selected for both the active detector layers, as well as the space between and around them, to realistically simulate all the components. Figure 5.1 depicts an illustration of the Lorenzetti Showers standard calorimeter. Its structure is very similar to the ATLAS calorimeter represented in Figure 2.8.

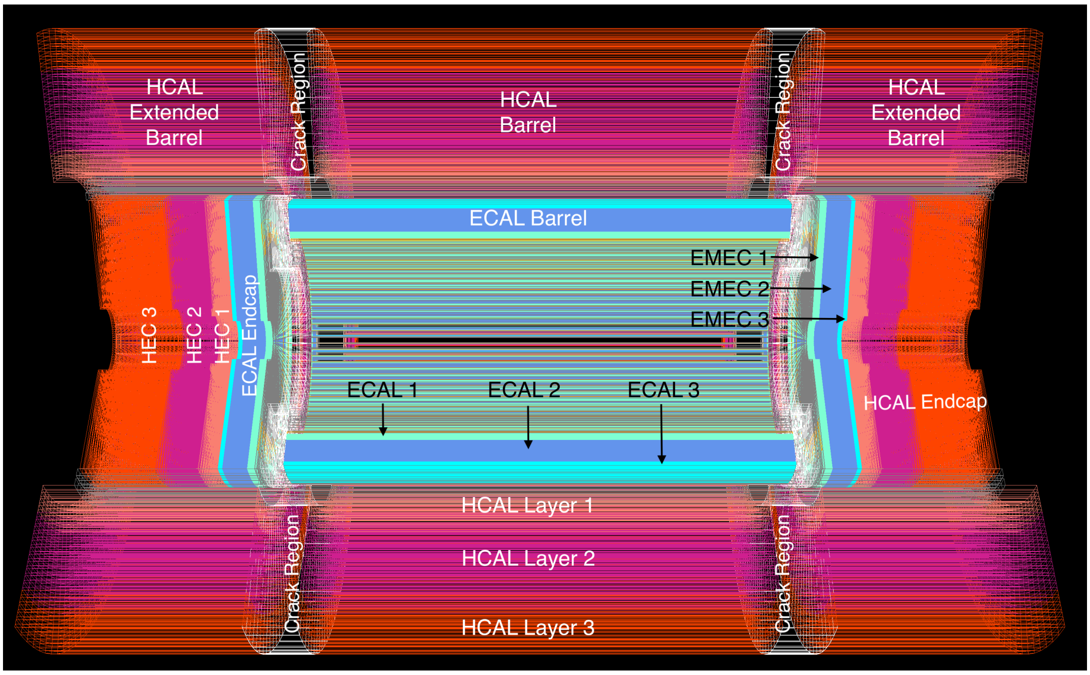

Figure 5.1: Visualisation of the cylindrical shaped Lorenzetti Showers standard calorimeter slightly modified from [7]. It has three ECAL barrel and three ECAL endcap layers. The HCAL also features three endcap layers and three barrel layers, the latter of which are further extended on both sides.

To simulate the passage of particles through the detector material Lorenzetti Showers employs the Geant4 toolkit. Thereby, electromagnetic showers are modelled with high precision, allowing to capture energy deposition in the fine-grained ECAL cells. Geant4 is also able to accurately simulate the complex interactions of hadronic showers, including the nuclear reactions and energy depositions in HCAL layers. The toolkit additionally tracks the creation of secondary particles within the showers, ensuring accurate modelling of energy depositions and spatial distributions. Geant4's modular physics lists allows to select and customize the level of detail in the simulation, balancing computational cost and accuracy.
The simulated energy depositions are then converted into the detector signals through a multi-step process. First, the energy deposited in each calorimeter cell is transformed into a detector-specific signal, as in photoelectrons or charge readout. Then, the formation and integration of signals by the detector's electronics,

including time constants and pulse shaping are modelled. Moreover, a realistic noise contribution, such as thermal noise or electronic interference, is added to the signal. This realistic signal generation pipeline enables testing and validation of reconstruction algorithms in near-experimental conditions.

Once signals are generated, the framework provides a comprehensive signal processing chain to extract physics information. It starts with initial processing steps to remove baseline shifts and reduce noise. Thereafter, algorithms calculate the energy deposited in each calorimeter cell by summing the processed signals. These algorithms can feature ML techniques to enhance accuracy. Subsequently, clusters of energy depositions corresponding to particle showers are identified. Clustering algorithms analyse spatial and temporal correlations to reconstruct a full shower profile. Finally, particles are classified based on their energy deposition patterns and shower shapes through the application of NNs or other advanced strategies.

The generation and processing steps performed by Lorenzetti Showers are shown in Figure 5.2. All those steps were executed in order to produce the samples used in the studies presented in Section 5.2 and Section 5.3. First, Python scripts are used to generate collision events via the Pythia 8 framework. Then, Python and C++ codes are executed to manage the propagation of the resulting particles through the simulated detector with the Geant4 tool. Further Python and C++ scripts are then used to simulate the conversion of analogue to digital signals. Thereafter, cells with energy deposits are clustered and the particle identification algorithms of choice can be run to find candidates of interest. Selection criteria for trigger or physics studies can also be implemented here. Lastly, the simulated events are fully reconstructed and organised in the ROOT “ntuple” tree structure which is the general type of container used to store data for analysis in experimental particle physics research [57].

Lorenzetti Showers also supports the development of triggering systems, like the one used by ATLAS, which is discussed in more detail in Chapter 3. The framework allows users to customize trigger algorithms, so that they can design and test triggering criteria, such as high-energy thresholds or specific shower shapes. Additionally, the latencies of hardware triggers can be simulated to ensure that algorithms meet real-time requirements.

In conclusion, the key strength of Lorenzetti Showers is its flexibility. As described, it allows for detector configurations with varying geometries, materials, and resolutions, making the framework applicable for diverse experiments. It can seamlessly integrate exterior frameworks like ML libraries for developing and testing advanced algorithms. Lorenzetti Showers supports the standard high-energy physics data formats, enabling high synergy with other commonly used tools.

The Lorenzetti Showers framework represents a significant advancement in calorimeter simulation and analysis. There’s a wide range of applications which could profit from Lorenzetti Showers. It can help in the development of new data processing tools, especially in facilitating the design and testing of novel signal

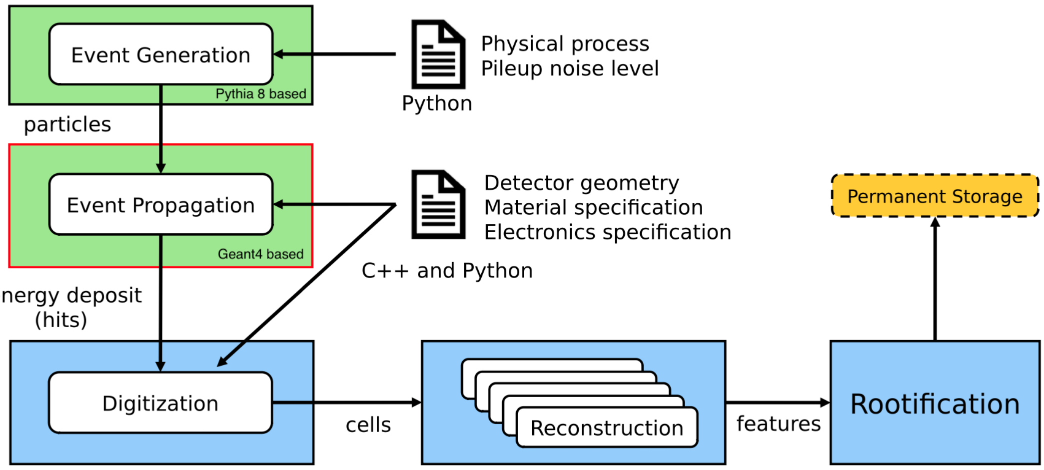

Figure 5.2: Schematics of the consecutive steps performed by Lorenzetti Showers in order to produce samples reconstructed from calorimeter data [7]. It starts with the generation of events through Pythia 8, continues by propagating the particles with Geant4, followed by the digitisation of the detector response and ends with particle reconstruction and the formatting of the outputs in a tree structure. This formatting in ROOT "ntuples" is termed "Rootification" in this schematics.

reconstruction and clustering algorithms. Moreover, it can support detector R&D by enabling studies of new detector technologies such as calorimeters featuring particularly high-granularity or alternative materials. Even phenomenological physics studies can benefit from Lorenzetti Showers, as it enables simulations of rare physics processes, including those relevant to future collider experiments.In that way Lorenzetti Showers contributes to the broader goal of advancing our understanding of the fundamental building blocks of the universe.

5.2 Studying Forward Electrons produced by Lorenzetti Showers with the NeuralRinger

The NeuralRinger algorithm can be seamlessly integrated in the reconstruction step of the Lorenzetti Showers processing seen in Figure 5.2. For its application, it must be ensured that the number of rings in each layer is chosen according to the specifications of the simulated calorimeter. For the studies presented here, the standard Lorenzetti Showers calorimeter depicted in Figure 5.1, with its close similarity to the ATLAS calorimeter, has been chosen. This allows for detailed comparisons with the studies presented in Chapter 4. All the detector layers from the standard calorimeter are listed in Table 5.1, together with their η coverages and granularities in $\eta \times \phi$.

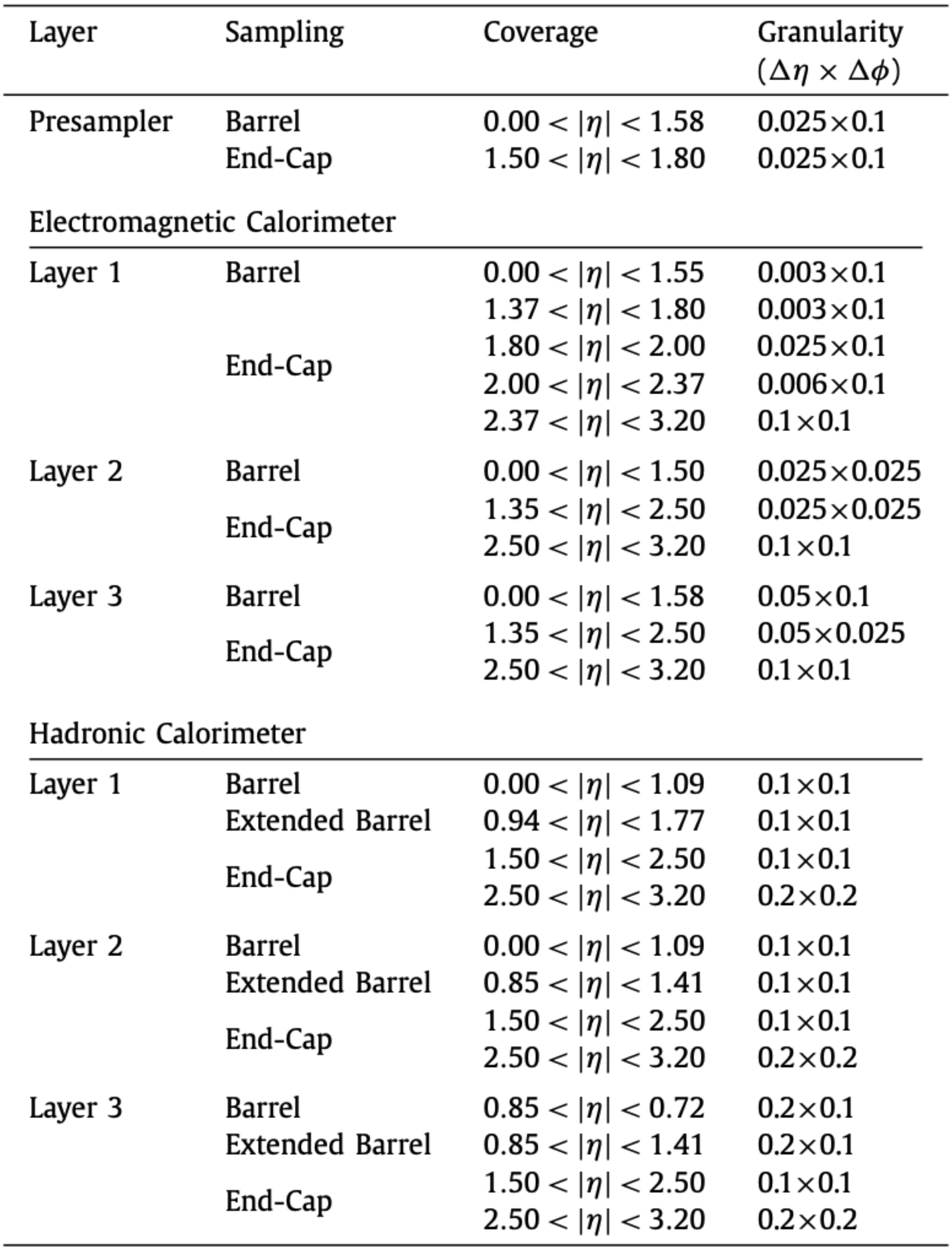

Layer	Sampling	Coverage	Granularity ($\Delta\eta \times \Delta\phi$)
Presampler	Barrel	$0.00 < \lvert\eta\rvert < 1.58$	0.025×0.1
	End-Cap	$1.50 < \lvert\eta\rvert < 1.80$	0.025×0.1
Electromagnetic Calorimeter			
Layer 1	Barrel	$0.00 < \lvert\eta\rvert < 1.55$	0.003×0.1
	End-Cap	$1.37 < \lvert\eta\rvert < 1.80$	0.003×0.1
		$1.80 < \lvert\eta\rvert < 2.00$	0.025×0.1
		$2.00 < \lvert\eta\rvert < 2.37$	0.006×0.1
		$2.37 < \lvert\eta\rvert < 3.20$	0.1×0.1
Layer 2	Barrel	$0.00 < \lvert\eta\rvert < 1.50$	0.025×0.025
	End-Cap	$1.35 < \lvert\eta\rvert < 2.50$	0.025×0.025
		$2.50 < \lvert\eta\rvert < 3.20$	0.1×0.1
Layer 3	Barrel	$0.00 < \lvert\eta\rvert < 1.58$	0.05×0.1
	End-Cap	$1.35 < \lvert\eta\rvert < 2.50$	0.05×0.025
		$2.50 < \lvert\eta\rvert < 3.20$	0.1×0.1
Hadronic Calorimeter			
Layer 1	Barrel	$0.00 < \lvert\eta\rvert < 1.09$	0.1×0.1
	Extended Barrel	$0.94 < \lvert\eta\rvert < 1.77$	0.1×0.1
	End-Cap	$1.50 < \lvert\eta\rvert < 2.50$	0.1×0.1
		$2.50 < \lvert\eta\rvert < 3.20$	0.2×0.2
Layer 2	Barrel	$0.00 < \lvert\eta\rvert < 1.09$	0.1×0.1
	Extended Barrel	$0.85 < \lvert\eta\rvert < 1.41$	0.1×0.1
	End-Cap	$1.50 < \lvert\eta\rvert < 2.50$	0.1×0.1
		$2.50 < \lvert\eta\rvert < 3.20$	0.2×0.2
Layer 3	Barrel	$0.85 < \lvert\eta\rvert < 0.72$	0.2×0.1
	Extended Barrel	$0.85 < \lvert\eta\rvert < 1.41$	0.2×0.1
	End-Cap	$1.50 < \lvert\eta\rvert < 2.50$	0.1×0.1
		$2.50 < \lvert\eta\rvert < 3.20$	0.2×0.2

Table 5.1: Summary of the standard Lorenzetti Showers calorimeter layers [7]. The pseudorapidity coverage and the $\eta \times \phi$ granularities of the cells of every layer are indicated as well.

Overall, the structure listed in Table 5.1 is almost the same as for the ATLAS calorimeter system, summarised in Table 2.1. Even most of the η ranges and the corresponding granularities match. One difference is for example that the Lorenzetti Showers standard calorimeter does not feature very forward calorimeters covering pseudorapidities values above 3.2. More importantly for the studies discussed here, there are three ECAL layers within $2.5 < |\eta| < 3.2$, whereas in ATLAS there are only two layers. Those three layers are called EMEC 1, EMEC 2 and EMEC 3, and the three HCAL layers, covering the same η range, are called HEC 1, HEC 2 and HEC 3. Given the same cell granularities as their counterparts from ATLAS, it's possible to reuse the same ring structures, developed in Section 4.3, for the EMEC and HEC layers in the Lorenzetti Showers simulation. That gives then a total number of 18 rings for electron candidates produced by Lorenzetti Showers within $2.5 < |\eta| < 3.2$. There are four rings more than in the ATLAS study because of the additional EMEC layer.

The thicknesses of the forward Lorenzetti Showers layers strongly differ from the ATLAS ones. Table 5.2 lists the layer thicknesses of both detectors in the $2.5 < |\eta| < 3.2$ region. The exact Lorenzetti Showers thickness values were extracted from its geometry library. They are the same for all the considered cells in one layer because of the flat geometry of the Lorenzetti Showers standard calorimeter. In ATLAS, the thickness of the cells in one layer varies. This is especially the case for the EMEC layers with their accordion shaped geometry and where the cell thickness increases towards the higher η values within $2.5 < |\eta| < 3.2$ [58]. No reference values are indicated in technical design reports. Therefore, an internal LAr identification translator tool was considered, which allows to get information of individual cells. For every layer, one cell of each η value was taken into account to get an averaged thickness. It was observed that the thickness of individual cells significantly varies by more than 10 mm. The ATLAS values in Table 5.2 are rounded to 10 mm to indicate the approximate thickness of the cells in the corresponding layer. Those values are taken as an overall reference for comparisons with the Lorenzetti Showers standard calorimeter but are not taken as a precise description of each cell.

Lorenzetti Showers standard calorimeter						
Layer	EMEC 1	EMEC 2	EMEC 3	HEC 1	HEC 2	HEC 3
z thickness [mm]	96	330	54	189	336	936

ATLAS calorimeter						
Layer	EMEC 1	EMEC 2	HEC 0	HEC 1	HEC 2	HEC 3
z thickness [mm]	420	80	320	500	610	360

Table 5.2: Layer thicknesses along the beam pipe (z) of the Lorenzetti Showers standard calorimeter and the ATLAS calorimeter in the $2.5 < |\eta| < 3.2$ region. Exact values are given for the Lorenzetti Showers layers where all the cells in one layer have the same thickness. The values for the ATLAS layers were reconstructed from information taken from an internal cell identification translator tool. Because of its non-flat geometry, the thicknesses of the cells in the ATLAS layers within $2.5 < |\eta| < 3.2$ vary significantly by more than 10 mm. The indicated values are averaged and rounded to 10 mm representing estimates for comparisons with the Lorenzetti Showers layers.

Table 5.2 shows big differences between the layer thicknesses of the Lorenzetti Showers standard calorimeter and the ATLAS calorimeter within $2.5 < |\eta| < 3.2$. It can be observed that the thickness of the ATLAS EMEC 1 compares well to the combined EMEC 1 and EMEC 2 thickness of Lorenzetti Showers.This is very important to note because the first layer is crucial for distinguishing signal from background candidates with the NeuralRinger, as it can be seen in the studies described in Chapter 4. The Lorenzetti Showers EMEC 3 layer is 1.5 times thinner than the ATLAS EMEC 2 layer and both are the two thinnest layers in the considered region, respectively. Also the HEC layer thicknesses strongly differ. The ATLAS HEC 0 is more than 1.5 times thicker than the Lorenzetti Showers HEC 1 layer. The combined ATLAS HEC 1 and HEC 2 are even more than three times thicker than the Lorenzetti Showers HEC 2. On the other hand, the Lorenzetti Showers HEC 3 layer is more than 2.5 times thicker than its ATLAS counterpart. All those differences make it very interesting to study whether the NeuralRinger performs similarly in the forward Lorenzetti Showers standard calorimeter geometry compared to the results from the ATLAS studies presented in Chapter 4.

The option to build the 18 forward rings was added in the Lorenzetti Showers reconstruction step. Thereby, it was relied on the previous integration of the NeuralRinger in the barrel region of the Lorenzetti Showers standard calorimeter. However, there were not yet any cutbased selection criteria implemented which could be used as reference to evaluate the NeuralRinger performance. Hence, the calculations of the same shower shape variables that are used for the cutbased selection of forward electrons in ATLAS, were implemented. They are listed and described in Table 4.1. Having them calculated for Lorenzetti Showers simulated samples, allows for comparisons between this study and the one from Chapter 4. The implementation of the shower shape variables proved to be more difficult than the integration of the forward rings. Specific calorimeter cell information needs to be called for the shower shape calculations, which were not yet passed on to the reconstruction step. This information can now be retrieved for reconstructing forward candidates and the their shower shape variables can now be calculated in the framework. Such challenges highlight the importance of studies like this one, which show the limitations of newly developed frameworks like Lorenzetti Showers. With the addition of the forward shower shape variables, the capabilities of Lorenzetti Showers are further expanded and calling specific cell features was made more accessible, making the environment more user-friendly.

5.2.1 Simulating and Studying Electron Gun Samples in Forward Regions with Lorenzetti Showers

For the first studies of using the NeuralRinger on forward Lorenzetti Showers samples, electron gun samples were simulated to have a direct comparison to the first studies performed in Section 4.4 for ATLAS. The electrons were produced only in the range of $2.5 < |\eta| < 3.2$ and with energies of $100\,\text{GeV} < E < 1\,\text{TeV}$.

The Lorenzetti Showers electron gun energies are defined in E and not in E_T. The selected energy range was motivated to well match the transverse energies of $20\,\mathrm{GeV} < E_\mathrm{T} < 100\,\mathrm{GeV}$ used in the ATLAS study for particles within $2.5 < |\eta| < 3.2$. This can be seen Figure 5.3, where the E_T and η distributions of the considered candidates from Lorenzetti Showers electron gun signal and dijet background samples are shown. The fake electron candidates from dijet events were simulated using Lorenzetti Showers with $E_\mathrm{T} > 20\,\mathrm{GeV}$. There was no upper energy limit set for the dijets but their distribution falls of exponentially for higher energies ($E_\mathrm{T} > 100\,\mathrm{GeV}$), as they were simulated through proton-proton collisions with LHC energies. The tail of the fake electron candidates' E_T distribution reaches up to 1.5 TeV. Like for the corresponding ATLAS studies, only candidates with $E_\mathrm{T} > 15\,\mathrm{GeV}$ are considered.

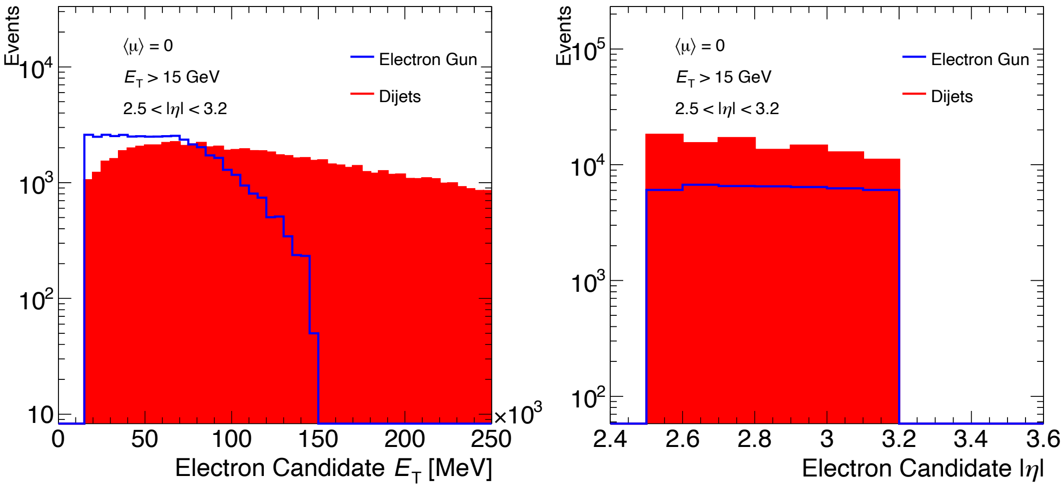

Figure 5.3: E_T and η distributions of the considered electron candidates from Lorenzetti Showers electron gun signal and dijet background samples. The E_T distribution on the left shows a steady number of candidates from electron gun samples within $20\,\mathrm{GeV} < E_\mathrm{T} < 70\,\mathrm{GeV}$, which then falls off to zero for $E_\mathrm{T} > 150\,\mathrm{GeV}$. The distribution of candidates from dijet samples slowly decreases with higher energies. Therefore, only the $E_\mathrm{T} < 250\,\mathrm{GeV}$ range is shown, to better depict the signal candidate distribution. The number of candidates from the electron gun samples is very evenly distributed over the considered η values and for the candidates from dijet samples it's slowly decreasing towards the higher η values.

It can be seen in Figure 5.3 that the number of candidates from electron gun samples is very evenly distributed within $15\,\mathrm{GeV} < E_\mathrm{T} < 75\,\mathrm{GeV}$ and then rapidly decreasing for higher energies. The number of candidates from dijet samples is firstly increasing until it reaches a maximum around 75 GeV and then slowly decreasing again. Both kind of samples show statistics of more than 1000 candidates per 5 GeV bin within $15\,\mathrm{GeV} < E_\mathrm{T} < 110\,\mathrm{GeV}$. Those statistics were limited for this study by the processing time needed for reconstructing the candidates. The average E_T of the background candidates is much higher than that of the signal candidates, which should give the NNs good statistics for learning how to discriminate high energetic jets too. The η distributions of the signal is very evenly distributed over the whole spectrum of $2.5 < |\eta| < 3.2$ with around 6000 candidates per 0.1 η bin. The number of candidates from the dijet samples is slightly decreasing with higher η values and there are more than 10000 candidates per 0.1 η bin.

Firstly, the six newly implemented forward shower shape variables were reconstructed for all the considered electron candidates. Then, the same selections were applied on those variables, as the ones used by ATLAS to obtain the three working points "loose", "medium" and "tight" for forward electrons. However, it became evident that those exact selections had much lower P_D values for candidates produced by Lorenzetti Showers than for the corresponding ATLAS samples used in subsection 4.4.1. The percentage of passed Lorenzetti Showers candidates was less than half for both, signal and background. This can be explained by these selections being derived and tuned very specifically for ATLAS and since there are several differences between the two calorimeter systems. Most prominently, the presence of a third EMEC layer in the Lorenzetti Showers calorimeter has a high impact on the resulting shower shape variables. Slightly loosening some of the selections on the shower shapes made it possible to strongly increase the P_D efficiencies. Therefore, the selections were refined, creating three new working points with efficiencies close to the ones used by ATLAS for the electron gun sample. The three new forward cutbased working points are called again "loose", "medium" and "tight" with corresponding P_D values around 94%, 92% and 90% respectively, for the considered electron candidates from the Lorenzetti Showers electron gun samples.

All the considered candidates from Figure 5.3 were also put through a reconstruction process where the 18 forward rings for the Lorenzetti Showers standard calorimeter were constructed. Then, their ring sums were calculated like the ATLAS ones from the studies in Chapter 4 and stored in a vector for each candidate. Thereafter, they were normalised and used to train a set of 900 MLPs which had the same tuning specifications as the one presented in subsection 4.4.1 with all candidates in a single bin. Figure 5.4 shows the normalised rings' mean profile for the Lorenzetti Showers electron gun signal and dijet background samples. It represents the mean values of the 18 direct inputs to the NNs that were trained. By comparing Figure 5.4 with the ring profile obtained for ATLAS in Figure 4.9, the difference in the yields of the EMEC 1 rings immediately stands out. But as discussed with Table 5.2, the combined yields of the Lorenzetti Showers EMEC 1 and EMEC 2 compares better to the ATLAS EMEC 1 layer. It can be observed that by comparing this way, the yields of the Lorenzetti Showers rings are more similar to the ATLAS ones. The first and fifth Lorenzetti Showers rings of the electron gun samples add up to a normalised energy of around 0.7 which compares to the yield of the first ATLAS the ring around 0.6. Also for the dijet samples, the yields are well comparable that way, with the first and fifth Lorenzetti Showers

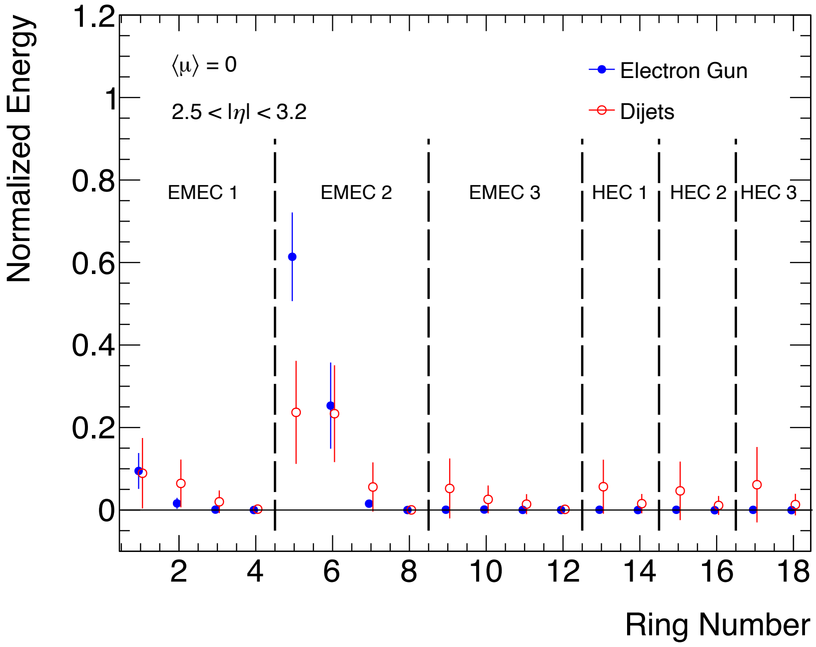

Figure 5.4: The rings' mean profiles for signal and background forward electron candidates from Lorenzetti Showers electron gun and dijet samples respectively. Both profiles are normalised such that the sum of the values across the 18 rings equals 1.0. The indicated errors represent the RMS width of the individual normalised ring sums. For clarity, the markers for both samples have been slightly offset within the same bin. Electron candidates from electron gun samples have much higher relative energy depositions in the 5th ring, whereas candidates from dijet samples have higher average depositions in the last six rings corresponding to the HEC layers.

ring yields adding up to close to 0.35 and the corresponding ATLAS yield close to 0.4. Also the yields from the added second and sixth Lorenzetti Showers rings are similar to the ones of the second ATLAS ring, where the Lorenzetti Showers yields of both types of samples are slightly lower. The other rings of the Lorenzetti Showers EMEC layers continue to give similar yields as the ones of the ATLAS study. However, it can be observed that the second ring in the Lorenzetti Showers HEC 1 and HEC 2 layers have lower yields than their ATLAS counterparts for the dijet samples. So it appears that the jets in the Lorenzetti Showers simulation stay more contained with less spreading. That can be caused by the more linear geometry of the cells in the Lorenzetti Showers simulation. Furthermore, the Lorenzetti Showers HEC 1 and HEC 2 layers are much thinner than the corresponding ATLAS layers, so they have less active volume which can measure the spreading. On the other hand, the first ring of the Lorenzetti Showers HEC 3 layer has a much higher yield than the one from the ATLAS HEC 3. This can be well explained with the much higher thickness of the Lorenzetti Showers

HEC 3 layer.
Compared with the forward rings for ATLAS, the NeuralRinger can profit from the additional information from one more EMEC layer in the Lorenzetti Showers standard calorimeter. Especially, the Lorenzetti Showers EMEC 1 layer can give more information. The yields of the very first ring in Figure 5.4 are very similar for the electron gun and the dijet candidates. But for the second ring, the dijet yields clearly have a higher average than the electron gun ones, which can further help the NNs in distinguishing signal from background. Overall, there are plenty of differences in the ring energy behaviour between the two types of candidates in Figure 5.4 which should allow for a good separation of signal and background.

After the successful tuning of the 900 MLP models, the results are compared with the three working points "loose", "medium" and "tight" which have been refined for the Lorenzetti Showers samples. Generally, a good performance of the NN tunings compared with the cutbased selections has been observed. It was found that almost all the models achieved a very low fake rate between 0.15% and 0.20% for all the working points. Only a tiny increase in average fake rate was seen between the "medium" and the "tight" working point. This means that the NNs were able to very well identify the great majority of 99.8% of background candidates as such. However, there seem to be around 0.15% of candidates from the Lorenzetti Showers dijet samples which have ring signatures very similar to the ones of the signal electron candidates and are therefore almost indistinguishable for the trained NN models. Overall, only a very small difference in performance for the MLP configurations with different numbers of neurons in the hidden layer has been observed, which was mostly seen for the "loose" working point. For the "medium" selection criteria, all but one of the configurations actually achieved the same average fake rate of 0.17%. This can be explained again if around 0.15% of Lorenzetti Showers dijet candidates have ring signatures very similar to the ones of the signal electron candidates. All the other background candidates can already be well distinguished from the signal by the MLPs with very few neurons. It can be seen in Table 5.3, where the average performances of the MLP models with different numbers of neurons in the hidden layer are compared to the cutbased selection at a P_D around 92%, matching the "medium" working point.
Table 5.3 shows an average reduction in F_R of almost a factor ten for all the trained models. This reduction factor is even more than doubled for the "loose" working point which has a fake rate F_R of 4.35% for the cutbased reference. However, for the "tight" cutbased selection the F_R was already down to 0.60% and could therefore only be reduced by a factor close to four. It can be concluded that applying the NeuralRinger on Lorenzetti Showers simulated forward electron candidates, mostly benefits looser selections with high P_D efficiencies. This might be more emphasised due to the very "clean" electron gun simulation which doesn't feature any other particles being produced and because all the samples don't feature any simulated pile-up. Therefore, this study was continued by including $Z \to ee$ samples (described in the following here) and further ones including

Configuration	$P_{\text{D}}[\%]$	$F_{\text{R}}[\%]$
Reference	92.28	1.54
2 Neurons	92.22 ± 0.06	0.17 ± 0.02
3 Neurons	92.29 ± 0.09	0.17 ± 0.02
4 Neurons	92.24 ± 0.06	0.17 ± 0.02
5 Neurons	92.30 ± 0.08	0.17 ± 0.02
6 Neurons	92.27 ± 0.06	0.17 ± 0.02
7 Neurons	92.32 ± 0.08	0.17 ± 0.02
8 Neurons	92.27 ± 0.06	0.17 ± 0.02
9 Neurons	92.29 ± 0.09	0.17 ± 0.02
10 Neurons	92.29 ± 0.05	0.16 ± 0.00

Table 5.3: Comparison of the average MLP performance for each number of neurons in the hidden layer with the cutbased selection evaluated at a P_{D} around 92% corresponding to the Lorenzetti Showers "medium" working point for electron gun samples. The reference belongs to the cutbased selection and the following entries show the average P_{D} and F_{R} values for the 100 models trained with the indicated number of neurons in the hidden layer. For the P_{D} values, the threshold was increased in steps of 0.01 along the NN output and stopped at the value which was closest to the reference. The errors given for P_{D} and F_{R} are the standard deviation of the values obtained by the 100 models with the same number of neurons in the hidden layer.

pile-up (described in Section 5.3).

5.2.2 Simulating and Studying $Z \rightarrow ee$ Samples in Forward Regions with Lorenzetti Showers

For producing $Z \rightarrow ee$ samples with electrons going into the forward regions, a new generator level cut has been implemented into Lorenzetti Showers, which requires at least one of the two electrons to be within $2.5 < |\eta| < 3.2$. This implementation was completed without any issues, and subsequently a larger number of around 100'000 $Z \rightarrow ee$ events with forward electrons are simulated. Alongside the $Z \rightarrow ee$ production, more dijet samples with the same specifications, as the ones already described in the beginning of this chapter, were simulated to increase statistics. In Figure 5.3 the E_{T} and η distributions of the considered candidates from Lorenzetti Showers $Z \rightarrow ee$ signal and dijet background samples are depicted. Again, only candidates with $E_{\text{T}} > 15\,\text{GeV}$ and within $2.5 < |\eta| < 3.2$ are taken into account.

Figure 5.5 shows that the candidates from the $Z \rightarrow ee$ samples predominantly have E_{T} values below 50 GeV. For the Lorenzetti Showers $Z \rightarrow ee$ production no specific E_{T} thresholds were selected. Therefore, the simulated Z bosons were typically produced with a longitudinal boost. That causes the electrons from

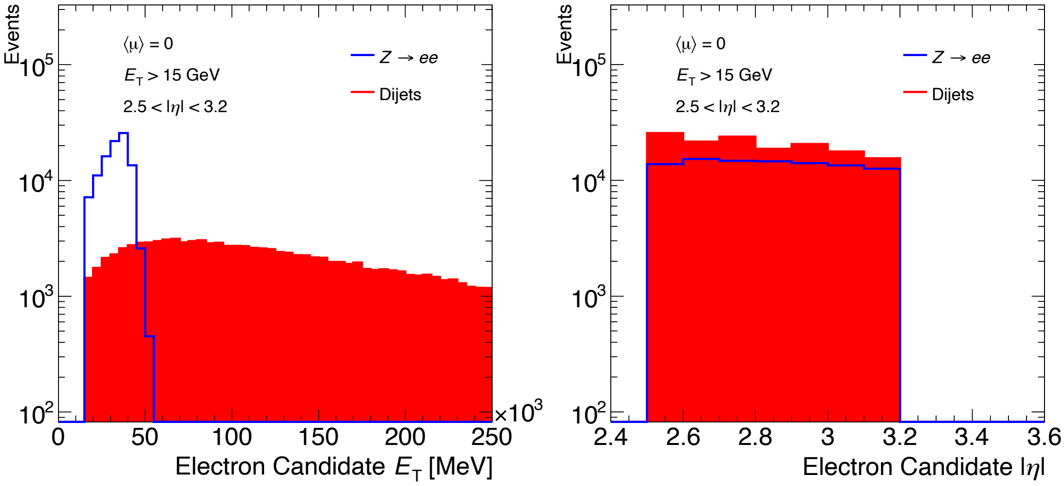

Figure 5.5: E_{T} and η distributions of the considered electron candidates from $Z \rightarrow ee$ signal and dijet background samples. The E_{T} distribution on the left shows a large number of candidates from $Z \rightarrow ee$ samples within $15\,\mathrm{GeV} < E_{\mathrm{T}} < 50\,\mathrm{GeV}$, which then falls off to zero for $E_{\mathrm{T}} > 55\,\mathrm{GeV}$. The distribution of candidates from dijet samples only slowly decreases with higher energies. Therefore, only the $E_{\mathrm{T}} < 250\,\mathrm{GeV}$ range is shown, to better depict the signal candidate distribution. The number of candidates from the $Z \rightarrow ee$ samples is very evenly distributed over the considered η values and for the candidates from dijet samples it's slowly decreasing towards the higher η values.

these Z boson decays to have lower average E_{T} values. The η values of signal and background candidates are well distributed over the whole spectrum of $2.5 < |\eta| < 3.2$.

For all the candidates from Figure 5.5 the forward shower shape variables were calculated and then the three forward Lorenzetti Showers selections were applied, corresponding to the "loose", "medium" and "tight" working points. The P_{D} efficiencies of the three working points naturally changed by using candidates from $Z \rightarrow ee$ instead of electron gun samples as signal. They were now at 92.82% for the "loose", 91.19% for the "medium" and 87.94% for the "tight" selection of candidates from the $Z \rightarrow ee$ samples.

Subsequently, the 18 forward Lorenzetti Showers rings were constructed for the newly produced candidates from dijet and the ones from the $Z \rightarrow ee$ samples. Then, their corresponding ring sums were calculated and stored again in a vector for each candidate. After the normalisation of each candidates' rings, another set of 900 MLPs with all the same tuning specifications as the previous ones described here was trained on them. In Figure 5.4 the normalised rings mean profile for the Lorenzetti Showers $Z \rightarrow ee$ signal and dijet background samples are presented, giving the mean values of the 18 direct inputs to the MLPs that were trained.

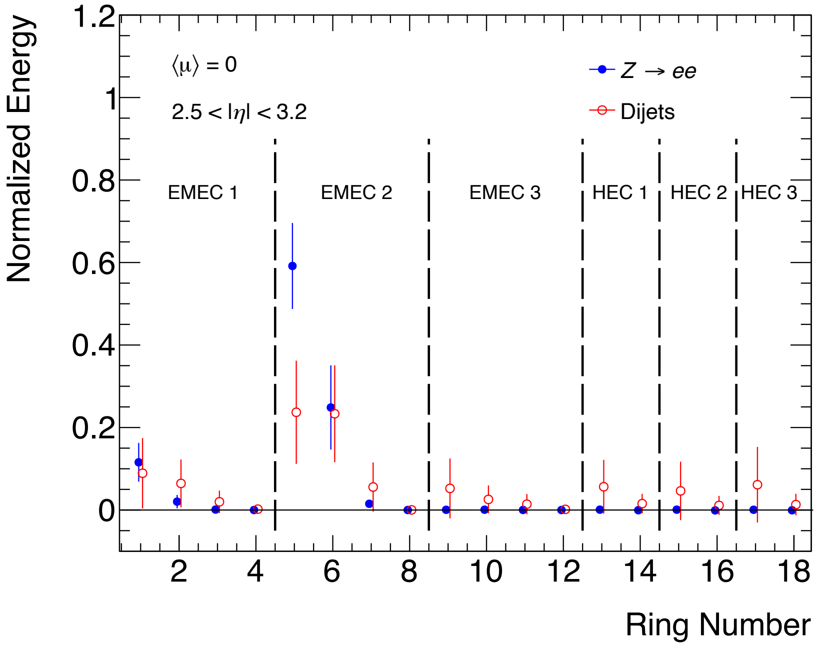

Figure 5.6: The rings' mean profiles for signal and background forward electron candidates from Lorenzetti Showers $Z \to ee$ and dijet samples, respectively. Both profiles are normalised such that the sum of the values across the 18 rings equals 1.0. The indicated errors represent the RMS width of the individual normalised ring sums. For clarity, the markers for both samples have been slightly offset within the same bin. Electron candidates from $Z \to ee$ samples have much higher relative energy depositions in the 5th ring, whereas candidates from dijet samples have higher average depositions in the last six rings corresponding to the HEC layers.

The $Z \to ee$ rings' mean profile in Figure 5.6 shows a very similar behaviour to the one of the Lorenzetti Showers electron gun samples in Figure 5.4. There are only a few small differences like for the first two rings, where the average $Z \to ee$ yields are slightly higher and then for the fifth ring where they are slightly lower in return. Therefore, also very similar results were to be expected for the tuning with the Lorenzetti Showers $Z \to ee$ samples. By comparing the rings mean profiles in Figure 5.6 with the ATLAS ones from Figure 4.12, it can mainly be noted that the average $Z \to ee$ yield in the combined first and fifth Lorenzetti Showers rings is much further away from the dijet one, than it is in the corresponding first ATLAS ring. Overall, the Lorenzetti Showers $Z \to ee$ forward ring properties seem much more similar to the electron gun ring properties, than they were for ATLAS.

The results of the successful MLP tuning of 900 models are compared again with the three forward Lorenzetti Showers working points “loose”, “medium” and “tight”. The NN tunings proved to outperform the cutbased selections once more. For all configurations the same average fake rates have been observed, which were at 0.20% for the “loose”, at 0.19% for the “medium” and at 0.17% for the “tight” working point. The F_R values are only slightly higher than the ones achieved in the tuning with the electron gun samples. Also, the average P_D values are identical for all the different MLP configurations. Because of this redundancy, no table like Table 5.3 is given here. Instead, the F_R efficiency distributions are depicted depending on the background candidates’ E_T and η, which are shown in Figure 5.7. Thereby, the cutbased working points are compared with the ones obtained in the tuning with the $Z \to ee$ signal candidates.

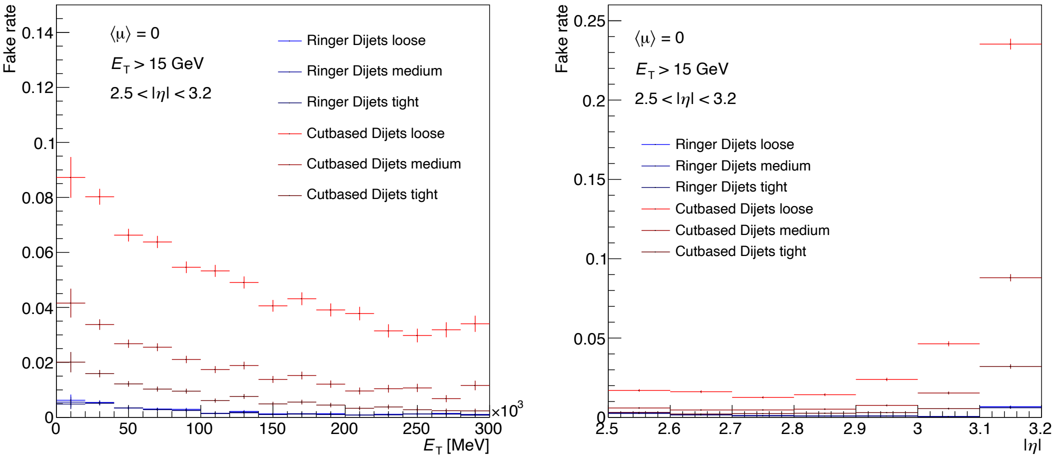

Figure 5.7: Fake rate F_R distributions depicting the acceptance rate of the considered background dijet candidates as a function of their E_T and η values. The dijet fake rates with the “Ringer” name in the legend correspond to the average NeuralRinger selections at the given working point, set in the tuning with $Z \to ee$ signal candidates. The fake rates are not given in percentage, so that 1.0 corresponds to a 100% acceptance. For the F_R rates in E_T dependence on the left, just the $E_T < 300$ GeV range is depicted, as thereafter the average efficiencies stay almost the same within statistical fluctuations due to reduced numbers of events in the bins. The η dependant distribution on the right shows a strong increase in the cutbased fake rates towards the upper boundary of $|\eta| = 3.2$.

It can be seen in Figure 5.7 that especially the cutbased selections accept way more background candidates with low transverse energies of $E_T < 40$ GeV. Low energetic jets are usually depositing a larger fraction of their energy in the ECAL than high energetic jets, which can make their shower shapes more similar to the ones of electrons and therefore harder to reject with the cutbased selection. These features can also be observed for the NeuralRinger selections but less emphasised. For the NeuralRinger selection this is most probably caused by the reduced number of low E_T background candidates, as seen in Figure 5.5. The η distributions in Figure 5.7 shows highly elevated fake rates for the cutbased selections towards the upper boundary of $|\eta| = 3.2$. Also the fake rates from the NeuralRinger selections are increased in the $3.1 < |\eta| < 3.2$ bin in comparison with the other bins.This feature at high pseudorapidities is mostly caused because the Lorenzetti standard calorimeter detector ends at $|\eta| = 3.2$, which leads to irregular clusters in the vicinity. Since the jets are clustered with a radius parameter of $R = 0.4$, a very significant part of jets with $|\eta| > 3.0$ cannot be registered.This issue could be addressed by adapting the selection criteria for candidates which are near the pseudorapidity boundary of $|\eta| = 3.2$.

For a complete discussion not only the F_R rates have to be compared. Also the P_D efficiencies have to be considered which were around one to two percent lower than the ones obtained for the forward Lorenzetti Showers electron gun samples. With the “medium” working point P_D of 91.19% and F_R of 0.19%, the NeuralRinger performs almost as good for identifying candidates from forward Lorenzetti Showers $Z \to ee$ samples as for the ones from electron gun samples. In the ATLAS studies using forward candidates from $Z \to ee$ samples, the corresponding P_D values were much lower. In summary, it can be assumed that the Lorenzetti Showers simulation produces “cleaner” signatures with less distortions in the forward regions than the ones that are produced for ATLAS. It could be that some of the signal interference effects considered by ATLAS are neglected or estimated at a lower value by the Lorenzetti Showers simulation, which is less detailed but in turn also less computationally demanding. Additionally, the $Z \to ee$ events were simulated without any pile-up, so that there were no interferences in the detector from particles produced in overlapping collision events. Therefore, the impact of pile-up on these forward electron studies with Lorenzetti Showers was investigated. This investigation is addressed in the following Section 5.3.

5.3 Using the NeuralRinger for Forward Electrons produced by Lorenzetti Showers with Pile-Up

For the production of samples including pile-up with Lorenzetti Showers, it is first required to simulate minimum-bias events [7]. The minimum-bias events used for this study were produced by simulating proton-proton collisions like the ones underlying the studied $Z \to ee$ and dijet samples. However, there are no stringent selection criteria, such as E_T thresholds, applied on them. In our case of proton-proton collisions, low energetic scattering processes are very common and make up a large fraction of the minimum-bias events. For the generation of minimum-bias samples, the required pile-up level can be defined to set how many minimum-bias interactions on average should be occurring per event. After the generation of minimum-bias events, Lorenzetti Showers propagates the resulting particles through the simulated detector, generating the energy deposits in the calorimeter cells. Those first two steps are analogous to the ones for producing any other sample with Lorenzetti Showers. Thereafter, the resulting minimum-bias energy deposits can be merged with the energy deposit samples of the process under study. The merged files are put through the further processing stages, which are depicted in Figure 5.2, to derive the "ntuples" for analyses with the desired process and pile-up.

For the studies presented here, a sample of 1000 simulated minimum-bias events with an average pile-up of 40 was generated and propagated through the Lorenzetti Showers standard calorimeter. This processing of the minimum-bias samples is quite computationally demanding, especially for higher pile-up values. Therefore, just 1000 minimum-bias samples were produced at an intermediate pile-up level of 40, which also corresponds to the dijet and $Z \rightarrow ee$ samples used for the ATLAS studies presented in subsection 4.4.2. For the first forward Lorenzetti Showers studies including pile-up, the energy deposits of all the electron gun samples used before in Section 5.2, were merged with the minimum-bias events with pile-up. As the minimum-bias sample is limited to 1000 events, the same minimum-bias events are merged several times with different electron gun events. Then, the 1000 minimum-bias events were also merged with the energy deposits of half of the dijet samples used in Section 5.2. Only a part of the previously used dijet events was used, as they were already exceeding the number of electron gun events and to reduce computational demands. After all the energy deposits of those samples were merged, they were put through the digitisation and reconstruction steps again. For the subsequent studies with the NeuralRinger, candidates with $E_{\mathrm{T}} > 15\,\mathrm{GeV}$ were considered. Figure 5.8 shows the E_{T} and η distributions of the considered candidates from Lorenzetti Showers electron gun signal and dijet background samples with an average pile-up of $\langle\mu\rangle = 40$.

The signal and background distributions from Figure 5.8 are similar to the ones from Figure 5.3 without pile-up $\langle\mu\rangle = 40$. The addition of $\langle\mu\rangle = 40$ impacts the candidates' E_{T} distribution and a reduction in average E_{T} of the signal candidates can clearly be seen. This effect can be caused by the Optimal Filter (OF) which Lorenzetti Showers uses for the energy estimation [7]. The Lorenzetti Showers OF has not yet been optimised and well calibrated in the more forward regions. Because of more energy depositions in the cells overall due to pile-up, the not fully calibrated forward OF is prone to overestimate the noise levels. This overestimation of noise leads to an underestimation of the candidates' energies.

As for the original samples without pile-up, the signal and background candidates are well distributed in $E_{\mathrm{T}} < 100\,\mathrm{GeV}$ and over the whole considered η range. All the considered candidates from Figure 5.8 had the 18 forward Lorenzetti Showers rings built in the reconstruction process and their ring sums stored in a vector. Thereafter, they were normalised again and used to train a set of 900 MLPs which had all the same tuning specifications as the ones before with all candidates in a single bin. Figure 5.9 shows the normalised rings mean profile for the Lorenzetti Showers electron gun signal and dijet background samples at an average pile-up of $\langle\mu\rangle = 40$.

Even though differences in the E_{T} distributions of the forward Lorenzetti Showers

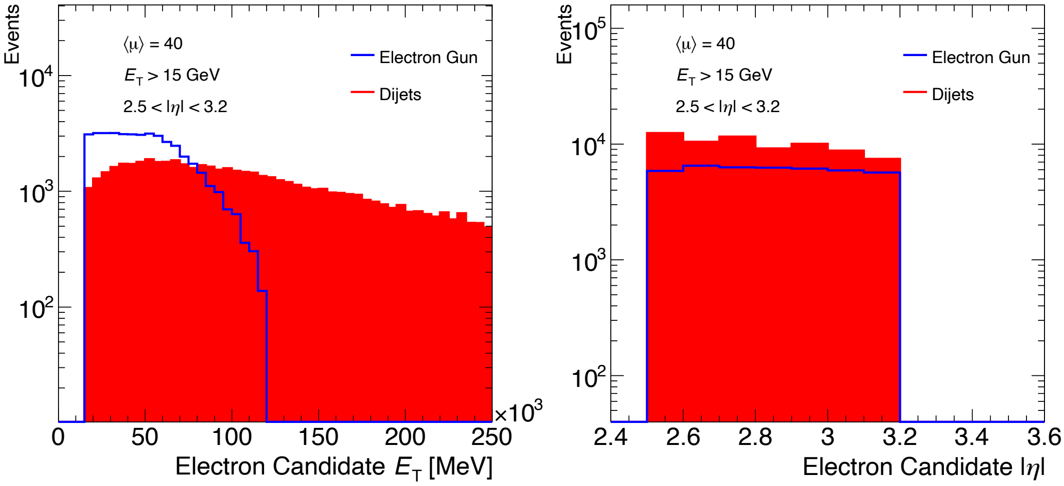

Figure 5.8: E_{T} and η distributions of the considered electron candidates from Lorenzetti Showers electron gun signal and dijet background samples with an average pile-up of 40. The E_{T} distribution on the left shows a steady number of candidates from electron gun samples within $20\,\mathrm{GeV} < E_{\mathrm{T}} < 60\,\mathrm{GeV}$, which then falls off to zero for $E_{\mathrm{T}} > 120\,\mathrm{GeV}$. The distribution of candidates from dijet samples slowly decreases with higher energies. Therefore, only the $E_{\mathrm{T}} < 250\,\mathrm{GeV}$ range is shown, to better depict the signal candidate distribution. The number of candidates from the electron gun samples is very evenly distributed over the considered η values and for the candidates from dijet samples it's slowly decreasing towards the higher η values.

electron gun samples with and without pile-up could be clearly seen by eye, it's very hard to see any difference between their rings' mean profiles. By comparing the rings' mean profile from electron gun samples with $\langle\mu\rangle = 40$ (Figure 5.9) and without pile-up (Figure 5.4), it can only be perceived that the yield of the first ring is little lower with pile-up. For the profiles from dijet samples virtually no difference can be seen. Therefore, the expected results of the NN tunings with pile-up are almost the same as for the corresponding tunings without pile-up.

After the training of the 900 MLP models, the results are compared once more with the three working points obtained by applying the forward Lorenzetti Showers selections. The P_{D} and F_{R} efficiencies of those working points were at 93.65% and 4.27% for the "loose", at 92.10% and 1.51% for the "medium", and at 90.23% and 0.58% for the "tight" selections respectively. All these P_{D} and F_{R} rates are slightly lower than for the studies without pile-up. The same could also be observed for the fake rates obtained from the NeuralRinger tunings which were around 0.01% lower for all of the three working points. The average performance of the MLP models with different numbers of neurons in the hidden layer compared to the "medium" cutbased selection can be seen in Table 5.4.

By comparing the efficiencies from Table 5.4 with the ones from Table 5.3 not in-

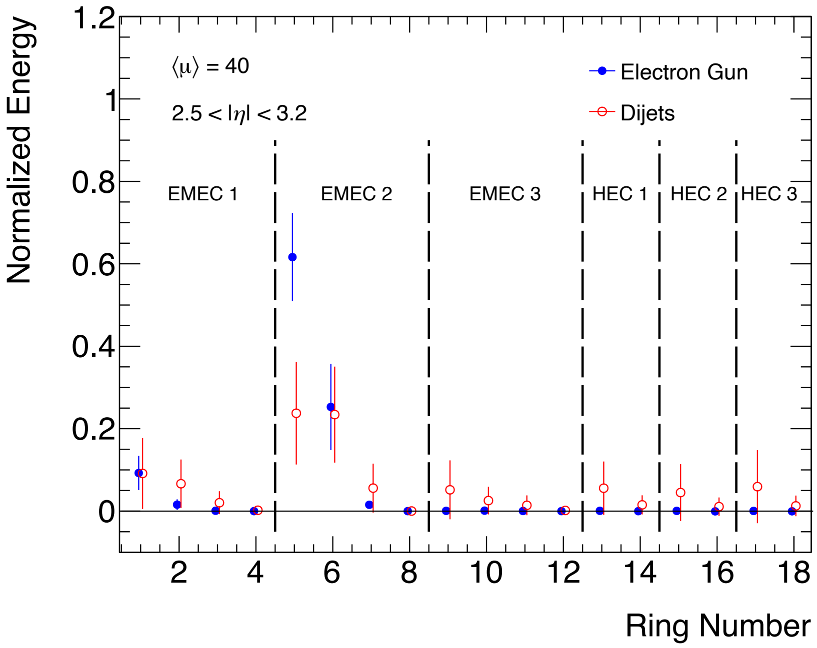

Figure 5.9: The rings' mean profiles for signal and background forward electron candidates from Lorenzetti Showers electron gun and dijet samples, respectively, with an average pile-up of 40. Both profiles are normalised such that the sum of the values across the 18 rings equals 1.0. The indicated errors represent the RMS width of the individual normalised ring sums. For clarity, the markers for both samples have been slightly offset within the same bin. Electron candidates from electron gun samples have much higher relative energy depositions in the 5th ring, whereas candidates from dijet samples have higher average depositions in the last six rings corresponding to the HEC layers.

cluding pile-up, it can directly be seen what has been described before, that both rates are generally slightly lower with pile-up. The F_{R} could again be reduced by a factor of almost ten on average. Overall, the F_{R} improvement factors stayed almost the same for all three working points in comparison with the zero pile-up studies. Therefore, it can be concluded that the NeuralRinger performance has not been decreased by the addition of an average pile-up of 40 in distinguishing forward Lorenzetti Showers electron gun signal and dijet background candidates.

To complete the studies including pile-up, the energy deposits of $Z \to ee$ samples from the previous studies in Section 5.2 were merged with the ones of the same minimum-bias sample with 1000 events of $\langle \mu \rangle = 40$. Thereby, just about every second $Z \to ee$ was merged to reduce computation time. The merged energy deposit samples were then put again through the full remaining Lorenzetti Showers processing and reconstruction steps to get the signal candidates for this study. The same dijet sample with an average pile-up of 40 was used once more

Configuration	$P_{\mathrm{D}}[\%]$	$F_{\mathrm{R}}[\%]$
Reference	92.10	1.51
2 Neurons	92.09 ± 0.09	0.16 ± 0.02
3 Neurons	92.08 ± 0.09	0.16 ± 0.01
4 Neurons	92.06 ± 0.15	0.16 ± 0.01
5 Neurons	92.11 ± 0.08	0.16 ± 0.00
6 Neurons	92.05 ± 0.09	0.16 ± 0.01
7 Neurons	92.09 ± 0.10	0.16 ± 0.01
8 Neurons	92.11 ± 0.08	0.16 ± 0.01
9 Neurons	92.10 ± 0.06	0.16 ± 0.00
10 Neurons	92.14 ± 0.10	0.16 ± 0.01

Table 5.4: Comparison of the average MLP performance for each number of neurons in the hidden layer with the cutbased selection evaluated at a P_{D} around 92% corresponding to the Lorenzetti Showers "medium" working point for electron gun samples with $\langle\mu\rangle = 40$. The reference belongs to the cutbased selection and the following entries show the average P_{D} and F_{R} values for the 100 models trained with the indicated number of neurons in the hidden layer. For the P_{D} values, the threshold was increased in steps of 0.01 along the NN output and stopped at the value which was closest to the reference. The errors given for P_{D} and F_{R} are the standard deviation of the values obtained by the 100 models with the same number of neurons in the hidden layer.

as background. Figure 5.8 shows the E_{T} and η distributions of the considered candidates from Lorenzetti Showers $Z \to ee$ signal and dijet background samples with an average pile-up of $\langle\mu\rangle = 40$.

The overall shape of the electron candidate distribution from $Z \to ee$ events with $\langle\mu\rangle = 40$ looks similar to the one without pile-up from Figure 5.5. However, in Figure 5.10 the same shift towards lower E_{T} values can be seen, that has been observed for the electron gun samples with pile-up in Figure 5.8. Therefore, the great majority of candidates from $Z \to ee$ samples with $\langle\mu\rangle = 40$ has an E_{T} below 40 GeV. During the reconstruction of those candidates again the 18 forward Lorenzetti Showers rings were built and their ring sums were stored in a vector. Then, they were normalised and used to train a set of 900 MLPs which had all the same tuning specifications as the ones before. Figure 5.11 depicts the normalised rings' mean profile of the Lorenzetti Showers $Z \to ee$ signal and dijet background samples at an average pile-up of $\langle\mu\rangle = 40$.

By comparing the rings' mean profile of electron candidates from $Z \to ee$ samples with (Figure 5.11) and without pile-up (Figure 5.6), they seem virtually identical. Even more so than for the comparison of the ones from electron candidates described before earlier in this section. The dijet rings' mean profile at $\langle\mu\rangle = 40$ is the same as the one used in comparison with the electron one from Figure 5.9, as exactly the same samples have been used. Since signal and background profiles

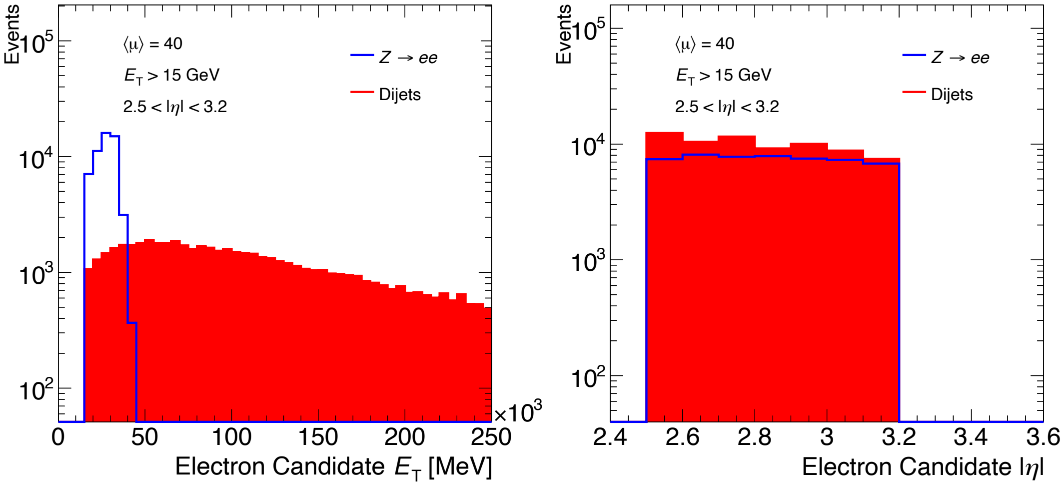

Figure 5.10: E_{T} and η distributions of the considered electron candidates from $Z \rightarrow ee$ signal and dijet background samples with an average pile-up of 40. The E_{T} distribution on the left shows a large number of candidates from $Z \rightarrow ee$ samples within $15\,\mathrm{GeV} < E_{\mathrm{T}} < 40\,\mathrm{GeV}$, which then falls off to zero for $E_{\mathrm{T}} > 50\,\mathrm{GeV}$. The distribution of candidates from dijet samples only slowly decreases with higher energies. Therefore, only the $E_{\mathrm{T}} < 250\,\mathrm{GeV}$ range is shown, to better depict the signal candidate distribution. The number of candidates from the $Z \rightarrow ee$ samples is very evenly distributed over the considered η values and for the candidates from dijet samples it's slowly decreasing towards the higher η values.

with an average pile-up of 40 look so similar to the corresponding ones without pile-up, almost the same performance from the NN tunings can be expected again.

The tuning results of the 900 MLP models are compared with the three working points obtained by applying the forward Lorenzetti Showers selections. The obtained P_{D} and F_{R} values of these working points are at 92.27% and 4.27% for the "loose", at 90.55% and 1.51% for the "medium", and at 86.23% and 0.58% for the "tight" selections, respectively. The fake rates F_{R} are exactly the same as for the study with electron gun samples with pile-up, as the exact same dijet samples have been used as background. All these P_{D} and F_{R} rates are again a bit lower than for the studies without pile-up, like it has already been observed for the study with electron gun candidates including pile-up. Similarly were the average fake rates obtained from the NeuralRinger tunings with $Z \rightarrow ee$ and dijet samples at $\langle \mu \rangle = 40$ slightly lower than for the same samples without pile-up. For the "loose" working point they varied between 0.19% and 0.20%, for "medium" between 0.18% and 0.19% and for "tight" between 0.16% and 0.17%. The higher of the two average F_{R} has always been observed for the configurations with fewer neurons in the hidden layer. The corresponding P_{D} values were thereby always

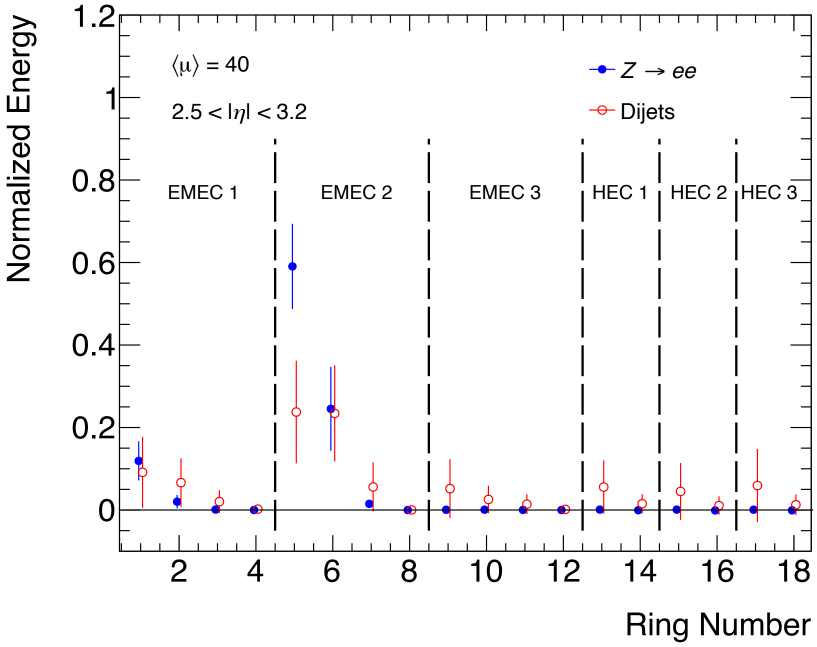

Figure 5.11: The rings' mean profiles for signal and background forward electron candidates from Lorenzetti Showers $Z \to ee$ and dijet samples, respectively, with an average pile-up of 40. Both profiles are normalised such that the sum of the values across the 18 rings equals 1.0. The indicated errors represent the RMS width of the individual normalised ring sums. For clarity, the markers for both samples have been slightly offset within the same bin. Electron candidates from $Z \to ee$ samples have much higher relative energy depositions in the 5th ring, whereas candidates from dijet samples have higher average depositions in the last six rings corresponding to the HEC layers.

exactly the same as for the cutbased selection without variation. As all the average outputs didn't show a lot of variation, very similarly to the tuning of $Z \to ee$ and dijet samples without pile-up, the F_{R} efficiency distributions are depicted depending on the background candidates' E_{T} and η again. This then also allows for comparison with the F_{R} efficiency distributions from the tunings without pile-up shown in Figure 5.7. Figure 5.12 shows the distributions of F_{R} efficiencies with respect to the background candidates' E_{T} and η, where the cutbased working points are compared with the ones obtained in the tuning with the $Z \to ee$ signal candidates at $\langle\mu\rangle = 40$.

As observed before in Figure 5.7, it can be seen in Figure 5.12 that the fake rates are higher for the lower E_{T} candidates and the ones with pseudorapidity values close to 3.2. There are a few small differences in some bins between the F_{R} efficiencies of the background candidates with and without pile-up. For example, the acceptance rate of $20\,\mathrm{GeV} < E_{\mathrm{T}} < 40\,\mathrm{GeV}$ candidates seems to be lower for candidates with $\langle\mu\rangle = 40$ for both, the NeuralRinger and the cutbased selections

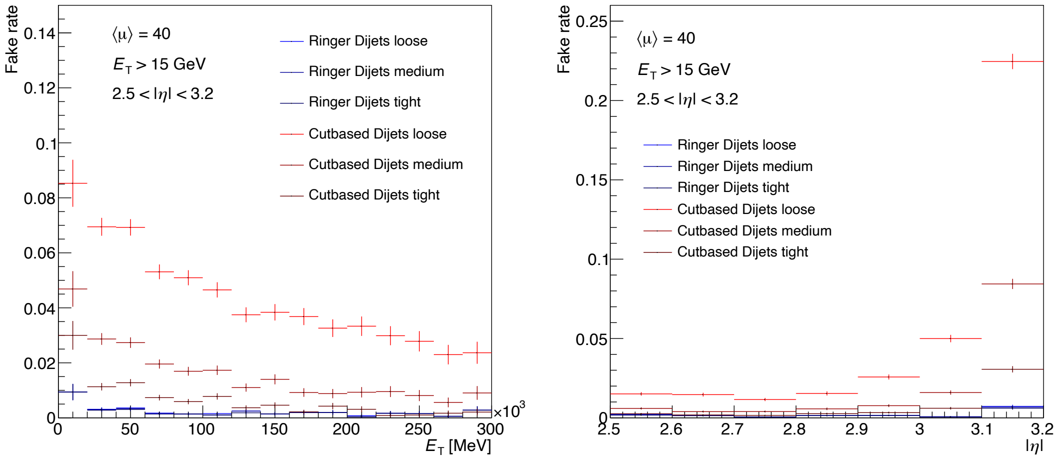

Figure 5.12: Fake rate F_R distributions depicting the acceptance rate of the considered background dijet candidates with $\langle\mu\rangle = 40$ in dependence of their E_T and η values. The dijet fake rates with the "Ringer" name in the legend correspond to the average NeuralRinger selections at the given working point, set in the tuning with $Z \to ee$ signal candidates. The fake rates are not given in percentage, so that 1.0 corresponds to a 100% acceptance. For the F_R rates in E_T dependence on the left, just the $E_T < 300$ GeV range is depicted, as thereafter the average efficiencies stay almost the same within statistical fluctuations due to reduced numbers of events in the bins. The η dependant distribution on the right shows a strong increase in the cutbased fake rates towards the upper boundary of $|\eta| = 3.2$.

over all the working points. The opposite can the be seen for candidates of $40\,\text{GeV} < E_T < 60\,\text{GeV}$ where the F_R is lower for the candidates without pile-up. Those features can mainly be explained with the general slight shift towards lower E_T values of the forward Lorenzetti Showers candidates at $\langle\mu\rangle = 40$. The fake rate F_R distributions depending on the candidates' η values stayed almost the same by including an average pile-up of 40.

The inclusion of $\langle\mu\rangle = 40$ to the forward Lorenzetti Showers electron candidates overall had only a small influence on the identification performance. This was observed for both, the cutbased and the NeuralRinger identification strategies which were explored. It has to be noted that these strategies are already successfully in use at average pile-up values way above 40 in ATLAS. So it would be very interesting to continue these studies with much higher pile-up values, for example $\langle\mu\rangle = 100$ or even more. For producing a good amount of such high pile-up samples with Lorenzetti Showers, machines with powerful processing capacities would be essential, so that the samples can be produced and operated efficiently. Furthermore, it has been seen that all the forward Lorenzetti Showers samples seemed to have rather clean signatures including the ones with added pile-up. Therefore, it could be further investigated whether all relevant effects, that can distort the signal, are included and whether their impact is well calibrated. Lastly, it has been noticed that the average E_{T} value attributed to forward electron candidates at $\langle\mu\rangle = 40$ is evidently lower than the one for candidates without pile-up. This could be caused by algorithms which are aimed at the energy estimation of candidates at even higher pile-up situations. To summarise, it is very important to investigate the responsible algorithms, such as the OF, to see whether the parameters are well set for the forward Lorenzetti Showers regions and to further refine them, if necessary. However, such studies wouldn't have been in the scope of this thesis. There's a group of researchers specifically working on the optimisation of the OF which could further optimise the forward region parameters.

Chapter 6

Searching for Top Squark Pair Production in non-leptonic Final States

Supersymmetric theories are among the most extensively studied extensions of the SM. Since these theories introduce many new particles and parameters, it is crucial to identify which ones are most promising to search for and how to do so effectively. Simplified models are used to guide analysis strategies of SUSY searches. These models allow searches to be directly optimised for specific predicted signatures and their interpretations to be well-defined.

This study focuses on a scenario where a pair of top squarks is produced which subsequently decays into all-hadronic final states. The search for such scenarios has regained more interest with the increase in centre-of-mass energy at the LHC Run 3 to 13.6 TeV. For various models, this leads to significantly higher production probabilities of SUSY particles. As described in Section 3.3, ATLAS now employs the new GN2 tagger, which leverages advanced ML techniques to identify the flavour of quark-initiated jets, including top quarks. This improved tagging method greatly enhances top squark searches.

The following chapter first discusses the motivations for searching for top squarks and studying models with non-leptonic final states. Next, it presents the results of the previous search targeting the same final states. The selection of MC samples for this study and their comparison with data from ATLAS Run 2 and Run 3 are then described. Finally, a definition of preliminary signal regions (SRs) is outlined, optimised to achieve high sensitivity to models with different SUSY particle mass assumptions.

6.1 Investigating Top Squark Pair Production Models with ATLAS

Simplified models used to guide SUSY searches often focus on the pair production of third-generation squarks. As discussed in Section 1.1, SM fermions acquire mass through their coupling to the Higgs field. The couplings to this Yukawa interaction varies for each SM fermion [3]. The heaviest fermions, the third-generation quarks t and b, have the strongest Yukawa coupling. In SUSY theories, this Yukawa coupling is assumed to be the same for SM fermions and their supersymmetric sfermion counterparts. Consequently, before SUSY breaking, third-generation squarks are expected to be strongly coupled to the Higgs field. To maintain naturalness in the theory after symmetry breaking, the top and bottom squarks are predicted to have masses around 1 TeV. The masses of the other squarks are less constrained and could be at much higher energies. This makes third-generation sfermions, particularly the top squark, prime candidates for experimental searches.
Since SM fermions are associated with two scalar fields in supermultiplets in the MSSM, as explained in Section 1.5, each quark has two squark partners corresponding to its left- and right-handed states. The superposition of these states results in two mass eigenstates, denoted $\tilde{t}_1$ and $\tilde{t}_2$, with $\tilde{t}_1$ being the lighter state. The Feynman diagrams in Figure 6.1 illustrate two possible squark-antisquark production channels from quark-antiquark interactions, probed by searches at the LHC. There are countless other possible squark production channels from squark and or gluon interactions.

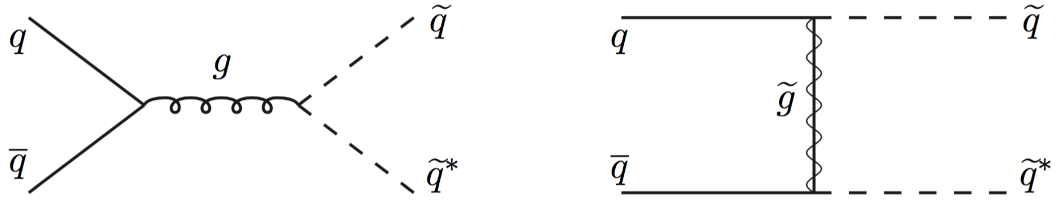

Figure 6.1: Two feynman diagrams of a squark-antisquark pair emeging from a quark-antiquark interaction from [3]. On the left the initial quark and antiquark are fused into a gluon which subsequently produces a squark-antisquark pair. The diagram on the right shows a scattering process where a squark and an antisquark are produced via a gluino.

Various decay modes of squarks can be investigated depending on the mass spectrum of supersymmetric particles. One well studied scenario involves the pair production of $\tilde{t}_1$, where each $\tilde{t}_1$ decays into a top quark and the lightest neutralino, $\tilde{t}_1 \rightarrow t\tilde{\chi}_1^0$. For this process to occur on shell, meaning that the relativistic energy-momentum relation must be satisfied, the $\tilde{t}_1$ must be more massive than the combined mass of the top quark and the neutralino. The top quark subsequently decays into a bottom quark and a W boson, which further decays into two fermions, which can either be a quark-antiquark pair of different flavours or a charged lepton and its corresponding neutrino.This results in a detectable state containing a b-jet, two fermions, and a neutralino, which appears as missing transverse energy in the detector. Signatures from the b-jet and the two fermions from the W can be integrated in a large radius jet, as described in subsection 3.3.4. Thanks to the GN2 tagger, those important features can now be top-tagged, which notably increases the sensitivity to signals matching $\tilde{t}_1$ decays. In models where the $\tilde{t}_1$ mass is smaller than the combined t and $\tilde{\chi}_1^0$ masses, the $\tilde{t}_1$ is decaying into a $\tilde{\chi}_1^0$ and into a W boson and a b quark. Even more compressed scenarios have been studied where $\Delta m(\tilde{t}_1, \tilde{\chi}_1^0) < m(W) + m(b)$. Here, top squarks are directly decaying into a bottom quark, two SM fermions and a neutralino. Figure 6.2 presents the current exclusion limits for $\tilde{t}_1$ pair production from ATLAS Run 2 data, considering the three previously described decay modes depending on the $\Delta m(\tilde{t}_1, \tilde{\chi}_1^0)$ mass splitting. In there, the limits are given at a 95% Confidence level (CL).

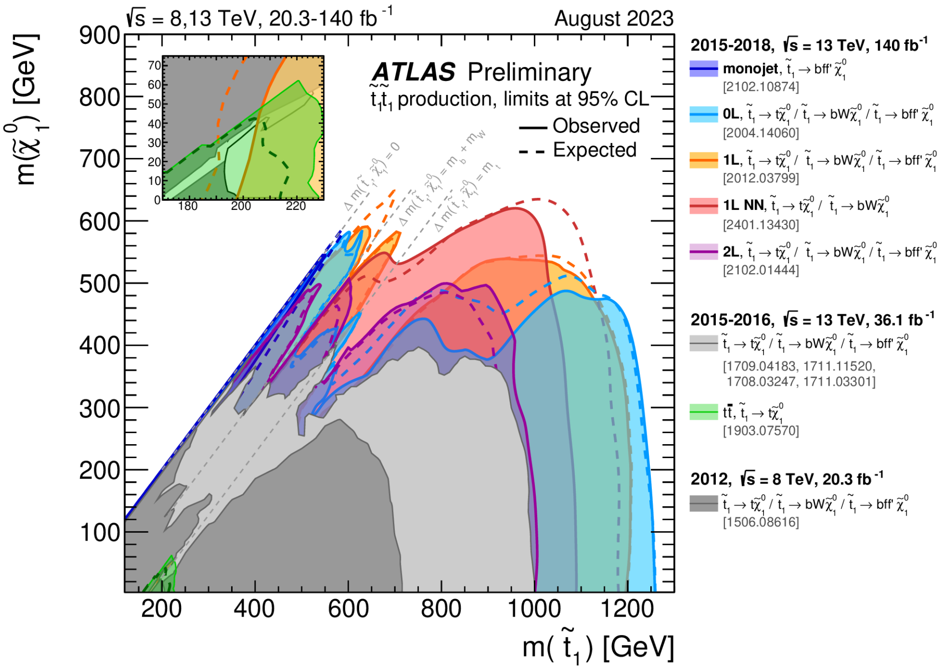

Figure 6.2: ATLAS Run 2 exclusion limits of $\tilde{t}_1$ pair production models from [59]. Expected and observed limits at 95% confidence level are indicated with dashed and solid lines respectively.

Figure 6.2 shows that almost all the simplified models with $m(\tilde{t}_1) < 1.2\,\text{TeV}$ and $m(\tilde{\chi}_1^0) < 500\,\text{GeV}$ could be excluded using $\sqrt{s} = 13\,\text{TeV}$ ATLAS Run 2 data. Now that ATLAS Run 3 data is available, it is of critical interest to resume this search for top squark pair production. Thanks to the increased centre-of-mass collision energies and integrated luminosity, many $\tilde{t}_1$ pair production models with mass spectra outside the current exclusion limits can be explored in more detail. Furthermore, the advancements that have been made in the application of ML techniques for analysis strategies, will further help in significantly increasing the sensitivity to the various SUSY models under consideration.

6.2 Previous Searches for All-hadronic Top Squark Decays

The analysis presented in the following Section 6.3 and Section 6.4 is searching for all-hadronic $\tilde{t}_1$ decays in ATLAS Run 2 and Run 3 data. Therefore, the pair production scenarios described in Section 6.1 are being considered, where all final decay products are assumed to be hadronic except for the neutralinos. In Figure 6.3, Feynman diagrams of three different $\tilde{t}_1$ decay chains with non-leptonic final states are presented. The various decays correspond to different $\Delta m(\tilde{t}_1, \tilde{\chi}_1^0)$ mass splittings, as previously described, and they all have been studied before with ATLAS Run 2 data [60]. In the Run 2 study, it was assumed that the $\tilde{t}_2$ mass is significantly higher than the $\tilde{t}_1$ mass, such that there would only be sensitivity towards the lower $\tilde{t}_1$ mass state.

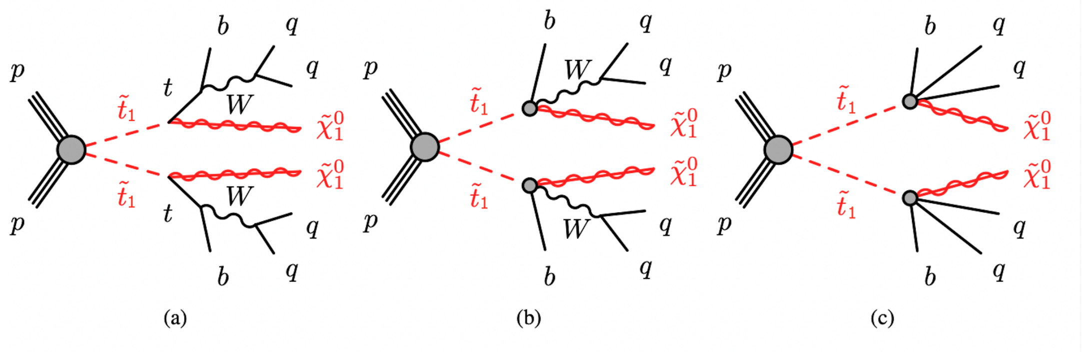

Figure 6.3: Three Feynman diagrams of $\tilde{t}_1$ pair production models with different mass parameters, resulting in all-hadronic final states, modified from [60]. The decay in (a) corresponds to a $\Delta m(\tilde{t}_1, \tilde{\chi}_1^0) > m(W) + m(t)$ mass splitting. (b) considers $\Delta m(\tilde{t}_1, \tilde{\chi}_1^0) > m(W) + m(b)$, whereas (c) describes the very compressed scenario of $\Delta m(\tilde{t}_1, \tilde{\chi}_1^0) < m(W) + m(b)$. The $\tilde{t}$ belong to the $\tilde{t}_1$ mass state in those scenarios.

Scenario (a) in Figure 6.3 considers a top squark decay into two bodies $\tilde{t}_1 \to t\tilde{\chi}_1^0$, where the top quark is produced on shell. Scenario (b) considers a three-body $\tilde{t}_1 \to bW\tilde{\chi}_1^0$ decay, where the top quark is off shell (not on shell) and a W boson and a bottom quark are produced on shell. In the scenario (c) a four-body $\tilde{t}_1 \to bqq\tilde{\chi}_1^0$ decay is considered, with both the top quark and the W boson are off shell. The studies presented in the following Section 6.3 and Section 6.4, are focusing on the first scenario (a) with the two-body decay. Therefore, this section

places more emphasis on the previous results of the non-compressed two-body scenario.
In the previous ATLAS Run 2 study, simulated MC samples were used to represent the signals from all considered SUSY models with different predicted $\tilde{t}_1$ and $\tilde{\chi}_1^0$ masses. To generate the underlying processes of these signals, the MadGraph5 software has been employed at leading order (LO) in QCD [61]. For the parton showering and hadronisation simulation, Pythia 8 was used. Further MC samples were used to describe the relevant background processes. The main backgrounds were V + jets ($V = W$ or Z), $t\bar{t} + V$, single top (tW), diboson, $t\bar{t}$, $t\bar{t}H$, tWZ and tZ processes. The MC generator Sherpa has been used to produce the V + jets and the diboson events and to simulate their parton showering and hadronisation processes [62]. $t\bar{t} + V$, $t\bar{t}H$, tWZ and tZ events were generated with the MadGraph5 and $t\bar{t}$ and tW events with the POWHEG-BOX software [63]. All the processes that were not generated with Sherpa, had Pythia 8 employed to simulate the parton showering and hadronisation. For all of the samples, Geant4 was used to simulate the propagation through the detector [56]. However, for the signal samples FastCaloSim was employed, allowing for faster execution of the calorimeter simulation [64]. All the samples were reconstructed with pre-defined requirements for the analysis.

Four different SRs, called SRA, SRB, SRC and SRD, were defined, targeting different regimes of $\tilde{t}$ and $\tilde{\chi}_1^0$ masses. SRC and SRD were defined for the three-body and four-body decays of the $\tilde{t}_1$, respectively. SRA was targeting the regions of high $\tilde{t}_1$ masses, whereas SRB was designed for sensitivity towards the intermediate mass region. Figure 6.4 depicts the $\tilde{t}_1$ and $\tilde{\chi}_1^0$ mass regimes targeted by the four signal regions.

SRA and SRB are mainly relying on the same signatures, whereas SRC and SRD are more focused on specific signatures for their narrow mass regimes. In the ATLAS Run 3 analysis presented in the following sections (Section 6.3, Section 6.4), only signatures of the high and intermediate $\tilde{t}_1$ mass scenarios were studied. Therefore, SRA and SRB are described in more detail here. Both, SRA and SRB, require the same jet (N_j) and b-jet (N_b) multiplicities, together with the absence of any lepton candidate ($N_\ell = 0$). Furthermore, they require an $E_\mathrm{T}^\mathrm{miss}$ threshold, as well as the acceptance by the $E_\mathrm{T}^\mathrm{miss}$ trigger. Other constraints are put on absolute values of the transverse momenta of the second and fourth leading jets ($p_{\mathrm{T},2}, p_{\mathrm{T},4}$).
As top-tagging for large-R jets was not yet available for the ATLAS Run 2 analysis, a jet reclustering strategy was performed in order to group jets which are likely to be originating from a boosted top quark. Thereby, regular $R = 0.4$ jets were reclustered using $R = 0.8$ and $R = 1.2$ radius parameters. Various selections on those reclustered jets were applied in the SRA and SRB regions, most prominently on the mass m calculated from the four-momenta of their sub-jets. From those requirements SRA and SRB were further split up in sub-regions with “TT”,

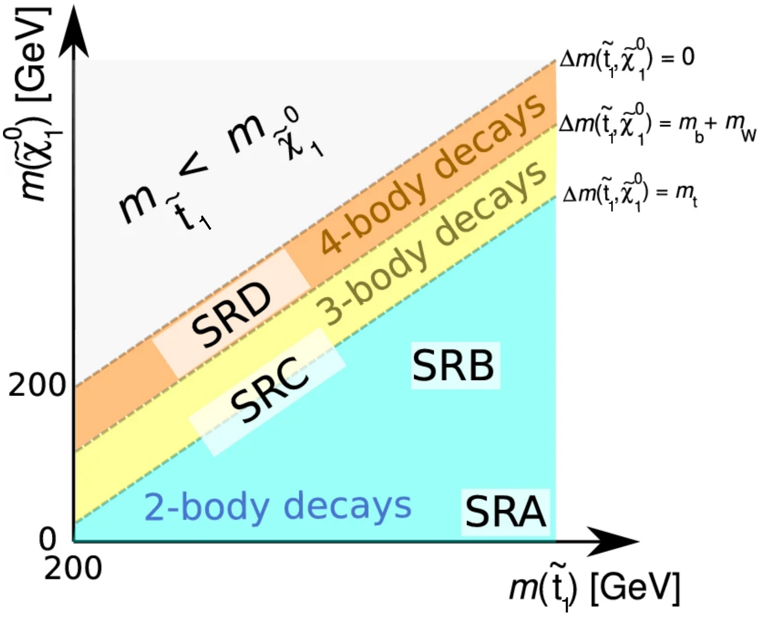

Figure 6.4: Schematics of the $\tilde{t}_1$ and $\tilde{\chi}_1^0$ mass regions targeted by the ATLAS Run 2 search for $\tilde{t}_1$ pair production in all-hadronic final states, modified from [60]. The $\tilde{t}$ stands only for the lower supersymmetric t mass state. SRA was optimised for high $\tilde{t}_1$ mass regions and SRB for scenarios with $\Delta m(\tilde{t}_1, \tilde{\chi}_1^0)$ mass splittings a bit higher than the t mass, allowing for two-body $\tilde{t}_1$ decays. SRC targets the region where three-body $\tilde{t}_1 \to bW\tilde{\chi}_1^0$ decays are favoured, whereas SRD targets the four-body $\tilde{t}_1 \to bqq\tilde{\chi}_1^0$ top squark decay region.

"TW" and "T0" tags. The "TT" regions aimed for signals with two well reconstructed top candidates, while "TW" regions aimed for one well reconstructed top and one W candidate and the "T0" regions only aimed for one well reconstructed top quark candidate. Requirements placed on the reclustered jets involved the jet masses $m_1^{R=0.8}$ and $m_1^{R=1.2}$ of the leading $R = 0.8$ and $R = 1.2$ jets, as well as the one of the subleading $R = 1.2$ jet ($m_2^{R=1.2}$). Furthermore, conditions were placed on the two leading $R = 1.2$ jets to be b-tagged ($j_1^{R=1.2}(b), j_2^{R=1.2}(b)$) within the SRA selections.

To eliminate events from multijet and hadronic $t\bar{t}$ decays with wrongly estimated $E_{\mathrm{T}}^{\mathrm{miss}}$, a selection was made on the minimum azimuthal angle difference between the missing transverse momentum and the four leading jets $|\Delta\phi_{\mathrm{min}}(\vec{p}_{\mathrm{T},1-4}, \vec{p}_{\mathrm{T}}^{\mathrm{miss}})|$. In order to reject further $t\bar{t}$ events, where one W decays leptonically ($W \to \ell\nu$), the transverse mass between $E_{\mathrm{T}}^{\mathrm{miss}}$ and the b-jet closest in ϕ to the $\vec{p}_{\mathrm{T}}^{\mathrm{miss}}$, was introduced. All regions were requiring this transverse mass to be above a certain threshold. It is calculated as

$$m_{\mathrm{T}}^{b,\mathrm{min}} = \sqrt{2|\vec{p}_{\mathrm{T}}^{\,b}|E_{\mathrm{T}}^{\mathrm{miss}}\,[1 - \cos\Delta\phi(\vec{p}_{\mathrm{T}}^{\,b}, \vec{p}_{\mathrm{T}}^{\mathrm{miss}})]}. \tag{6.1}$$

For further rejection of $t\bar{t}$ background with leptonically decaying W bosons, events with hadronic τ-leptons were overall discarded (τ-veto). Hadronic τ-candidates were obtained from regular jets, without b-tag, which were required to have a limited number of ID tracks and to be close in ϕ to the $\vec{p}_{\mathrm{T}}^{\mathrm{miss}}$. In SRB, a selection was also made on the $m_{\mathrm{T}}^{b,\max}$, which is calculated like the $m_{\mathrm{T}}^{b,\min}$ but with the b-jet that has the largest distance in ϕ to the $\vec{p}_{\mathrm{T}}^{\mathrm{miss}}$. This prevents both leading b-jets from being close to the $\vec{p}_{\mathrm{T}}^{\mathrm{miss}}$. Further requirements are put on the angular distance of the two leading b-jets $\Delta R(b_1, b_2)$, which helps rejecting events where b-jets were created through gluon splitting.

The most important variable to help discriminating background events in this Run 2 study was the $E_{\mathrm{T}}^{\mathrm{miss}}$ significance $\mathcal{S}$. It indicates the quality of the $E_{\mathrm{T}}^{\mathrm{miss}}$ calculation of each event, based on the p_{T} and ϕ resolution of each object. The $E_{\mathrm{T}}^{\mathrm{miss}}$ significance is given by

$$\mathcal{S} = \frac{E_{\mathrm{T}}^{\mathrm{miss}}}{\sqrt{\sigma_L^2(1-\rho_{\mathrm{LT}}^2)}}, \tag{6.2}$$

where σ_L is the total longitudinal momentum resolution of all objects in an event, in dependence of their $|\vec{p}_{\mathrm{T}}^{\mathrm{miss}}|$. Additionally, ρ_{LT} is the correlation factor of every object's longitudinal and transverse momentum resolution.

Lastly, a new variable, denoted as m_{T2,χ^2}, was introduced, which enabled to make SRA and SRB orthogonal from each other and thereby statistically combinable. All events in SRA were required to have the m_{T2,χ^2} above 450 GeV and all SRB events were rquired to have the m_{T2,χ^2} below that threshold. This threshold of 450 GeV, allows for an optimal separation between the signal events targeted by SRA from the ones targeted by SRB. m_{T2,χ^2} is calculated like the m_{T2} variable [65] from $\vec{p}_{\mathrm{T}}^{\mathrm{miss}}$ and the $\vec{p}_{\mathrm{T}}$ direction of two top candidates, which were obtained with a strategy similar to the χ^2 method. For both selected top quark candidates, the mass was set to 173.2 GeV in the m_{T2,χ^2} calculation. The two candidates with minimal χ^2 values were thereby selected, which was calculated as $(m_{\mathrm{cand}} - m_{\mathrm{true}})^2/m_{\mathrm{true}}$, where m_{cand} was the candidate's mass and for m_{true} both energies, 80.4 GeV and 173.2 GeV were tested. The former energy corresponded to the reference value of the W boson and the latter to the one of the top quark at the time of this previous study.

Table 6.1 lists all the selections of the SRA and SRB with their sub-regions.

By checking the distributions of the MC background samples in SRA and SRB, Z + jets events, with the Z boson decaying into neutrinos, are found to have the highest contributions. Other important contributions come from W + jets, Wt and from $t\bar{t}$ + Z samples. Separate orthogonal Control Regions (CRs) are defined for estimating contributions from the relevant background processes. They are all requiring at least one lepton. In this manner, they can easily be orthogonalised to the SRs. The specific CRs are selected so that they keep similar topologies to the SRs while being enriched with events of the targeted background process. By comparing the background yields with ATLAS data in the CRs, scale factors

Variable/SR	**SRA-TT**	**SRA-TW**	**SRA-T0**	**SRB-TT**	**SRB-TW**	**SRB-T0**
Trigger	$E_{\mathrm{T}}^{\mathrm{miss}}$					
$E_{\mathrm{T}}^{\mathrm{miss}}$	> 250 GeV					
N_{ℓ}	exactly 0					
N_{j}	≥ 4					
$p_{\mathrm{T},2}$	> 80 GeV					
$p_{\mathrm{T},4}$	> 40 GeV					
$\left\lvert\Delta\phi_{\mathrm{min}}\left(\mathbf{p}_{\mathrm{T},1-4}, \mathbf{p}_{\mathrm{T}}^{\mathrm{miss}}\right)\right\rvert$	> 0.4					
N_{b}	≥ 2					
$m_{\mathrm{T}}^{b,\mathrm{min}}$	> 200 GeV					
τ-veto	✓					
$m_{1}^{R=1.2}$	> 120 GeV					
$m_{2}^{R=1.2}$	> 120 GeV	60–120 GeV	< 60 GeV	> 120 GeV	60–120 GeV	< 60 GeV
$m_{1}^{R=0.8}$	> 60 GeV			–		
$j_{1}^{R=1.2}(b)$	✓			–		
$j_{2}^{R=1.2}(b)$	✓	–				
$\Delta R\left(b_{1}, b_{2}\right)$	> 1.0	–		> 1.4		
$m_{\mathrm{T}}^{b,\mathrm{max}}$	–			> 200 GeV		
$\mathcal{S}$	> 25			> 14		
$m_{\mathrm{T2},\chi^{2}}$	> 450 GeV			< 450 GeV		

Table 6.1: Summary of all requirements used for the SRA and SRB with their “TT”, “TW” and “T0” subregions from [60].

were identified which are used to extrapolate the best background yields to the SRs.

Validation Regions (VRs) for the major background processes are defined in kinematic topologies closer to the SRs' and also vetoing any event with leptons. In those regions it was verified with ATLAS data whether the normalisation factors from the CRs give correct yields. Systematic uncertainties were identified and combined for the theoretical predictions of the relevant processes, for the scale factors and for detector related sources, separately for each SR. In the SRA and SRB subregions, the total combined systematic uncertainties were in a range between 9% and 15% of the total background estimates.

Finally, the yields of the background estimates were compared to ATLAS Run 2 data with the SR selections. Generally, the total background estimates agree well with the data. A profile-likelihood-ratio test is used to provide a top squark pair production exclusion fit for every signal region. Thereby, the 95% CL exclusion limits on the lower $\tilde{t}_1$ and $\tilde{\chi}_1^0$ masses are given for the direct top squark pair production models under consideration. Figure 6.5 depicts the obtained exclusion contours by combining the limits of all the SRs, from SRA to SRD.

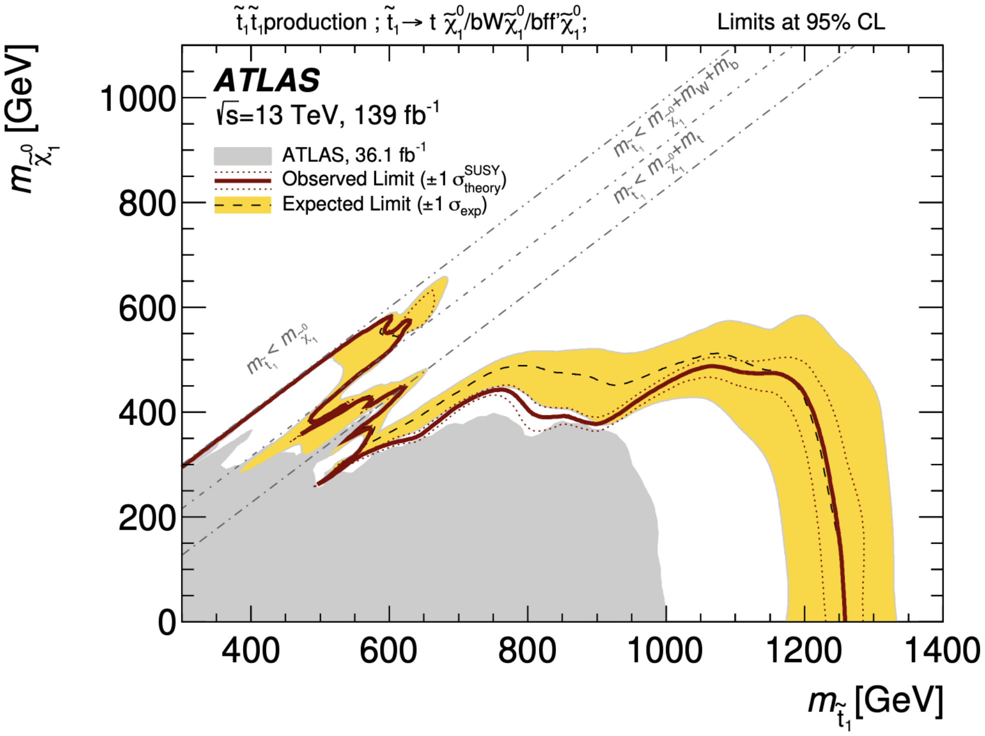

Figure 6.5: Observed and expected 95% CL exclusion limits for $\tilde{t}_1$ and $\tilde{\chi}^0_1$ masses from the previous search for stop quark pair production in all-hadronic final states, modified from [60]. The scenarios with masses confined by the contours in the bottom left part are excluded. The yellow and the red-dotted bands represent the uncertainties obtained from varying the expected limit and the total signal cross sections respectively by $\pm1\sigma$. The results from earlier ATLAS searches are indicated with the gray shaded area.

It can be seen in Figure 6.5 that $\tilde{t}_1$ masses could be excluded up to 1250 GeV for most scenarios with $\tilde{\chi}^0_1$ masses below 400 GeV. Thereby, it was possible to give the highest limits for $\tilde{t}_1$ masses in searches for direct pair production, as it is shown in Figure 6.2. With the ongoing search for $\tilde{t}_1$ pair production including ATLAS Run 3 data, described in the next two sections, the sensitivity to signals with mass parameters beyond the Run 2 limits is anticipated to increase. This would allow for a potential discovery or a significant extension of the exclusion limits if no excess in data is found.

6.3 Data MC Comparison and Pre-selections

The search for top squark pair production in all-hadronic final states presented here, is using both, ATLAS Run 2 and Run 3 data. Only scenarios where the $\tilde{t}_1$

decays into a top quark and a neutralino are considered here. A requirement of $\Delta m(\tilde{t}_1, \tilde{\chi}_1^0) > m(\tilde{\chi}_1^0) + m(t)$ is applied and with that requirement the compressed scenarios with 3-body or 4-body $\tilde{t}_1$ decays are not considered. Figure 6.6 shows the Feynman diagram of the single scenario under consideration.

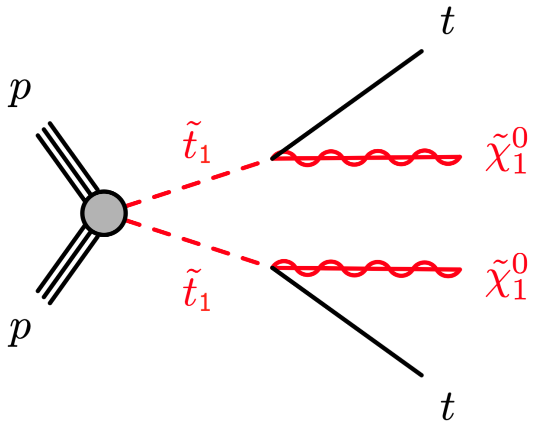

Figure 6.6: Feynman diagram for $\tilde{t}_1$ pair production, leading to the final state with two top quarks and $E_{\mathrm{T}}^{\mathrm{miss}}$.

Two separate analysis strategies are being explored for this search, one based on ML and the other one based on the traditional cut-and-count method. The ML approach can benefit from novel architectures which allow to let SRs be fully designed with ML tools. The SR optimisation strategies for the cutbased method will be described in the next Section 6.4. Also the cut-and-count strategy can benefit from advancements in ML because of the improved analysis object identification and reconstruction algorithms. The ML and the cutbased strategy are relying on the same data and MC simulated samples.

This search for top squarks uses data collected during ATLAS Run 2 and Run 3. The full Run 2 dataset of 140.1 fb^{-1} at $\sqrt{s} = 13\,\mathrm{TeV}$ is considered [66]. Run 3 data taken by the ATLAS detector during the years of 2022, 2023 and 2024 at $\sqrt{s} = 13.6\,\mathrm{TeV}$ are also considered. However, the data from 2024 has not yet been fully processed for this search at the time of writing of this thesis. Therefore, only data and MC simulated samples from the years of 2022 and 2023, corresponding to 53.3 fb^{-1}, have been used for the studies presented here. It is important to note that ATLAS recorded a total integrated luminosity of 118 fb^{-1} in 2024 [67], which is going to have a major impact on statistics. The studies presented here are still preliminary for that reason.

Simulated MC samples were used to represent the signals from all the considered SUSY models with different predicted $\tilde{t}_1$ and $\tilde{\chi}_1^0$ masses, similarly to the previous analysis. The MadGraph5 software was used again for the generation of the underlying signal processes and Pythia 8 for simulating the parton showering and hadronisation. Likewise, the FastCaloSim tool was again used for the calorimeter simulation, whereas the other parts of the detector were simulated by Geant4. Once more MC simulated samples were used for the description of the

background processes. Very similar processes were again identified as the main backgrounds. Sherpa has been used to simulate Z + jets, W + jets and diboson events. $t\bar{t}Z$ events were generated with the MadGraph5 and tW events with the POWHEG-BOX software. For both the Pythia 8 framework was employed for parton showering and hadronisation. The simulation of $t\bar{t}$ events in ATLAS Run 2 conditions was performed by Sherpa, whereas for Run 3 the POWHEG-BOX and Pythia 8 frameworks were used. Further background processes, such as triboson or $t\bar{t}H$ events, were also simulated but then usually summarised in the “other” category. The detector simulation of all the background samples was performed by Geant4.
Firstly, some initial requirements were placed on the samples which are loosely selecting final state topologies of interest. The goal of these pre-selections is to set a region where the simulated background processes cumulativelyl match well the data yields. Similarities between these requirements and the ones used in the previous Run 2 search, listed in Table 6.1, can be seen, since the same topologies are being investigated. Since $E_{\mathrm{T}}^{\mathrm{miss}}$ is a very essential variable for this search, as it represents the $\tilde{\chi}_1^0$ signatures, the default $E_{\mathrm{T}}^{\mathrm{miss}}$ triggers for both runs were applied [68, 69]. For these triggers a cut on $E_{\mathrm{T}}^{\mathrm{miss}}$ is desired at an energy where they becomes almost fully efficient. For finding that threshold, the $E_{\mathrm{T}}^{\mathrm{miss}}$ trigger efficiencies of data and background were compared for ATLAS Run 2 and Run 3. They are shown in Figure 6.7.

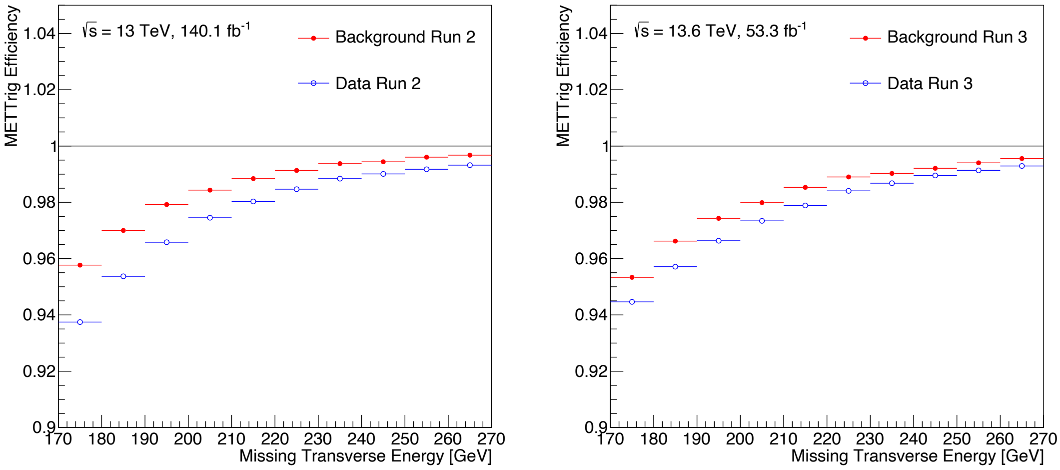

Figure 6.7: $E_{\mathrm{T}}^{\mathrm{miss}}$ trigger (METTrig) efficiency distributions depicting the acceptance rates of ATLAS data and the considered background samples in dependence on their $E_{\mathrm{T}}^{\mathrm{miss}}$. The distribution on the left shows the Run 2 efficiencies and the one on the right shows the Run 3 efficiencies.

It can be seen in Figure 6.7 that the efficiencies for both data and background samples are increasing more strongly with $E_{\mathrm{T}}^{\mathrm{miss}}$ at the lower $E_{\mathrm{T}}^{\mathrm{miss}}$ values and then above 200 GeV only small improvements are visible. Therefore, an $E_{\mathrm{T}}^{\mathrm{miss}} > 220\,\mathrm{GeV}$

cut is applied, from where efficiencies above 98% are observed. This cut allows for better agreement between the data and the simulated MC samples. Additionally, an $E_{\mathrm{T}}^{\mathrm{miss}}$ > significance $\mathcal{S} > 5$ selection is required. Further selections are made involving $N_{\mathrm{j}} \geq 4$ and $N_b \geq 1$ to require at least four jets coming from the two $t \to W + b$ decays, of which at least one must be b-tagged. As jets originating from top quarks are not low-energetic, also a $p_{\mathrm{T},\,4} > 40\,\mathrm{GeV}$ cut on the four leading jets is included. Together, all those cuts form the initial selections. They serve as a starting point for finding optimal pre-selections where data and MC background yields agree well. If strong disagreements are present, the initial selections are adjusted by modifying or extending cuts. All the cuts forming the initial selections are listed in Table 6.2.

Requirement	Initial selection
Trigger	$E_{\mathrm{T}}^{\mathrm{miss}}$
$E_{\mathrm{T}}^{\mathrm{miss}}$ [GeV]	> 220
$E_{\mathrm{T}}^{\mathrm{miss}}$ $\mathcal{S}$	> 5
N_ℓ	$= 0$
N_{j}	≥ 4
N_b	≥ 1
$p_{\mathrm{T},\,4}$ [GeV]	> 40

Table 6.2: The initial selections found to match the data and MC background yields for the top squark pair production search using ATLAS Run 2 and Run 3 data.

By checking the data versus MC background distributions of numerous variables after applying the initial selections, the MC yields were observed to be missing events in specific topologies. In these regimes another background from dijets, produced in QCD interactions, is dominant. Figure 6.8 shows the Run 2 $E_{\mathrm{T}}^{\mathrm{miss}}$ significance and the $|\Delta\phi_{\min}(\vec{p}_{\mathrm{T},1-4}, \vec{p}_{\mathrm{T}}^{\mathrm{miss}})|$ data and background distributions with the initial selection cuts applied, where the missing contributions are strongly visible. To apply appropriate blinding, three signal sample distributions with fairly different $\tilde{t}_1$ and $\tilde{\chi}_1^0$ masses were also included. Bins were blinded and shaded in grey, where one of the signal yields exceeds 10% of the combined background process yields.

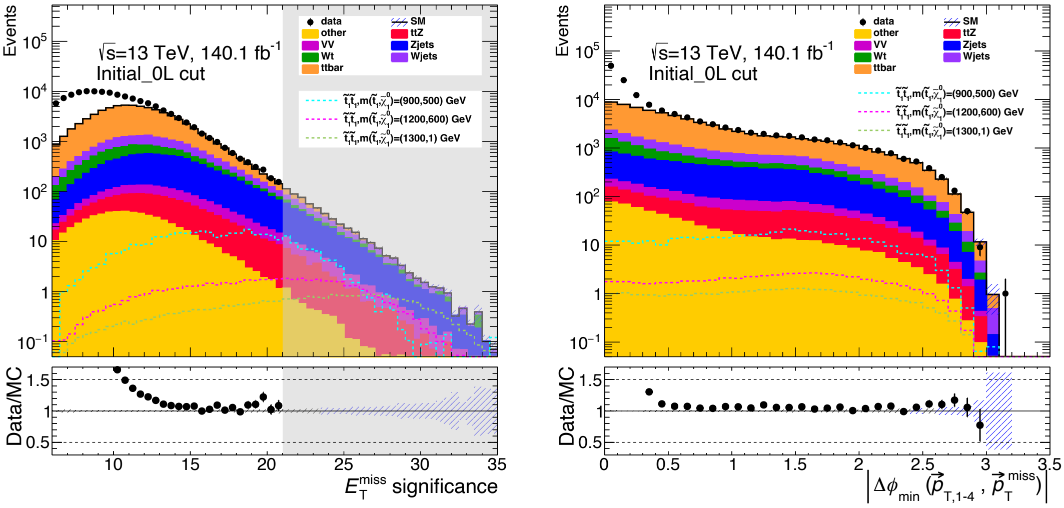

Figure 6.8: ATLAS Run 2 $E_{\mathrm{T}}^{\mathrm{miss}}$ significance and $|\Delta\phi_{\mathrm{min}}(\vec{p}_{\mathrm{T},1-4}, \vec{p}_{\mathrm{T}}^{\mathrm{miss}})|$ data and background distributions with the initial selections, not including dijet samples. Three signal samples were added to blind bins in grey where at least one of the signals exceeds 10% of the total background. Major background contributions are missing at $E_{\mathrm{T}}^{\mathrm{miss}}$ significance values below 12 on the left and at $|\Delta\phi_{\mathrm{min}}(\vec{p}_{\mathrm{T},1-4}, \vec{p}_{\mathrm{T}}^{\mathrm{miss}})|$ values below 0.4 on the right. Statistical uncertainties are indicated with a black line on the data points and with a blue shade for the total background prediction.

In Figure 6.8 it can be seen that crucial background contributions in the lower $E_{\mathrm{T}}^{\mathrm{miss}}$ significance and $|\Delta\phi_{\mathrm{min}}(\vec{p}_{\mathrm{T},1-4}, \vec{p}_{\mathrm{T}}^{\mathrm{miss}})|$ regimes are missing. Therefore, dijet samples were also included to the MC backgrounds, which are dominant in those topologies. It was found that the missing contributions were indeed mostly originating from dijets. However, the dijet samples are not well modelled in the regimes that are being investigated. This is especially due to the high $E_{\mathrm{T}}^{\mathrm{miss}}$ values that are being required. Since ATLAS is built to very well contain jets, dijet samples are expected to have low $E_{\mathrm{T}}^{\mathrm{miss}}$ values. Figure 6.9 shows the $E_{\mathrm{T}}^{\mathrm{miss}}$ significance and leading jet η Run 2 distributions of data and background, including dijets.

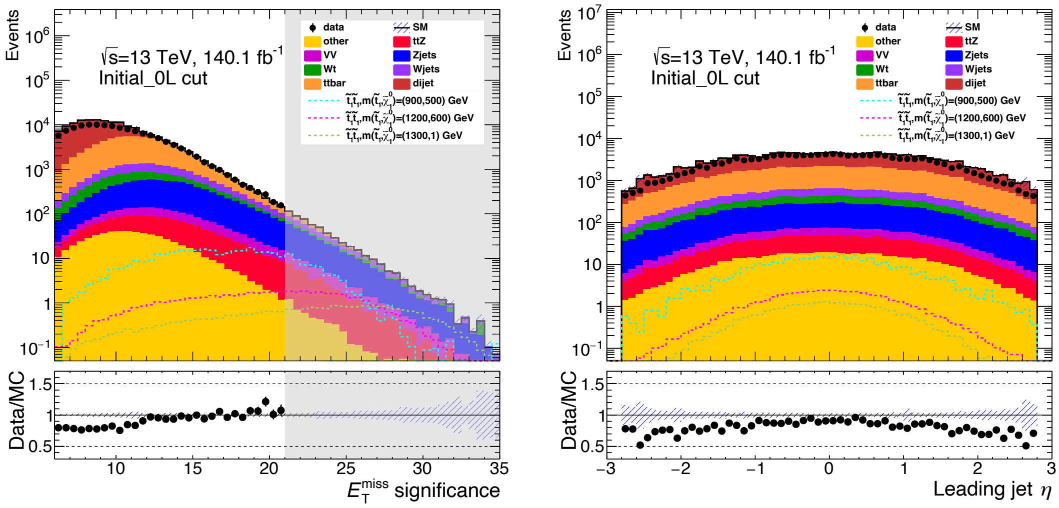

Figure 6.9: ATLAS Run 2 $E_{\mathrm{T}}^{\mathrm{miss}}$ significance and leading jet η data and background distributions with initial selections including dijet samples. Three signal samples were added to blind bins in grey where at least one of the signals exceeds 10% of the total background. The dijet samples dominate the low $E_{\mathrm{T}}^{\mathrm{miss}}$ significance regimes in the diagram on the left and they are distributed over all η values in the diagram on the right. Statistical uncertainties are indicated with a black line on the data points and with a blue shade for the total background prediction.

Figure 6.9 shows that the dijet background is indeed dominant in the low $E_{\mathrm{T}}^{\mathrm{miss}}$ significance regions. But it is also visible in both distributions that the yields from the dijet samples are generally overestimated, so that the total yields of the backgrounds exceeds the ATLAS data. Additionally, it can be seen in the leading jet η distribution that there are some bins which show particularly high dijet yields. These features are caused by issues with the modelling of the dijet samples and not by wrong weights attributed to certain simulated dijet events. Therefore, the strategy was changed to adding more selections which strongly discriminate dijet contributions, such that those overestimated, fluctuating samples can be ignored. These additional requirements involve an increase in the $E_{\mathrm{T}}^{\mathrm{miss}}$ significance to $\mathcal{S} > 9$ and two cuts on $|\Delta\phi_{\mathrm{min}}(\vec{p}_{\mathrm{T},1-\mathrm{n}}, \vec{p}_{\mathrm{T}}^{\,\mathrm{miss}})|$ variables. Those $|\Delta\phi_{\mathrm{min}}(\vec{p}_{\mathrm{T},1-\mathrm{n}}, \vec{p}_{\mathrm{T}}^{\,\mathrm{miss}})|$ variables consider different numbers of n leading jets. At first, only one cut on the $|\Delta\phi_{\mathrm{min}}(\vec{p}_{\mathrm{T},1-4}, \vec{p}_{\mathrm{T}}^{\,\mathrm{miss}})|$ variable, like the one from the previous Run 2 search, was investigated, but still some deviations from dijet contributions were found in further $|\Delta\phi_{\mathrm{min}}(\vec{p}_{\mathrm{T}}, \vec{p}_{\mathrm{T}}^{\,\mathrm{miss}})|$ variables. Figure 6.10 shows the Run 2 $|\Delta\phi_{\mathrm{min}}(\vec{p}_{\mathrm{T},1-5}, \vec{p}_{\mathrm{T}}^{\,\mathrm{miss}})|$ distribution after applying the initial selections with $\mathcal{S} > 9$ and a $|\Delta\phi_{\mathrm{min}}(\vec{p}_{\mathrm{T},1-4}, \vec{p}_{\mathrm{T}}^{\,\mathrm{miss}})| > 0.4$ cut.

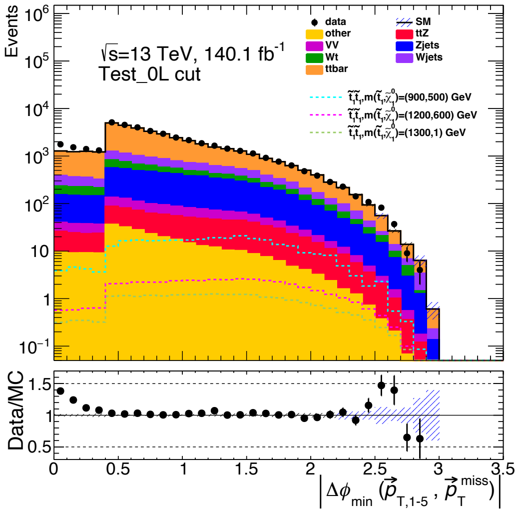

Figure 6.10: ATLAS Run 2 $|\Delta\phi_{\mathrm{min}}(\vec{p}_{\mathrm{T},1-5}, \vec{p}_{\mathrm{T}}^{\mathrm{miss}})|$ distribution after applying the initial selections (Table 6.2) and with a more stringent $E_{\mathrm{T}}^{\mathrm{miss}}$ $\mathcal{S} > 9$ and a $|\Delta\phi_{\mathrm{min}}(\vec{p}_{\mathrm{T},1-4}, \vec{p}_{\mathrm{T}}^{\mathrm{miss}})| > 0.4$ cut. Three signal samples were added to blind bins in grey if applicable where at least one of the signals exceeds 10% of the total background. Statistical uncertainties are indicated with a black line on the data points and with a blue shade for the total background prediction.

It can be seen in Figure 6.10 that there are still some discrepancies, especially at low $|\Delta\phi_{\mathrm{min}}(\vec{p}_{\mathrm{T},1-5}, \vec{p}_{\mathrm{T}}^{\mathrm{miss}})|$ values. Those discrepancies are still arising from dijet contributions which have not yet been discriminated enough. Additionally, Figure 6.10 shows a step at $|\Delta\phi_{\mathrm{min}}(\vec{p}_{\mathrm{T},1-5}, \vec{p}_{\mathrm{T}}^{\mathrm{miss}})| = 0.4$. These lower yields for $|\Delta\phi_{\mathrm{min}}(\vec{p}_{\mathrm{T},1-5}, \vec{p}_{\mathrm{T}}^{\mathrm{miss}})| < 0.4$ is expected because of the application of the $|\Delta\phi_{\mathrm{min}}(\vec{p}_{\mathrm{T},1-4}, \vec{p}_{\mathrm{T}}^{\mathrm{miss}})| > 0.4$ cut. To discriminate the dijet contributions even more, the $|\Delta\phi_{\mathrm{min}}(\vec{p}_{\mathrm{T},1-4}, \vec{p}_{\mathrm{T}}^{\mathrm{miss}})| > 0.4$ cut from the previous Run 2 search was dropped. Instead it was found that applying a $|\Delta\phi_{\mathrm{min}}(\vec{p}_{\mathrm{T},1-3}, \vec{p}_{\mathrm{T}}^{\mathrm{miss}})| > 0.4$ and a $|\Delta\phi_{\mathrm{min}}(\vec{p}_{\mathrm{T},1-5}, \vec{p}_{\mathrm{T}}^{\mathrm{miss}})| > 0.3$ selection allows for an even better dijet discrimination. For the cut on $|\Delta\phi_{\mathrm{min}}(\vec{p}_{\mathrm{T},1-5}, \vec{p}_{\mathrm{T}}^{\mathrm{miss}})|$, at least 5 jets must be present in the selected events. All the requirements from these final pre-selections are summarised in Table 6.3.

Requirement	Pre-selection
Trigger	$E_{\mathrm{T}}^{\mathrm{miss}}$
$E_{\mathrm{T}}^{\mathrm{miss}}$ [GeV]	> 220
$E_{\mathrm{T}}^{\mathrm{miss}}$ $\mathcal{S}$	> 9
N_{ℓ}	$= 0$
N_{j}	≥ 5
N_{b}	≥ 1
$p_{\mathrm{T},\,4}$ [GeV]	> 40
$\lvert\Delta\phi_{\min}(\vec{p}_{\mathrm{T},1-3}, \vec{p}_{\mathrm{T}}^{\mathrm{miss}})\rvert$	> 0.4
$\lvert\Delta\phi_{\min}(\vec{p}_{\mathrm{T},1-5}, \vec{p}_{\mathrm{T}}^{\mathrm{miss}})\rvert$	> 0.3

Table 6.3: The pre-selections found to match the data and MC background yields for the top squark pair production search using ATLAS Run 2 and Run 3 data.

The yields of the background processes and ATLAS Run 2 and Run 3 data were again compared after applying these final pre-selections. For both runs an overall very good agreement between data and MC yields has been found. Figure 6.11 shows the Run 2 and Run 3 data and MC distributions of the $E_{\mathrm{T}}^{\mathrm{miss}}$ $\mathcal{S}$ and $\lvert\Delta\phi_{\min}(\vec{p}_{\mathrm{T},1-5}, \vec{p}_{\mathrm{T}}^{\mathrm{miss}})\rvert$ variables next to each other, so they can be optimally compared. Very similarly are the Run 2 and Run 3 leading jet p_{T} and number of b-jets distributions shown in Figure 6.12. Further distributions after applying the pre-selections are shown in the Appendix.

In Figure 6.11 and Figure 6.12, a very good agreement between the data and the total background yields can be observed in the statistically significant bins. Discrepancies from QCD dijet contamination at low $E_{\mathrm{T}}^{\mathrm{miss}}$ significance values, like the ones in Figure 6.8, can no longer be seen. The same holds for the $\lvert\Delta\phi_{\min}(\vec{p}_{\mathrm{T},1-5}, \vec{p}_{\mathrm{T}}^{\mathrm{miss}})\rvert$ distributions, which do not show the disparity from Figure 6.10 any longer. The various considered p_{T} distributions, like the ones from regular jet, b-jet, large-R jet and $p_{\mathrm{T}}^{\mathrm{miss}}$ variables, generally showed a great agreement between data and MC background yields. The $p_{\mathrm{T},1}$ distributions from the leading jets were used as an example in Figure 6.12 to demonstrate the good match over a wide range of energies. Also, the discrete distributions representing the numbers of different types of jets demonstrated a good agreement of the yields, as shown by the number of b-jets distributions. By comparing the Run 2 with the Run 3 yields in Figure 6.11 and Figure 6.12, it can be seen that the overall shapes of the very different kinds of distribution are very similar. This is true for the various types of background, the ATLAS data and even for the three signal distributions that were included, with mass points $m(\tilde{t}_1, \tilde{\chi}_1^0) = (900,\ 500)$ GeV, $m(\tilde{t}_1, \tilde{\chi}_1^0) = (1200,\ 600)$ GeV, and $m(\tilde{t}_1, \tilde{\chi}_1^0) = (1300,\ 1)$ GeV. It can be understood as a consistent modelling over both runs.

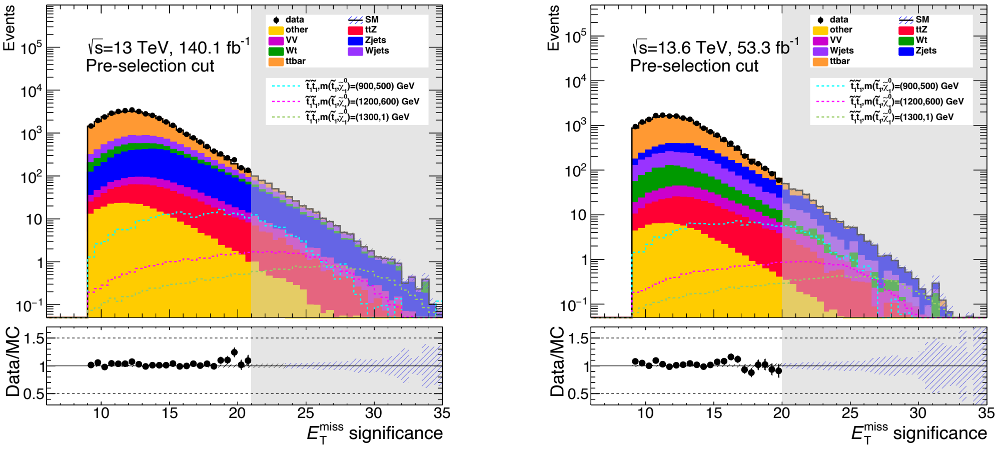

(a) Run 2 $E_{\mathrm{T}}^{\mathrm{miss}}$ $\mathcal{S}$ (b) Run 3 $E_{\mathrm{T}}^{\mathrm{miss}}$ $\mathcal{S}$

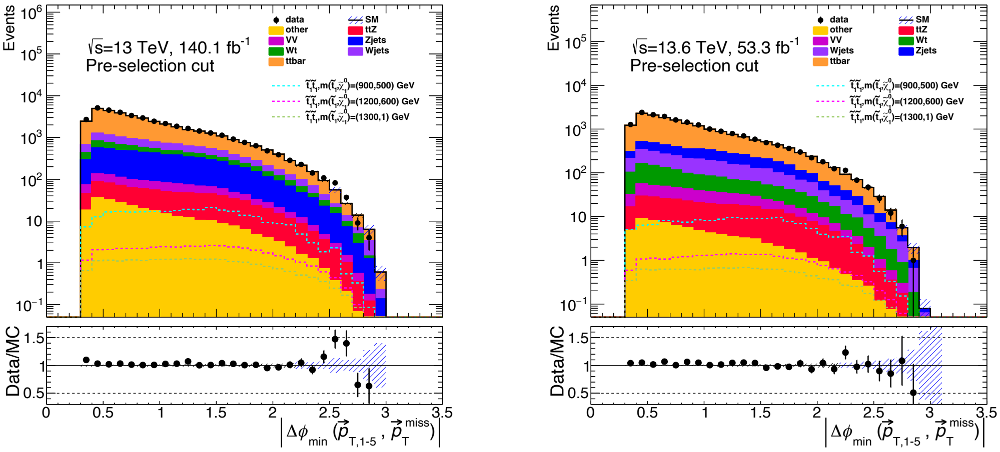

(c) Run 2 $|\Delta\phi_{\mathrm{min}}(\vec{p}_{\mathrm{T},1-5}, \vec{p}_{\mathrm{T}}^{\mathrm{miss}})|$ (d) Run 3 $|\Delta\phi_{\mathrm{min}}(\vec{p}_{\mathrm{T},1-5}, \vec{p}_{\mathrm{T}}^{\mathrm{miss}})|$

Figure 6.11: ATLAS Run 2 and Run 3 $E_{\mathrm{T}}^{\mathrm{miss}}$ $\mathcal{S}$ and $|\Delta\phi_{\mathrm{min}}(\vec{p}_{\mathrm{T},1-5}, \vec{p}_{\mathrm{T}}^{\mathrm{miss}})|$ distributions after applying the pre-selection cuts from Table 6.3. These distributions demonstrate good agreement between data and MC background events in selected kinematic regions. Three signal samples were added to blind bins in grey where at least one of the signals exceeds 10% of the total background. Statistical uncertainties are indicated with a black line on the data points and with a blue shade for the total background prediction.

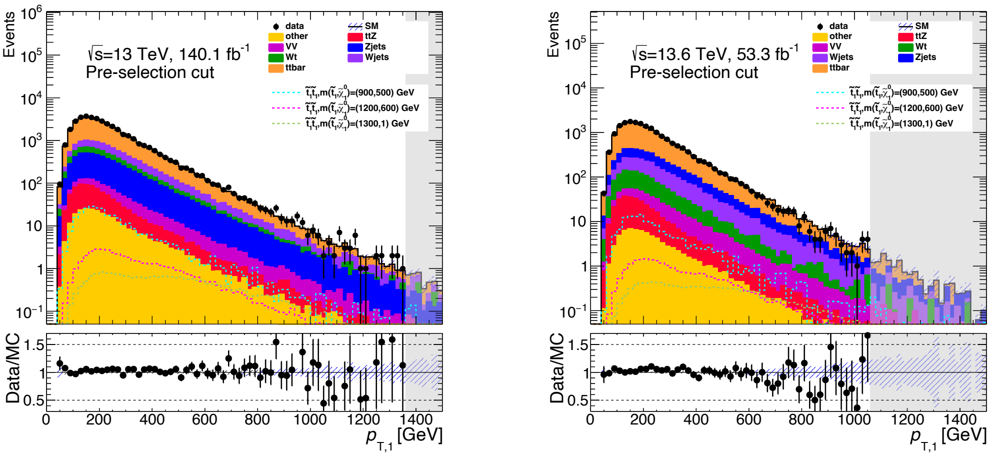

(a) Run 2 leading jet p_{T} (b) Run 3 leading jet p_{T}

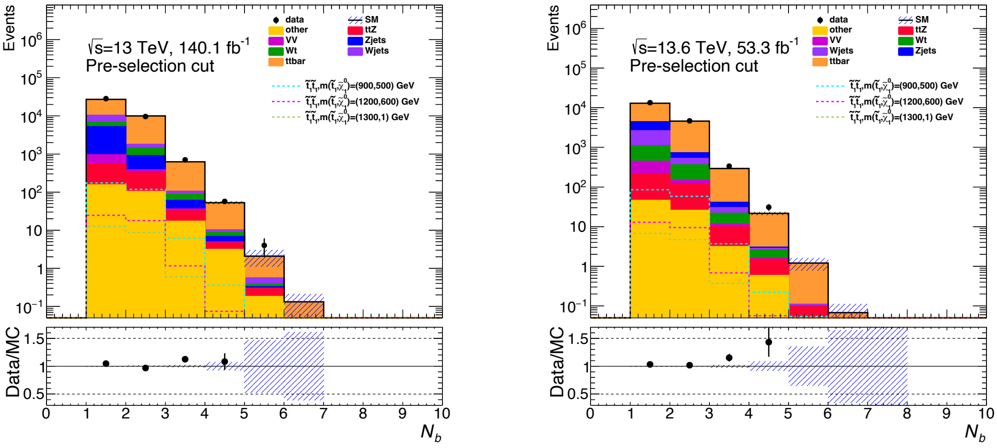

(c) Run 2 number of b-jets (d) Run 3 number of b-jets

Figure 6.12: ATLAS Run 2 and Run 3 leading jet p_{T} and b-jet multiplicity distributions after applying the pre-selection cuts from Table 6.3. These distributions demonstrate good agreement between data and MC background events in selected kinematic regions. Three signal samples were added to blind bins in grey where at least one of the signals exceeds 10% of the total background. Statistical uncertainties are indicated with a black line on the data points and with a blue shade for the total background prediction.

The generally good agreement of ATLAS data with the total background yields by applying the pre-selections, provides an optimal starting point for creating SRs optimised for high sensitivity towards specifically targeted models, which were not yet excluded by the previous Run 2 search. However, a separate background fit obtained and validated in yet to be defined CRs and VRs will still be necessary to ensure adequate agreement in the SRs. A cutbased approach for designing two SRs for top squark pair production events with all-hadronic final states is described in the next chapter.

6.4 The Cutbased Optimisation Strategy

Like for the previous search presented in Section 6.2, two main cutbased SRs were created for the scenarios involving two body $\tilde{t}_1$ decays. The alternative ML strategy has an advantage, as it can individually find optimal selections for every single signal under consideration. Like that it is more flexible to exploit small changes in kinematics over the range of $m(\tilde{t}_1, \tilde{\chi}_1^0)$ mass points. Therefore, the ML approach is expected to provide better results for the majority of scenarios. However, it is still important to have a traditional cut-and-count based analysis alongside it, allowing for direct comparison between the two approaches. In that way, the cutbased strategy can be used as a baseline and the benefits of using ML analysis strategies will become more evident. Additionally, the previous Run 2 study was using the cut-and-count approach, so that some strategies can be adapted or even adopted. Furthermore, a new strategy can be developed to optimise cuts for more sensitivity towards the targeted signals. Lastly, also the cutbased method is expected to have major benefits with regards to the previous Run 2 search, originating from the inclusion of novel ML based particle reconstruction and identification algorithms.

The simulated samples from all the considered mass point models form a signal grid, which has been mainly set up with $\tilde{t}_1$ and $\tilde{\chi}_1^0$ mass steps of 100 GeV. Only in the compressed regions, some models are considered with $\tilde{t}_1$ or $\tilde{\chi}_1^0$ mass differences of 50 GeV, which are not in the focus of this study. Naturally, mass points which are past the exclusion limits presented in the previous Run 2 search (Figure 6.5) are targeted. Those involve especially $\tilde{t}_1$ masses at 1300 GeV in the high $\Delta m(\tilde{t}_1, \tilde{\chi}_1^0)$ regions and $\tilde{\chi}_1^0$ masses at 500 GeV and 600 GeV for lower to intermediate $\Delta m(\tilde{t}_1, \tilde{\chi}_1^0)$ mass splittings. The two preliminary SRs presented here are especially optimised for these scenarios. As in the Run 2 search, the first signal region targets the high $\tilde{t}_1$ mass region and the second one targets the lower to intermediate mass splitting range, mostly within $300\,\text{GeV} < \Delta m(\tilde{t}_1, \tilde{\chi}_1^0) < 600\,\text{GeV}$. Those two signal regions will be called SRa and SRb respectively, to not confuse them with SRA and SRB from the previous search.

Initially, a hadronic τ-veto was added for both SRs to further discriminate $t\bar{t}$ background events with leptonically decaying W bosons and all hadronic final states, as for the Run 2 selections. This veto was left out of the pre-selections because events with τ-leptons were potentially interesting for the ML approach. As τ-leptons can be produced in the decay chain of both, signal and background processes, ML studies could test whether NNs can efficiently discriminate τ-leptons in signal from the ones in background samples. By observing the $E_{\mathrm{T}}^{\mathrm{miss}}$ distributions of signal samples targeted by SRb, it could be noticed that only very few signal events were fulfilling $E_{\mathrm{T}}^{\mathrm{miss}} > 750\,\text{GeV}$, in contrast to the signal samples targeted by SRa, where the $E_{\mathrm{T}}^{\mathrm{miss}}$ values are quite evenly spread between 500 GeV and 1000 GeV. Figure 6.13 shows the Run 3 $E_{\mathrm{T}}^{\mathrm{miss}}$ distributions of the total MC background and several signal samples targeted by one of the SRs, after applying the pre-selections and the hadronic τ-veto.

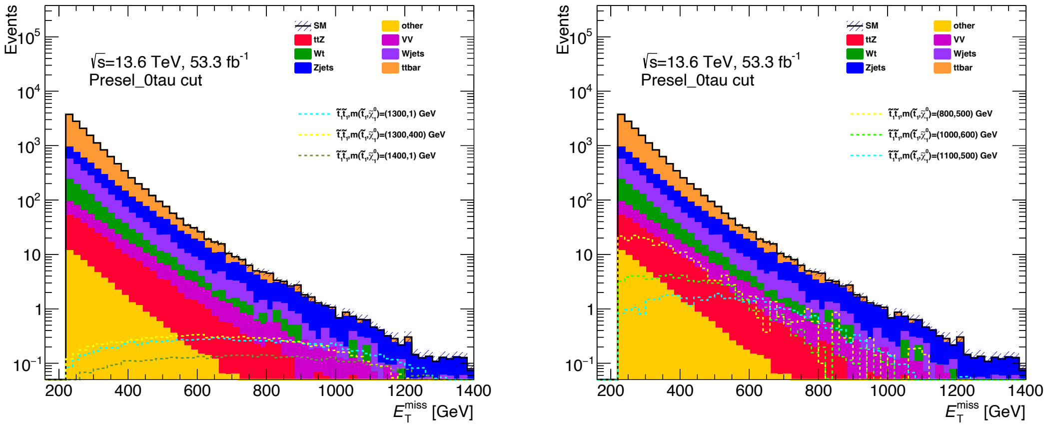

Figure 6.13: ATLAS Run 3 $E_{\mathrm{T}}^{\mathrm{miss}}$ distributions of six signal samples and the MC background by applying the pre-selections with a hadronic τ-veto. The three signal samples on the left are in the kinematic regime targeted by SRa and the three on the right are in the regime targeted by SRb.

Figure 6.13 shows that the MC background contributions fall off exponentially with increasing $E_{\mathrm{T}}^{\mathrm{miss}}$ values. This makes it very interesting for SRa to target events with high $E_{\mathrm{T}}^{\mathrm{miss}}$ to increase the sensitivity to the signal. For that reason an orthogonal separation of SRa and SRb based on an $E_{\mathrm{T}}^{\mathrm{miss}}$ threshold was applied. By requiring $E_{\mathrm{T}}^{\mathrm{miss}} > 750\,\mathrm{GeV}$ for SRa and $E_{\mathrm{T}}^{\mathrm{miss}} < 750\,\mathrm{GeV}$ for SRb, the regions are orthogonalised without discarding most of the signal events in one of the regions. However, this requirement is substantial for SRa and could result in high uncertainties in the background estimation of the region, as events with such high $E_{\mathrm{T}}^{\mathrm{miss}} > 750\,\mathrm{GeV}$ values are rare. The uncertainties will have to be checked when CRs are defined and then, the $E_{\mathrm{T}}^{\mathrm{miss}}$ cut can be lowered if necessary.

To quantify the sensitivity to a signal in a selected region, a discovery significance Z_{A} is introduced, which takes systematic uncertainties on the background estimation into account [70, 71]. It is calculated from the numbers of signal and total background events, S and B, and from the total systematic uncertainty on the background estimation, σ_B, by

$$Z_{\mathrm{A}} = \sqrt{2\left((S+B)\ln\left[\frac{(S+B)(B+\sigma_B^2)}{B^2+(S+B)\sigma_B^2}\right] - \frac{B^2}{\sigma_B^2}\ln\left[1+\frac{\sigma_B^2 S}{B(B+\sigma_B^2)}\right]\right)}. \tag{6.3}$$

This Z_{A} gives a good estimate of the fluctuation caused by the addition of S signal events to the predicted total background B. If data is unblinded in a SR and no excess with regards to the background prediction is found, then the corresponding signal scenario is expected to be excluded at a certain CL, depending on how strong the significance value Z_{A} is. But for this search Z_{A} will only be used for guiding the optimisation strategy and not for evaluating potential discoveries or

exclusion limits after the unblinding. Sophisticated tools performing likelihood fits, such as pyhf, are going to be used for the latter [72].
As the previous Run 2 study had total systematic uncertainties of 9% - 15% for the SRA and SRB subregions, σ_B was set to 20% for the optimisation studies presented here, to have a reasonable but more conservative estimate.

In the following, it was analysed how the Z_A value evolves by applying further selections on individual variables for signal samples targeted by SRa. Large improvements to the significance Z_A are observed by applying additional cuts on the $E_\mathrm{T}^\mathrm{miss}$ significance, the number of large-R jets, on the p_T of the leading and sub-leading large-R jet, on $m_\mathrm{T}^{b,\mathrm{min}}$ and by requiring the leading large-R jet to be top-tagged (large-R jet$_1(t)$). Figure 6.14 shows how the selections for SRa are motivated by representing how the significance evolves after applying a cut at the value of each consecutive bin. Here, the distributions are not shown in the traditional way as the ones in the last Figure 6.13 for example. The yield in each bin represents the total number of events with a value greater than the bin's lower edge. The lower panels depict the development of the significance Z_A accordingly. This specific kind of depiction allows to very well see how cuts are motivated. In Figure 6.14, the signal for the $m(\tilde{t}_1, \tilde{\chi}_1^0) = (1300,\, 1)$ GeV scenario is presented, which overall very well represents the behaviour of the models targeted by SRa. The SRa cuts were thereby applied on the MC Run 3 samples, by leaving out the selection on the variable that is featured in the x-axis. Also, cuts on highly correlated variables were left out. Highly correlated variables are $E_\mathrm{T}^\mathrm{miss}$, $E_\mathrm{T}^\mathrm{miss}$ significance and $m_\mathrm{T}^{b,\mathrm{min}}$, or the large-$R$ jet$_1(t)$, the number of large-R jets and the leading or subleading large-R jet p_T. This means that different selections were applied for the distributions in Figure 6.14, resulting in very different ranges of Z_A values shown in the lower panels.

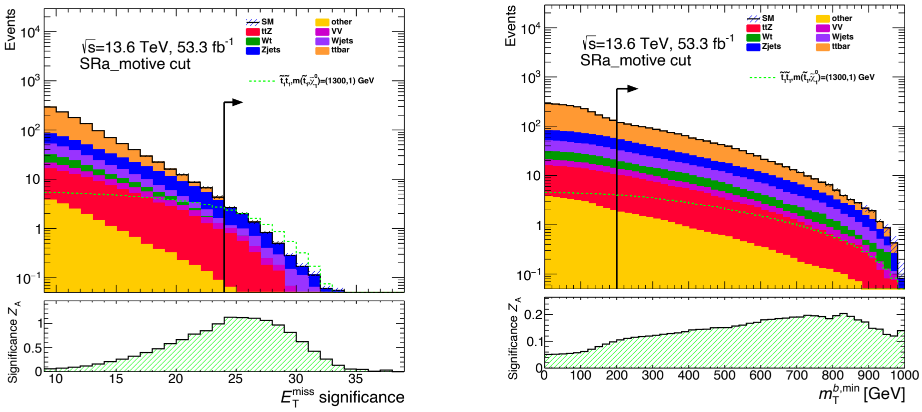

(a) SRa $E_{\mathrm{T}}^{\mathrm{miss}}$ $\mathcal{S}$ cut (b) SRa $m_{\mathrm{T}}^{b,\mathrm{min}}$ cut

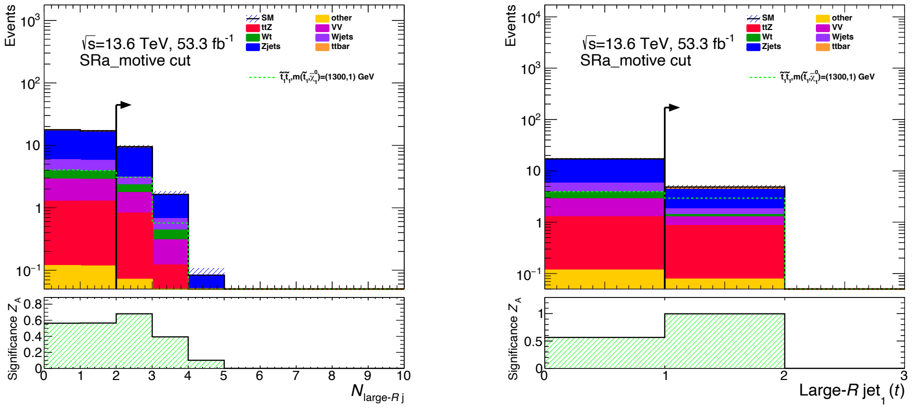

(c) SRa $N_{\text{large-}R\text{ j}}$ cut (d) SRa large-R jet$_1$ (t) cut

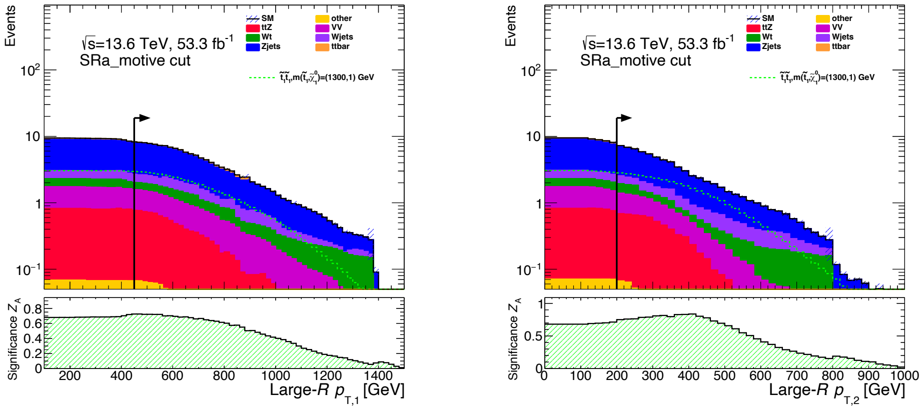

(e) SRa large-R $p_{\mathrm{T},1}$ cut (f) SRa large-R $p_{\mathrm{T},2}$ cut

Figure 6.14: Evolution of the Run 3 background, the $m(\tilde{t}_1, \tilde{\chi}_1^0) = (1300, 1)$ GeV signal and the significance Z_{A} yields for the specific SRa selection variables. In each bin the total number of events is given, which have a higher value than the bin's starting value. The lower panels show the resulting significance for consecutive cuts bin by bin, discarding all events before. All the SRa requirements, except for the selection on the indicated variable and other highly correlated variables, are set. An arrow signalises where a cut is applied for the SRa selection.

Figure 6.14 demonstrates, that especially by applying selections on the $E_{\mathrm{T}}^{\mathrm{miss}}$ significance and by requiring the leading large-R jet to be top-tagged a lot of significance Z_{A} is gained.

After the SRa optimisation, the same strategy was followed to find selections for SRb. However, the kinematics change quite substantially for signal samples with different $\Delta m(\tilde{t}_1, \tilde{\chi}_1^0)$ mass splittings in SRb. Especially signal samples with $\Delta m(\tilde{t}_1, \tilde{\chi}_1^0) > 400\,\mathrm{GeV}$ have significantly more events with a top-tagged large-R jet than the ones with $\Delta m(\tilde{t}_1, \tilde{\chi}_1^0) \leq 400\,\mathrm{GeV}$. Therefore, SRb is split into two orthogonal subregions, called SRb-l and SRb-h. SRb-l is mostly targeting the lower $\tilde{t}_1$ mass models, having smaller mass splittings, whereas SRb-h is also targeting scenarios with higher $\tilde{t}_1$ masses and more intermediate mass splittings. To compensate for the lack of top-tagged large-R jets in the SRb-l region, additional selections on b-jets were found to increase sensitivity to the signals. These selections include cuts on the number of b-jets, the $\Delta R(b_1, b_2)$ and the $m_{\mathrm{T}}^{b,\mathrm{min}}$ and $m_{\mathrm{T}}^{b,\mathrm{max}}$ variables, which are also considering the $\vec{p}_{\mathrm{T}}^{\mathrm{miss}}$. Further selections were again placed on the $E_{\mathrm{T}}^{\mathrm{miss}}$ significance and to require at least one large-R jet (non top-tagged).

As indicated, the SRb-h is requiring one large-R jet to be top-tagged. More SRb-h cuts are placed on the number of large-R jets, the $E_{\mathrm{T}}^{\mathrm{miss}}$ significance and the $m_{\mathrm{T}}^{b,\mathrm{min}}$. The Z_{A} based motivations for the SRb-l and SRb-h selections are shown in Figure 6.15 and Figure 6.16, respectively. The same type of depictions is used as in Figure 6.14 for SRa. Figure 6.15 uses a $m(\tilde{t}_1, \tilde{\chi}_1^0) = (900,\ 500)$ GeV signal to represent the SRb-l signatures and a $m(\tilde{t}_1, \tilde{\chi}_1^0) = (1000,\ 500)$ GeV signal is used as SRb-h signature. Even though those two scenarios seem to be very close and similar with regards to the mass parameters, many differences can be seen in the distributions of their kinematic variables. The $m(\tilde{t}_1, \tilde{\chi}_1^0) = (900,\ 500)$ GeV signal shows more similarities with other signals in the more compressed region, whereas there are more similarities between the more intermediate $\Delta m(\tilde{t}_1, \tilde{\chi}_1^0)$ signals and the $m(\tilde{t}_1, \tilde{\chi}_1^0) = (1000,\ 500)$ GeV one. With their $\tilde{\chi}_1^0$ masses of $500\,\mathrm{GeV}$, both of these targeted mass points are right above the exclusion limit of the previous Run 2 search shown in Figure 6.5.

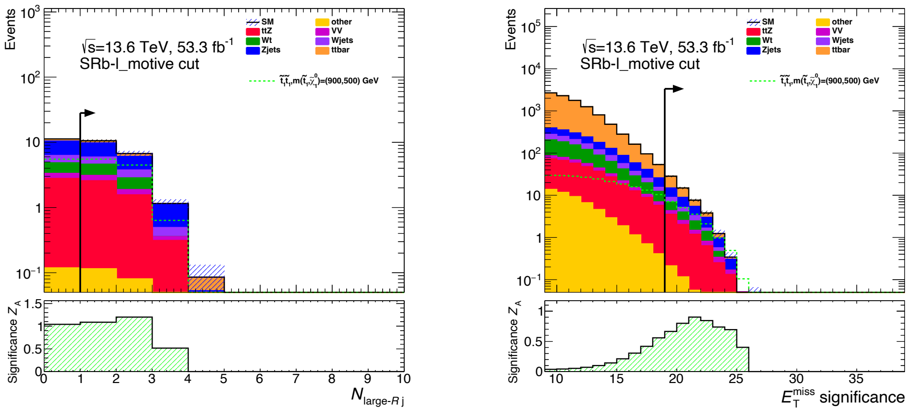

(a) SRb-l $N_{\text{large-}R\text{ j}}$ cut

(b) SRb-l E_T^{miss} $\mathcal{S}$ cut

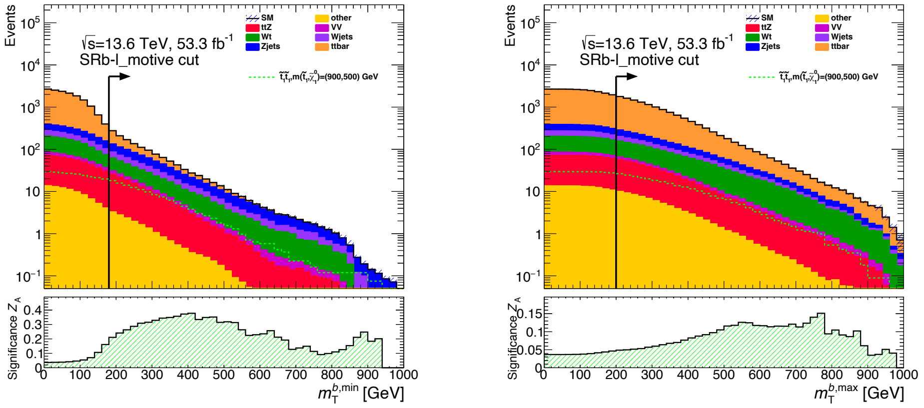

(c) SRb-l $m_T^{b,\text{min}}$ cut

(d) SRb-l $m_T^{b,\text{max}}$ cut

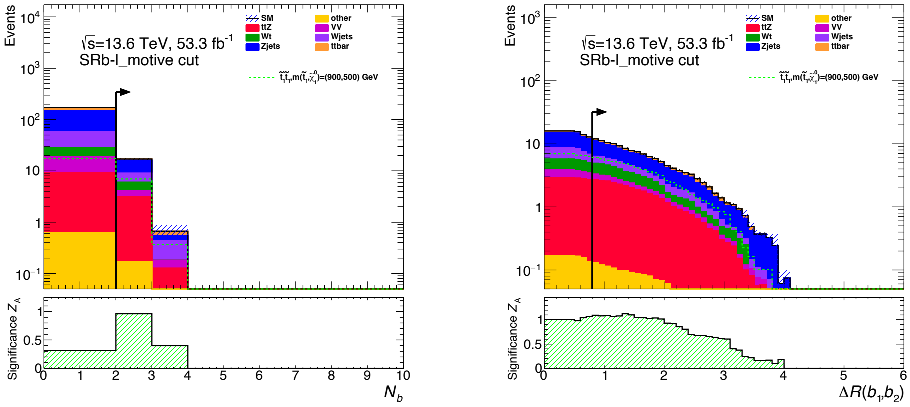

(e) SRb-l N_b cut

(f) SRb-l $\Delta R(b_1, b_2)$ cut

Figure 6.15: Evolution of the Run 3 background, the $m(\tilde{t}_1, \tilde{\chi}_1^0) = (900, 500)$ GeV signal and the significance Z_A yields for the specific SRb-l selection variables. In each bin, the total number of events is given, which have a higher value than the bin's starting value. The lower panels show the resulting significance for consecutive cuts bin by bin, discarding all events before. All the SRb-l requirements, except for the selection on the indicated variable and other highly correlated variables, are set. An arrow signalises where a cut is applied for the SRb-l selection.

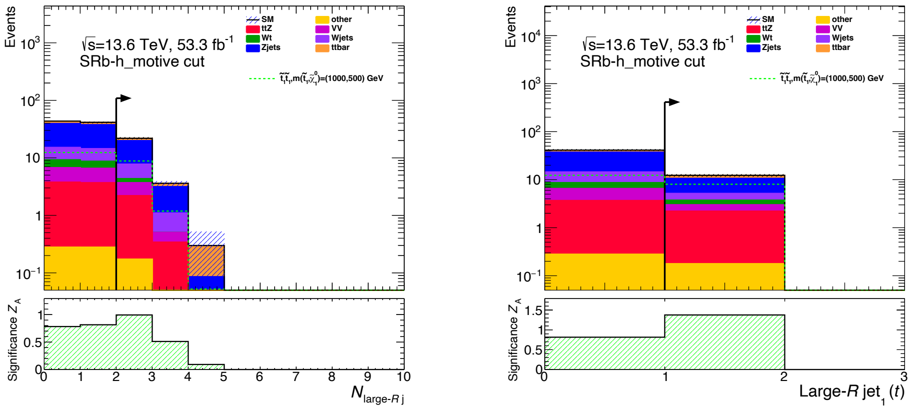

(a) SRb-h $N_{\text{large-}R\text{ j}}$ cut (b) SRb-h large-R jet$_1$ (t) cut

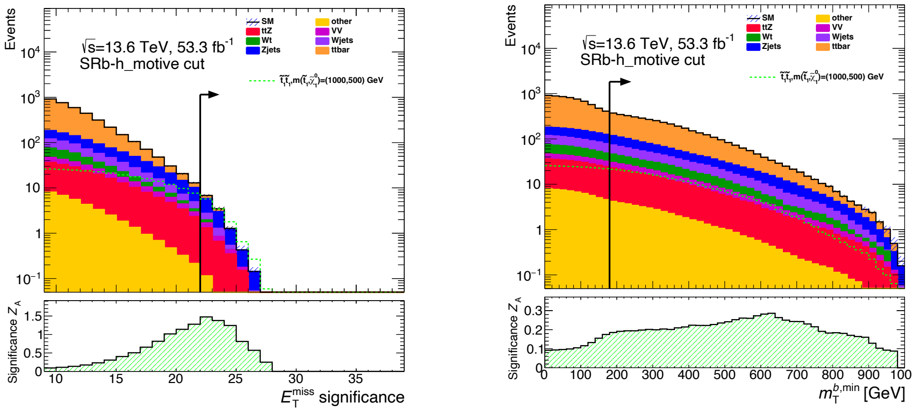

(c) SRb-h $E_{\mathrm{T}}^{\mathrm{miss}}$ $\mathcal{S}$ cut (d) SRb-h $m_{\mathrm{T}}^{b,\mathrm{min}}$ cut

Figure 6.16: Evolution of the Run 3 background, the $m(\tilde{t}_1, \tilde{\chi}_1^0)$ =(1000, 500) GeV signal and the significance Z_{A} yields for the specific SRb-h selection variables. In each bin, the total number of events is given, which have a higher value than the bin's starting value. The lower panels show the resulting significance for consecutive cuts bin by bin, discarding all events before. All the SRb-h requirements, except for the selection on the indicated variable and other highly correlated variables, are set. An arrow signalises where a cut is applied for the SRb-h selection.

By comparing Figure 6.15 with Figure 6.16, it can be seen that requirements on $E_{\mathrm{T}}^{\mathrm{miss}}$ significance are crucial for both SRb regimes. SRb-l can additionally benefit a lot by requiring a second b-jet, while SRb-h gains a lot of significance from having the leading large-R jet top-tagged.
All the additional selections found for the signal regions SRa, SRb-l and SRb-h, which are extending the pre-selections from Table 6.3, are summarised in Table 6.4.

Requirement	SRa	SRb-l	SRb-h
τ-veto	✓	✓	✓
$E_{\mathrm{T}}^{\mathrm{miss}}$[GeV]	> 750	< 750	< 750
$E_{\mathrm{T}}^{\mathrm{miss}}\ \mathcal{S}$	> 24	> 19	> 22
N_b	-	≥ 2	-
$N_{\text{large-}R\text{ j}}$	≥ 2	≥ 1	≥ 2
Large-R jet$_1(t)$	✓	×	✓
Large-R $p_{\mathrm{T},1}$[GeV]	> 450	-	-
Large-R $p_{\mathrm{T},2}$[GeV]	> 200	-	-
$m_{\mathrm{T}}^{b,\mathrm{min}}$[GeV]	> 200	> 180	> 180
$m_{\mathrm{T}}^{b,\mathrm{max}}$[GeV]	-	> 200	-
$\Delta R(b_1, b_2)$	-	> 0.8	-

Table 6.4: The SRa, SRb-l and SRb-h selections found for optimising the signal sensitivity in the targeted regimes. Only the cuts extending the pre-selections from Table 6.3 are listed. Checkmarks indicate that the corresponding requirement needs to be fulfilled, whereas a cross means that the requirement must not be valid and a dash (-) signifies that no additional selection is required for that variable.

The following Figure 6.17, Figure 6.18 and Figure 6.19 depict Run 2 and Run 3 leading jet p_{T} distributions of the MC background and two signal samples targeted by SRa, SRb-l and SRb-h respectively. Additionally, the corresponding significances Z_{A} and the numbers of signal and background events are given. That allows to very well compare the sensitivities of the three regions and also their Run 2 and Run 3 performance.

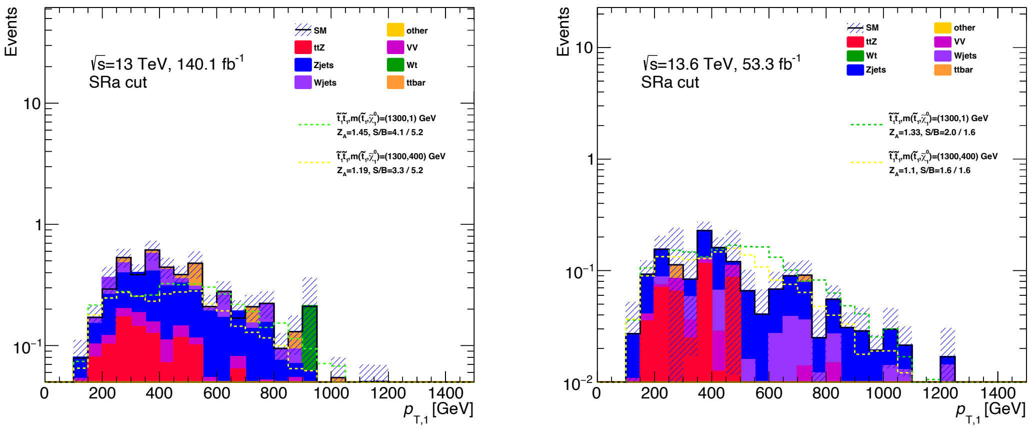

Figure 6.17: Leading jet p_{T} distributions with SRa selections of the MC background and two signals targeted by SRa. On the left, the distributions corresponding to the ATLAS Run 2 are shown, while on the right they are shown for ATLAS Run 3.

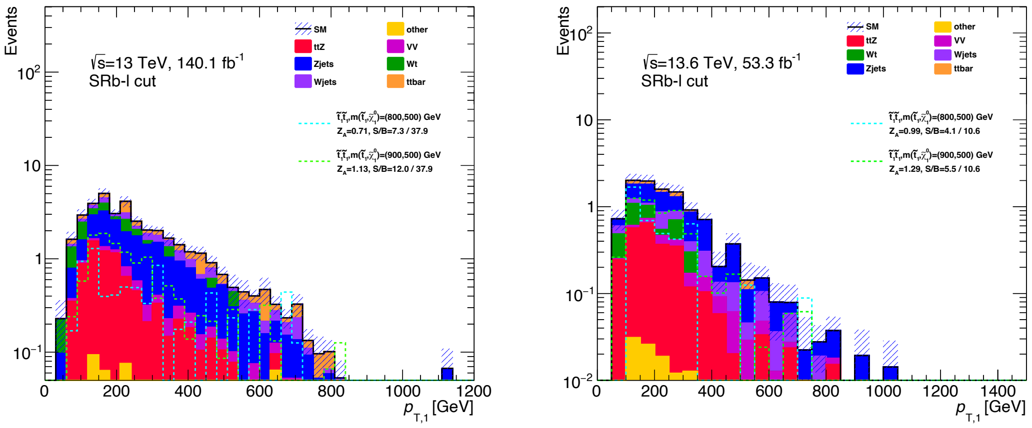

Figure 6.18: Leading jet p_{T} distributions with SRb-l selections of the MC background and two signals targeted by SRb-l. On the left, the distributions corresponding to the ATLAS Run 2 are shown, while on the right they are shown for ATLAS Run 3.

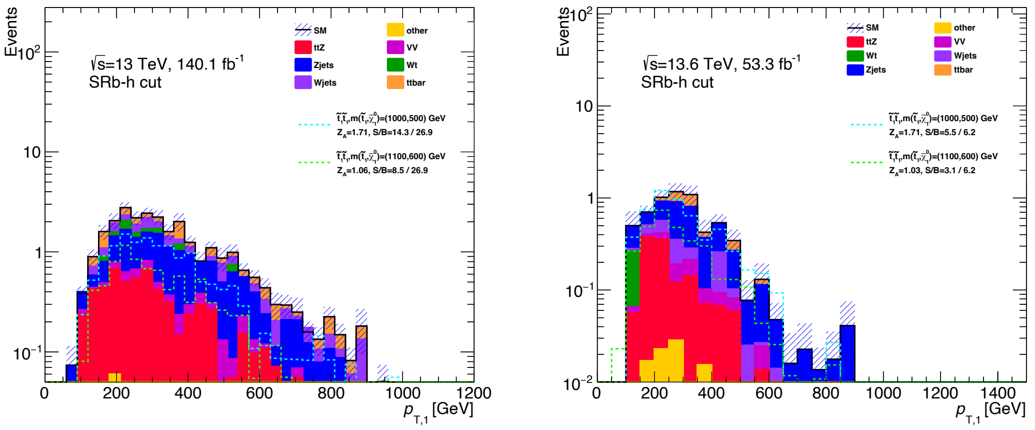

Figure 6.19: Leading jet p_{T} distributions with SRb-h selections of the MC background and two signals targeted by SRb-h. On the left, the distributions corresponding to the ATLAS Run 2 are shown, while on the right they are shown for ATLAS Run 3.

The distributions and significances depicted in Figure 6.17 show that better sensitivities are achieved for Run 2. However, this seems to be the case because of the higher statistics, which is indicated with the ratio of signal and background (S/B). Those ratios are higher in the Run 3 distributions. Therefore, it can be assumed that higher Z_{A} values will be achieved once the ATLAS data 2024 is included, effectively tripling the Run 3 statistics.
The significances obtained with the SRb-l selections in Figure 6.18 are slightly lower than the ones from the other selections, especially for the more compressed mass point signals. But it is vital to note that significantly better sensitivities are achieved when SRb-l is statistically combined with the orthogonal SRb-h selection, which is also sensitive to some of the scenarios targeted by SRb-l.
As shown in Figure 6.19, SRb-h achieved a high Z_{A} value of 1.71 in both, Run 2 and Run 3, for the $m(\tilde{t}_1, \tilde{\chi}_1^0) = (1000, 500)$ GeV mass point. Over all the targeted mass points in all the SRs, higher S/B ratios are observed in the Run 3 distributions. This is expected, as improvements in the Run 3 contributions are more strongly considered in the SR optimisation process. This stronger focus is motivated because the Run 2 contributions are naturally already studied more with the previous search. Furthermore, the increase in centre-of-mass energy from $\sqrt{s} = 13$ TeV to 13.6 TeV benefits the Run 3 ratios, since the cross sections of most signal production processes increased slightly. However, should the kinematic differences of the Run 2 and Run 3 distributions in the targeted regimes become more significant after the inclusion of 2024 data, it is best to introduce a separate cutbased SR for Run 2.

The SR sensitivities were also evaluated over a range of mass points. As SRa is targeting mostly high mass splitting scenarios with $m(\tilde{t}_1)$ values around 1300 GeV, only close by mass points were further examined, with $\tilde{\chi}_1^0$ masses up to 400 GeV.

Figure 6.20 depicts the significance Z_A values obtained by applying the SRa selections on this regime.

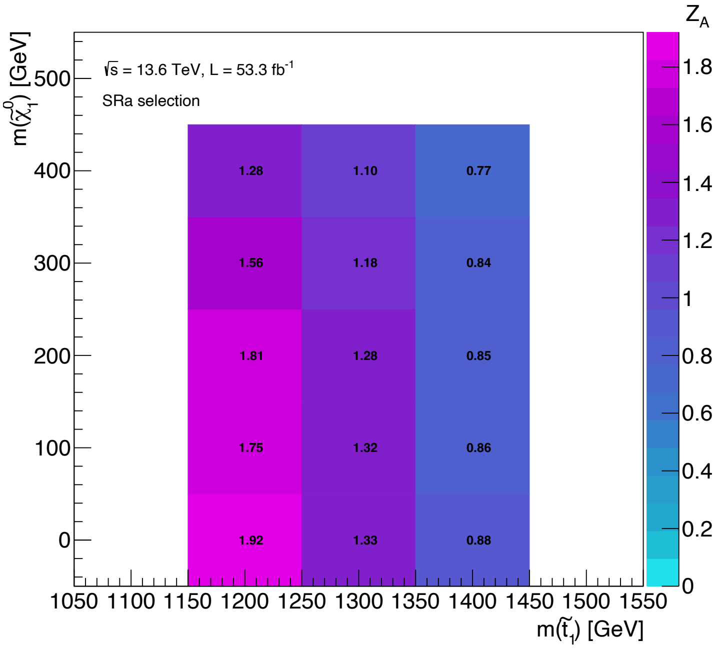

Figure 6.20: Significance Z_A distribution for the ATLAS Run 3 signal grid targeted by SRa with the application of the corresponding selections listed in Table 6.4.

Figure 6.20 demonstrates that good sensitivities with $Z_\mathrm{A} > 1$ are achieved for the signals with $m(\tilde{t}_1) = 1300\,\mathrm{GeV}$. Unfortunately, the significances for the $m(\tilde{t}_1) = 1400\,\mathrm{GeV}$ mass points are indicating lower sensitivities. High Z_A values, getting close to two, are achieved for the already excluded mass points with $m(\tilde{t}_1) = 1200\,\mathrm{GeV}$. A value of $Z_\mathrm{A} > 1.645$ is usually required for an expected 95% exclusion of the corresponding model [73]. All the significances are expected to be improved with the addition of data 2024. After this addition it also makes sense to continue the optimisation of the SRs that will further improve the significance Z_A values. Also, with the statistical combination of the orthogonal SRb regions more sensitivity is gained, optimal for potential discoveries in the high $m(\tilde{t}_1)$ parameter space.

Scenarios with $m(\tilde{\chi}_1^0) \geq 500\,\mathrm{GeV}$, $m(\tilde{t}_1) \leq 1200\,\mathrm{GeV}$ and $\Delta m(\tilde{t}_1, \tilde{\chi}_1^0) \geq 300\,\mathrm{GeV}$ were considered as interesting for the SRb selections, because they are well in the intermediate $\Delta m(\tilde{t}_1, \tilde{\chi}_1^0)$ mass regime and not yet excluded by the previous Run 2 search. In Figure 6.21, the Run 3 significance distributions over these considered mass points are shown for the SRb-l and the SRb-h selections.

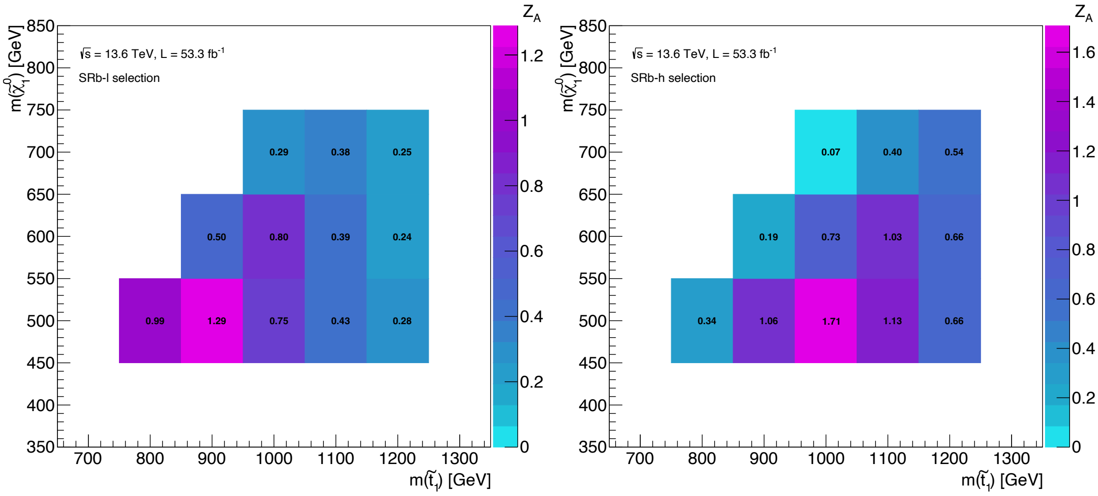

Figure 6.21: Significance Z_A distributions for the ATLAS Run 3 signal grid targeted by the SRb selections with the application of the corresponding cuts listed in Table 6.4. On the left, the Z_A values are shown by applying the SRb-l selections, whereas on the right the ones by applying the SRb-h selections are depicted.

By looking at the significance values in Figure 6.21, it can be seen that the $m(\tilde{\chi}_1^0) = 500\,\mathrm{GeV}$ mass points are well covered with significance values around one or higher by SRb-l or by SRb-h. Only for the $m(\tilde{t}_1) = 1200\,\mathrm{GeV}$ mass points lower Z_A values are observed in both regions. However, this can be compensated by the statistical combination of SRb-h with the SRa selections, which are more sensitive to the $m(\tilde{t}_1) = 1200\,\mathrm{GeV}$ mass points. With the orthogonal definitions of the proposed SRs these sensitivities to different phase spaces can be exploited. With the statistical combination of mainly the two SRb regions, also good sensitivities to the $m(\tilde{\chi}_1^0) = 600\,\mathrm{GeV}$ signals can be achieved.

Additionally, the SRa, SRb-l and SRb-h performances are compared to the SRA and the SRB selections of the previous Run 2 study. Not all their requirements listed in Table 6.1 could be easily reproduced, especially as the specific reclustering algorithms used for the $R = 0.8$ and $R = 1.2$ jets were not readily available. To best imitate the selections, the same cuts were applied for large-R jets ($R = 1.0$). Also the χ^2 method used to obtain the m_{T2,χ^2} variable was not reproduced. However, the main purpose of that variable was anyway just to orthogonalise SRA and SRB and not to gain a lot of additional sensitivity. By observing the significances obtained from imitating the various SRA and SRB subregions at the mass points examined in Figure 6.20 and Figure 6.21, it becomes evident that the SRA-TT and SRB-TT selections achieve much higher Z_A values, up to an order of magnitude, than the other Run 2 search subregions. Figure 6.22 shows the Z_A performances of the SRA-TT selection in the signal grid of Figure 6.20 and the ones of SRB-TT in the signal grid of Figure 6.21.

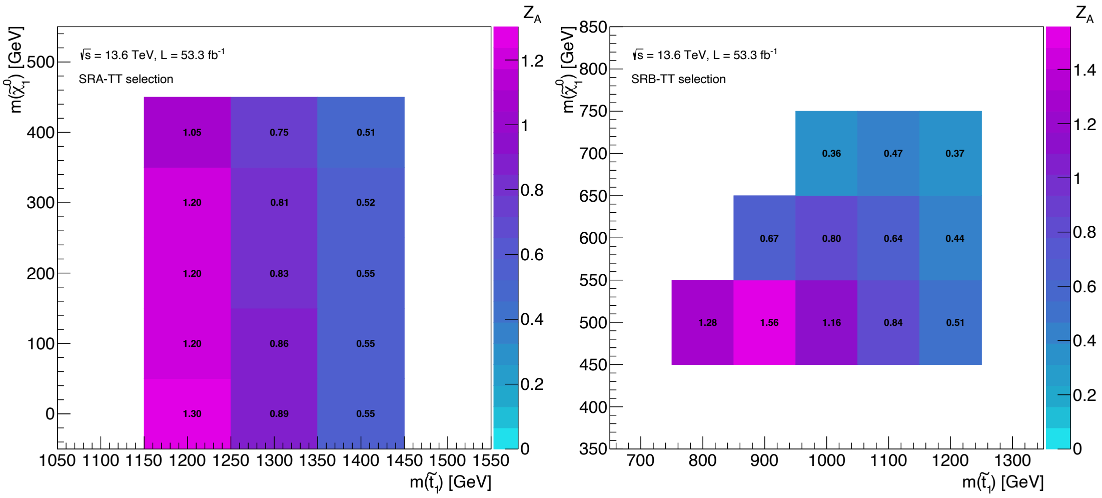

Figure 6.22: Significance Z_A distributions for the ATLAS Run 3 signal grids targeted by SRa and SRb with the application of the reproduced SRA-TT and SRB-TT cuts respectively, which are listed in Table 6.1. On the left the Z_A values are shown by imitating SRA-TT selections on high $\tilde{t}_1$ mass points. The intermediate $m(\tilde{t}_1, \tilde{\chi}_1^0)$ signal grid on the right shows the significance values by applying the reproduced SRB-TT cuts.

By comparing the Z_A values of the SRA-TT selections from Figure 6.22 with the SRa ones from Figure 6.20, it can be observed that SRa performs overall significantly better. An important factor for this increase in performance most likely originates from the availability of top-tagged large-R jets, which were not yet accessible in the previous Run 2 study. As it can be seen in Figure 6.14, a lot of significance is gained for SRa by requiring the leading large-R jet to be top-tagged. However, the reason for the increased sensitivities definitely is not only thanks to the more efficient tagging, but also thanks to the newly optimised cuts, presented in Table 6.4. Looking at the SRB-TT selections in Figure 6.22, it can easily be noticed that especially good sensitivities are achieved for the mass points with smaller $\Delta m(\tilde{t}_1, \tilde{\chi}_1^0)$ mass splittings. The Z_A values obtained with the SRB-TT selection are generally better than the ones from the SRb-l selection. However, similar sensitivies to the SRB-TT selections for the more compressed mass points arise after statistically combining SRb-l and SRb-h. Those mass points are also more in the regions where the search for $\tilde{t}_1$ pair production, with each $\tilde{t}_1$ decaying via an off-shell t, becomes more sensitive. Therefore, a stronger emphasis was placed on the more intermediate mass points, which are mainly targeted by SRb-h.

Overall, good sensitivities to the mass points surrounding the exclusion limits of the previous Run 2 search, shown in Figure 6.5, are obtained through the application of the SRa, SRb-l and SRb-h selections. Additionally, the combined selections perform well for several scenarios with intermediate $\Delta m(\tilde{t}_1, \tilde{\chi}_1^0)$ mass splittings and higher $\tilde{\chi}_1^0$ masses which are further from the previous limits around $m(\tilde{\chi}_1^0) = 400\,\text{GeV}$. These high sensitivities, represented by Z_A values over 1.0, are expected to increase even further through the inclusion of ATLAS data and MC samples from 2024. The corresponding datasets are anticipated to be included within the next few months, as they are already available and only require some specific processing for the analysis. With those good prospects and the already high sensitivities to signals beyond the current exclusion limits, evidence for top squarks could potentially be found within the next year in the newly explored regions of phase space. Otherwise, the exclusion limits for $\tilde{t}_1$ pair production models using ATLAS data can be further extended. Even higher sensitivities towards a potential top squark discovery are expected from the ML based search, which is anticipated to be even better optimised to individually targeted signal points.

Preliminary results from the ML based approach already demonstrate very good sensitivities to the signals of the targeted mass points and they outperform the cutbased selections so gar. However, there is also a lot of scepticism faced towards the application of the non-traditional ML methods. The cut-and-count analysis alongside the ML approach helps as a baseline, allowing for optimal comparison and also as a backing in case difficulties with the ML methodologies arise.

The work presented here played a major role in establishing the pre-selections for the ATLAS Run 3 top squark search in all-hadronic final states. Those selections serve as a basis for both, ML based and cutbased optimisation strategies, ensuring good agreement between data and MC background samples. SR selections for a cut-and-count strategy have been derived, which provide good sensitivities to signals beyond the current exclusion limits. Based on these SRs, preliminary CRs are currently being defined in the pyhf framework. In the near future also initial VRs will be defined. There is still a big effort laying ahead in checking all the systematics in the CRs and VRs to ensure a very precise background prediction. A very well controlled background estimation is essential for BSM searches like this one. All the preliminary signal, validation and control regions provide a great foundation for when the full datasets including data 2024 are available for this analysis, so that it can be efficiently concluded.

Conclusions

This thesis has explored critical advancements in high-energy physics through the integration of novel ML techniques in particle identification and the search for BSM physics. The presented research primarily focused on three key projects, the adaptation and testing of the NeuralRinger algorithm for forward electron identification within the ATLAS detector, the implementation of the NeuralRinger within the Lorenzetti Showers framework to improve the study of forward electrons in simulated environments, and the search for top squark pair production in all-hadronic final states. The findings presented in this thesis contribute to the broader efforts of optimising particle detection and refining BSM search strategies in the current and future runs of the LHC.

Electron identification is a crucial component of physics analyses at the LHC, particularly in electroweak interaction studies and in searches for new physics. While identification methods have been optimised to be highly effective in the central region of the ATLAS detector, the performance of electron reconstruction in the forward regions has always been less efficient due to the increased presence of background noise, the reduced granularity of the calorimeter, and the absence of tracking information. The introduction of the NeuralRinger algorithm to forward electron identification represents a significant step forward in addressing these challenges.

The NeuralRinger algorithm, initially developed for electron identification in the central region, leverages an NN-based approach to analyse calorimeter ring patterns and improve classification accuracy. By expanding this strategy to forward regions of $2.5 < |\eta| < 3.2$, the algorithm has demonstrated an enhanced ability to distinguish genuine electrons from background noise. This improvement can be used to increase the number of forward electrons selected by the trigger. The resulting higher rates could be particularly beneficial for SM and BSM studies targeting forward lepton signatures.

A key achievement of this work was the successful adaptation of the NeuralRinger to handle the lower granularity of the forward calorimeter while maintaining efficiency. Performance studies using electron gun, $Z \to ee$ and dijet samples have shown that the NeuralRinger provides highly superior discrimination power compared to traditional cutbased methods. These findings make the NeuralRinger a highly interesting tool for the future ATLAS Run 4 upgrades, where data rates and pile-up effects will be significantly increased. The NeuralRinger for forward electrons becomes especially interesting to go along the Run 4 ITk upgrade which will provide tracking information up to $|\eta| = 4$. For a potential integration of the NeuralRinger for forward electrons in Run 4, however, complementary studies, using simulated samples with very high pile-up, must be carried out.

To further validate and enhance the NeuralRinger's performance for forward electrons, this thesis explored its integration into the Lorenzetti Showers framework, a general-purpose calorimetry simulation tool. Lorenzetti Showers provides a robust environment for modelling electromagnetic and hadronic showers with high precision, making it an ideal testbed for evaluating high-energy particle identification and reconstruction techniques.
By embedding the NeuralRinger within this framework, a complementary study of forward electron signatures was conducted, allowing to fine-tune the environment to replicate the conditions faced in the ATLAS study. It was revealed that the forward ring features obtained in Lorenzetti Showers simulation closely resemble the ones obeserved in the ATLAS studies. In the same manner, trainings of the NeuralRinger with those ring inputs showed very promising results. This implies a successful reproduction of the ATLAS environment with the Lorenzetti Showers simulation.
One of the major challenges addressed was the impact of pile-up on forward electron reconstruction. However, it proved to be very time-consuming to produce a sufficient quantity of events with very high pile-up values, as the ones expected for the HL-LHC. Therefore, the conducted studies were only comparing pile-up values of $\langle\mu\rangle = 0$ with $\langle\mu\rangle = 40$. Those studies demonstrated a high resilience of the NeuralRinger performance for this increase in pile-up. Unfortunately, this optimal behaviour cannot be extrapolated to much higher pile-up situations and will have to be evaluated in further studies. It is planned to allocate a significant amount of computing resources for several weeks to produce an appropriate sample of Lorenzetti Showers simulated events with high pile-up of $\langle\mu\rangle > 100$ to draw meaningful conclusions. This would allow for extensive studies to evaluate the NeruralRinger performance under extreme pile-up conditions. Thereby gained insights will be crucial for future upgrades to the ATLAS experiment, where increasing luminosity and detector occupancy demand for more sophisticated reconstruction techniques.
The successful validation of the NeuralRinger for forward electrons within Lorenzetti Showers further underscores the growing importance of AI in high-energy physics. As future colliders continue to push the frontiers of particle interactions, simulation-based refinements of ML approaches will play a pivotal role in improving signal detection and analysis precision. This work highlights how a synergistic approach between advanced simulation frameworks and AI-driven identification methods can significantly enhance the capabilities of modern collider experiments.

The final major component of this thesis was the search for top squark pair production in all-hadronic final states using ATLAS Run 2 and Run 3 data. SUSY remains one of the most promising theories for addressing fundamental limitations of the current physics understanding, including the hierarchy problem and the nature of dark matter. The search focused on scenarios, where both top squarks decay into a top quark and a neutralino, followed by hadronic decays of the top quarks. In the first steps, MC simulated samples of background processes with similar signatures to the targeted scenarios, were studied. Pre-selections were applied, ensuring good agreement between ATLAS data and the combined background yields. It was especially important to discriminate contributions from QCD dijet backgrounds which exhibited modelling issues.

A cutbased optimisation strategy was conducted to define event selections that maximise sensitivity to the top squark signal by suppressing backgrounds. This traditional cut-and-count method was conducted alongside a novel ML approach, serving as a baseline. The study leveraged jet signatures identified by a newly implemented GNN tagger to help distinguishing signal from background events. Other very important variables for this analysis were derived from missing transverse energy, which is very specific for collision events containing particles like neutralinos, which do not interact with the detector components. Together with more elaborate selections, preliminary SRs were defined, which achieved high sensitivities towards signals which have not yet been excluded by previous searches. These new SRs proved to outperform the selections from the previous Run 2 search, targeting the same scenarios in most of the relevant phase space.

The search can be concluded once ATLAS data from 2024 is fully processed for the analysis requirements. Once it is available, the final selections for SRs, CRs and VRs will be derived to compare the background yields with the data in the dedicated regions. This unblinding could reveal an excess in data, indicating strong hints for SUSY or other BSM physics models. However, if the data represents the SM predictions well, this analysis will help extending the exclusion limits of the considered models. In general, these findings contribute to the ongoing efforts in SUSY searches and help refine future experimental strategies in the search for new physics.

In summary, the work presented in this thesis highlights the impact of integrating advanced computational techniques with traditional experimental methodologies in high-energy physics. The adaptation of the NeuralRinger for forward electron identification has set the stage for improved object reconstruction in more challenging regions of the ATLAS detector. Furthermore, its successful integration within the Lorenzetti Showers framework has demonstrated the value of simulation-driven optimisation in enhancing ML models. Finally, the work put in the search for top squark pair production guarantees a great foundation for the analysis to be concluded once all required data is available. This search will further explore SUSY parameter space and provide valuable insights that will inform future searches at the LHC.

Looking ahead, several key directions emerge for future development of the NeuralRinger. First, it can be further refined by exploring novel deep learning archi-

tectures, such as GNNs or transformers, which could further enhance its classification capabilities. Additionally, its application to other particle signatures, such as photons and τ leptons, could expand its utility beyond electron identification.
With regards to SUSY searches, upcoming LHC runs will provide increased luminosity and improved detector performance, enabling the continued exploration of the top squark parameter space. ML based approaches, for guiding extensive searches or identifying intricate anomalies, may provide novel ways to identify rare signals from potential BSM physics in large datasets.
As the LHC enters its next phase of operation, the methodologies explored here will continue to play a crucial role in shaping the future of particle physics research.

Bibliography

[1] Lyndon Evans and Philip Bryant. LHC machine. *Journal of Instrumentation*, 3(08):S08001, August 2008. URL: `https://doi.org/10.1088%2F1748-0221%2F3%2F08%2Fs08001`, `doi:10.1088/1748-0221/3/08/s08001`.

[2] ATLAS Collaboration. The ATLAS Experiment at the CERN Large Hadron Collider. *Journal of Instrumentation*, 3(08):S08003, August 2008. URL: `https://doi.org/10.1088%2F1748-0221%2F3%2F08%2Fs08003`, `doi:10.1088/1748-0221/3/08/s08003`.

[3] Stephen P. Martin. A Supersymmetry Primer. *Advanced Series on Directions in High Energy Physics*, pages 1–98, July 1998. URL: `http://dx.doi.org/10.1142/9789812839657_0001`, `doi:10.1142/9789812839657_0001`.

[4] Steven Schramm. Machine learning at CERN: ATLAS, LHCb, and more. In *Proceedings of The 39th International Conference on High Energy Physics — PoS(ICHEP2018)*, volume 340, page 158, 2019. `doi:10.22323/1.340.0158`.

[5] ATLAS Collaboration. Graph neural network jet flavour tagging with the ATLAS detector. Technical report, CERN, Geneva, 2022. URL: `https://cds.cern.ch/record/2811135`.

[6] ATLAS Collaboration. Performance of electron and photon triggers in ATLAS during LHC Run 2. *The European Physical Journal C*, 80(47), January 2020. `doi:10.1140/epjc/s10052-019-7500-2`.

[7] M.V. Araújo et al. Lorenzetti Showers - A general-purpose framework for supporting signal reconstruction and triggering with calorimeters, February 2023. URL: `https://data.mendeley.com/datasets/sy64367452/1`, `doi:10.17632/sy64367452.1`.

[8] ATLAS Collaboration. Observation of a new particle in the search for the Standard Model Higgs boson with the ATLAS detector at the LHC. *Physics Letters B*, 716(1), September 2012. URL: `http://dx.doi.org/10.1016/j.physletb.2012.08.020`, `doi:10.1016/j.physletb.2012.08.020`.

[9] S. Navas et al. Review of particle physics. *Phys. Rev. D*, 110(3):030001, 2024. `doi:10.1103/PhysRevD.110.030001`.

[10] Peter W. Higgs. Broken symmetries and the masses of gauge bosons. *Phys. Rev. Lett.*, 13:508–509, October 1964. URL: `https://link.aps.org/doi/10.1103/PhysRevLett.13.508`, `doi:10.1103/PhysRevLett.13.508`.

[11] Steven Weinberg. A Model of Leptons. *Phys. Rev. Lett.*, 19:1264–1266, 1967. `doi:10.1103/PhysRevLett.19.1264`.

[12] A. Pich. The Standard Model of electroweak interactions, 2005. `arXiv:hep-ph/0502010`.

[13] ATLAS Collaboration. Standard Model Summary Plots June 2024. Technical report, CERN, Geneva, 2024. URL: `https://cds.cern.ch/record/2903866`.

[14] Albert Einstein. The foundation of the general theory of relativity. *Annalen der Physik*, 49:769–822, 1916. English translation. URL: `https://einsteinpapers.press.princeton.edu/vol6-trans/433`.

[15] Barbara Ryden. *Introduction to Cosmology*. Addison-Wesley, 2003.

[16] Planck Collaboration. Planck 2018 results. VI. cosmological parameters, 2018. `arXiv:1807.06209`.

[17] Jonathan L. Feng. Naturalness and the status of supersymmetry. *Annual Review of Nuclear and Particle Science*, 63:351–382, 2013. URL: `https://www.annualreviews.org/content/journals/10.1146/annurev-nucl-102010-130447`, `doi:https://doi.org/10.1146/annurev-nucl-102010-130447`.

[18] Klaus Wille. Synchrotron Radiation, January 2013. URL: `https://indico.cern.ch/event/218284/contributions/1520454/attachments/352184/490697/JUAS2013_Synchrotron_Radiation_1.pdf`.

[19] Maurizio Vretenar et al. *Linac4 design report*, volume 6 of *CERN Yellow Reports: Monographs*. CERN, Geneva, 2020. URL: `https://cds.cern.ch/record/2736208`, `doi:10.23731/CYRM-2020-006`.

[20] ATLAS Collaboration. ATLAS Event Displays: First 13.6 TeV collisions of 2023. General Photo, 2023. URL: `https://cds.cern.ch/record/2856820`.

[21] W. Herr and B. Muratori. Concept of luminosity. pages 361–377, 2003. URL: `http://doc.cern.ch/yellowrep/2006/2006-002/p361.pdf`.

[22] CMS Collaboration. The CMS experiment at the CERN LHC. *Journal of Instrumentation*, 3(08):S08004, August 2008. URL: `https://dx.doi.org/10.1088/1748-0221/3/08/S08004`, `doi:10.1088/1748-0221/3/08/S08004`.

[23] LHCb Collaboration. The LHCb Detector at the LHC. *Journal of Instrumentation*, 3(08):S08005, August 2008. URL: https://dx.doi.org/10.1088/1748-0221/3/08/S08005, doi:10.1088/1748-0221/3/08/S08005.

[24] ALICE Collaboration. The ALICE experiment at the CERN LHC. *Journal of Instrumentation*, 3(08):S08002, August 2008. URL: https://dx.doi.org/10.1088/1748-0221/3/08/S08002, doi:10.1088/1748-0221/3/08/S08002.

[25] ATLAS Collaboration. Measurement of underlying event characteristics using charged particles in pp collisions at $\sqrt{s} = 900$ GeV and 7 TeV with the ATLAS detector. *Physical Review D*, 83(11), May 2011. URL: http://dx.doi.org/10.1103/PhysRevD.83.112001, doi:10.1103/physrevd.83.112001.

[26] Karolos Potamianos. The upgraded Pixel detector and the commissioning of the Inner Detector tracking of the ATLAS experiment for Run-2 at the Large Hadron Collider, 2016. arXiv:1608.07850.

[27] Glenn F. Knoll. *Radiation Detection and Measurement, Fourth Edition*. Wiley, September 2010.

[28] T. Kawamoto et al. New Small Wheel Technical Design Report. Technical report, 2013. ATLAS New Small Wheel Technical Design Report. URL: https://cds.cern.ch/record/1552862.

[29] O. Aberle et al. *High-Luminosity Large Hadron Collider (HL-LHC): Technical design report*. CERN Yellow Reports: Monographs. CERN, Geneva, 2020. URL: https://cds.cern.ch/record/2749422, doi:10.23731/CYRM-2020-0010.

[30] ATLAS Collaboration. Technical Design Report for the ATLAS Inner Tracker Pixel Detector. Technical report, CERN, Geneva, 2017. URL: https://cds.cern.ch/record/2285585, doi:10.17181/CERN.FOZZ.ZP3Q.

[31] ATLAS Collaboration. Technical Design Report for the ATLAS Inner Tracker Strip Detector. Technical report, CERN, Geneva, 2017. URL: https://cds.cern.ch/record/2257755.

[32] ATLAS Collaboration. Technical Design Report for the Phase-II Upgrade of the ATLAS TDAQ System. Technical report, CERN, Geneva, 2017. URL: https://cds.cern.ch/record/2285584, doi:10.17181/CERN.2LBB.4IAL.

[33] ATLAS Collaboration. ATLAS Liquid Argon Calorimeter Phase-II Upgrade: Technical Design Report. Technical report, CERN, Geneva, 2017. URL: https://cds.cern.ch/record/2285582, doi:10.17181/CERN.6QIO.YGHO.

[34] ATLAS Collaboration. Technical Design Report for the Phase-II Upgrade of the ATLAS Tile Calorimeter. Technical report, CERN, Geneva, 2017. URL: https://cds.cern.ch/record/2285583.

[35] ATLAS Collaboration. Technical Design Report for the Phase-II Upgrade of the ATLAS Muon Spectrometer. Technical report, CERN, Geneva, 2017. URL: https://cds.cern.ch/record/2285580.

[36] ATLAS Collaboration. The ATLAS experiment at the CERN Large Hadron Collider: a description of the detector configuration for Run 3. *JINST*, 19(05):P05063, 2024. URL: https://cds.cern.ch/record/2859916, arXiv:2305.16623, doi:10.1088/1748-0221/19/05/P05063.

[37] ATLAS Collaboration. The ATLAS trigger system for LHC Run 3 and trigger performance in 2022. *Journal of Instrumentation*, 19(06):P06029, June 2024. URL: https://dx.doi.org/10.1088/1748-0221/19/06/P06029, doi:10.1088/1748-0221/19/06/P06029.

[38] Joao Pequenao and Paul Schaffner. How ATLAS detects particles: diagram of particle paths in the detector. 2013. URL: https://cds.cern.ch/record/1505342.

[39] H. Gray and J. Degenhardt. First collisions with the pixel detector, December 2009. URL: https://atlas.cern/updates/atlas-blog/first-collisions-pixel-detector.

[40] Pavel Weber. *ATLAS Calorimetry: Trigger, Simulation and Jet Calibration*. PhD thesis, 2008. URL: http://www.kip.uni-heidelberg.de/Veroeffentlichungen/details.php?id=1824.

[41] Matteo Cacciari, Gavin P. Salam, and Gregory Soyez. The anti-kt jet clustering algorithm. *Journal of High Energy Physics*, 2008(04):063–063, April 2008. URL: https://doi.org/10.1088%2F1126-6708%2F2008%2F04%2F063, doi:10.1088/1126-6708/2008/04/063.

[42] Panos Charitos. Deep learning and the quest for new physics at the LHC, December 2017. URL: https://ep-news.web.cern.ch/content/deep-learning-and-quest-new-physics-lhc.

[43] Arnaud Duperrin on behalf of the ATLAS Collaboration. Flavour tagging with graph neural networks with the ATLAS detector. Technical report, CERN, Geneva, March, 2023. URL: https://cds.cern.ch/record/2860610, arXiv:2306.04415.

[44] ATLAS Collaboration. Constituent-based top-quark tagging with the ATLAS detector. Technical Report ATL-PHYS-PUB-2022-039, CERN, 2022. ATLAS public note. URL: https://cds.cern.ch/record/2825328/files/ATL-PHYS-PUB-2022-039.pdf.

[45] João Pinto. An ensemble of neural networks for online filtering implemented in the ATLAS trigger system. *Journal of Physics: Conference Series*, 1162:012039, January 2019. doi:10.1088/1742-6596/1162/1/012039.

[46] Dan Guest, Kyle Cranmer, and Daniel Whiteson. Deep learning and its application to lhc physics. *Annual Review of Nuclear and Particle Science*, 68(1):161–181, October 2018. URL: http://dx.doi.org/10.1146/annurev-nucl-101917-021019, doi:10.1146/annurev-nucl-101917-021019.

[47] Marius-Constantin Popescu et al. Multilayer perceptron and neural networks. *WSEAS Transactions on Circuits and Systems*, 8, 07 2009.

[48] Andrea Apicella et al. A survey on modern trainable activation functions. *Neural Networks*, 138:14–32, 2021. URL: https://www.sciencedirect.com/science/article/pii/S0893608021000344, doi:https://doi.org/10.1016/j.neunet.2021.01.026.

[49] Jonathan Shlomi, Peter Battaglia, and Jean-Roch Vlimant. Graph neural networks in particle physics. *Machine Learning: Science and Technology*, 2(2):021001, January 2021. URL: http://dx.doi.org/10.1088/2632-2153/abbf9a, doi:10.1088/2632-2153/abbf9a.

[50] A. Rogozhnikov et al. New approaches for boosting to uniformity. *Journal of Instrumentation*, 10(03):T03002–T03002, March 2015. URL: http://dx.doi.org/10.1088/1748-0221/10/03/T03002, doi:10.1088/1748-0221/10/03/t03002.

[51] Werner Spolidoro Freund on behalf of the ATLAS Collaboration. An ensemble of neural networks for online electron filtering at the ATLAS experiment. *Journal of Physics: Conference Series*, 1525(1):012076, April 2020. URL: https://dx.doi.org/10.1088/1742-6596/1525/1/012076, doi:10.1088/1742-6596/1525/1/012076.

[52] ATLAS Collaboration. Electron performance measurements with the ATLAS detector using the 2010 LHC proton-proton collision data. *The European Physical Journal C*, 72(3), March 2012. URL: http://dx.doi.org/10.1140/epjc/s10052-012-1909-1, doi:10.1140/epjc/s10052-012-1909-1.

[53] ATLAS Collaboration. Software and computing for Run 3 of the ATLAS experiment at the LHC. *European Physical Journal C*, 2024. arXiv:2404.06335. URL: https://arxiv.org/abs/2404.06335, arXiv:2404.06335.

[54] Torbjörn Sjöstrand et al. An introduction to PYTHIA 8.2. *Computer Physics Communications*, 191:159–177, 2015. URL: https://www.sciencedirect.com/science/article/pii/S0010465515000442, doi:https://doi.org/10.1016/j.cpc.2015.01.024.

[55] Martín Abadi et al. TensorFlow: Large-scale machine learning on heterogeneous systems, 2015. Software available from tensorflow.org. URL: `https://www.tensorflow.org/`.

[56] S. Agostinelli et al. Geant4—a simulation toolkit. *Nuclear Instruments and Methods in Physics Research Section A: Accelerators, Spectrometers, Detectors and Associated Equipment*, 506(3):250–303, 2003. URL: `https://www.sciencedirect.com/science/article/pii/S0168900203013688`, `doi:https://doi.org/10.1016/S0168-9002(03)01368-8`.

[57] Rene Brun and Fons Rademakers. ROOT — An object oriented data analysis framework. *Nuclear Instruments and Methods in Physics Research Section A: Accelerators, Spectrometers, Detectors and Associated Equipment*, 389(1):81–86, 1997. New Computing Techniques in Physics Research V. URL: `https://www.sciencedirect.com/science/article/pii/S016890029700048X`, `doi:https://doi.org/10.1016/S0168-9002(97)00048-X`.

[58] ATLAS Collaboration. *ATLAS liquid-argon calorimeter*. Technical design report. CERN, Geneva, 1996. URL: `https://cds.cern.ch/record/331061`, `doi:10.17181/CERN.FWRW.FOOQ`.

[59] ATLAS Collaboration. SUSY July 2024 Summary Plot Update. Technical report, CERN, Geneva, 2024. URL: `https://cds.cern.ch/record/2904978`.

[60] ATLAS Collaboration. Search for a scalar partner of the top quark in the all-hadronic $t\bar{t}$ plus missing transverse momentum final state at $\sqrt{s} = 13$ tev with the ATLAS detector. *The European Physical Journal C*, 80(8):737, 2020. `doi:10.1140/epjc/s10052-020-8102-8`.

[61] J. Alwall et al. The automated computation of tree-level and next-to-leading order differential cross sections, and their matching to parton shower simulations. *Journal of High Energy Physics*, 2014(7), 2014. URL: `http://dx.doi.org/10.1007/JHEP07(2014)079`, `doi:10.1007/jhep07(2014)079`.

[62] Enrico Bothmann et al. Event generation with Sherpa 2.2. *SciPost Physics*, 7(3):034, 2019. URL: `https://arxiv.org/abs/1905.09127`, `doi:10.21468/SciPostPhys.7.3.034`.

[63] C. Oleari. The POWHEG BOX. *Nuclear Physics B - Proceedings Supplements*, 205–206:36–41, August 2010. URL: `http://dx.doi.org/10.1016/j.nuclphysbps.2010.08.016`, `doi:10.1016/j.nuclphysbps.2010.08.016`.

[64] ATLAS Collaboration. The simulation principle and performance of the ATLAS fast calorimeter simulation FastCaloSim. Technical report, CERN, Geneva, 2010. URL: `https://cds.cern.ch/record/1300517`.

[65] Alan Barr, Christopher Lester, and Phil Stephens. A variable for measuring masses at hadron colliders when missing energy is expected; mT2: the truth behind the glamour. *Journal of Physics G: Nuclear and Particle Physics*, 29(10):2343, September 2003. URL: https://dx.doi.org/10.1088/0954-3899/29/10/304, doi:10.1088/0954-3899/29/10/304.

[66] ATLAS Collaboration. Luminosity determination in pp collisions at $\sqrt{s} = 13$ TeV using the ATLAS detector at the LHC. *The European Physical Journal C*, 83(10), October 2023. URL: http://dx.doi.org/10.1140/epjc/s10052-023-11747-w, doi:10.1140/epjc/s10052-023-11747-w.

[67] ATLAS Collaboration. ATLAS Public Luminosity Results from Run 3, 2025. Accessed: 2025-02-27. URL: https://twiki.cern.ch/twiki/bin/view/AtlasPublic/LuminosityPublicResultsRun3.

[68] ATLAS Collaboration. 2015 start-up trigger menu and initial performance assessment of the ATLAS trigger using Run-2 data. Technical report, CERN, Geneva, 2016. URL: https://cds.cern.ch/record/2136007.

[69] ATLAS Collaboration. The ATLAS trigger system for LHC Run 3 and trigger performance in 2022. *Journal of Instrumentation*, 19(06):P06029, June 2024. URL: http://dx.doi.org/10.1088/1748-0221/19/06/P06029, doi:10.1088/1748-0221/19/06/p06029.

[70] Glen Cowan. Discovery sensitivity for a counting experiment with background uncertainty, May 2012. Accessed: 2025-02-28. URL: https://www.pp.rhul.ac.uk/~cowan/stat/notes/medsigNote.pdf.

[71] ATLAS Collaboration. Formulae for Estimating Significance. Technical report, CERN, Geneva, 2020. URL: https://cds.cern.ch/record/2736148.

[72] Matthew Feickert, Lukas Heinrich, and Giordon Stark. pyhf: pure-python implementation of histfactory with tensors and automatic differentiation, 2022. URL: https://arxiv.org/abs/2211.15838, arXiv:2211.15838.

[73] Prudhvi N. Bhattiprolu, Stephen P. Martin, and James D. Wells. Criteria for projected discovery and exclusion sensitivities of counting experiments. *The European Physical Journal C*, 81(2), February 2021. URL: http://dx.doi.org/10.1140/epjc/s10052-020-08819-6, doi:10.1140/epjc/s10052-020-08819-6.

Appendix

Here further ATLAS Run 2 and Run 3 distributions after applying the pre-selections from Table 6.3 are shown. They are extending the distributions shown in the end of Section 6.3. Three signal samples were added to blind bins in grey if applicable where at least one of the signals exceeds 10% of the total background.

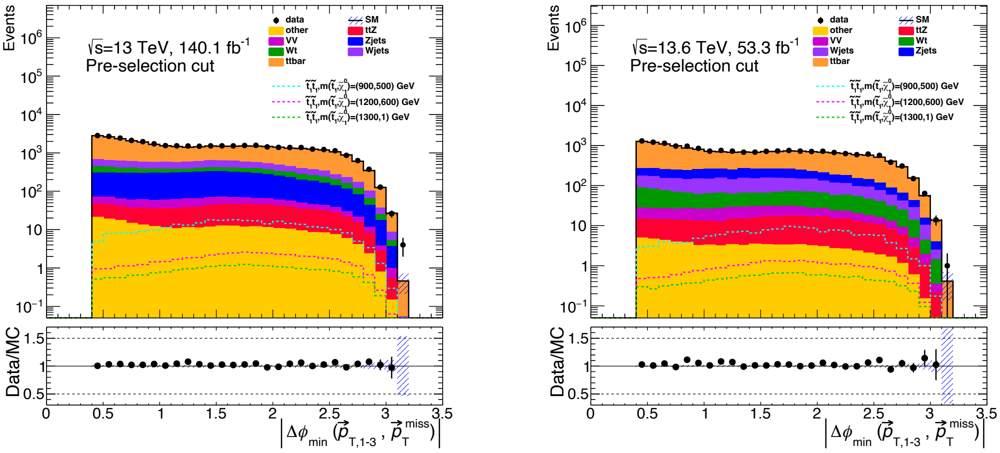

(a) Run 2 $|\Delta\phi_{\min}(\vec{p}_{\mathrm{T},1-3},\vec{p}_{\mathrm{T}}^{\,\mathrm{miss}})|$

(b) Run 3 $|\Delta\phi_{\min}(\vec{p}_{\mathrm{T},1-3},\vec{p}_{\mathrm{T}}^{\,\mathrm{miss}})|$

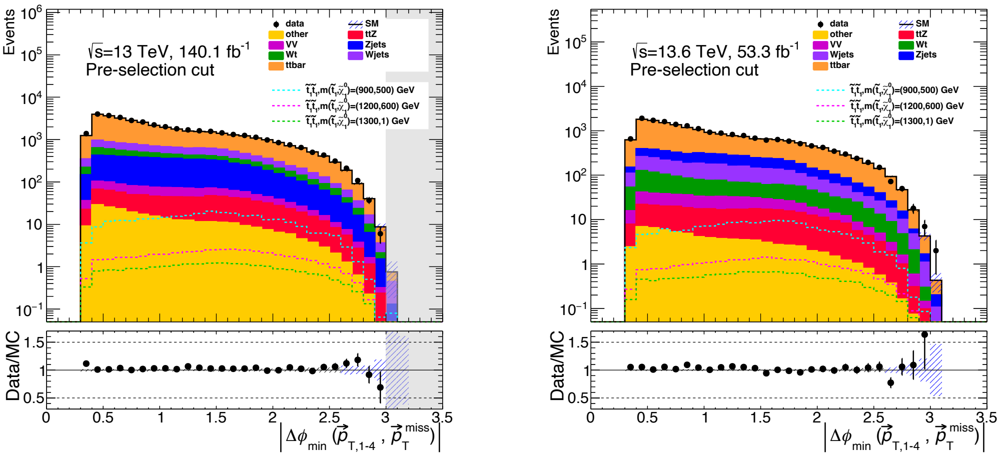

(c) Run 2 $|\Delta\phi_{\min}(\vec{p}_{\mathrm{T},1-4},\vec{p}_{\mathrm{T}}^{\,\mathrm{miss}})|$

(d) Run 3 $|\Delta\phi_{\min}(\vec{p}_{\mathrm{T},1-4},\vec{p}_{\mathrm{T}}^{\,\mathrm{miss}})|$

Figure A.1: ATLAS Run 2 and Run 3 $|\Delta\phi_{\min}(\vec{p}_{\mathrm{T},1-\mathrm{n}},\vec{p}_{\mathrm{T}}^{\,\mathrm{miss}})|$ distributions after applying the pre-selections from Table 6.3.

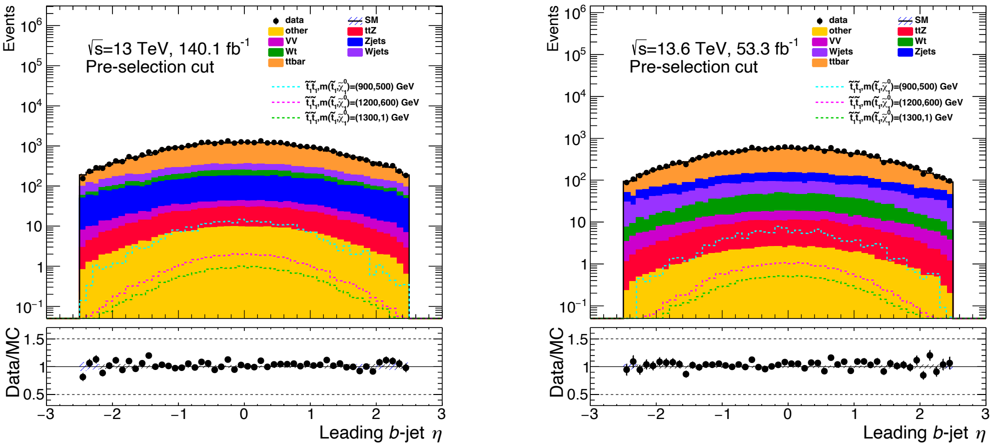

(a) Run 2 leading b-jet η (b) Run 3 leading b-jet η

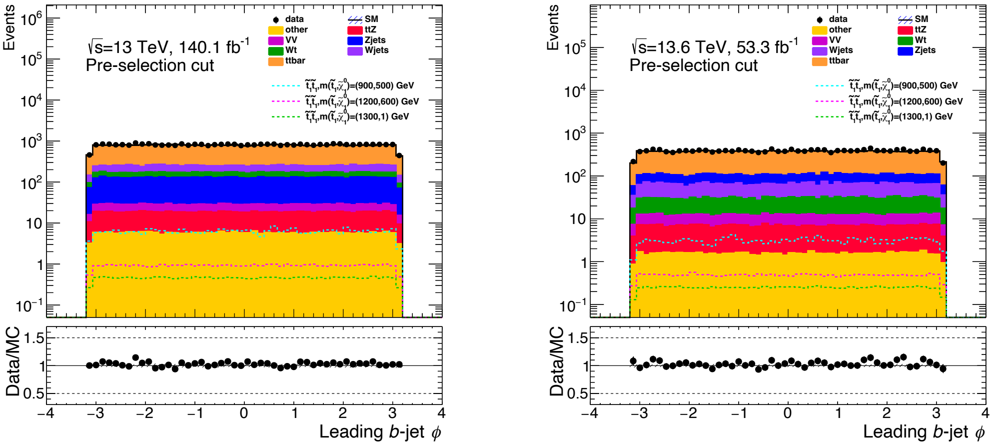

(c) Run 2 leading b-jet ϕ (d) Run 3 leading b-jet ϕ

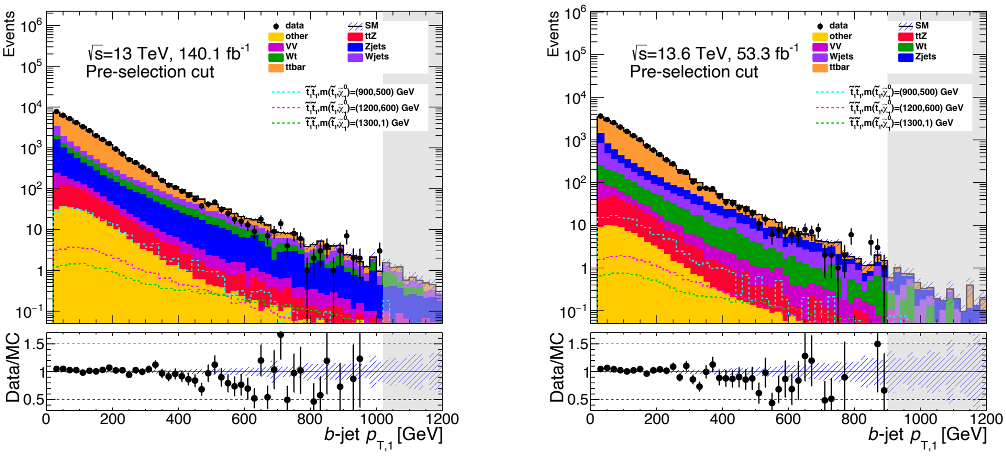

(e) Run 2 leading b-jet p_{T} (f) Run 3 leading b-jet p_{T}

Figure A.2: ATLAS Run 2 and Run 3 leading b-jet η, ϕ and p_{T} distributions after applying the pre-selections from Table 6.3.

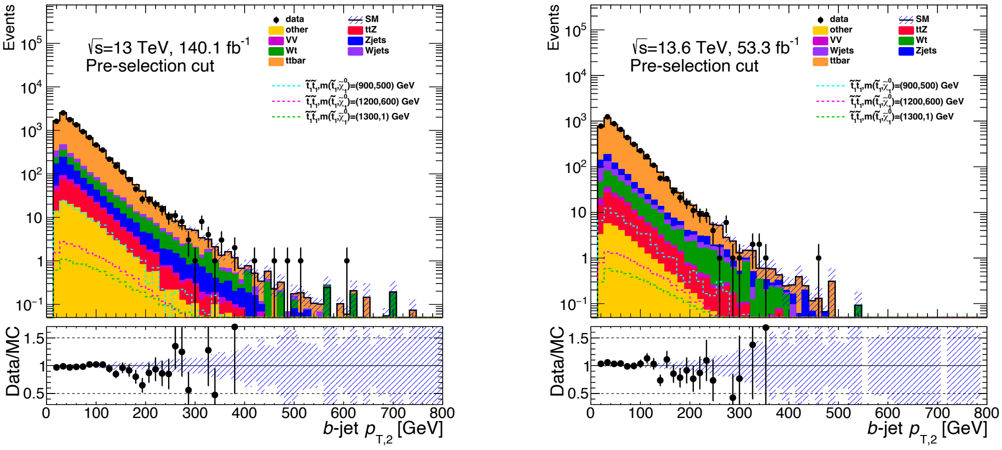

(a) Run 2 subleading b-jet p_{T} (b) Run 3 subleading b-jet p_{T}

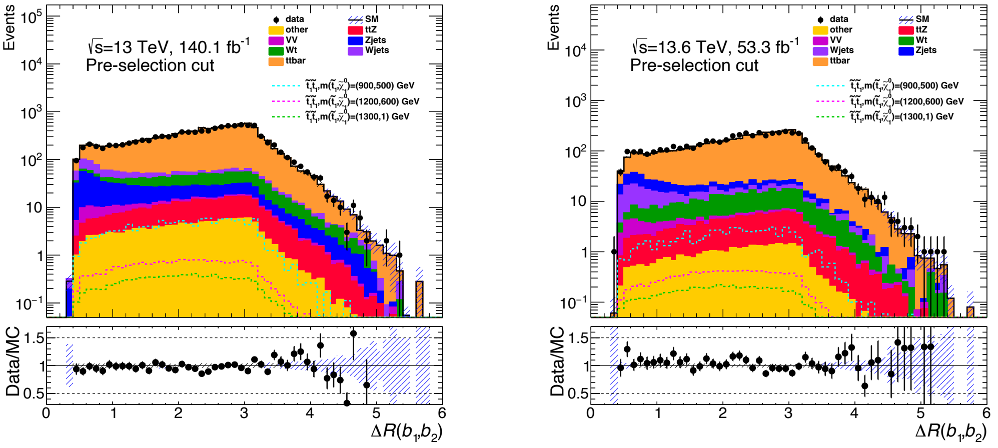

(c) Run 2 $\Delta R(b_1, b_2)$ (d) Run 3 $\Delta R(b_1, b_2)$

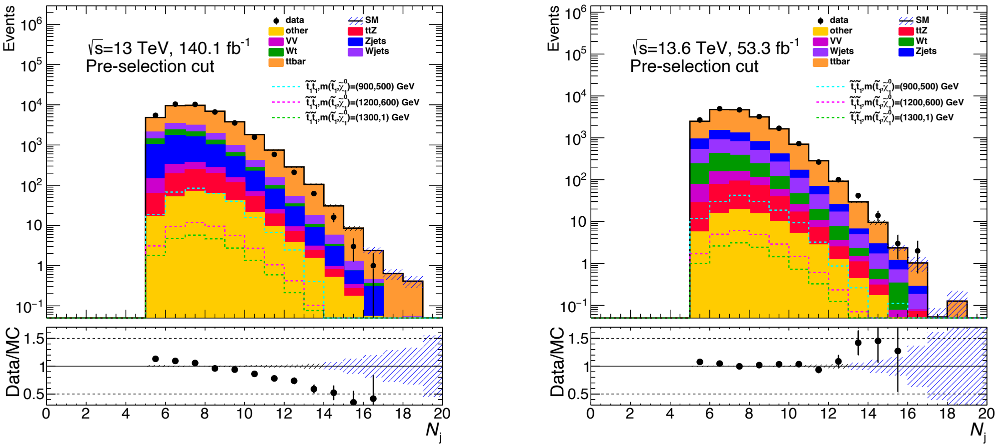

(e) Run 2 number of jets (f) Run 3 number of jets

Figure A.3: ATLAS Run 2 and Run 3 subleading b-jet p_{T}, $\Delta R(b_1, b_2)$ and N_{j} distributions after applying the pre-selections from Table 6.3.

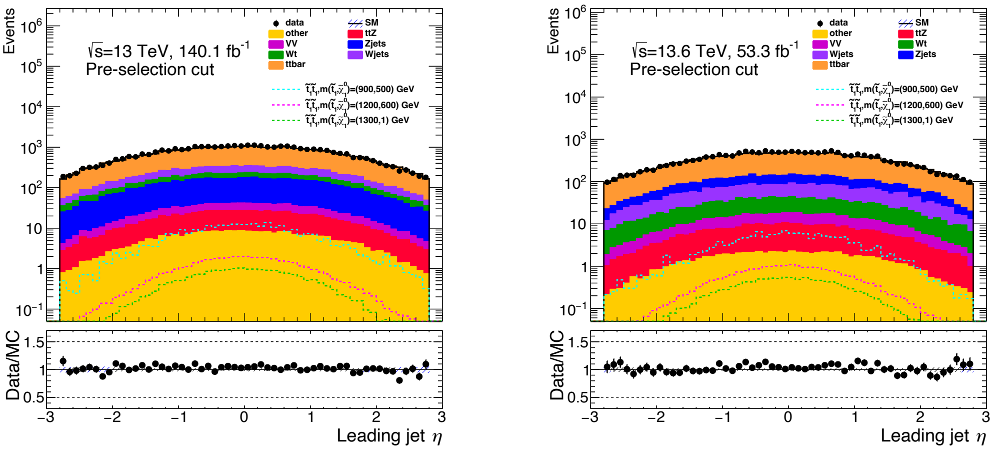

(a) Run 2 leading jet η (b) Run 3 leading jet η

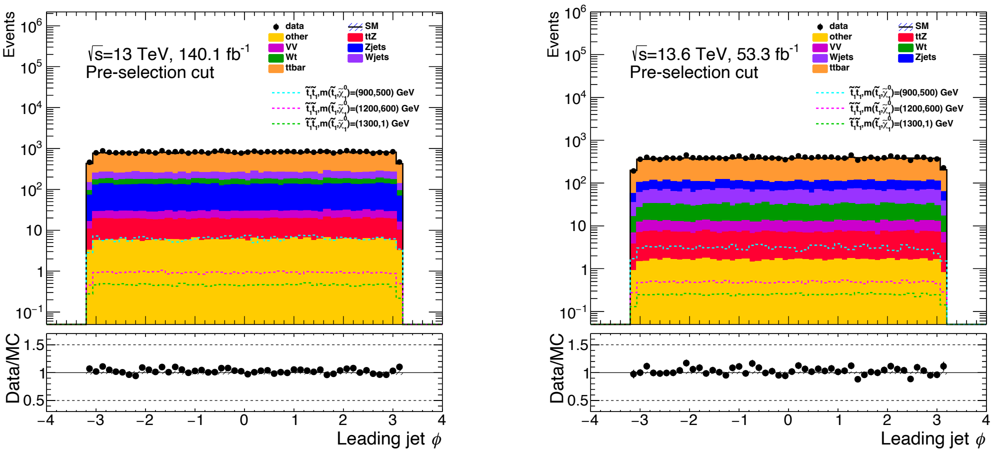

(c) Run 2 leading jet ϕ (d) Run 3 leading jet ϕ

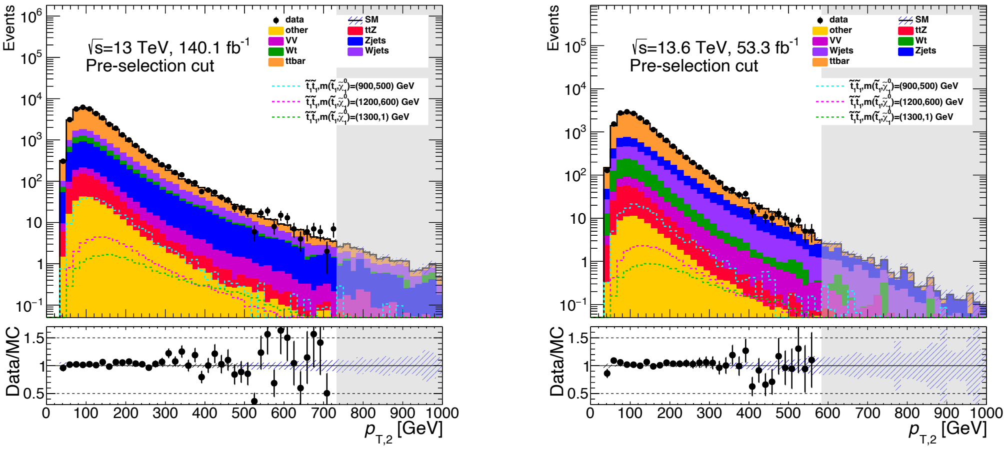

(e) Run 2 subleading jet p_{T} (f) Run 3 subleading jet p_{T}

Figure A.4: ATLAS Run 2 and Run 3 leading jet η and ϕ and subleading jet p_{T} distributions after applying the pre-selections from Table 6.3.

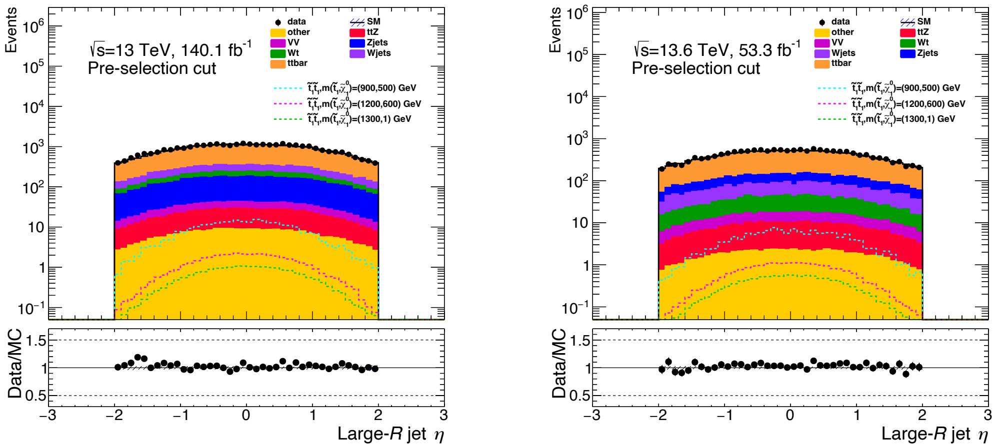

(a) Run 2 leading large-R jet η (b) Run 3 leading large-R jet η

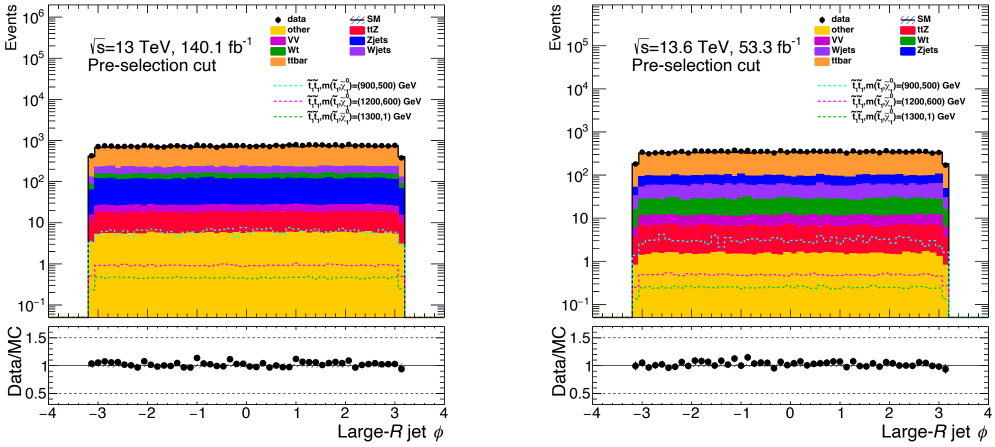

(c) Run 2 leading large-R jet ϕ (d) Run 3 leading large-R jet ϕ

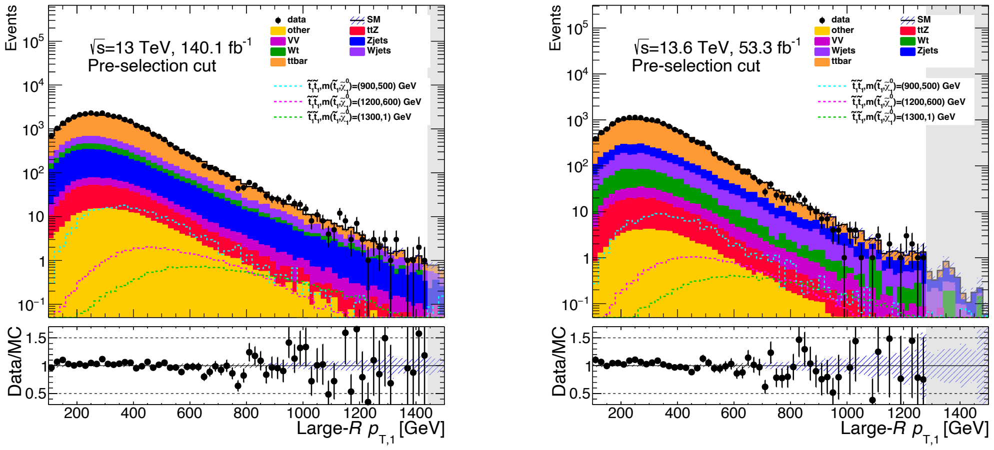

(e) Run 2 large-R $p_{\mathrm{T},1}$ (f) Run 3 large-R $p_{\mathrm{T},1}$

Figure A.5: ATLAS Run 2 and Run 3 leading large-R jet η, ϕ and p_{T} distributions after applying the pre-selections from Table 6.3.

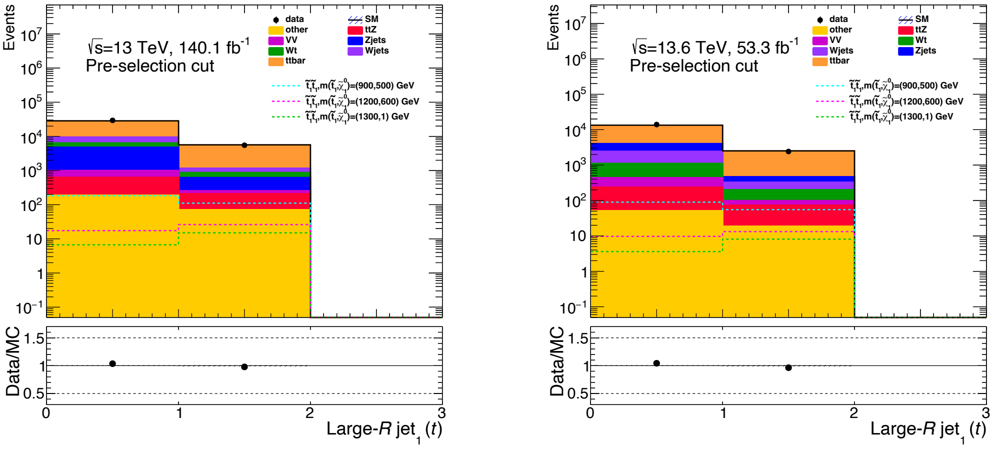

(a) Run 2 large-R jet$_1$ (t) (b) Run 3 large-R jet$_1$ (t)

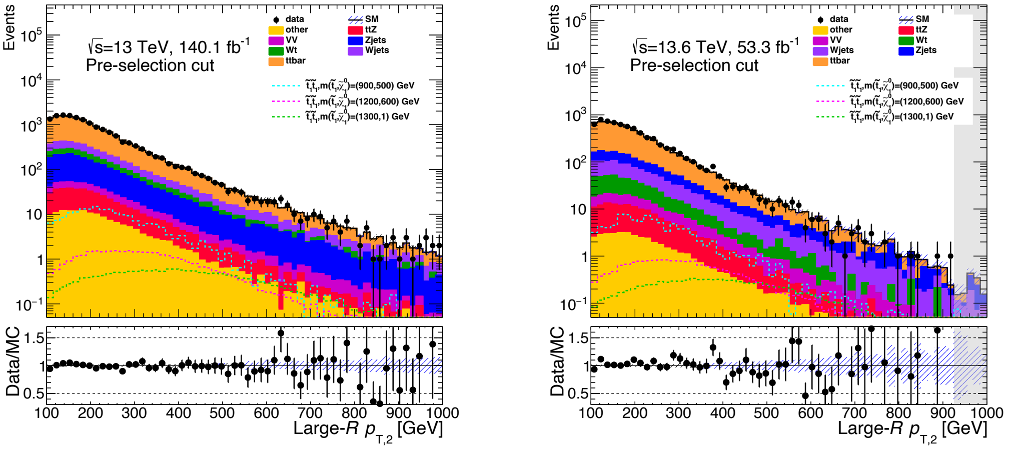

(c) Run 2 large-R $p_{\mathrm{T},2}$ (d) Run 3 large-R $p_{\mathrm{T},2}$

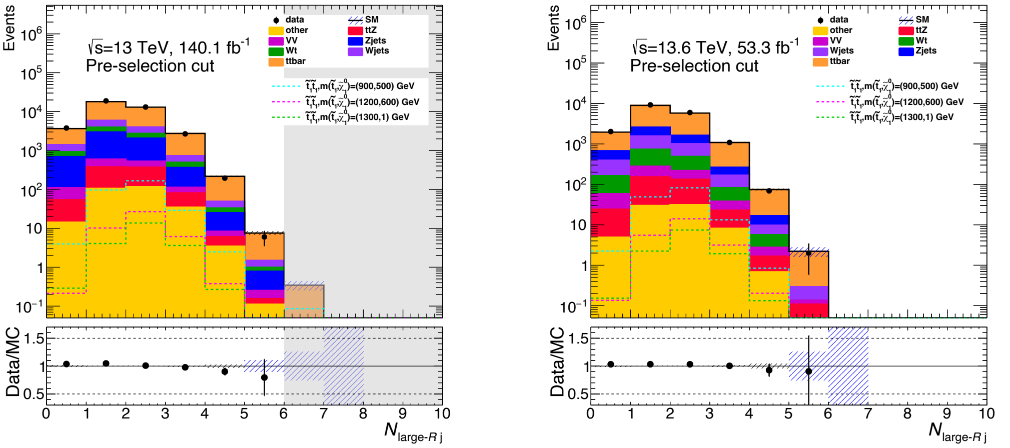

(e) Run 2 number of large-R jets (f) Run 3 number of large-R jets

Figure A.6: ATLAS Run 2 and Run 3 large-R jet$_1$ (t), subleading large-R jet p_T and $N_{\text{large-}R\text{ j}}$ distributions after applying the pre-selections from Table 6.3.

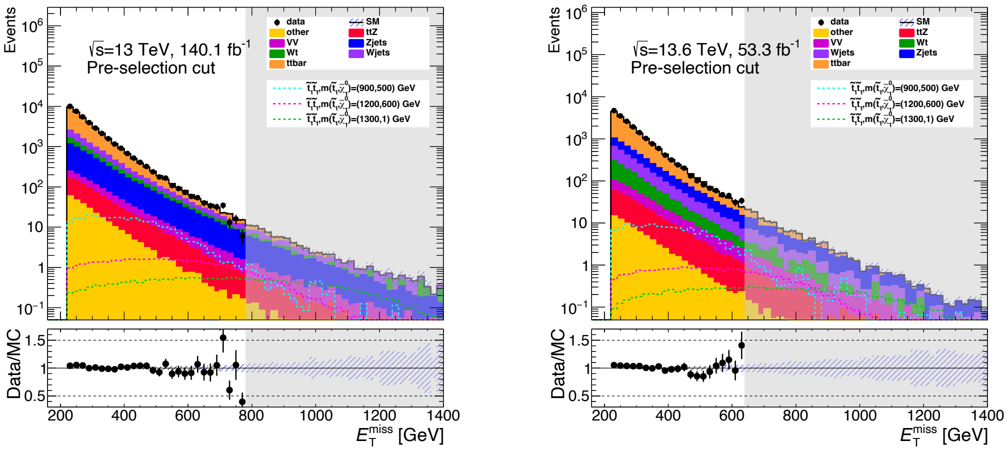

(a) Run 2 $E_{\mathrm{T}}^{\mathrm{miss}}$ (b) Run 3 $E_{\mathrm{T}}^{\mathrm{miss}}$

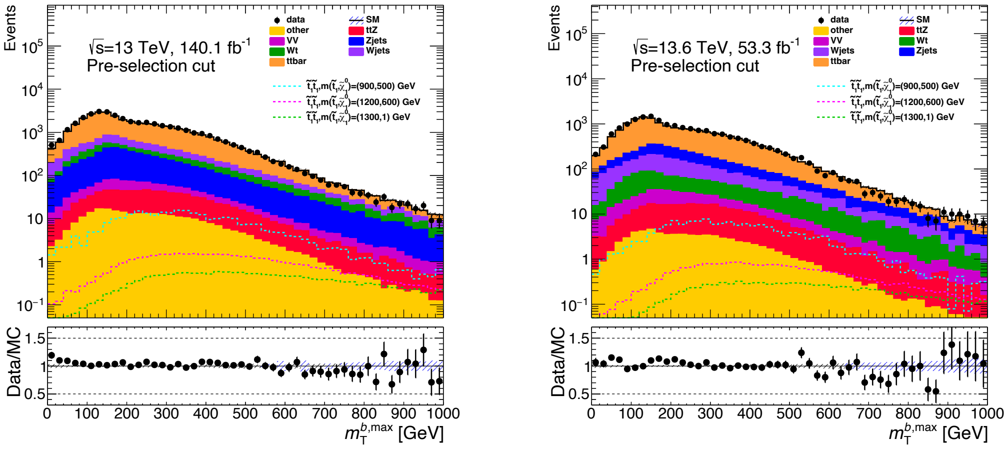

(c) Run 2 $m_{\mathrm{T}}^{b,\mathrm{max}}$ (d) Run 3 $m_{\mathrm{T}}^{b,\mathrm{max}}$

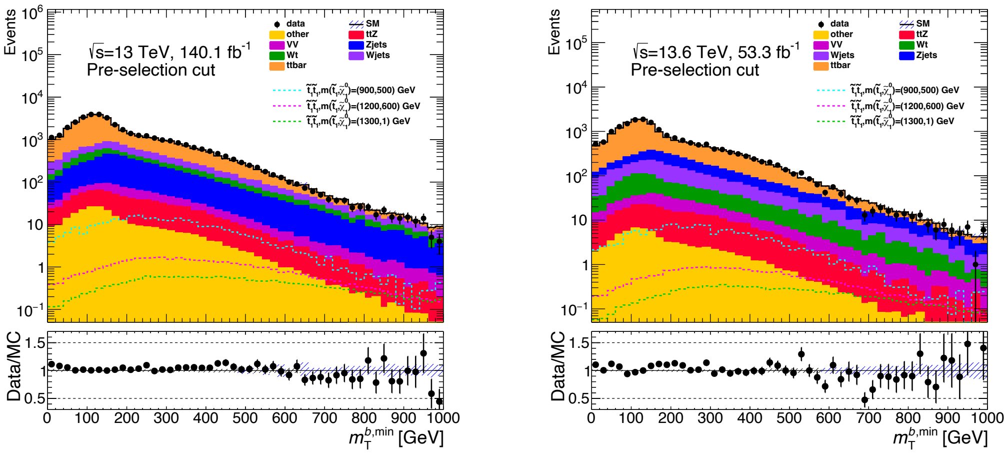

(e) Run 2 $m_{\mathrm{T}}^{b,\mathrm{min}}$ (f) Run 3 $m_{\mathrm{T}}^{b,\mathrm{min}}$

Figure A.7: ATLAS Run 2 and Run 3 $E_{\mathrm{T}}^{\mathrm{miss}}$, $m_{\mathrm{T}}^{b,\mathrm{max}}$ and $m_{\mathrm{T}}^{b,\mathrm{min}}$ distributions after applying the pre-selections from Table 6.3.

Declaration of consent

on the basis of Article 18 of the PromR Phil.-nat. 19

Name/First Name:

Registration Number:

Study program:

Bachelor ☐ Master ☐ Dissertation ☐

Title of the thesis:

Supervisor:

I declare herewith that this thesis is my own work and that I have not used any sources other than those stated. I have indicated the adoption of quotations as well as thoughts taken from other authors as such in the thesis. I am aware that the Senate pursuant to Article 36 paragraph 1 litera r of the University Act of September 5th, 1996 and Article 69 of the University Statute of June 7th, 2011 is authorized to revoke the doctoral degree awarded on the basis of this thesis.

For the purposes of evaluation and verification of compliance with the declaration of originality and the regulations governing plagiarism, I hereby grant the University of Bern the right to process my personal data and to perform the acts of use this requires, in particular, to reproduce the written thesis and to store it permanently in a database, and to use said database, or to make said database available, to enable comparison with theses submitted by others.

Place/Date

M. Schet

Signature